Experimental Simulation of Reduction of Erosion Damage in Dies Used in Aluminium Casting

Ali Hashim Mohammed

Summary

A review of damage mechanisms in dies used for aluminium casting revealed that erosion due to the molten/semi-solid aluminium droplets entering the die was a major cause of wear. It was also clear that no laboratory tests were available to simulate the die/aluminium interactions. Existing test methods use actual casting machines which is time consuming and expensive.

The aim of this work was to develop a laboratory test and then to use it to evaluate current die materials as well as possible treatments/coatings that could be used to reduce the problem. A test was developed that used a shot blaster to propel aluminium balls at flat or cylindrical specimens (to cover possible die geometry variations). It was also possible to heat the specimens.

A pulsed method was used for the ball application to simulate multiple castings. Ball motion was evaluated and specimen wear characterised across a range of ball impact velocities. Different impact angles were used for flat specimens and for cylindrical specimens central and eccentric ball flows were used.

High speed video was used to investigate the actual impact velocities and also observe the behaviour of the aluminium balls impacting at different angles to see how the wear mechanisms actually occurred. Four regimes of particles behaviour: impact only, impact and sliding, sliding only and pressed only were seen.

Wear testing showed that wear increased with impact velocity, but different effects were seen when varying the impact angle as seen previously in studies on erosive wear of spherical solid particles for ductile materials. At 30° impacts, a higher erosion rate was seen than those at 60° and 90° impact angle. Zig zag indentations were seen at high impact angles indicating a higher displacement and removal of material by plastic flow keeps advancing downstream until the individual peaks and valleys meet. Wear rate results highlighted four periods with exposure time: incubation period, acceleration or accumulation period, deceleration period and steady-state period.

Tests on cylindrical H13 specimens showed that a high amount of wear occurred at an eccentric position due to increased cutting action. The effects of elevation the temperature in the system on the erosion behaviour were also studied. At high temperature materials soften and the erosion increased.

Treated surfaces were also studied to evaluate selected candidate coatings and generate data on their wear resistance. The results showed that coating can have a large effect on erosion damage. The knowledge gained by experiment has contributed to the understanding of die failure and will increase die lives as well as reducing maintenance, machine downtime and labour costs.

Contents

Acknowledgements

Dedication

Firstly, I would like to dedicate this work to God. Thanks for being always with me.

I also dedicate of this work to my parents, brothers and sisters. They always were my support during all this period. Thank you very much.

Also, I would like to dedicate to my wife, my sons Mustafa and Hussain for their patience throughout all these years.

1

Introduction

1.1 Statement of the problem

The technology of die casting is complex, and includes many subjects. Each die casting currently in production presents a challenge for the improvement of its output and quality. Experience with metal molds for aluminium permanent mold casting has established that the primary cause for failure is erosive wear as shown in Figure 1.1 [1].

Figure 1.1 Die surface pits and cracks after less than a thousand shots [1].

Erosive wear is material removal by impingement of solid particles or liquid droplets. Erosion can cause severe damage to the die resulting in loss of equipment and production downtime. The erosion problem in dies is due to the high velocity of melt alloys hitting the parts of the die cavity typically 30-60 m s^{-1} for aluminium alloys [2]. In addition, it is important to mention that with respect to the molten metal used in die casting, currently many efforts to replace fully molten with semi-solid metalworking processes. This is due to the minimal time required for solidification, it means though that the erosive wear failure will increase. The progression of a die cavity filling with a molten metal front is different depending on the casting process and the complex geometry of the die cavity [3, 4]. Typically, the first metal to enter the die strikes the far side of the die cavity and solidifies immediately. A graphical illustration of this phenomenon is shown in Figure 1.2.
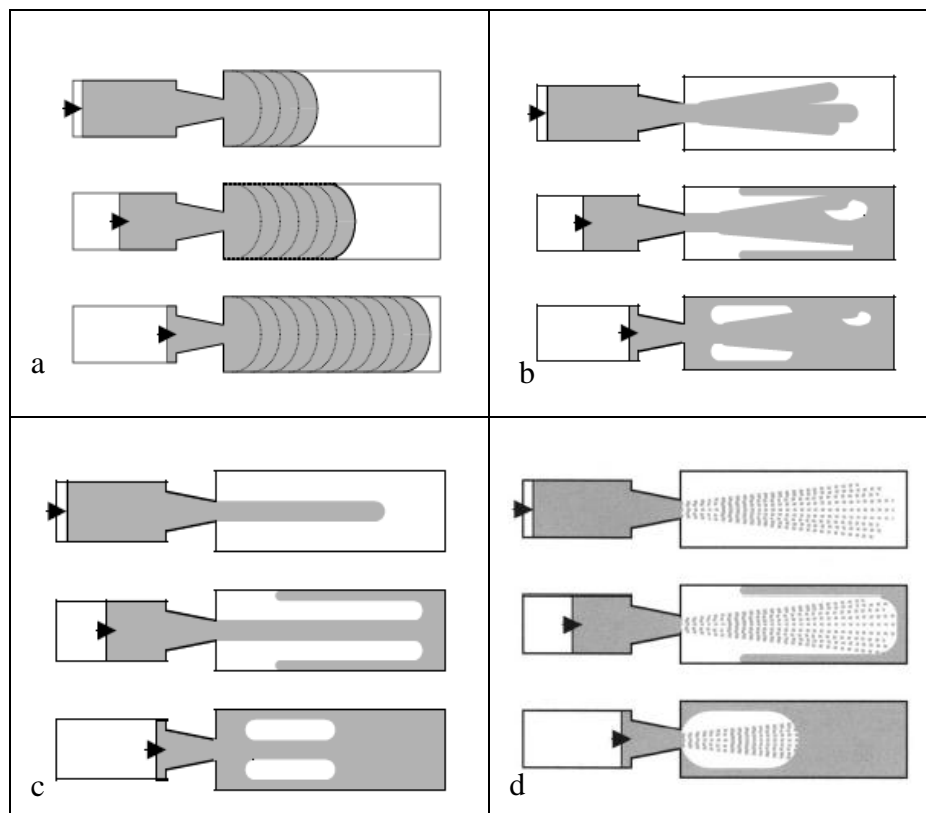
Figure 1.2 Progression of a die cavity filling with, (a) planar metal, (b, c) nonplanar metal, (d) atomized metal [3].

There are two problems which this thesis will deal with. One is the laboratory measurement and the other is the study of erosive wear of H13 die material steel with different types of impacts.

There are three methods by which erosive wear at the die can be studied. These are by using industrial field, modeling, and laboratory based measurements. Each of these techniques have their respective benefits. In the case of the industrial field, in which one can measure the wear directly, the wear being a gradual loss of material could be long term taking more than 100 000 shots and costly. The alternative is laboratory measurement which is widely used in studies. Laboratory tests generally offer greater controllability of test parameters than industrial tests such as, impact angle, impact velocity, mass loss and exposure time.

This study offers one of the closest representations of the actual processes in aluminium die casting to accelerate the wear effects. There is little scientific knowledge available on performance of die material and coating materials in the field of impact and erosive wear and there is no standard test which they need to pass before they are used in the productions. Therefore, a blast testing machine was utilised in order to closely measure the performance treated and untreated surface materials in terms of wear. These surfaces were analysed using Scanning Electron Microscope (SEM) and Optical Microscopes each with a different level of resolution. The die geometry is complex and the injected metal is impacting many different geometries. The erosive wear happens on flat and curved surfaces in the die. The strongest erosion is at the gate and core where the molten jet hits directly. In many applications surfaces of die casting die could be experiencing different wear mechanisms acting independently as a result of variations in stages of the wear process or different wear scenarios, such as: solid particle impingement, solid particles entrained in molten metal or slurry erosion, liquid droplet or jets impingement, cavitations erosion as result of the formation and collapse of bubbles that contain vapours or gas, and the partially solidified or semi-solid state of the eroding metal [5-7].

There are many ways to extend the life of die casting tools, that can reduce the problems identified above such as:

- Choice of a suitable metal, manufacturing parameters, optimum heat treatment for a tool and coatings.

- Development of new wear resistant die materials.

- Develop better lubricants that can protect the die material.

- Redesign the dies to reduce thermo-mechanical loads.

It is possible to observe from the above, that some like the redesign of the dies are extremely difficult to carry out, as well as developing new cast or die materials. It is clear that coating to improve the wear resistance of the die surface shows the best promise for increasing life as well as reducing maintenance, machine downtime and labour costs.

1.2 Aims and Objectives

The aim of the study was to develop an improved test for assessing the effects of impacting particles of liquid or semi-solid aluminium onto die materials, and to use this to identify possible coatings/surface treatments to reduce wear. The objectives of the work were as follows:

- Find out what wear mechanisms are involved during the wear process of the dies used in aluminium die coating, by examination of actual dies and studying the literature.

- Develop a laboratory test method for propelling particles at a die material.

- Fully analyse the particle motion using high speed video techniques.

- Carry out a full test programme using the test method to assess the effects of contact condition, geometry, particle velocity, material hardness, temperature etc.

- Fully analyse tested specimens using a range of techniques such as optical microscopy, nanoindentation etc.

- Investigate the coatings/surface treatment literature to identify candidates for testing and carry out tests.

1.3 Thesis Layout

- Chapter 2. Presents the methodology of die casting with focus on aluminium die casting.

- Chapter 3. Failure mechanisms of dies for aluminium casting are presented.

- Chapter 4. An overview of liquid erosion and solid particle erosion (SPE) are presented extensively, where it is possible to observe the similarities in erosion between the liquid/solid particles and a description corresponding to different wear mechanisms such as adhesion, abrasion and erosive wear.

- Chapter 5. A description of the new test approach and a motion analysis of the aluminium balls in two cases: firstly, when aluminium balls impact a flat target and secondly, when they impact a cylindrical surface.

- Chapter 6. Use of the new technique test to evaluate the erosion damage on flat H13 specimens with three different impact angles is presented.

- Chapter 7. Solid particle erosion tests on cylindrical H13 surfaces, specimens mounted in two positions: central to and offset from the particle flow.

- Chapter 8. Study of the effects of a temperature on the erosion behaviour of H13 steel (at $200^{o}C$ and $400^{o}C$).

- Chapter 9. Presents analysis of hardness and modulus of the work hardened layers on the cylindrical H13 steel specimen.

- Chapter 10. Introduction of surface coatings and treatments and identification of test candidates and study of the erosion damage results obtained from the candidate coatings.

- Chapter 11. General Conclusions.

- Chapter 12. References.

<div align="right">

2

</div>

Die Casting

2.1 Introduction

This chapter describes and illustrates the die casting process and the technology used. Detail is then given of ferrous casting alloys and non-ferrous casting alloys. Finally, extensive descriptions and illustrations are presented for aluminium die casting.

2.2 Die casting overview

Die casting is a high volume production process of forcing metal under high pressure into a mold called a die. The high pressure ranges from 7 to 700 MPa. Because of the high pressures involved in die casting, casting processes are usually major productions. Excellent dimensional accuracy and smooth surfaces can be achieved though, without machining except to remove the flash around the edge and possible drilling and tapping of holes. Casting can produce very complex shapes with a high degree of accuracy. Parts with internal cavities and hollow sections with smooth surfaces can be produced as shown in Figure 2.1 which illustrates samples of components manufactured using high pressure die casting [3].
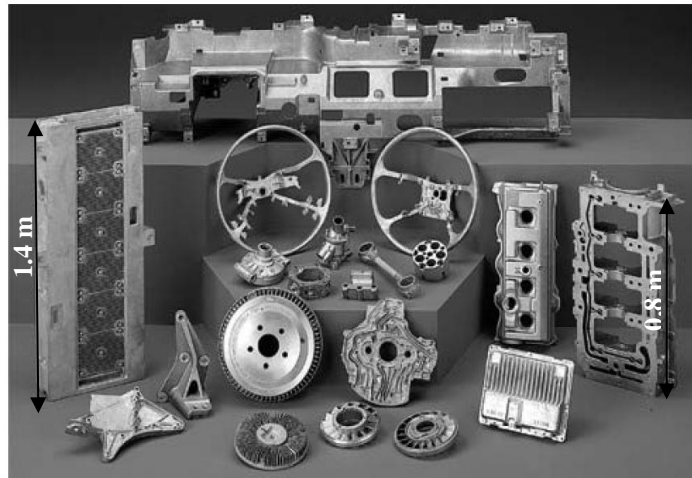
Figure 2.1 Components manufactured using high pressure die casting [3].

Die casting has incredibly strong features, it is considered one of the fastest methods of production and the most economical to make metal products, when compared to other manufacturing methods, such as, rolling or forging. It can be used to make components high, but with high production and there is less need for subsequent manufacturing operations [8, 9]. Two basic types of die cast systems are available: hot-chamber and cold-chamber systems. Most die castings are made from non-ferrous metals, specifically aluminium, magnesium, copper, lead and tin based alloys, although ferrous metal die castings are possible. For example, mild steel casting, cast iron casting, aluminium bronze castings, stainless steel casting, phosphorus bronze castings and grey cast iron casting. The die casting method is especially suited for applications where a large quantity of small to medium sized parts is needed with good detail, a fine surface quality and dimensional consistency [10, 11].

Much progress has also been made in die casting techniques during the past five decades. The control of die casting variables, such as metal and die temperatures, pressures, and shot speeds, is much advanced [12]. Considerable improvement has been made in the evolution from the first manually operated plunger type die casting machine, which required the work of three or four men to operate, to the present, practically automatic plunger machine, which requires only one man to control and which performs up to 300 to 500 casting cycles per hour.

2.3 Die casting dies

A casting die is specifically designed for use in the die casting process. A die casting must be split into two halves so that the casting can be removed after it has been formed. These two halves of the casting die are called the cover die or stationary half and moving half or ejector die. The cover die is fastened to the stationary platen on the casting machine and does not move during the casting cycle. The ejector half is mounted on the movable platen of the machine. The surfaces of the halves must be smooth and finished to fit closely together, otherwise molten metal could escape, if a gap exists, when metal is forced into the cavity under pressure. All dies must be designed to fit the specific die casting machine they are going to be used in. Essential die components of a simple die casting die are shown in Figure 2.2, these include the die base or ejector box, ejector plate, ejector pins, surface pins and, of course, a means of removing die components [13, 14]. The ejector pins, mounted in the ejector plate, are used to push the solidified part out of the die, and slide through holes in the ejector die half. When the machine opens, this plate is pushed forward by some means usually by a rack and pinion. In addition to these components there are other members that must be considered to allow the machine to perform its function. Slide cores are used to form internal passageways or additional geometry on the exterior of the part. Die gates and runners are used to ensure paths exit to allow the metal to flow to all parts of the cavity. Core pins are used to create holes in the die casting at precise sizes and locations. Vents, which provide a path of escape for entrapped air and release gases. Water lines are critical to cool the liquid metal in an even manner.

To obtain economical life for any die, the steel used in manufacturing the die must be of a suitable composition and must be prepared under the best possible steel mill conditions. The die assembly, ejector and cover die blocks actually represent the major problem in proper selection of materials because they are exposed to the most severe operating conditions.

(a)

(b)
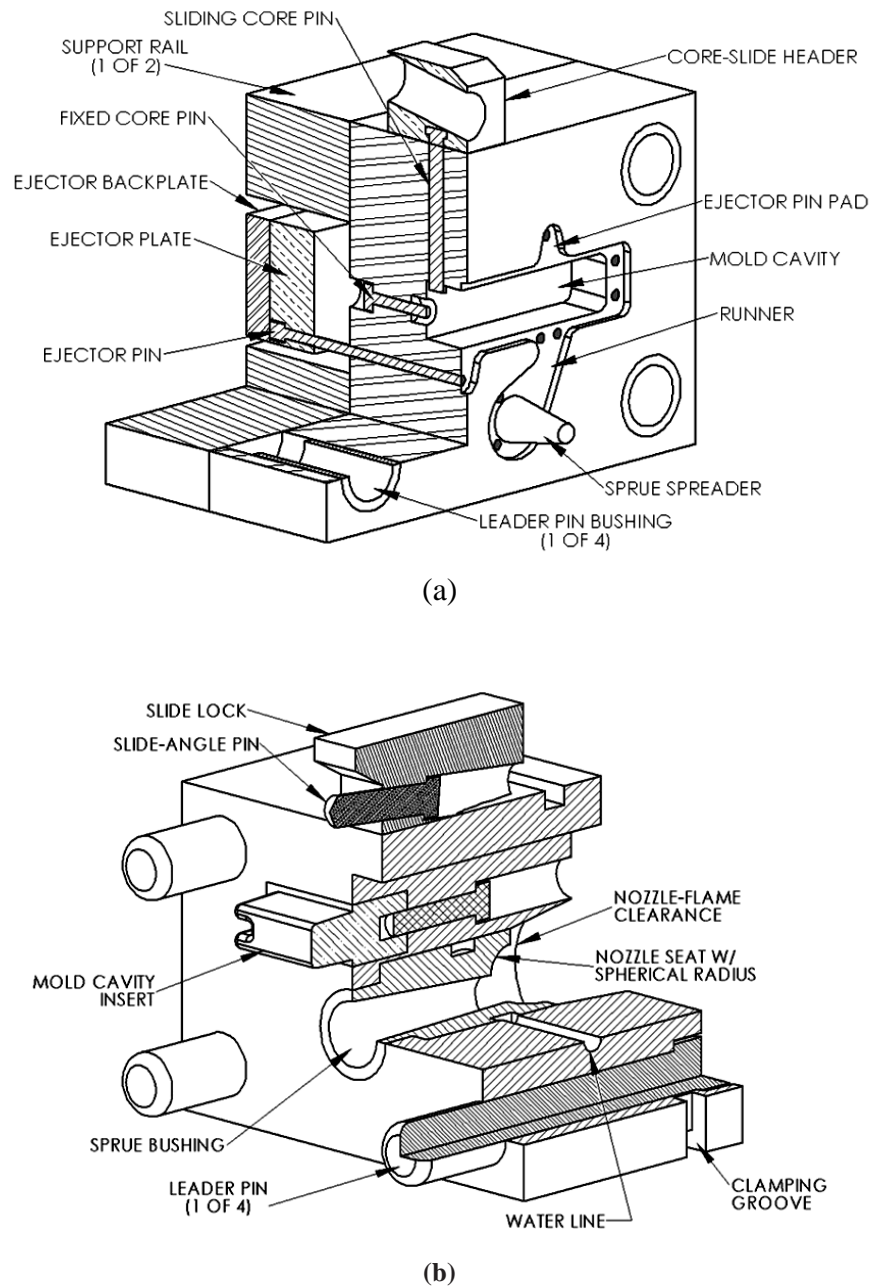
Figure 2.2 Components of a simple die casting die, (a) Ejector die half, (b) Cover die half.

The die casting process has significant thermal stresses due to the cycling of hot metal across the face of the tool. Also other factors must be considered to avoid the failures in dies such as: die design, heat treatment, and care and handling of the die in production, any errors in these factors can result in an uneconomical die life even with the best type and quality of die steel [15, 16].

The steel used in die casting should have the following characteristics:

- Good machinability.

- High resistance to erosive wear and heat checking.

- Sufficient toughness, strength and hardness resist deformation in service.

- Dimensional stability in heat treatment.

Die steels for casting aluminium and magnesium must have a special composition because aluminium alloys aggressively attack the die steel chemically causing wear. A die steel type that is often used has a nominal composition of 0.4%C, 0.4%Mg, 1%Si, 5.25%Cr, 1%Mo, and 1% V. The cavity section of the tool is made from a premium steel alloy, such as H13, to stand up to this stress. Table 2.1 shows the mechanical properties of H13 steel [17].

Table 2.1 Mechanical properties of H13 steel.

H13 Steel Mechanical Properties	
Tensile Strength, Yield (MPa)	1650
Elongation at Break	9%
Poisson's Ratio	0.3
Hardness (H_v)	300-400
Modulus of Elasticity (GPa)	210

2.4 Die casting process

The die casting process is fundamentally simple and consists of injecting the casting alloy under high pressure into a steel mold called a die. There are two types of chamber, hot and cold. The cycle of die casting could be a short time, less than one second for small size production especially for producing non-ferrous metal parts or, up to two to three minutes for casting large size products.

2.5 Die casting machines

There are numerous types and sizes of machines available for die casting. Models are from 140 to 2,500 tons for cold-chamber and hot-chamber models are from 140 to 1,300 tons. Die casting machines are sized by their closing tonnage. These types of machine were built to operate for many years in a complicated and varied environment with a minimum of maintenance and attention. Pressure die casting is characteristically a high speed production process and is considered the fastest of all casting processes and competes with stamping, die forging, plastic injection molding, etc. For this reason it is naturally suited to economical production on a quantity basis. Like many technological processes, die casting machine tool generally has mechanical, electrical, hydraulic and pneumatic features. In most designs a die casting machine generally consists of three components to allow it to perform its function [8, 12, 5]:

- A hydraulic cylinder for closing and opening the die.
- Injection systems, which force the molten metal into the die under pressure.
- A frame in which is mounted the actuating equipment.

It is very important that the two halves of the die are held tightly together for the production of good quality die castings. The two halves must also open easily to permit removal of the finished casting**.** There are two types of machine that are used in die casting. First is the hot chamber machine, also called the piston or gooseneck machine, and the second is the cold chamber machine. Most die casting machines are designed in such a manner that the speed or cycle for making the shot to produce the casting is of as short duration as possible. The operator usually starts the cycle by pushing a button and removes the casting, which is ejected from the cavity by automatic or manual means, as the machine is opened. Although this sequence sounds quite simple, the machine is exceedingly complex [16].

A hot-chamber machine cannot be used for alloys having a high melting point like aluminium, magnesium and copper because the steel or cast iron surface of the plunger and cylinder, are submerged in the furnace at all time and this causes direct interaction with molten metal. They must be cast in a cold-chamber, the alloy is in contact with the plunger and cylinder for only a short period of time, and the components are usually kept relatively cool. The furnace that holds the metal at casting temperature is not an integral part of the latter type. The metal is ladled, either manually or automatically into the die cavity [8].

2.5.1 Hot-chamber die casting

Hot chamber die casting, as shown in Figure 2.3, has the melt injection device, or gooseneck, submerged in the molten metal in the holding furnace. At first the molten metal fills the gooseneck and it is then forced out by the piston, and the metal goes into the die. The metal is forced into the die by means of an immersed cylinder and plunger or by means of compressed air [11, 15]. Hot chamber machines may be pneumatically or hydraulically operated. Not all metal alloys can be used in the hot chamber machine. Due to this, cold chamber die casting must be made. Aluminium and metals with high melting points like copper and zinc alloys need the cold chamber machine. Metal is melted in a container, and a piston injects liquid metal under high pressure into the die. The mechanisms of injection of molten metal in the hot chamber machine are quite similar to that on a cold chamber machine, except that the plunger is vertical and immersed in the molten metal. The advantages of a hot chamber are high production rates (500 parts per hour are not uncommon), but the applications are limited to low melting point metals that do not chemically attack plungers and other mechanical components. The hot chamber is used for casting metals such as: zinc, tin and lead [8, 18].
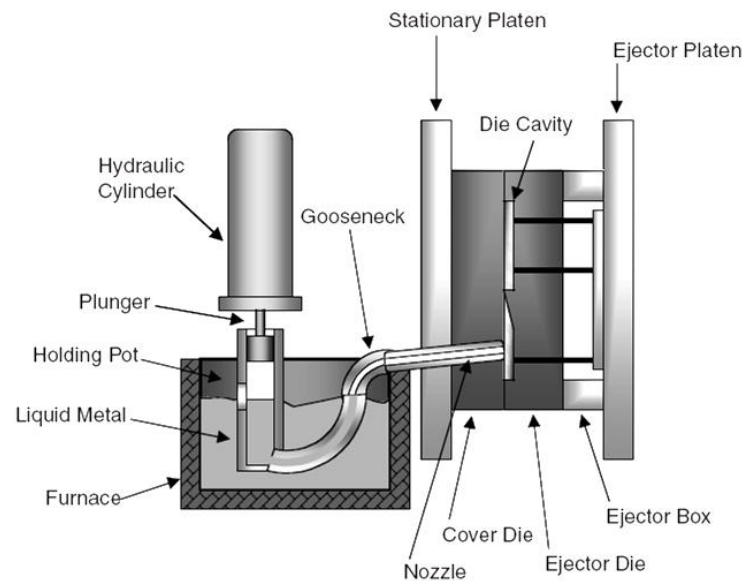
Figure 2.3 Graphical illustration of a hot-chamber die casting machine [3].

2.5.2 Cold-chamber die casting machine

Figure 2.4 illustrates the operating principles of a cold-chamber machine in which the high pressure is generated by a large press hydraulic system which closes the die, a plunger injects the molten metal under high pressure. The molten metal from an external melting container is poured into a shot sleeve and the plunger pushes the molten metal through a runner and a gate into the die cavity [8, 17, 19].
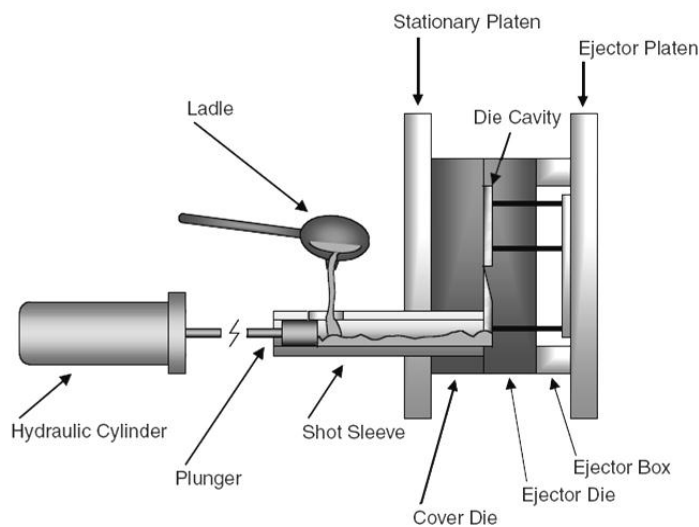
Figure 2.4 Graphical illustration of a cold-chamber die casting machine [3].

Two basic types of cold–chamber die casting machine are available, a vertical injection machine and a horizontal injection machine. The vertical injection machines have advantages and disadvantages. When molten metal is ladled into the injection chamber, any oxide would float on the metal and, being the last to be injected remains in the slug of surplus metal attached to the die casting. In the horizontal machine the molten metal, before injection, lies in the sleeve, from where it is forced into the die by the plunger, along with any oxide which would thus be included in the die casting itself. This was a disadvantage in the early years, when the movement of the injection plunger of the horizontal machine was not regulated, but even then horizontal machines had the advantage of being less wasteful in terms of maintenance time. The disadvantage of the cold chamber with a vertical machine system is a metal entrapped between the pistons and the cylinder wall, leading to production delays and piston replacements. The advantage of a cold chamber is high production, but it is slower than hot chamber machines because of the pouring step and it was also found to be unsuitable for casting low melting point alloys like (zinc, tin and lead). The cold chamber can be used for casting alloys which have a higher melting point like aluminium, brass and magnesium. A number of problems exist with the cold-chamber machines. First the air in the shot sleeve and in the die cavity can be entrapped during the molten metal pouring. The entrapped air in the shot sleeve during the metal ladling is reduced by delaying the plunger movement one to two seconds after completing the metal ladling. However, air is trapped during of the plunger movement, both high and low plunger speeds can be cause air entrapment. At a high plunger speed, waves are created and a low speed wave reflection occurs [10, 11, 15]. During the casting process, entrapped air causes porosity in the solidified casting and can have adverse effects on the mechanical properties of the castings and then it leads to casting rejection. Another problem is the solidification of molten metal; a chill layer which is rapidly formed when the molten metal touches the cold shot sleeve, this problem can cause gate blockage.

2.6 Casting metals

Most casting metals are commercial alloys. A lot of research has been done to develop new alloys that will provide increased strength and corrosion resistance, combined with good diecastability and cost. Most metals are soluble in each other when liquid, and many of them can retain another metal in a state of solid solution, there is usually a eutectic composition which has a freezing point lower than that of either of the constituents, the choice of alloys to be used for present production and in the future depends on economic and industrial developments. Raw material price, as always, has been a powerful factor in deciding which alloy shall be used, but the price of a metal depends on the availability of its ores and the amount of energy required to convert it from ore to metal. Alloy properties are better than pure metals and easier to cast. Casting alloys can be classified as ferrous and nonferrous [14, 15].

2.6.1 Ferrous casting alloys (cast iron)

Ferrous die casting materials were initially developed in the mid 1960s, when experimental production was first carried out by pressure die casting. Most pressure pipes for gas and water or parts in industries such as automotive are manufactured from ferrous metals. These ferrous die casting metals are:

- Grey cast iron, spherical or nodular graphite iron, malleable cast iron, white cast iron.
- Steels.

Any progress in ferrous die casting would have been impossible without a suitable heat resisting die material due to high melting temperatures of ferrous casting alloys. The basic machine for die casting at this high temperature is a horizontal cold chamber, usually about 100 to 400 tons locking load and pouring temperature is approximately $1600^{o}C$, but this depends on the composition [8, 15].

2.6.2 Non-ferrous casting alloys

The main non-ferrous die casting alloys are aluminium alloys which are generally considered to be very castable. Pouring temperatures are low as the melting temperature of aluminium is 660°C. Aluminium has light weight, high dimensional stability for complex shapes and thin walls can be achieved good strength retention at high temperature, good mechanical properties, good corrosion resistance and high thermal and electrical conductivity. Other castable alloys include [2, 20]:

- Copper alloys; bronze, brass, and aluminium bronze which have good corrosion resistance, excellent appearance, high wear resistance and highest mechanical properties.
- Zinc alloys: These are highly castable and have a low melting point (melting point of zinc is 419° C), high ductility, high impact strength, and are easy plated, economical for small parts, and have good fluidity for easier casting.
- Lead and Tin alloys: These have high corrosion resistance, give good dimensional accuracy, and have a high density.

2.7 Advantages and disadvantages of die casting

Advantages of die casting are [8, 12]*:*

- High productivity.
- Good dimensional accuracy.
- Good surface finish: (0.5-2.5 μm) $R_{a.}$
- Thin wall parts may be cast.
- Very economical process at high volume production.
- Fine grain structure and good mechanical properties are achieved.
- Intricate shapes may be cast.
- Small size parts may be produced.

Disadvantages of die casting are [8, 12]:

- Not applicable for high melting point metals and alloys (e.g. steels).
- Large parts cannot be cast.
- High die cost.
- Long lead time.
- Some gases may be entrapped in the form of porosity.

2.8 Aluminum die casting process overview

Small amounts of aluminum had been extracted by chemical processes early in the 19th century, and in 1886 the way was opened for the industrial production of the metal [8]. Aluminium is the most plentiful metal in the earth's crust. It appears in many minerals, ranging from the oxide in bauxite to complex compounds of the metal with oxygen, silicon, calcium, magnesium and iron in clays. The specifications of the aluminium casting alloys developed during the past 40 years represent a sensible compromise between what is necessary to provide good mechanical properties, castability, and competitive prices, and the requirements of the secondary metal smelters who have to produce their alloys from available materials as economically as possible [21].

The production of aluminium alloy castings was well established at the last century, the most widely used alloy containing about 10% of zinc. Early in the 20th Century, aluminium alloys were being cast in sand and gravity casting permanent molds, but the higher melting point (about 600°C compared with 400°C for zinc alloys) introduced problems in pressure die casting. At first efforts were made to use the submerged plunger air pressure machines that had been successful for zinc alloys, but the higher temperature and the tendency of molten aluminium alloy to attack the iron and steel parts of the machine limited the scope of the hot chamber process. In 1920, a significant development was made in the invention of the cold chamber machine built by Carl Roehri.

The alloys were melted separately, and hand ladled into an injection sleeve, immediately after pouring, a plunger forced molten metal into the die, then the casting was ejected with excess metal attached to it in the form of a cylindrical slug. High pressure die casting of aluminium is carried out using cold chamber machines. The definition of high pressure die casting effectively covers the squeeze or the intensification phase of the metal injection process where the aluminium pressure is taken above 50MPa. Cold chamber die casting machines are ones where the shot sleeve, which metal is poured into prior to injection, is not heated [3, 22, 23].

2.8.1 Aluminium melting process

Die casting requires that aluminium is heated well into its liquid phase for injection. The melting point of aluminium is specifically dependent on its alloy, but generally full liquid phase is melting at 700°C. Aluminium temperatures generally must be taken several hundred degrees higher than this in order to assure that alloy chemistry is maintained. Aluminium is melted in central natural gas fired reverbatory furnaces. Ingots purchased from qualified aluminium smelters are used and added to re-melted excess material from the casting process. Alloy chemistry is checked on a routine basis to ensure that metal chemistry meets alloy specifications. Once melted and taken up to proper temperature, the aluminium is transferred to each die cast machine. A filtration method is used to take out impurities and oxides of the liquid aluminium as the aluminium is pumped out of the reverbatory furnace. Each die cast machine has its own holding furnace which maintains the molten aluminium at a temperature while waiting for use in the die cast machine [24, 25].

2.8.2 Die cast injection process

When a die casting machine is ready for its next cycle (die is closed ready for the shot), an automated or manual ladle removes a prescribed volume of molten aluminium from the holding furnace and pours it into the shot sleeve. Once pouring is complete, the injection phase begins [12, 26]. The first injection phase is the slow shot phase where the shot plunger moves forward at a low speed to begin pushing air out of the sleeve and to move past the pour hole in the sleeve. After a prescribed distance, depending on process setup, the plunger enters an intermediate speed phase where the speed is increased to fill the runner system with aluminium. Once this is complete, the machine enters a fast shot phase where velocity is greatly increased to fill the part cavity with aluminium. After the part cavity is filled and the plunger has stopped moving, the hydraulic cylinder pushing the plunger is pressurized to a higher pressure. This intensification or squeeze phase takes the aluminium pressure over 50MPa to ensure proper fill and to minimize aluminium shrinkage problems [15, 27].

2.8.3 Solidification phase

The die cast machine continues to hold the die halves together at its rated tonnage during the solidification phase. Die cast dies are water or oil cooled to remove heat from the molten aluminium during solidification. The machine also maintains intensification pressure to minimize shrink porosity as the aluminium solidifies. After a prescribed amount of time, when the casting is sufficiently solidified and cooled, the die opens the ejector or moving half of the die [28, 29].

2.8.4 Part removal

Die cast dies have ejector pins through the part cavity. These pins are mounted in an ejector plate on the back of the die cast tool. This plate is actuated by hydraulics on the die cast machine. Castings are removed by automated machines or 6 axis robots or manually. This device then takes the die casting to cooling equipment where the part is taken to a temperature suitable for subsequent operations. This cooling can be achieved with fan driven air cooling or the parts can be water quenched. Quenching reduces casting temperature more rapidly, but the process must be controlled to prevent part distortion [8, 12].

2.8.5 Die lubrication

The pressure die casting die consists of many parts moving against one another, to prevent wear and to reduce friction also to prevent the die cast metal from adhering to the die requires lubricant application to moving parts. After the die casting is taken out of the die cast tool, another piece of equipment automatically lubricates the die. The most common types of lubricant used in aluminium die casting are, LUBRICAST 814 ZR, LUBRICAST 898NS, and LUBRICAST 677 WS. These are mixed with water and sprayed on to the dies to clean them. This lubricant serves to both cool the die surface to proper temperatures for the next cycle and creates a film on the die surface which allows for part release. Once complete, the die casting machine closes and is ready for the next cycle [30, 31].

3

Failures in Die Casting Dies

3.1 Introduction

This chapter presents the failure analysis of the casting dies. Here, failure analysis processes from previous research were considered to establish the nature and causes of the failures occurring on a die casting die with respect to the failures on the aluminium casting die. These were done to verify if these defects are significant issues affecting the lifetime of the die.

3.2 Failure Analysis of Die Casting Dies

Die life is normally limited by heat checking (thermal fatigue), erosion, erosion-corrosion or chemical attack and soldering due to the frequent contact of the tool surface to the molten casting alloy. In a casting die the surface defects and failure are shown in schematic form in Figure 3.1, are significant issues and major causes of premature die failure.
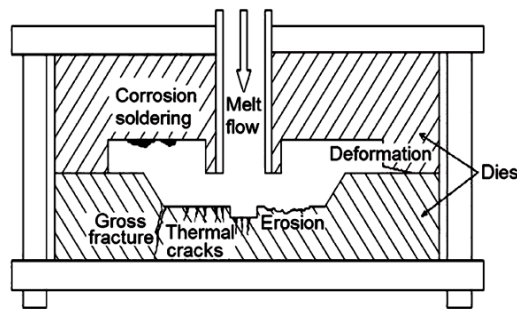
Figure 3.1 Schematic illustration of defect occurrence on a casting die [32].

Die casting dies are exposed to high mechanical, chemical and thermal loads which cause surface defects. These defects are:

(a) Thermal fatigue, which causes heat checks on the surface of the die. Thermal fatigue cracking is an important tool life-limiting failure mode in die casting dies. Dies are exposed to high temperature gradients and high metal pressure during the injection cycle, for example in aluminium die casting is shown in Figure 3.2. The difference in the temperature between the surface and the die core cause thermal stresses, which can exceed the yield strength of die material and cause surface cracks due to the accumulation of local plastic strains on the die surface. However, the cracking is caused by the cycling of stress, strain and temperature on the surface of the die through the thermal cyclic nature of the casting process [32-37].
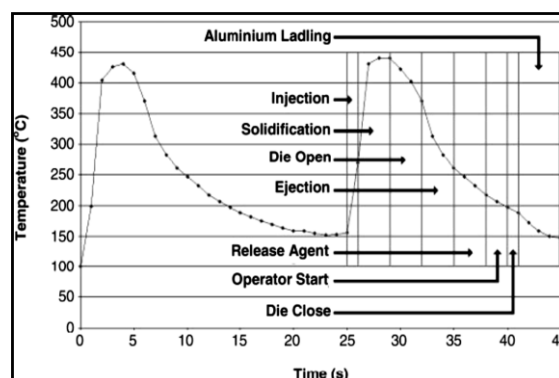
Figure 3.2 Thermal cycle at high-pressure aluminium die casting [35].

(b) Erosion, due to impacts by liquid or solid particles. In aluminium die casting, the high velocity of molten metal causes erosive damage is shown in Figure 3.3 (image taken at a local aluminium company). In many applications surfaces of casting dies could have different wear mechanisms acting independently from variations of different stages of the wear process, such as, solid particle impingement, in other applications solid particles entrained in molten metal or slurry erosion, liquid droplet or jets impingement, cavitations as result of the formation and collapse of bubbles that contain vapours or gas, eventually, partially solidified or semi-solid state of the eroding metal [4, 7].

Figure 3.3 Illustration of erosive wear (picture was taken in Hallam Casting Company).

Erosive damage is one of the major wear mechanisms leading to premature failure in a casting die and primarily seen on the die surface where the molten metal jet first impingement the parts of the die casting die. However, the different wear mechanisms often interact and coexist and it is typical to find evidence of different mechanisms when examining wear scars [5]. It seems clear that an understanding of erosive damage may be divided into [4-7]:

- Slurry erosion is caused by the interaction of solid particles suspended in a molten metal and the surface of a die. The repeated impacts of particles cause mass loss from the surfaces of the die by the displacing or cutting action of the high velocity of molten metal.

- Liquid erosion in a casting die may be found due to the impact of liquid drops or jets upon a solid surface leading to the temporal development of pressure fields owing to the passage of stress waves causing a series of failures in compression and tension from which erosion of the material and reduction in strength results.

- Cavitation erosion is caused by the cavities or bubbles that contain vapour or gas, within a liquid. Normally, cavitation originates from changes in pressure in the liquid brought about by turbulent flow or by vibration, but can also occur from changes in temperature (boiling). Cavitation erosion occurs when bubbles or cavities collapse on or very near the eroded surface. The mechanical shock induced by cavitation is similar to that of liquid impingement erosion causing direct localised damage of the surface or by inducing fatigue. Erosion wear can occur in both cases due to the fatigue by passage of stress waves causing a series of failures in compression and tension.

(c) Corrosion and soldering, corrosion failures in aluminium die casting are a result of dissolution of the die tool material into liquid form which causes intermetallic compounds of Al-Fe on the surfaces of the die wall. Soldering may occur as a result of interaction between the die material and the casting alloy through the injection of the molten metal or after injection as remnants of the casting alloy on the die wall [38]. This affects the surface finish and dimensional tolerances of the cast products. Consequently, premature die failure may occur, which ends in higher production costs.

Generally, failures in die casting have been widely shown through different studies, Further, a brief description of failure analysis processes from previous reviews were considered to establish the nature and causes the failures of aluminium die casting die. Mitterer et al. [39] carried out a study to observe the damage of tools or work pieces in aluminium die casting (shown in Figure 3.4). The tools were subjected to damage during the process by all the mechanisms outlined above. Aluminium casting dies are exposed to high thermal and mechanical loads. Heat checking (thermal fatigue) and gross cracking occurred due to the cycling of stress, strain through the thermal cycling of casting process and from oxidation due to high pouring temperatures. Erosion was seen, caused by aluminium injection. Corrosion and soldering were also observed.

These failures strongly affected the surface finish and dimensional tolerances of the cast products. Consequently, premature die failure occurred.
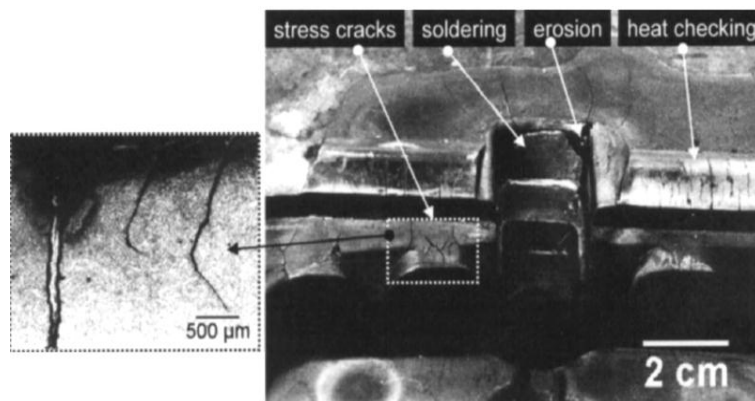
Figure 3.4 Damage mechanisms in aluminium die casting (the inset on the left shows a microscope cross-section) [39].

Muhic et al. [32] mentioned that the thermal fatigue is a big problem in die casting dies. Many factors like, surface finish, hardness, residual stresses and microstructure influence the thermal fatigue and thermal cracks due to accumulation of local plastic strain that occurs during each casting cycle. In addition it was mentioned that the dies are exposed to high mechanical, thermal and chemical loads which cause surface defects.

These defects are shown in Figures 3.5, including thermal fatigue cracks, erosion of the melt flow, corrosion and soldering of aluminium to the die surface. Figure 3.5a, shows a worn-out surface, which is caused by the erosion by aluminium alloy melt flow. Figure 3.5b shows thermal fatigue cracks which occurred due to thermal stresses during die casting. Figure 3.5c shows damage on aluminium casting due to corrosion and soldering of aluminium on the die surface. Deformation of die parts is shown in Figure 3.5d.
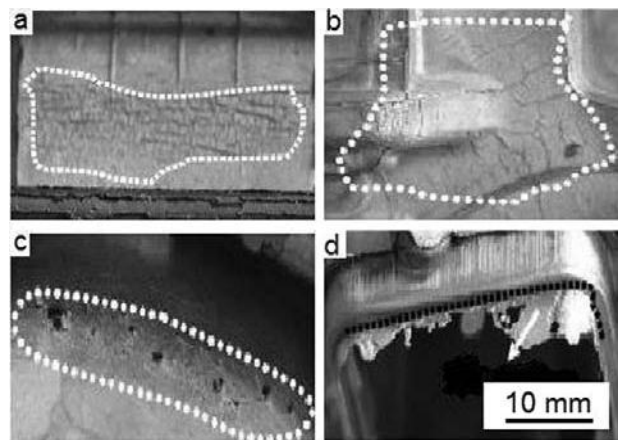
Figure 3.5 Surface defects of castings: a) erosion, b) thermal cracks, c) corrosion and soldering, d) deformation [32].

Joshi et al. [40] studied the soldering or die sticking due to the chemical attack at high temperature between the molten aluminium alloy and the die. It was mentioned that the main reasons for inadequate filling are soldering and ejection problems. Figure 3.6 shows soldering on a core pin soldering, or die sticking, occurs during die casting when molten aluminium welds or stick on the die surface. These failures in aluminium die cause process downtime and loss of casting quality in aluminium die-casting.
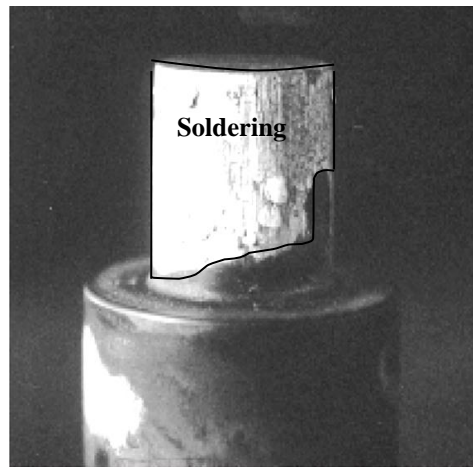
Figure 3.6 Soldering damage on a core pin [40].

Srivastava et al. [41] studied the failure of die casting by using FEM software for a prediction model for thermal fatigue cracking. Two models were described for direction of cracking and the number of cycles to cause the failure in die casts. In Figure 3.7 an example for thermal fatigue cracks forming on the surface of die due to compression during heating and tension during cooling is shown. Figure 3.8 shows that the direction of cracking will be perpendicular to the plane of maximum stress from model [41].
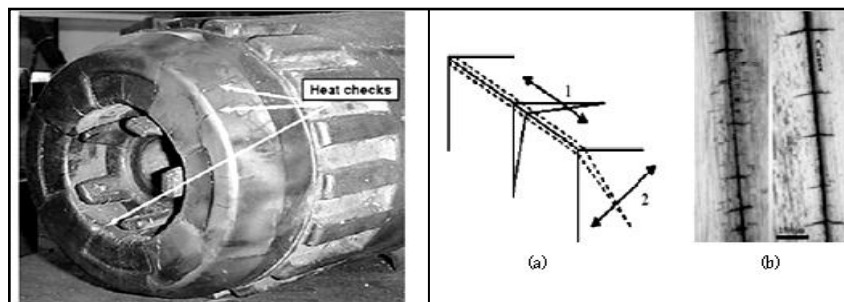
Figure 3.7 Heat checking in die-casting dies [41].   **Figure 3.8 (a) Schematic of crack direction,**
                                                                 (b) Corner cracks [41].

3.3 Failure Mitigation and Testing Methods

These studies were aimed at finding a solution related to erosion problems found to aluminium die casting dies, some of which are now described.

Salas et al. [42] carried out a study to observe the tribological behaviour of candidate coatings such as: CrC, CrN, TiAlN and TiN/TiC for aluminium die casting dies. Scratch testing and wear tracks were analyzed by optical microscopy. Optical profilometry was used to characterize the coatings. In addition, they were mentioned that it was impossible to obtain a value for the wear volume, especially in the shallow tracks, and then data obtained was incomplete to compare the wear performance. It is important to mention from previous studies that the erosive wear is strongly dependent on impact angle which means no useful information on erosion resistance could be described from scratch testing.

Panjan et al. [43] carried out tests on die casting tools with a duplex treatment, we studied the applications of CrN, PN + CrN and PN + TiAlN in aluminium die casting and evaluated the coatings by optical and SEM microscopy. The performance tests were made under real manufacturing conditions and surfaces and duplex treated cores were checked after 2700, 4150 and 7490 shots.

Klimek et al. [44] described duplex treatments consisting of plasma nitriding and hard PACVD coating, which were improved wear, fatigue, corrosion resistance. They used a scratch test to evaluate the coating layers.

Pfohl et al. [45] carried out tests on the wear resistance of PACVD coatings in aluminium die casting. They assessed their suitability using adhesion (scratch test) and friction behaviour (pin on disk) as indicators of performance.

Rie et al. [46] chose zirconium and boron containing coatings to develop the aluminium die casting tools by means of MO-PACVD. For erosion tests, the samples were rotated horizontally at 800 rpm for 20 min in liquid aluminium at 700 $^\circ$C. After the test, the surface was examined by light microscopy. They classified erosion resistance according to the appearance of substrates under microscopy after 16000 revolutions in molten aluminium also they used scratch tracks for assessment of the layer coating adhesion on the substrates.

Lousa et al. [47] conducted tests on multilayered chromium/chromium nitride coatings to increase the hardness and wear resistance of semi-solid forming tools for high pressure die casting of low melting point metals. They were evaluating the coating layers using a spherical diamond indenter. The failure mechanisms have been established by scanning electron microscopy SEM images of scratch wear.

Heim et al. [5] mentioned the advantage of using hard coatings produced by PACVD in the field of aluminium die casting. They analysed some cores cut after service and analysed then using SEM. Those failure cores were achieved using 32000 shots in an actual casting machine.

Shivpuri et al. [6] suggested accelerated testing to evaluate of coatings for erosive wear resistance in die casting by using a multi-pin die under actual production conditions. They were mentioned that the wear being a gradual loss of material could be long term more than 100 000 shots and costly, so to accelerate the wear effects to allow for quantitative erosive wear in a reasonable number of shots chosen operating conditions to accelerate the erosive wear such as the shot velocity, accumulator pressure, cycle time and so on.

From the various different methods employed, there are essentially two main methods to evaluate die materials or surface coatings. The first method involves a range of experimental laboratory measurements using scratch testing which identified the adhesion of coating layers: friction behaviour (pin on disk), diamond indenter, and corresponding scanning electron microscopy (SEM) used after testing. Erosive wear has not been considered.

The second method for evaluating the wear resistance in die materials and coating surfaces, involves experiments achieved under actual production conditions in the actual casting machines. It is important to mention these experiments are costly and could take a very long time to achieve wear. In addition, it is important to mention that in the overall evaluation of erosion it is important to consider the mass loss versus time behaviour. In previous testing this has not been done.

Clearly further work is needed to optimize the wear resistance of dies using coating materials. The mechanical properties such as: tensile strength, yield strength, ductility, toughness and hardness are frequently of most importance when selecting metals for dies. Also where erosive wear may occur on flat and cylinder surfaces in dies, strong erosion happens at the gate and core where the molten jet hits directly as shown in Figure 3.9. Different geometries therefore need to be tested.

Figure 3.9 Illustration the erosive wear on flat surface represented by the gate velocity, and cylinder surface represented by core pin; this picture was taken at Hallam Casting Company for aluminium die casting.

In addition, it is most important to mention that during the last 20 years, metal working industries have shown great interest in improving technologies used in aluminium die casting processes, such as use of semi-solid charges. These semi-solid technologies are much improved in comparison to conventional die casting components. Semi-solid metalworking extends the capabilities of conventional die casting by [3, 48]:

- Reducing the amount of entrapped gases.
- Reducing the amount of solidification shrinkage, and modifying the microstructure of the alloy.

Semi-solid metalworking has been applied to numerous metal systems, including aluminium, magnesium, zinc, titanium, and copper as well as numerous ferrous alloys. The most common commercial alloy systems in use are aluminium and magnesium die casting alloys. These alloys are ideal for use in a semi-solid state. In Figure 3.10 a semi-solid billet of aluminium is cut with a knife. The engineering use of semi-solid charges may allow the use of solid particles in possible testing approaches.
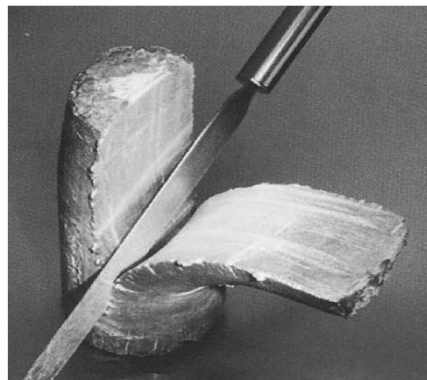
Figure 3.10 Shows aluminium in a semi solid state [12].

3.4 Conclusions

In this chapter, failure analysis processes from previous reviews were considered to establish the nature and causes the failures in aluminium die casting die. It was possible to find out the significant issues and major causes of premature die failure. Heat checking (thermal fatigue), erosion, erosion-corrosion or chemical attack and soldering were highlighted as being the major problems causing the damage and failure in aluminium die.

Erosion can cause severe damage to the die resulting in loss of equipment and production downtime science it decreases of production quality.

Test methods used for assessing solutions to the failure mechanisms have typically involved actual casting machines. No laboratory based approach has been developed for assessing, for example, erosion resistance. Some coatings have been assessed for use in dies, but have not been tested for erosion resistance.

4

Wear Mechanisms

4.1 Introduction

This chapter presents a brief description for wear and wear mechanisms with regard to those observed in adhesive and abrasive wear. Then, an overview with respect to liquid erosion and solid particle erosion (SPE) is presented extensively, where it is possible to observe the similarities in erosion between liquid droplets and solid particle erosion and the difference between wear mechanisms produced on ductile materials, and on brittle materials. Finally, the wear mechanisms of aluminium die casting caused by the high velocities of the molten metal impinging on parts of the die cavity.

4.2 Wear

Wear can be defined as a removal of material from solid surfaces as a result of mechanical and/or chemical action and is generally accelerated by frictional heating or thermal means [49]. The surface damage caused by wear can manifest itself in many forms, such as, pitting, surface fatigue, surface cracking, fretting, plastic deformation, etc.

Different wear mechanisms such as, erosive, sliding, abrasive and oxidative often coexist, interact and compete. When examining wear scars it is typical to find evidence of different mechanisms acting independently or there could be features indicating different stages of a complex wear process [50, 51]. Some wear patterns are presented in Figure 4.1.

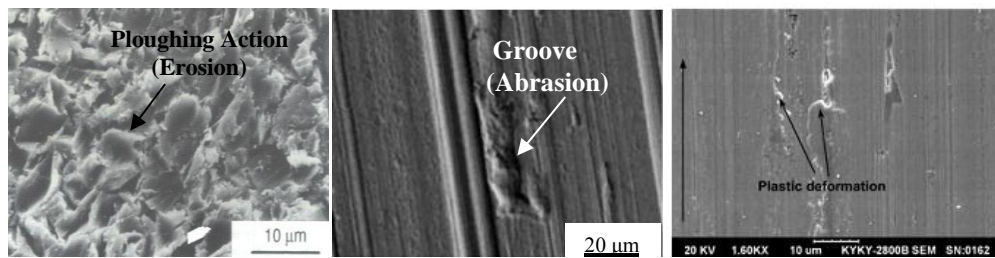**Figure 4.1 Wear Patterns, (a) Erosive wear [49], (b) Abrasive wear [52], (c) Sliding wear [53].**

It is essential to recognise that there are different types of wear where several distinct and independent mechanisms are involved. Wear can be categorised into a number of major types, the main four of which are shown below in Figure 4.2 [54, 55].
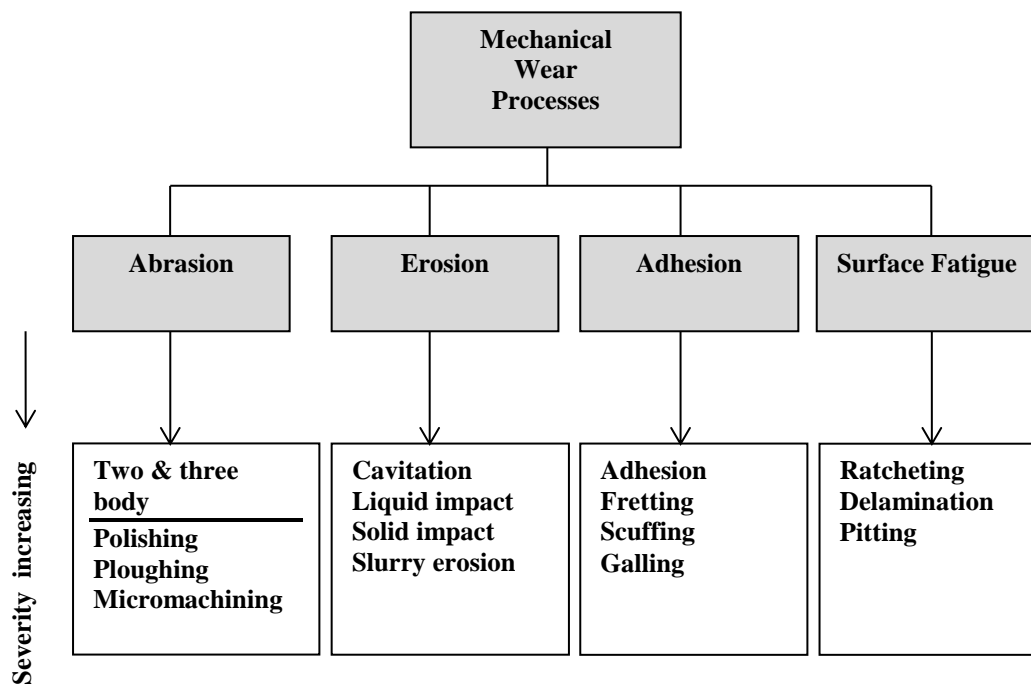

Figure 4.2 Classification of mechanical wear processes.

4.2.1 Adhesive Wear

Adhesive wear is caused by the strong adhesive force that develop between the tips of mating materials asperities where the pressures are extremely high. When two sliding surfaces come into contact, normal and tangential loads are transmitted through the contact points by adhesive and ploughing actions [56]. Asperities of the softer surface are easily deformed and some are fractured by the repeated loading action. A relatively smooth surface is generated, either when these asperities are deformed or when they are removed. Once the surface becomes smooth, the contact is not just an asperity-asperity contact, but rather an asperity-plane contact. Each point along the softer surface experiences cycling loading as the asperities of the harder surface plough it. The surface traction exerted by the harder asperities on the soft surface induces plastic shear deformation which accumulates with repeated loading [49]. Provided adhesive wear is moderate, no debris forms and the resulting small degree of wear may be acceptable, depending on the desired service life. On the other hand, metals which adhere strongly are more liable to cause debris and are therefore more susceptible to galling [57]. A typical example of adhesive wear is shown in Figure 4.3**.**

Adhered asperities
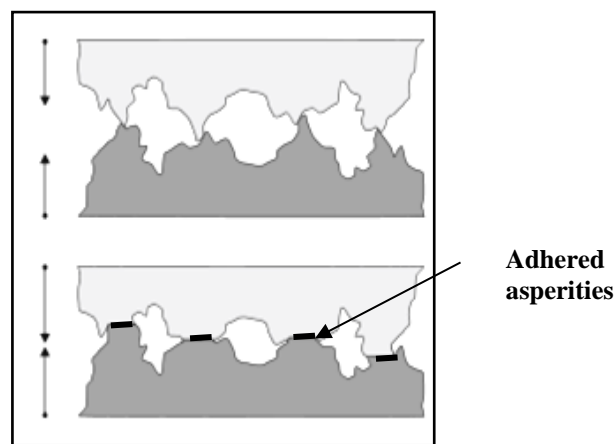
Figure 4.3 Adhesive Wear, the top image shows asperities under no load the bottom image depicts the same surface after applying a load.

4.2.2 Abrasive Wear

Abrasive wear is the result of one very hard material cutting or ploughing grooves into a softer material. Abrasive wear covers two types of situation, known, respectively, as two-body abrasion and three-body abrasion, in each of which a soft surface is ploughed by a relatively hard material. In two-body abrasion a rough hard surface slides against a relatively soft opposing surface, whereas in three-body abrasion rough hard particles trapped between the two sliding surfaces cause one or both of them to be abraded [49, 51]. In Figure 4.4 both types of wear mechanisms are shown.

The abrasive wear rates are greatly influenced by the following parameters such as; particle size, particle speed or cutting speed, particle loading , the nominal load carried by each particle of abrasive, abrasive particle shape, abrasive particle properties, namely hardness and strength. Abrasive wear presents surface topography consisting of long parallel grooves running in the rubbing direction. The size of grooves varies from light scratching to deep grooves.
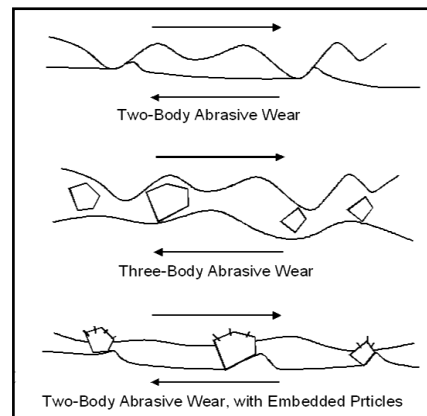
Figure 4.4 Types of Abrasive Wear.

4.2.3 Erosive Wear

Erosive wear is the result of impingement of solid particles, or liquid droplets on the target surface. Erosion is a rather broad term and can be further classified into a number of more specific terms. These include cavitation erosion, and slurry erosion. Erosion has caused problems in a number of industries, such as rain erosion of aircraft and droplet erosion of steam turbines, the high velocities of the molten metal impinges parts of the die cavity, causing steel to be washed away with the melt. On the other hand, it also finds useful application as a material removal process such as sand blasting which can be used for cleaning surfaces and water jet cutting used for cutting materials [58, 59].

4.2.3.1 Liquid Erosion

In erosion by liquid, the liquid impacts as a droplet or jet causes a number of erosion wear mechanisms in many applications naturally and industrial processes such as; rain erosion of aircraft, particularly the windows, missiles travelling at high speed through rain, droplet erosion of steam turbine blades and erosive die wear as die casting die steel washed away with the melt due to the high velocity of the molten metal impinges the cavity of the mould [60, 61]. The studies on erosion by liquid impact dates back to the last century when they had been carried out to find solutions to reduce the erosive wear problem for rotating blades of steam turbines, recently several other studies of liquid erosion problems have appeared in recent years due to the rain erosion damage on the aircraft or missiles travelling, also the erosion damage by molten metal wash out the mould and they have given an added stimulus to research in this area.

Field and Lesser [62] have given abundant reviews on liquid impacts. Field also carried out experimental tests on various areas of application and techniques for increasing the impact velocity from a few metres to several thousands of metres per second in the laboratory which were conducted to produce materials for aircraft windows have sufficient strength to resist erosion damage by rain, sand, ice and bird-strikes.

Previous studies [63, 64] for investigating drop impacts onto solid surfaces pointed out that when a spherical water drop impacts a solid surface, a shock wave forms inside the water drop due to the compressibility of the liquid. The water drop thus imposes a high edge pressure and the boundary of the contact area will be travelling at supersonic speeds with respect to the expanding shock wave speed from the impact between the liquid drop and a solid target. The high edge pressures are responsible for the damage of the solid target when the velocity of the contact zone exceeds the expanding shock wave speed. This information is used in conjunction with a simple model (a schematic of impact water drop is shown in Figure 4.5) of the drop collision to obtain quantitative evaluations of the transient stress states in the target material [65].
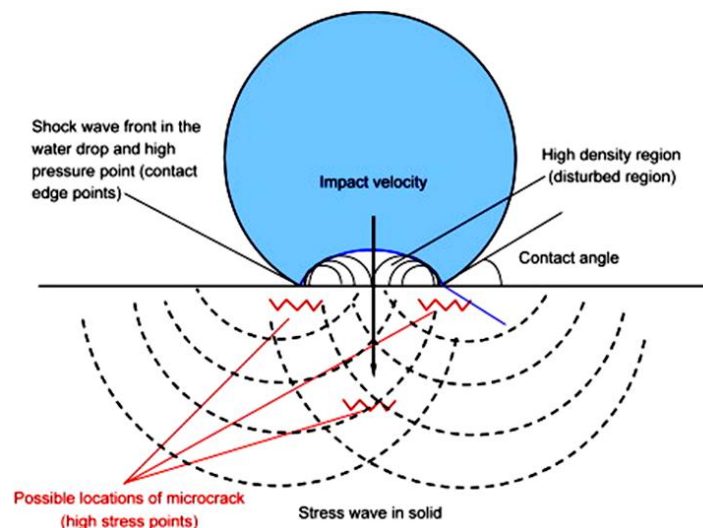
Figure 4.5 The schematic of the liquid–solid impact problem [65].

4.2.3.2 Solid Erosion

Solid particle erosion as shown in Figure 4.6 is damage and material removal that results from the impact of particles against a solid surface. The erosion wear rate (designated as *E*) is dependent on the velocity of particle impact and response of materials to solid particle impact which can be ductile or brittle [66, 7]:

$$E = \text{constant} \times V^{n}$$

4.1

where, *V* is the particle velocity, and *n* is an experimentally determined wear index, (for most materials *n* is in the range of 2-2.5) [66].
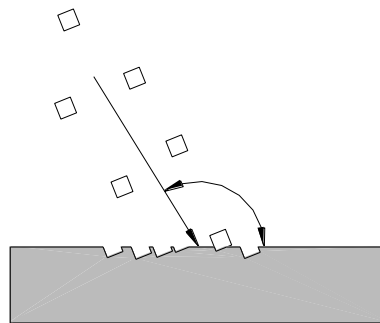
Figure 4.6 Solid Particle Erosion.

The environmental variables effect on erosion rates are separated into three types [67]. Table 4.1 shows these variables.

Table 4.1 Variables affecting erosion

Parameters	Variables
Impingement	Particle Flux Particle Velocity (v) Angle of incidence (α) Orientation of the particle relative to the surface at the point of impact Particle rotational speed
Particle	Shape Density Size Hardness Friability (ease of fracture)
Material	Hardness Work Hardening behaviour Microstructure

Several studies studied the removal of material from a metal surface by solid particle impact and cover ductile and brittle materials under multiple and single impacts, with emphasis on the wear mechanisms. It is well known that there is a dramatic difference in the response of ductile and brittle materials when the weight loss in erosion is measured as a function of the angle of impact. This is illustrated by Figure 4.7, which is based on curves which Sheldon & Finnie reported in 1966 [68]. It is indicated for brittle materials, such as ceramics, the maximum is at or near 90° ($\alpha > 45°$), while ductile materials, such as pure metals, have a maximum erosion rate, *E*, at low angles of incidence (typically $\alpha < 45^{o}$).
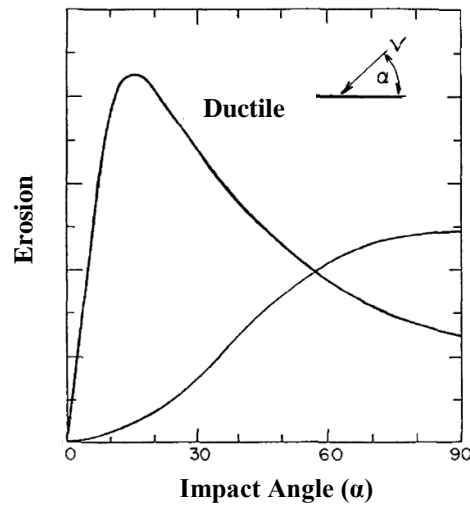
Figure 4.7 Comparison of erosion between ductile and brittle materials eroded [61].

The early work of Finnie [7] suggested that two main types of material behaviour, ductile and brittle. In respect to erosion of a ductile material, Finnie conducted an investigation on the impact of a rigid particle on the surface of an annealed steel target, from experimental results, it was concluded that the mechanisms of removing material in erosion due by cutting wear or micro-machining.

In addition, it was found that the important variables in the erosion process were: the mass and velocity of the eroding particles as well as the impingement angle of the particles [69]. Finnie indicated that no erosion would occur at normal impingement, and also mentioned that the erosion mechanisms in metals are frequently divided into "oblique" and "normal" angles of particle incidence. The dramatic difference in the response of ductile and brittle materials is when the weight loss in erosion is measured as a function of the angle of impact. The rate of loss for ductile metals approaches zero at very low angles of impact rises to a maximum when the incident makes an acute angle of 20° to 30° to the surface, and falls by a factor of 2 or 3 as normal impact is approached [70].

Also, Finnie showed that at low impact angles the particle strikes the surface, forms a crater and then leaves the surface (Figure 4.8, curve 1). Later observations with stereo scanning electron microscopy showed that some particles remove a chip as in metal cutting, others leave material piled up at the sides or the end of the crater (curve 2). This raised material is removed easily by subsequent particles. In other cases the particles hit on flat faces and do little damage. Moving to higher angles, the analysis predicted that just beyond the angle for maximum erosion, the particles come to rest while cutting. The material is piled up around and ahead of the particle (curve 3). Again, it was assumed that this material was vulnerable to removal by subsequent particles and also was taken the volume removed as they swept out by the tip of the particle.
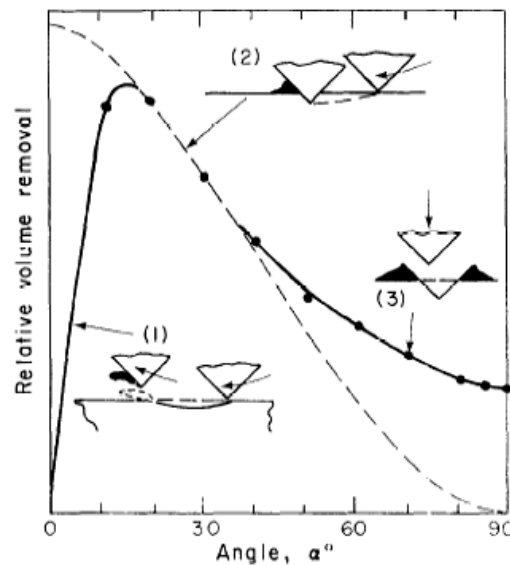
Figure 4.8 Predicted variation of volume removal with angle curves 1 and 2 and experimental values (curve 3 and data points) normalized to the same value of maximum erosion [70].

In addition, in this work discussed the fundamental issues to understanding the material removal by erosion presses such as, criteria of lips or platelet formation and fracture, they mentioned that the lip formation is the result of the localization of deformation in the near surface regions of the target material during the impact process.

Another issue mentioned was thermal effects, while all workers agree on the existence of a substantial temperature rise in the target accompanying an impact, there is little agreement on the role this temperature rise plays in determining metal loss.

Hutchings & Winter [71] carried out studies of the oblique impact of 3 mm steel balls at velocities up to 250 ms^{-1} showing the mechanism of metal removal. The mechanisms envisaged to involve the formation of a lip in front of the particle. The initial stage is the formation of a lip at the exit end of the crater by shearing of the surface layers. This lip is detached from the surface by the propagation of ruptures at the base of the lip as shown in Figure 4.9.
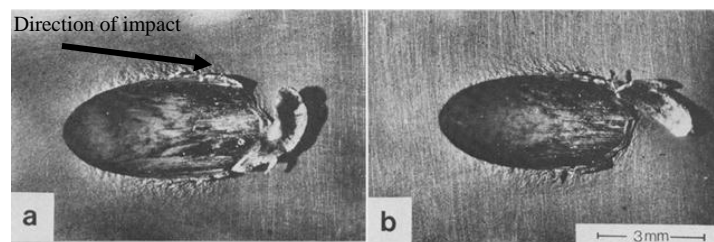
Figure 4.9 Damage in aluminium caused by 3 mm steel spheres impacting at velocities was, (a) 220 ms^{-1} and (b) 210 ms^{-1} [71].

In addition, studies of the effect of work hardening on lip formation showed that the material was more readily removed from fully work-hardened metals than from annealed metals. It was suggested that it was because of work-hardened metals, flow are concentrated in the surface layers and intense localized shearing occurred leading to lip formation, whereas in annealed metals the work-hardening process causes the deformation energy to be spread through a large volume of the material as shown in Figure 4.10.
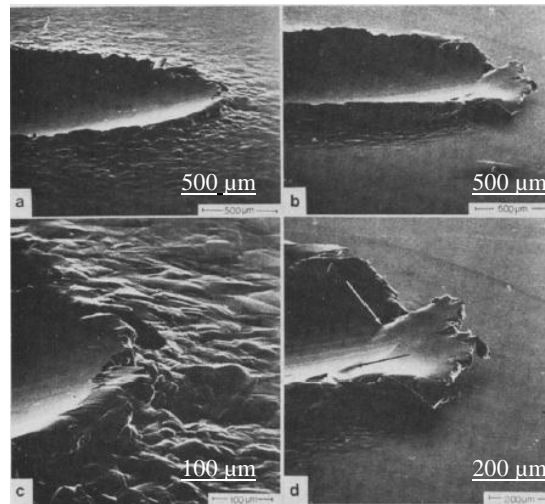
Figure 4.10 Scanning electron micrographs of copper targets impacted by 3mm steel balls at (a) and (c) annealed copper, (b) and (d) work-hardened copper [72].

Hutchings [49, 72] mentioned that in the case of ductile metals when the maximum erosive wear is at an impact angle of 20°, the front face of the particle exhibits a large angle of attack which corresponds to the greatest loss of material by machining or cutting. Studies at 30° showed three types of impact damage. Rounded particles deform the surface by ploughing, displacing material to the side and in front of the particle. Subsequent impacts lead to the detachment of heavily-strained material from the rim of the crater or from the terminal lip. With respect to angular particles, the orientation that they strike the surface and the form that the particle rolls forwards or backwards during contact determines the impact damage.

In this mode, type I cutting exists when the particle rolls forwards, indenting the surface and raising material into a prominent lip, which is vulnerable to removal by subsequent nearby impacts and type II cutting occurs when the particle rolls backwards, a true machining action occur, in which the sharp corner of the abrasive grain cuts a chip from the surface. Figure 4.11, shows the three types of damage.
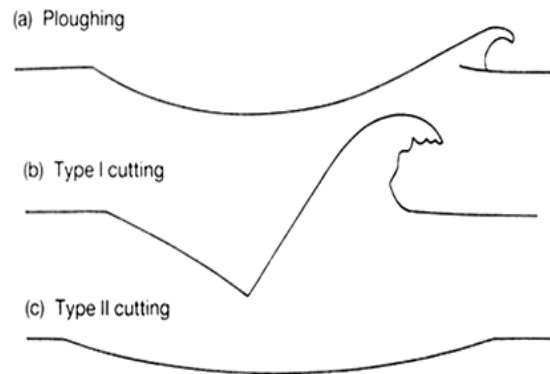
Figure 4.11 Three types of impact damage (from [49]).

Hutchings [73] proposed a critical strain by theoretical analysis for the erosion of ductile metal by spheres at normal incidence. It was mentioned that plastic strain was associated with one impact is assumed to be directed radially outwards in the plane of the surface and the removal of fragment occurs when the maximum plastic strain within the fragment reaches a critical value $\Delta\varepsilon_P$ as shown in Figure 4.12. Although, it was illustrated the energy balance before and after the single impact of a spherical particle as shown in Figures 4.13. In addition, it was determined for good resistance to erosive wear; both dynamic hardness and ductility are needed.
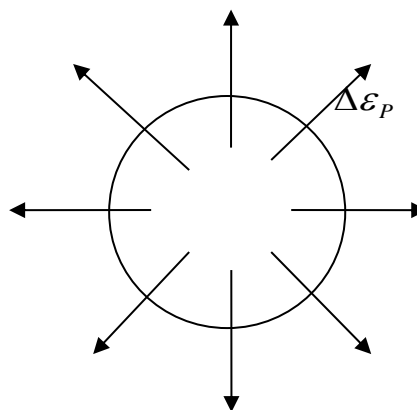
Figure 4.12 Pattern of plastic deformation in the target on impact. The strain is directed in a circular symmetry about the line of impact of the spheres.
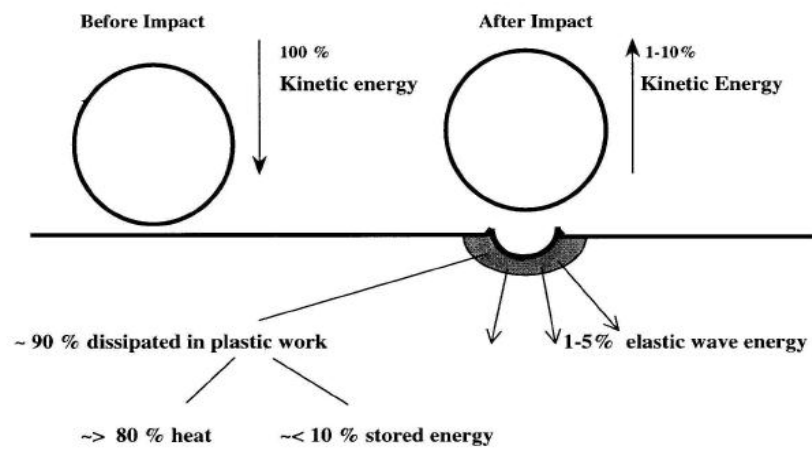
Figure 4.13 Energy balance for a single particle impact [66].

Bitter [59, 74] considered that the surface damage in ductile materials caused by the sum of two wear mechanisms, cutting wear and deformation wear. Deformation wear occurred when the target surface was repeatedly deformed by impacting particles which caused the surface to work-harden and crack. Spreading and propagation of the cracks caused the material removal.

Tilly & Sage [75, 76] in their work with nominally ductile targets, presented a concept of erosion which occurred in two stages: (a) the surface is pitted and material extruded to form a lip or hump and (b) particle fragments impact at secondary sites causing additional damage which may form a radial pattern around the pit". In this case, the fragmentation behaviour of the particles is most important in determining the extent of damage. Examination of the particles and target chips after impact showed that small particles do not break up but require many impacts to produce a chip. Increase in particle size results in fragmentation, but involves few impacts per chip and produces bigger chips. The influence of impact angle has also been explained descriptively by the two stage process, the primary stage predominating for glancing impacts and the secondary stage predominating for normal impacts.

For brittle materials erosion mechanisms were introduced by Finnie [7]. It is generally considered that material would be removed by the intersection of cracks Figure 4.14 illustrates the crack shape schematically.
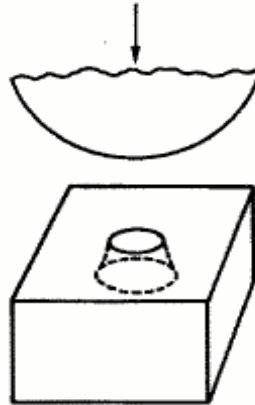
Figure 4.14 Schematic drawing of the ring crack produced by a steel sphere striking a section of a relatively large glass surface [7].

Erosion tests were carried out on spherical steel impacted glass, which revealed a ring crack around the circumference of the contact area although slightly was laid outside the contact area. In the very early stages of these tests each sphere produced a ring crack, but no material was removed. Eventually, with an increasing number of impacts, the cone-shaped fracture surfaces, associated with the ring cracks, began to intersect and material was removed.

Buijs [77], found that the high stress under the indenting particle cause elastic and plastic deformation of the brittle material. When the fracture threshold is exceeded, cracks develop whose final length is determined by the residual stress field resulting from the strain mismatch between the plastically deformed zone and its elastically deformed surrounding. There are two types of cracks: lateral cracks, which extend parallel to the surface at the level of the bottom of the plastic zone, and radial/median cracks, which are perpendicular to the surface. The patterns are schematically represented in Figure 4.15.
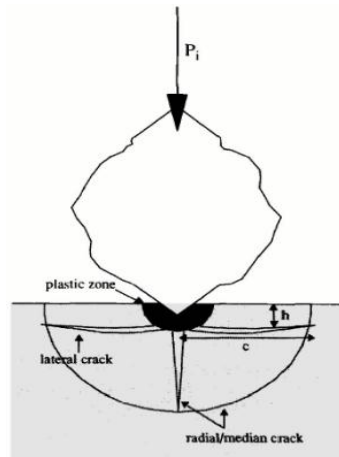
Figure 4.15 Schematic representation of indentation on glass caused by impacting erosive particle [77].

The erosion of a range of brittle materials by different types solid particles such as: silica, silicon, silicon carbide and alumina has been conducted by Shipway and Hutchings [78], which showed that the erosion rates decrease rapidly, and the velocity exponents of erosion rate increase, as the ratio of particle to target hardness decreases towards unity. As this ratio falls towards unity, less damaging mechanisms of erosion dominate. Indentation-induced fracture models for erosion of brittle materials are not valid when this mechanism ceases to operate. However, the erosion rate for brittle materials is determined by kinetic energy, particle size, hardness and toughness of erodent [79].

4.2.3.3 Slurry Erosion

Slurry erosion can be described as a surface impinged by solid particles in a liquid stream or a gas in dry erosion, which is the dry (gas-solid) erosion in contrast to the (liquid-solid) in slurry erosion by viscosity and density of the carrier medium. Slurry erosion is a serious problem in many industrial applications, such as hydraulic turbines, mineral processing equipment, slurry pumps, valves and pipe-lines conveying solid particles and die casting molds in which the erosion occurs when there is a fast flow of molten metal relative to the surface of the die.

It becomes more severe in the presence of hard particles, such as primary solid silicon in 390 aluminium alloys or SiC particles in metal matrix composites [80-83]. The slurry erosion study has been motivated by many authors due to the numerous industrial applications in which this particular wear mechanism occurs. In a study undertaken by Levy and Hickey [84], it was postulated that the medium carrier liquid reduces the kinetic energy of the particles that is transferred to the target metal surface and hence their erosive, compared with the gas medium carrier. There are higher erosion rates with impacts of larger particles. Removal of material by the mechanism of platelet formation is the same for solid particles in a liquid or a gas carrier medium. Sometimes, the liquid carrier medium acts as a lubricant and a coolant to reduce the erosion by impacting solid particles in slurry erosion. Eventually, there was no correlation between the measured erosion rates and tensile properties and hardness of their testing alloys, but it would relate to the strain-hardening coefficient of the alloys.

4.2.3.4 Cavitation Erosion

Cavitation erosion is damage produced by bubbles or gas collapsing near a solid surface and may occur in liquid under pressure gradients in static as in dynamic conditions. As the bubbles move along the material surface, the pressure around the bubbles begins to increase until a point is reached where the pressure outside of the bubble is higher than the pressure inside the bubble. The bubble then collapses as shown in Figure 4.16. The cavitation erosion phenomenon can be found in mainly engineering problems such as: hydraulic equipment, ship propellers, molds for die casting [85, 86].
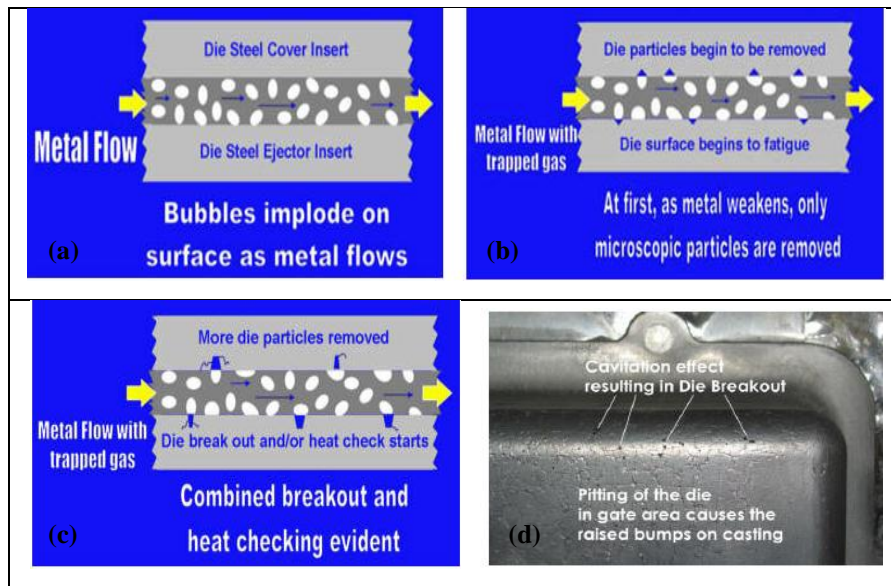
Figure 4.16 Cavitations erosion process in a die steel, a, b and c, schematic drawing for steps of cavitations erosion processed damage pattern in die steel [87].

4.4. Summary of Liquid /Solid Approach

From the previous studies, it is possible to study the approach to considering erosion due to either the sphere solid particle or liquid drop impacting the solid targets in the same way.

Bargman [88, 89] presented a solution for considering the problem of erosion by either liquid or solid impact. It was postulated that liquid or solid impact is a capable of generating specific loss of material (loss of target volume per impact) by a simplified attack process as craters are generated on the target surface. For the both cases liquid or solid impact, when excluding the fatigue and brittle failure, the erosion is ductile by material loss considered to occur from the lips of the craters by ductile rupture.

Andrews & Field [90] studied the erosion of mild steel as targets strike by hardened steel spheres. It was mentioned that the deforming region under the impacting sphere solid impacting was similar to that done by liquid drop impacting. From the results, it was mentioned that the material losses from the solid targets due to the high pressure edges as the initial supersonic regime has been identified when the contact circle expands supersonically causes compressible behaviour in the liquid drop or solid sphere, and then generation of high transient pressures. These high edge pressure associated with the shock attacks the target which causes the metal to flow and extrude.

4.5. Conclusions

In this chapter, the methodology has been presented from previous research which was used to explain and discuss the phenomenon of wear and wear mechanisms. Wear patterns obtained from different wear mechanisms have been presented. It undoubtedly will help to identify the mechanisms involved in each wear process.

In addition, wear mechanisms involved in adhesive, abrasive and erosive wear were presented. Focus was placed on wear mechanisms of liquid/solid erosion. In respect to solid particle erosion (SPE), the main differences between wear mechanisms in ductile and brittle materials were shown and more important variables are mentioned such as impact angle, particle velocity and particle properties such as shape, and material properties changes.

5

Test-Rig Development

5.1 Introduction

In this chapter a complete description of the test apparatus and approach is outlined. Analysis of the motion of the aluminium balls as erodent particles on flat and cylindrical target surfaces is also presented, when they were propelled at different velocities and orientations. Different regimes of particle behaviour for different impact angles (30°, 60° and 90°) for a flat surface, and different locations (central to and offset from the particle flow) for cylindrical surfaces were studied by high speed photography. In this instance, high speed photography was also used to calculate the time of pulsed shots (used to replicate multiple castings).

5.2 Erodent particle properties

6061 Aluminium alloy balls were used as erodent particles to investigate the erosion damage on flat and cylindrical target surfaces made from H13 steel. Balls were 3mm in diameter and 0.04 g in weight. These were selected as it was considered that the size of free droplets of molten 99.99% pure aluminium is between 1 and 3 mm in diameter [91]. The chemical composition and the mechanical properties of the aluminium balls are presented in the Tables 5.1 and 5.2, supplied by *Atlas Ball & Bearing Co. Ltd*.

Table 5.1 Chemical composition of balls

Composition	Al	Si	Fe	Cu	Mn	Mg	Cr	Zn	Ti
Wt%		0.4-0.8	0.7	0.15-0.40	0.15	0.8-1.2	0.04-0.35	0.25	0.15

Table 5.2 Mechanical properties of balls

6061 Aluminum Balls Mechanical Properties	
Yield (MPa)	103
Ultimate Tensile Stress (MPa)	228
Hardness H_v	107
Roughness Ra (μm)	0.843
Ultimate Shearing Strength (MPa)	152

Measurement of the roughness of the aluminium balls was carried out used equipment shown in Figure 5.1. A 3D profilometer seems to be the most appropriate tool to obtain a precise picture of the surface, and evaluate more precisely the surface parameters.
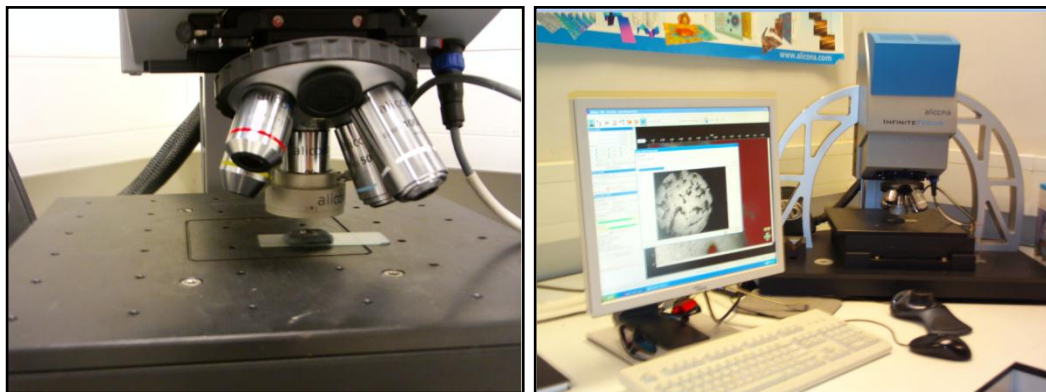
(a)   (b)
Figure 5.1 (a) 3D Alicona optical device, (b) software.

5.3 Rig Development Flow Chart

The rig development flow chart is depicted in Figure 5.2, which shows the tracks of tests and the main factors that were considered.
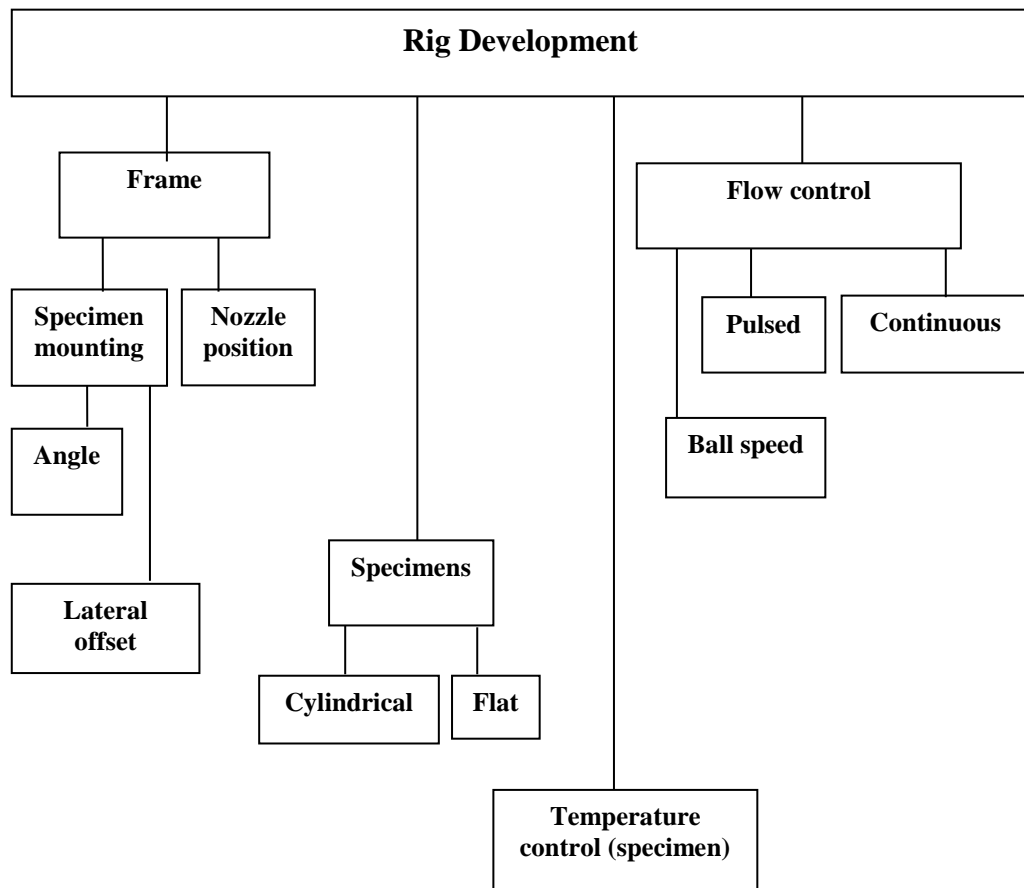
Figure 5.2 Rig-Development Flow Chart.

5.4 Rig Development

This study deals with the development of a test to evaluate erosive wear of H13 steel specimens to approach the realistic simulation of erosive wear in aluminium die casting dies by replicating the important aspects involved in die casting such as: dynamic load, temperature, pulsed load, ductile spherical particle erodent (to approximate the wear from liquid/semi-solid impingement) particle and variable of the impact velocities, and contact geometries.

A technique has been developed using a shot blasting machine to accelerate the wear effects and to allow for quantifiable erosive wear in a reasonable number of shots. These consist of aluminium particles propelled at different velocities. Different surfaces, flat impacted at different angles (30°, 60° and 90°), and a cylindrical surface mounted in two positions, central to and offset from the particle flow. In addition, tests can be run in the laboratory and provide a cheap way of providing an extreme environment similar to industrial operation.

The experimental apparatus used to carry out the tests is a shot blasting machine shown in Figure 5.3. It consists of a frame of 300 x 300 mm, shown in Figure 5.4, to support a gun to supply the aluminium ball/air mixture and a steel rod that holds a specimen holder. The steel rod has dimensions of: 300 mm length, 27 mm diameter and can be rotated, and has an indicator to point out the tilt angle of the specimen. If the specimen holder is tilted at angle 30^0 this means the impact angle will be 60^0. The distance used in every test was 30 mm between the tip of supply gun and the specimen surface.

(a)   (b)
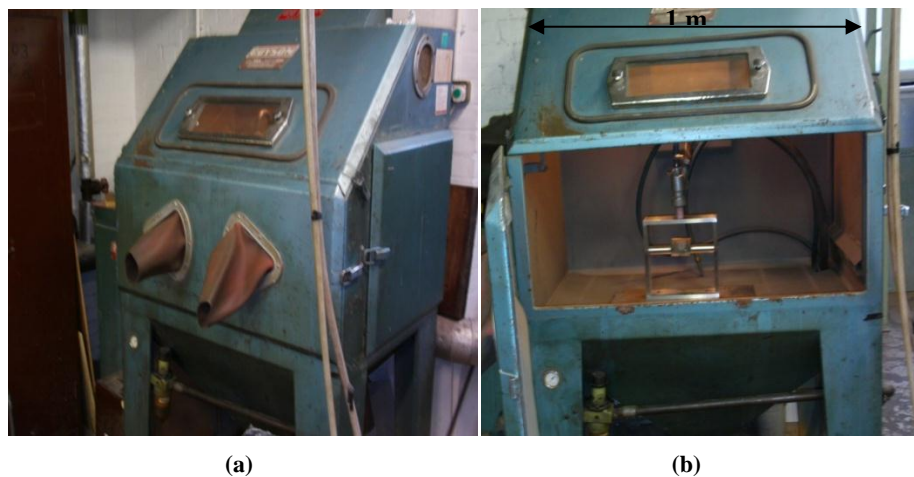
Figure 5.3 A shot blasting machine, (a) outside, (b) inside.
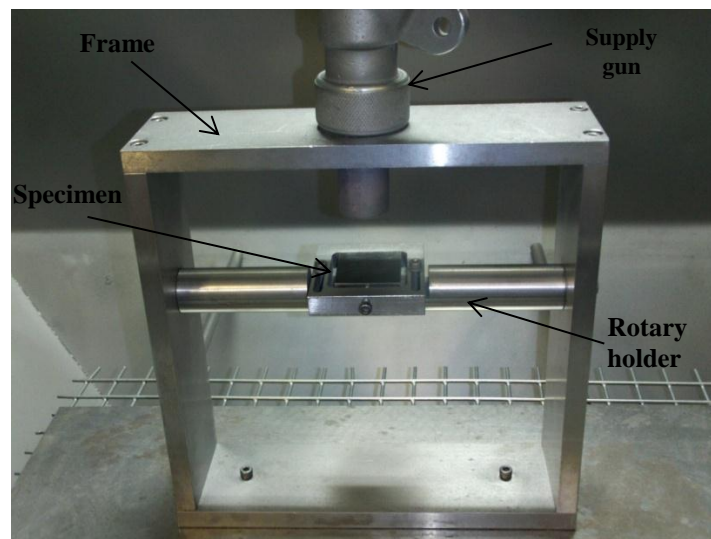
Figure 5.4 Frame inside cabinet.

In Figure 5.5 it is possible to observe that the steel rod that holds the specimen holder has an indicator to point out the tilt angle of the specimen, which helped to set the impact angle used through the test. Also it is seen marked on the left side plate presented an angular graduation scribed every 10° through 90° to indicate exactly the tilt angle used in every test. It means that the specimen holder is tilted at a 0° angle; in this case the attack angle was 90°.

(a)

Graduation 0° to 90°
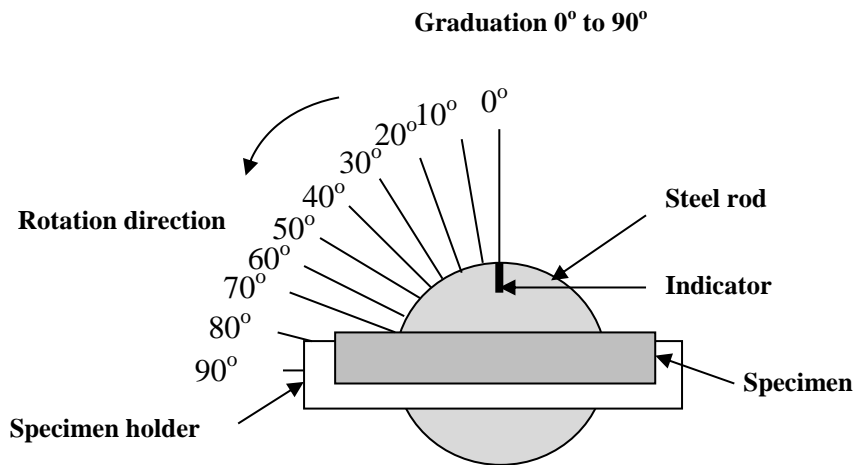
Figure 5.5 Position of specimen being attacked at 90°impact angle, (a) Location in the frame, (b) Schematic diagram of the angular graduation approximation.

High speed photography was used to investigate the motion of the aluminium balls as they impacted the surface of the target H13 steel. Continuous and pulsed shots for aluminium balls were used in testing. It was observed there was a difference with continuous and pulsed. In continuous the balls all have the same kinetic energy. Balls in pulsed shots have a higher kinetic energy at the beginning of a pulse than at the end. Balls fired at the target surface at the beginning of a pulse had a higher velocity balls than the later balls which lost kinetic energy due to friction on the inside of the wall nozzle or friction with the other balls in the flow. The fired balls will rebound after impact, hence they might be crashing with the incoming balls from the nozzle causing them to change the direction and reduce their energy. Pulsed shot was used to simulate a die casting process.

The pulsed time was controlled by a pedal which is mounted at the bottom of the blasting machine. The duration time of the pulsed flow was measured by video footage which registered the time from when the first aluminium ball struck the surface to the point when the last ball struck the surface of the target.

It was found that the time of the pulse was equal to 1.5 seconds. Duration times were calculated for a pulse at four different pressures in the shot blaster (20, 40, 60 and 80 psi).

In addition, the pulse times were measured for the three different counterface positioned at angles of 0°, 30° and 60° (for which the specimen was inclined at angles 90°, 60° and 30° respectively). For cylindrical specimens measurements impingements were studied at central and eccentric positions. For all cases, aluminium balls were fired from a nozzle 30 mm from the specimen, see Figure 5.6.
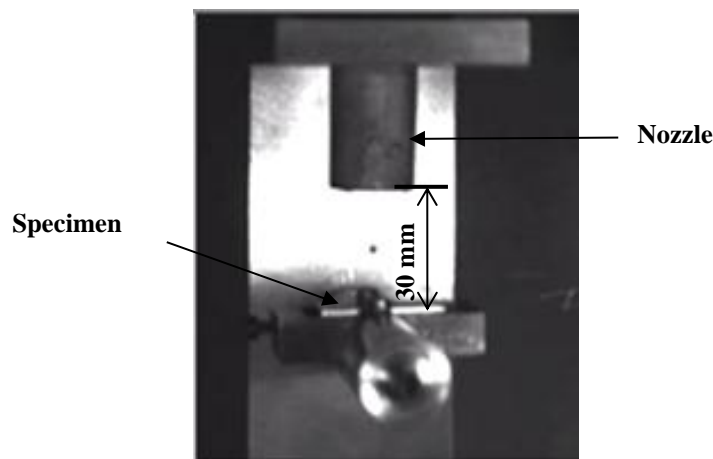
Figure 5.6 Aluminium ball fired onto counterface.

It was possible to use the video to analyse the motion of single and multiple impacts of the aluminium balls. In both cases, four different air pressures (20, 40, 60 and 80 psi) which controlled by the pressure regulator in the shot blaster were used for every impact angle (30°, 60° and 90°). It was possible to determine the velocity of the aluminium balls by firstly measuring the distance that the aluminium ball was displaced frame by frame as it hit the target surface and secondly, by measuring the time that the balls spent in striking the target surface, then by summing the number of frames that was taken in every case to determine the velocity of the balls. It was noticed that the velocity of the ball was increased as increased the air pressure.

5.5 Measurement of Velocity

The video footage from the High Speed Camera was taken to calculate the velocities of the aluminium balls for different operating pressures dependence on the changed parameters of the erosion tests. The software Richimas v3.2 was used to calculate the ball velocities. The measurement of velocity involved determining accurately, the travelled distances between every frame of the ball towards the target surface. Results are shown in Figure 5.7. It is possible to observe that in the case of conduct a 20 psi pressure, the aluminium ball spent at least four frames to impact the surface of the specimen that is mean that the aluminium ball was carried out four displacements from the gun tip to the specimen surface, with respect to the velocity of the aluminium ball that the number of frames were decreased as the velocity of the ball increased. The standard distance from the top point at the gun nozzle and the bottom point on the specimen surface was 30 mm always used to drop the aluminium balls.
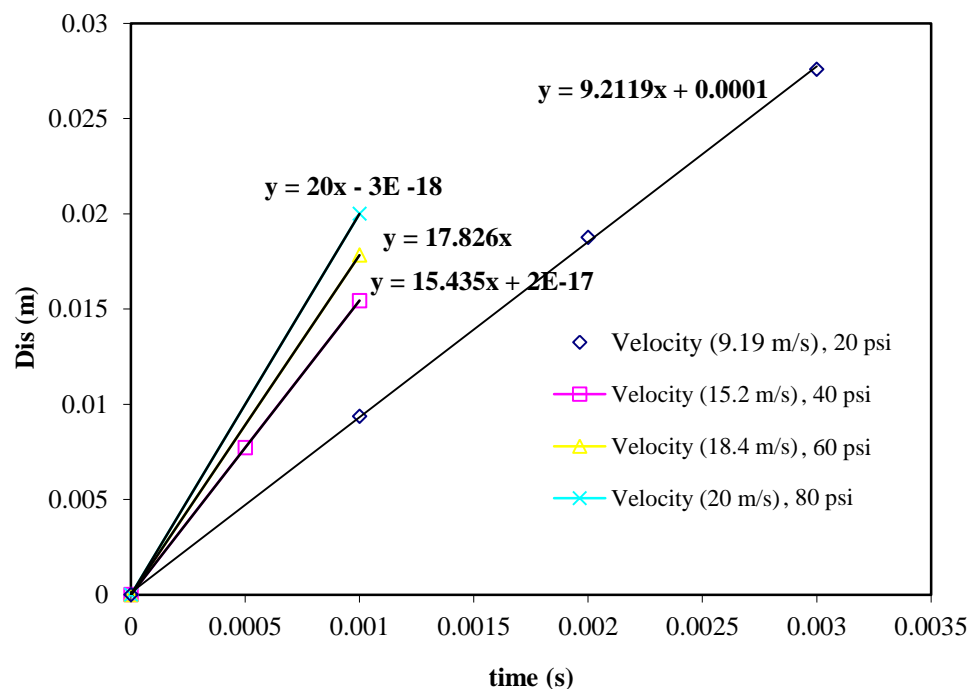

Figure 5.7 The values of "y" and the frames.

In Figure 5.8 an Excel spreadsheet shows the values imported to calculate the velocity of the aluminium balls. The measurments were carried out three times. In the first, it is possible to observe the "x" and "y" values for each one of the points selected in the top and bottom in the software. In this instance, the most important "y" values for calculations the velocities of the balls from the mentioned distance between the top and bottom point and the time between every frame. It varies in accordance with the pressure used to conduct the tests. It is possible to determine the distance for each point in pixels and then converted to millimetres and metres. Then the velocities were calculated straightforwardly as the times were known for every pressure.

	A	B	C	D	E	F	G	H	I	J	K
1											
2		105.7143									
3		127.619									
4	pixels	metre									
5	21.90476	0.01									
6	2190.476	1									
7	time	x	y		Distance pixels		Distance mm	m	Velocity m/s	Pressure (psi)	
8											
9	0	170.4762	70.47619		0		0				
10	0.001	169.5238	90.98781		20.51161952		0.009364	9.36400022	9.19	20	
11	0.002	168.5714	111.5714		41.0952381		0.01876087	9.39686935			
12	0.003	167.619	130.8764		60.40023952		0.027574022	8.81315283			
13											
14											
15											
16											
17	0	173.3333	57.61905		0		0	0	15.2	40	
18	0.0005	173.3333	74.52381		16.9047619		0.007717391	15.4347826			
19	0.001	173.8095	91.42857		33.80952381		0.015434783	15.4347826			
20											
21											
22											
23	0	174.7619	65.71429		0		0	0	18.4	60	
24	0.001	174.2857	104.7619		39.04761905		0.017826087	17.826087			
25	0.002	174.7619	146.1905		80.47619048		0.03673913	18.9130435			
26											
27	0	161.4286	87.14286		0		0	0	20	80	
28	0.001	160.9524	130.9524		43.80952381		0.02	20			
29											
30											

Figure 5.8 Excel sheet corresponding to the velocity calculations.

5.6 Flow Rate

The flow rate for every shot pulsed was determined by weighing the aluminium balls which were ejected from the nozzle after the end of shot pulsed at a fixed amount of time. Table 5.3 shows the values of flow rate for the four different velocities which were used in the erosion tests.

Table 5.3 Velocity of aluminium ball in different pressures

| Particle velocity (m/s)	Flow rate (g per shot)
9.19	14
15.2	30
18.4	41
20	55

5.7 Motion Analysis of Flat Specimens

A high speed camera was used to analyse the motion of single and multiple impacts of aluminium balls on a flat surface. The video footage corresponds to motion analysis of the aluminium balls. Three regimes emerged showing particle behaviour on the surfaces of specimens, (a) impact only, (b) impact and sliding, (c) Pressure only (no impact, no sliding) are shown in Figure 5.9.

(a)   (b)   (c)
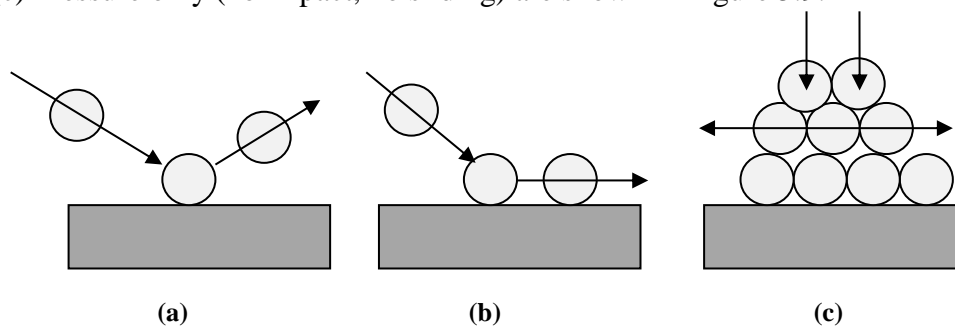
Figure 5.9 Three regimes showing particle behaviour and wear mechanisms on the surfaces of specimens, (a) Impact only, (b) Impact and Sliding, (c) Pressure only (No Impact, No Sliding).

Aluminium balls were dropped individually at first to show the behaviours of a single aluminium ball. It was observed that the aluminium balls exhibited the behaviours outlined in Figure 5.9. The angle of impact had a significant influence on the impact behaviour of the aluminium ball. Every aluminium ball dropped, impacted the specimen surface differently. This produced different deflection angles as shown in Figure 5.10.
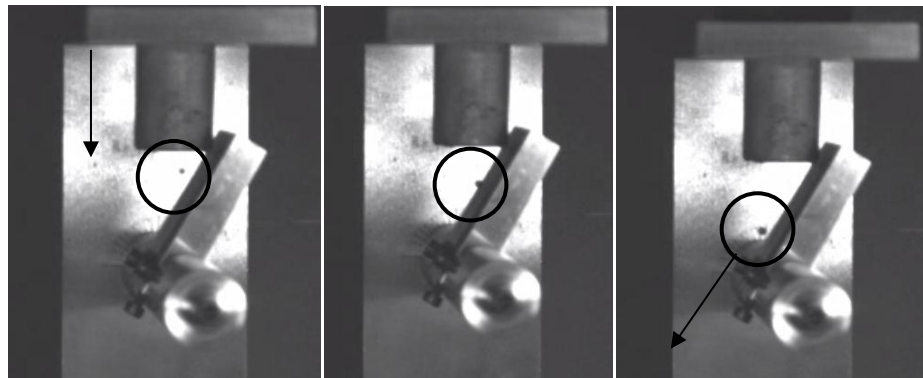
(a)   **First Displacement**   **Impact**   **Deflection**
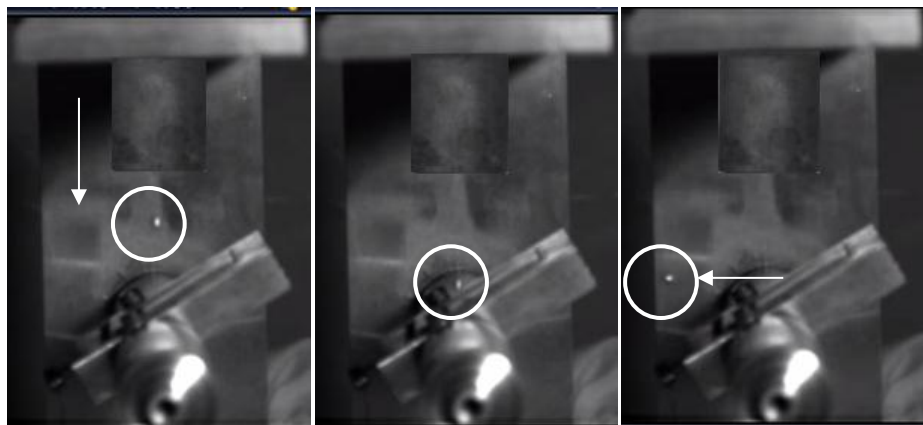
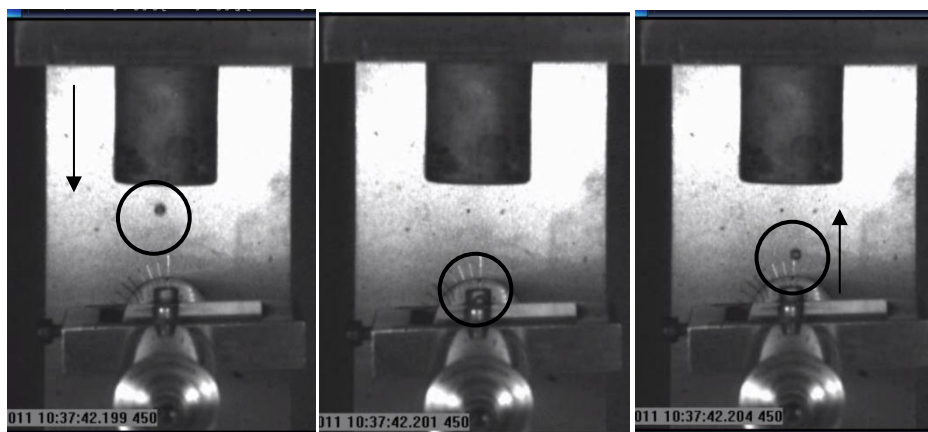(b)   **First Displacement**   **Impact**   **Deflection**

(c)   **First Displacement**   **Impact**   **Rebound**

Figure 5.10 Sequence of aluminium ball impacting at (a) 30°, (b) 60°, (c) 90° angles, fired at 9.19 m/s.

5.7.1 Motion Analysis at 30°

Figure 5.11 shows that the aluminium balls travelling during the pulse time to impinge on the flat specimen surface when it was fired at 9.19 m/s and the specimen surface was tilted at 60° to be impinged at 30°, it is possible to see that the aluminium balls struck in the top and the central part of the specimen and then were directed downwards as shown in Figure 5.12. Aluminium balls at the start of the pulse had high kinetic energy and tended to rebound. Conversely, at the end of the pulse energy was lower and balls tended to slide.
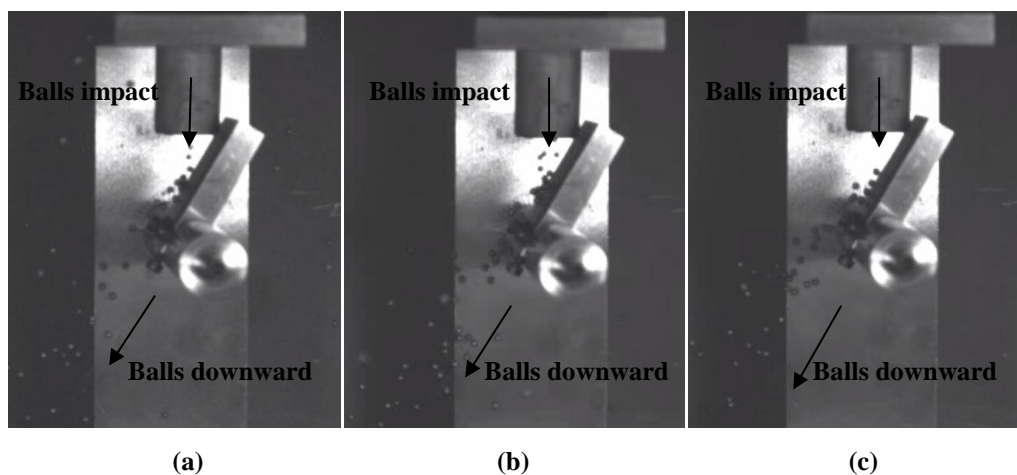

(a) **(b)** **(c)**

Figure 5.11 Multiple impacts of aluminium balls at 30°, (a) at 0.1 sec, (b) at 0.6 sec, (c) at 1.2 sec, of pulsed time
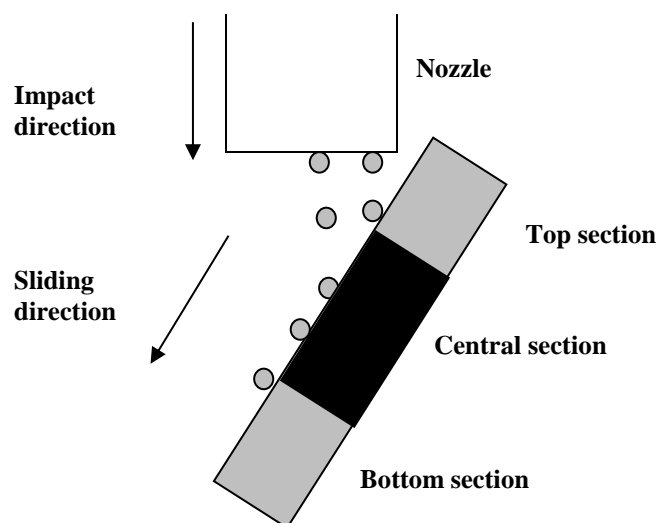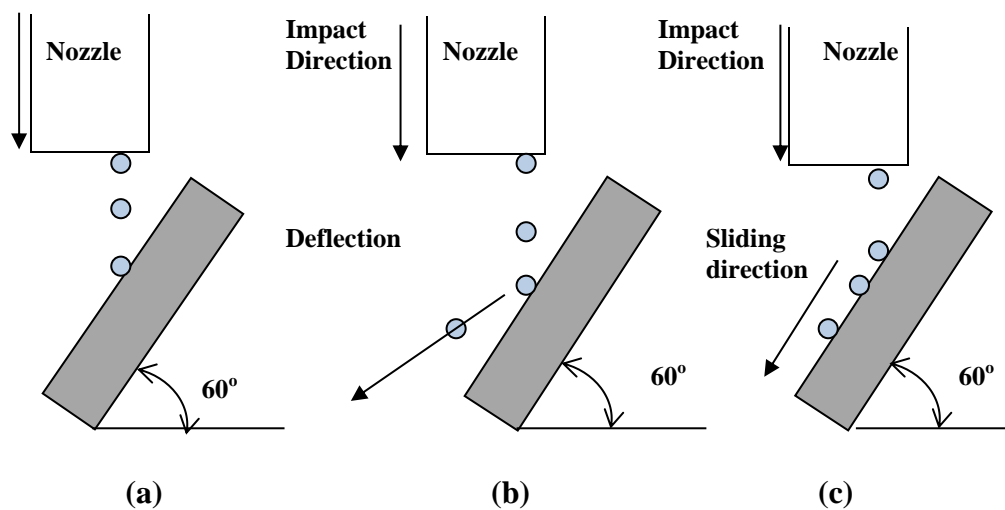

Figure 5.12 Aluminium balls impacting at different parts of the specimen.

In addition, the analysis carried out at an impact angle of 30° showed that the aluminium balls had a different behaviour than when they impacted at 60° or 90°. Sliding was seen after impact due to the horizontal force being larger than the vertical force when the aluminium balls impinged the surface, together with a few interrupted layers of balls. Video footage was captured at different times of during the 1.5s pulse at, ($t_1 = 0.1s$, $t_2 = 0.6$, $t_3 = 1.2s$) representing the start, middle and the end of a pulse respectively, to distinguish the behaviour of the balls. It was seen that at t_1 most of the balls rebounded due to having high kinetic energy, while at t_2, the aluminium balls impacted the surface at the top and the centre of the specimen and then slid down the surface. On the other hand, at t_3, it was seen that many aluminium balls impacted the surface, it meant some of the balls formed interrupted layers. Figure 5.13 illustrates the regimes seen for aluminium balls, impact, impact and sliding, another regime for balls when they interrupted, particularly, at the mid duration time of the pulse.

Figure 5.13 Aluminium balls impacting at 30°. (a) ball impact, (b) ball rebound at t_1 of pulse, (c) ball sliding at t_2 and t_3.

In Figure 5.14, the damage on the aluminium ball is clearly seen, which illustrates the regimes of the aluminium balls behaviour through the pulse for an impact angle of 30°.

From the video footage the damage presented a flat surface with scratch lines on the aluminium ball, it means that an impact with sliding could be happening when the ball strikes the surface of the specimen, on the other hand, damage with flat area did not involve scratch lines, it means that only impact happened. In addition some damaged areas were concave, it means that the ball could have been pressed by other balls.
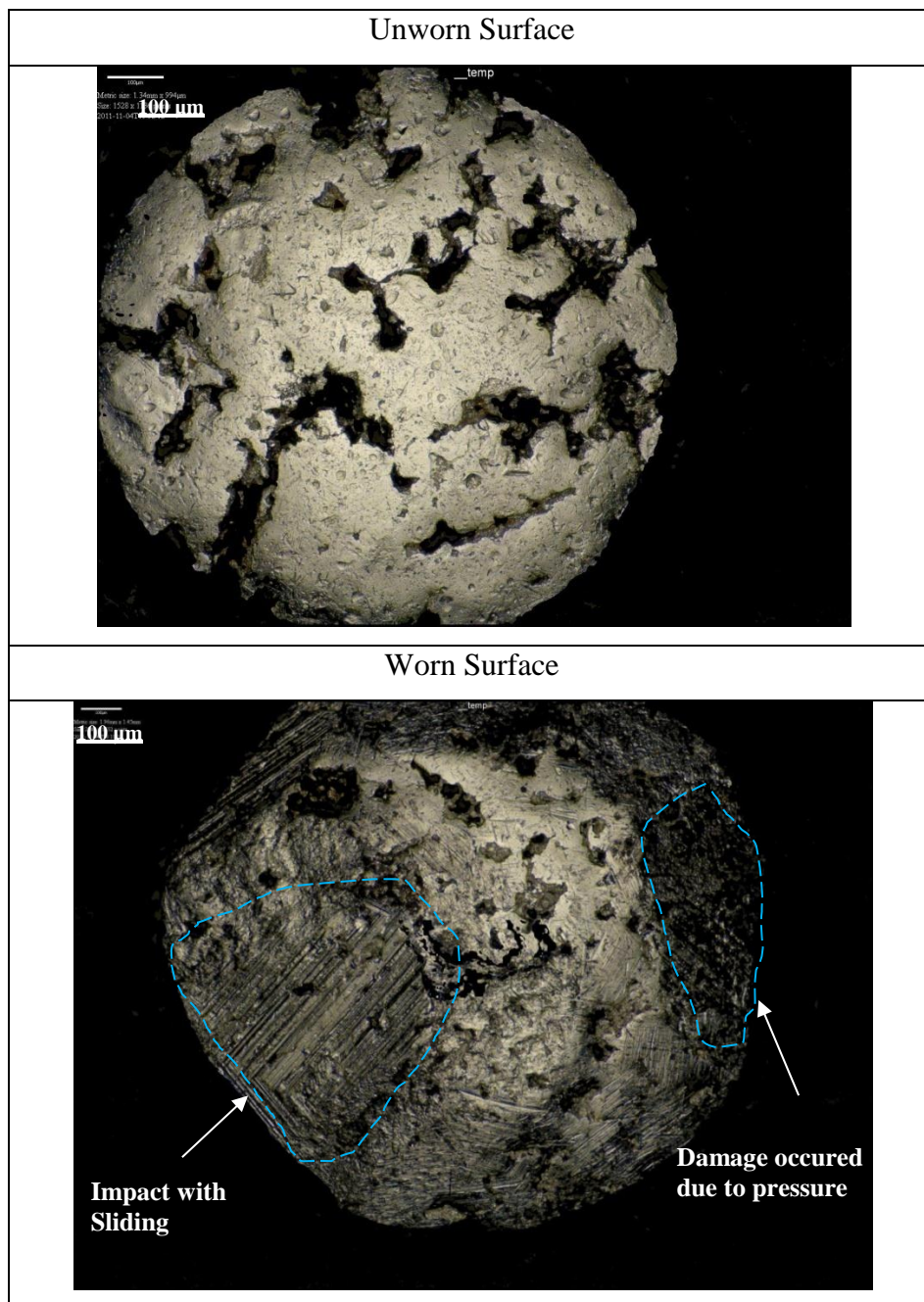

Figure 5.14 Aluminium ball impacting at 30°, fired at 15.2 m/s.

5.7.2 Motion Analysis at 60°

The specimen holder was positioned at 30° so that the specimen was impacted at 60°. In the video shown in Figure 5.15, it is possible to see that the tendency is the same as in the first case when the specimen struck at an impact angle of 30°, the aluminium balls struck in the top and the central part of the specimen and then were directed downward. However, it was noticed from the video frames that the rebound angle was higher than at impact 30°. The same behaviour was seen for all velocities, except that the movement of aluminium balls when 9.19 m/s was used is slightly shorter than at a 20 m/s was used.

| (a) | (b) | (c) |
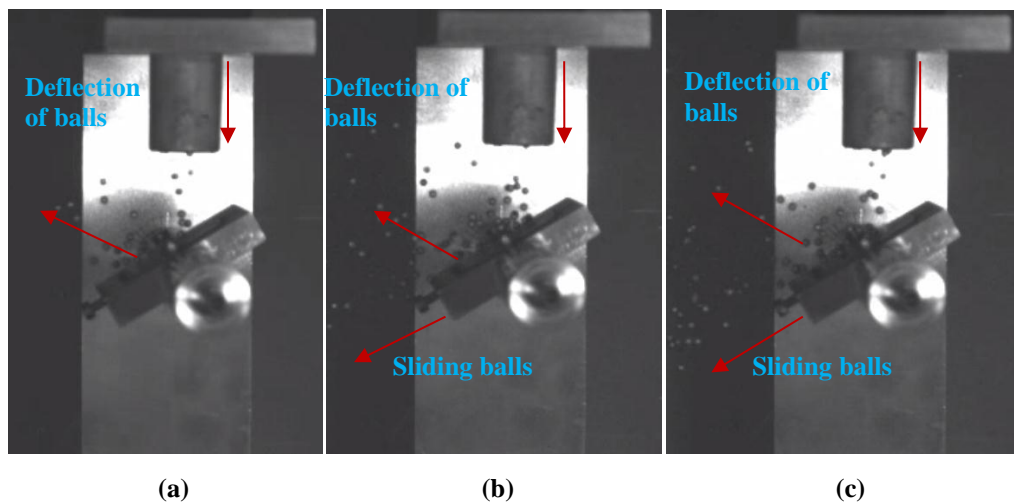
Figure 5.15 Multiple impacts of aluminium balls at 60°, (a) at t$_1$ (b) t$_2$, (c) t$_3$, of the pulse.

From the frames of videos taken at t_1, t_2 and t_3 of the pulse, the aluminium balls behaviour at t_1 indicated that fewer aluminium balls impacted the surface than at t_2 and t_3. In this case, the aluminium balls impacted directly on the surface, meaning that the journey of the aluminium balls was not interrupted by a layer of aluminium balls also they had high kinetic energy and rebounded from the surface. In addition, it was observed that a few of the aluminium balls were sliding slightly before rebounding from the surface. It was noticed that more sliding with aluminium balls occurred when they impacted on the bottom of the surface.

Also seen in videos was that a few balls when they were rebounded upwards were struck by incoming aluminium balls so that these balls were propelled to re-impact the target surface.

The schematic in Figure 5.16 illustrates the three regimes seen during the pulses: (a) impact only, (b) impact and sliding, (c) pressure only, which the analysis registered higher for two regimes at the impact 60°, impact only and impact with sliding.

The regime of impact only was done by the individual balls which impacted at the start of the pulse, another regime for balls occurred when they impacted and slid, particularly, at the bottom of the surface. However, the pressure regime registered when the balls trapped between beneath layers of balls, practically registered at the t_2 point of the pulse.

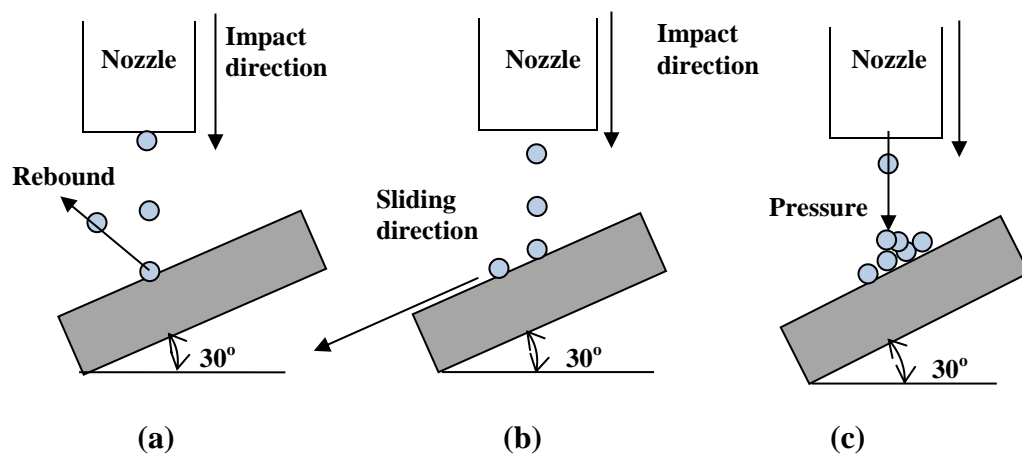**Figure 5.16 Aluminium balls impacting at 60°. (a) ball rebound, (b) ball sliding, (c) ball pressure.**

5.7.3 Motion Analysis at 90°

From the video footage in Figure 5.17, captured at different times in a similar way to those at impact angles of 30° and 60°, it is possible to observe that the behaviour of the aluminium balls when they were impacted on the flat surface at an incident angle of 90°.

At the start of the pulse, most of aluminium balls impinged directly onto the surface and as the progress of the aluminium balls were not interrupted by a layer of aluminium balls and had high kinetic energy, so they rebounded from the surface after impacting the surface. Also it was seen a few of balls impacted with sliding depended on the location of the impact on the surface. It means this time the pulse had three regimes, impact only, impact with sliding and pressure only.
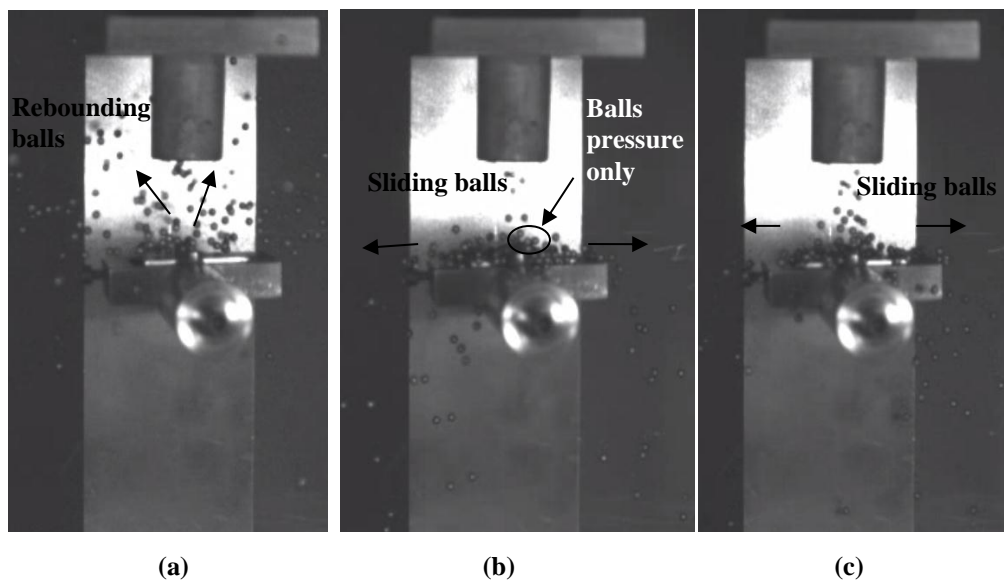
Figure 5.17 Multiple impacts of aluminium balls at 90°, (a) at t_1 (b) t_2, (c) t_3, of the pulse.

Schematic Figure 5.18 illustrates three regimes that occurred during the pulse period at t_1, t_2 and t_3, (a) impact only, (b) impact and sliding, (c) pressure only respectively. The images show the higher for two regimes at the 90°, impact with the sliding and pressed regime. The regime of impact only occurred by the individual balls with high kinetic energy which impacted at the t_1 of the pulse, impact and sliding regime particularly, at t_2 and t_3 of the pulse, However, together with press regime showed at the t_2 and t_3 of the pulse when the journey of incoming aluminium balls was interrupted by the upper layers of aluminium balls above them which contributed to disruption the balls from rebounding after impacting the surface.
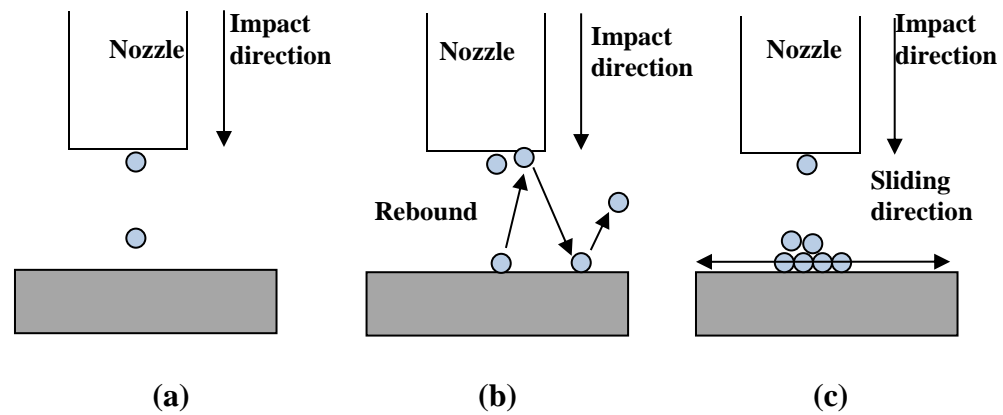
Figure 5.18 Aluminium balls impacting at 90°. (a) Ball impact, (b) Ball rebound, (c) Ball sliding

In Figure 5.19 the damage on the aluminium ball is clearly seen. It is possible to observe the regimes of the aluminium ball behaviour through the pulsed shot for impacting angle 90°. From the video footages the damage is presented on a flat surface with scratch lines, which means that impact with sliding happened when the ball struck the surface of the specimen. On the other hand, the flat area of damage without scratch lines means that only impact happened when the ball struck the surface. In addition it is seen some damage of areas are concave which means that the ball was pressed by other balls. Also it is seen that the damage area caused by the impact and sliding regime is larger than those for impact only, and the pressure regime.
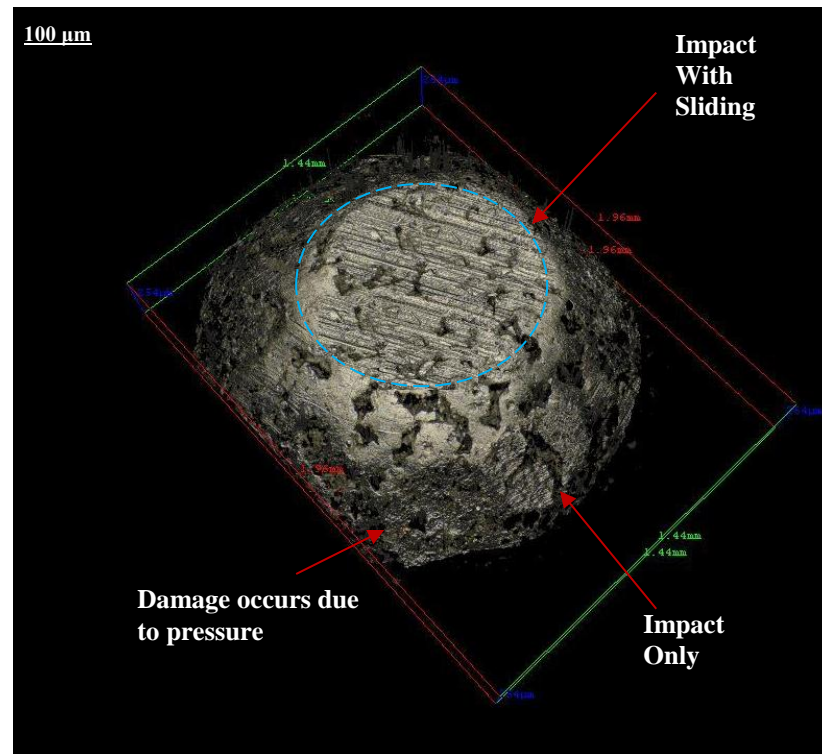
Figure 5.19 Aluminium ball impacting at 90°, fired at 15.2m/s.

5.8 Motion Analysis with Cylindrical Specimens

5.8.1 Tests Apparatus and Method

Motion analysis was conducted by using a high speed camera to investigate the behaviour of aluminium balls impacted against H13 steel cylindrical specimens mounted at two locations in the frame, centrally and eccentrically as shown in Figure 5.20. Initially, the video footage was used to determine the duration of a pulse. Exposure time for a pulse was measured by registering the time the first ball struck the surface and the last ball struck the surface. It was found the time of a pulse was equal to 1.5 second for each velocity (15.2 and 20 m/s).

In the second case, video footage was used to analyse the motion of balls. The tests were conducted in the shot blasting machine with a nozzle of internal diameter 10 mm and length 50 mm. Air pressures of 40 and 80 psi were used in the shot blaster to conduct the tests with velocities of aluminium balls of 15.2 and 20 m/s respectively. For the all cases, aluminium balls were fired from a height of 30 mm.
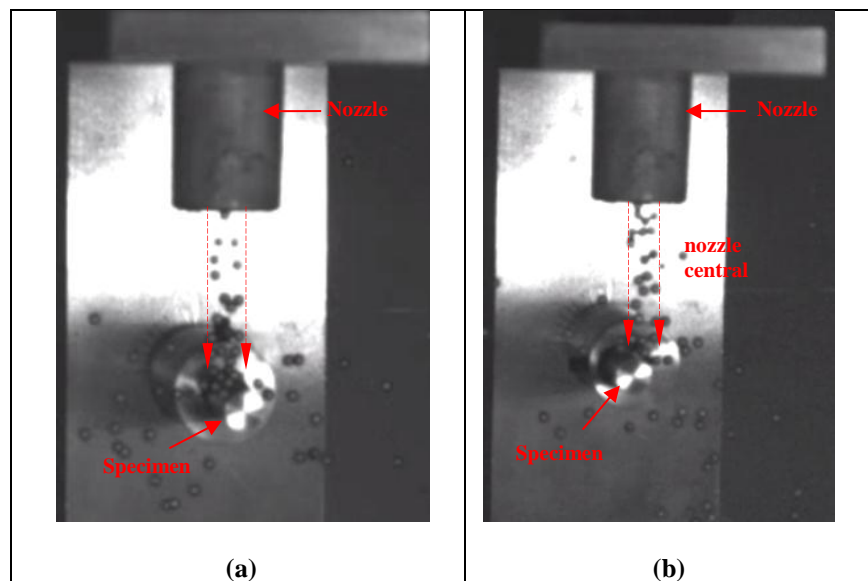
Figure 5.20 Impact of aluminium balls at two locations, (a) Central, (b) Eccentric.

Motion analysis was carried out to examine the behaviour of the aluminium balls when they were impacted on the surface material in two cases, a central and eccentric location. In the first case, when the particles impacted the surface centrally, the specimen mounted in the holder was designed to allow for the particles to strike at the central zone of the surface (see Figure 5.20).

The surface of the specimen was split up to 12 radial zones and angles, as shown in Figure 5.21. The zones start of at 0, or angle 0°, and finished at zone 12, or angle 180°, with each radial zone being 15°. This was done to show the different motion in each one of the impact zones. This could help to understand more completely the particle behaviour in each zone and later to explain the relationship between the motion and the damage seen.

(a)
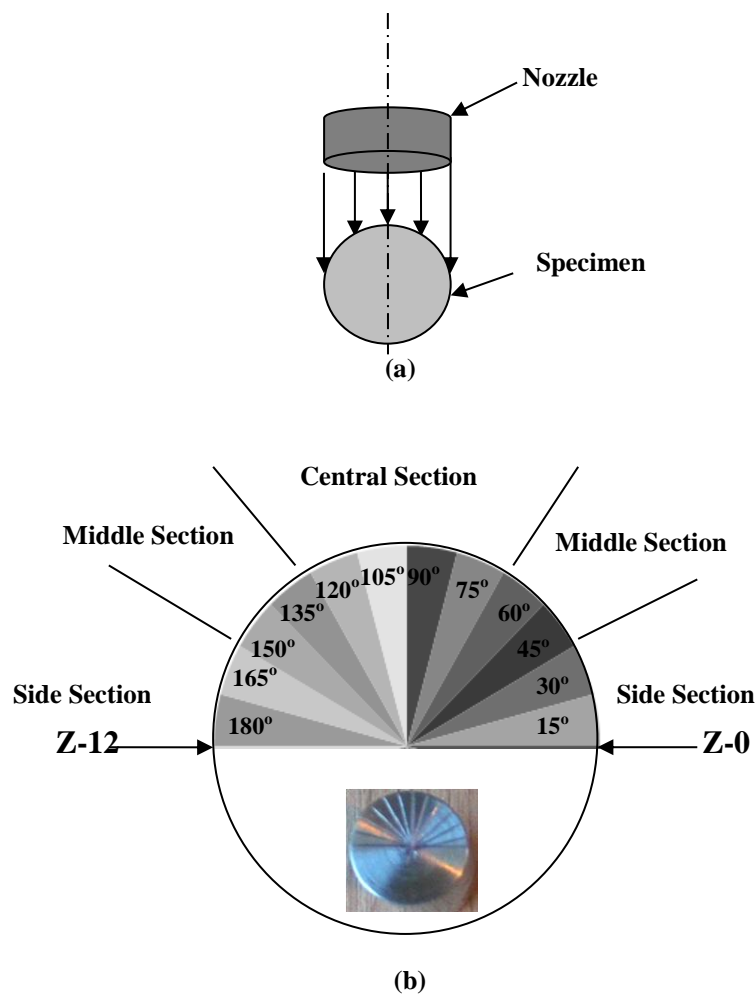
(b)
Figure 5.21 Impact zone at, (a) central location, (b) angles and radial zones.

From high speed camera footages, it seems suitable to define four regimes as follows: (a) impact only, rebound after impact, (b) impact and sliding, (c) sliding only, (d) pressure only, no impact no sliding, for the behaviour of particles striking on a cylindrical surface mounted in a central position, depending on the initial ball location as shown in Figure 5.22. The behaviour of the aluminium balls of both velocities was similar.
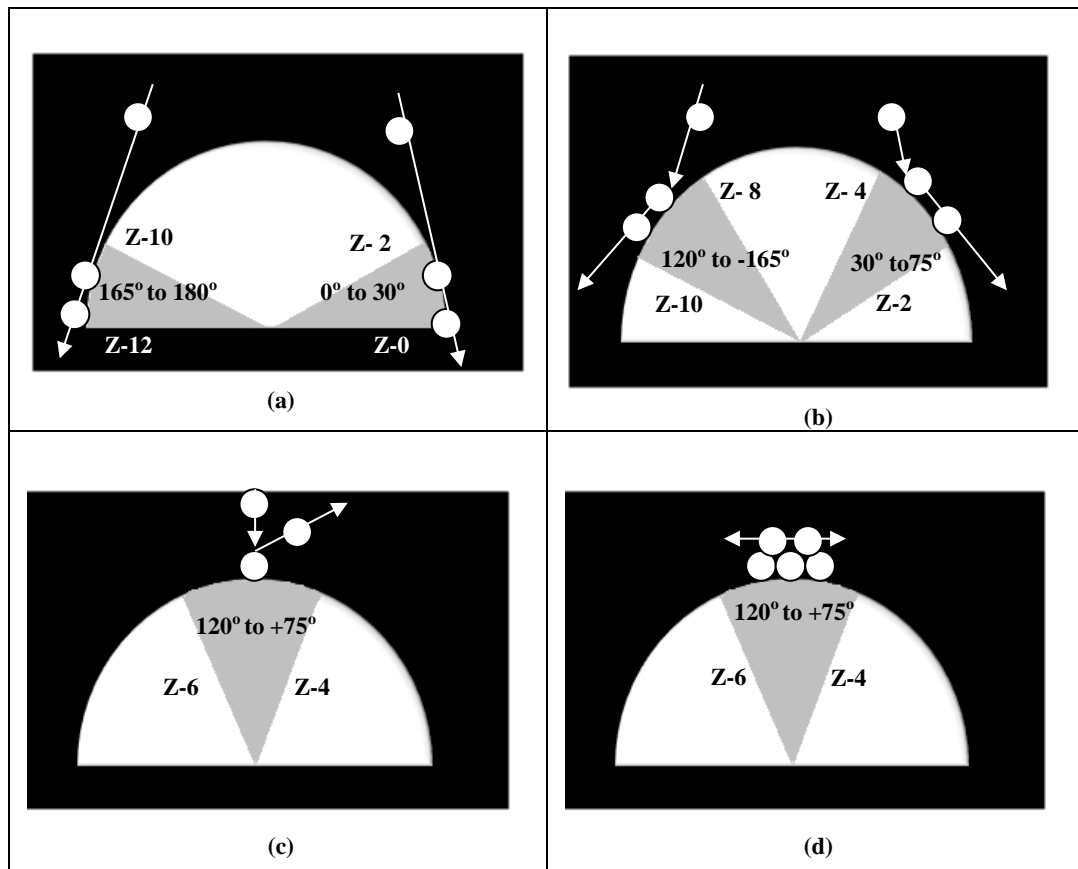
Figure 5.22 Schematic drawing to illustrate the regimes of particle behaviour impacting   a specimen at a central location, (a) Sliding only, (b) Impact and sliding, (c) Impact only, (d) Pressure only, No Impact, No Sliding.

In light of the above, it is clear that the impact and sliding are two independent mechanisms of erosion which can exist either separately or sequentially which means impact is not necessarily required in order for sliding to occur. The analysis of motion showed different behaviour for the balls. It was observed in all ball velocities used, the impact regime occurred at the central section between the angles 75° and 120° or radial zones (4-8). However, it was observed that most of balls impacted and then rebounded in this zone. It was seen that the most of the balls were sliding after impact in the sections between, angles 30° to 75° and 120° to 165°, or radial zones 2-4 and 8-10. Also, the sections showed that the impact and sliding coexist, and compete more than in other sections on the material surface. The higher angle, the higher is the portion of impact, and vice versa at lower angles.

In addition, analysis has shown that the sliding regime occurred in zones between, angles 0° to 30° and 165° to 180° on the surface, or radial zones 0-2 and 10-12. Balls in this zone only slid and no rebound occurred. Finally, the regime of pressure for the balls was shown at the section between the angles 75° and 120° or radial zones 4-8. However, the phenomenon of pressure only occurred due to the pulse shot which caused accumulation of balls in the central zone. In the second case, the specimen holder was positioned to allow particles to impact the specimen surface at an eccentric location as shown in Figure 5.23a. The samples and pulse time were exactly the same as in the first of tests. Unlike the first set of tests, when the specimen was at an eccentric position, some particles were acting on the surface and some missed it. Like the previous case, the surface of the specimen was split up to 6 radial zones and angles as shown in Figure 5.23b, the zones and the angles start at zone 0, or angle 0°, and finished at zone 6, or zone 90°, each radial zone is 15°.

(a)

(b)
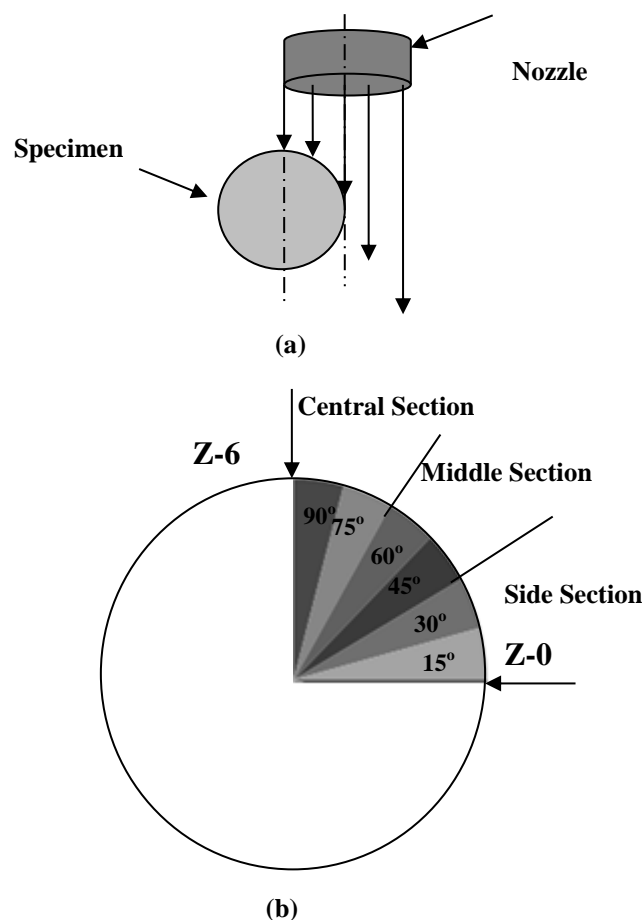
Figure 5.23 Impact zone at, (a) eccentric location, (b) angles and radial zones.

Four behaviours were observed when the aluminium balls impacted the surface at an eccentric location, as shown in Figure 5.24. Firstly, balls impact and rebound. It was seen that the zone range of impact is between angles 75° to 90°, or radial zones 5-6. The second behaviour was observed in the section between angles 30° to 75°, or zones 3-5 when the balls slid after impacting the material surface. The third behaviour was indicated that balls only slid on the surface in the section between angles 0° to 30°, or zones 0-2. Unlike the first case when the specimen was at a central position, very low behaviour for the pressure regime was acting on the section between angles 75° to 90°, or zones 5-6.
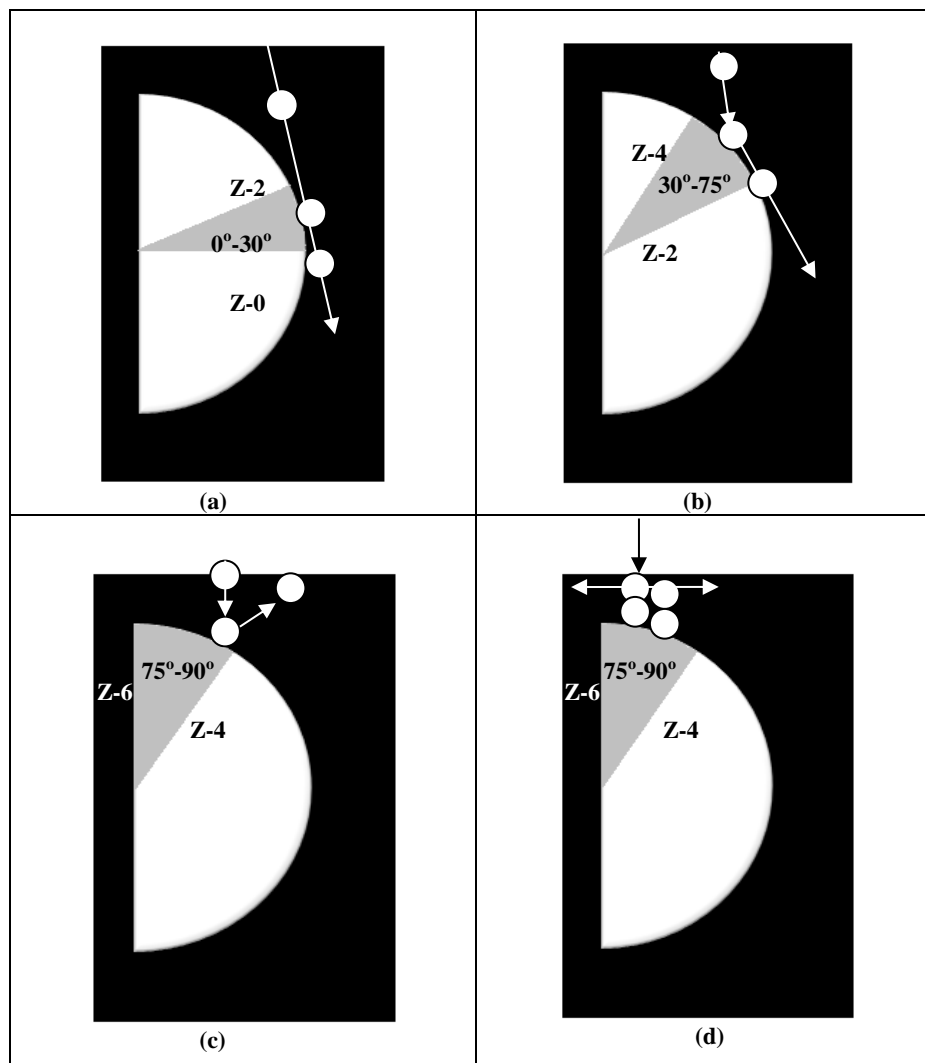
Figure 5.24 Schematic drawing to illustrate the regimes of particle behaviour impacting a specimen at an eccentric location, (a) Sliding only, (b) Impact and Sliding, (c) Impact only, (d) Pressure only, No Impact, No Sliding.

5.9 Conclusions

A test-rig has been developed to study the erosive wear in aluminium die casting and provide an environment similar to industrial operation that is more practical than using actual machines. Motion analysis for aluminium balls was carried out using video footage to determine that they impacted the surface target at different orientations which gave different rebound angles and different three regimes observed for the aluminium balls behaviour at each impact angle on the surfaces of specimens. In addition, it was observed that the aluminium balls were more interrupted at impacted angles 60° and 90° which the videos are showing more aluminium balls were sliding after impact target surface at impacted angle 30°. From these observations, it was concluded that the ploughing and cutting wear mechanisms had a strong effect on the erosion damage by sliding impact.

The use of high speed video technique gave an idea about the different motion of the aluminium balls and also how the wear mechanisms were produced.

6

Erosion Testing on Flat Surfaces

6.1 Introduction

This chapter describes the erosion tests carried out at on flat specimens. A new test has been established for the study of erosive wear resistance of die materials on three stages: without treatment, is presented in this chapter, after heat treatment and with coating surface will present in subsequent chapters. Experimental testing was carried out on H13 steel specimens as this material used to make dies. In the experimentation, four different velocities and three impact angles were carried out to evaluate the erosion rate with these parameters. Therefore, it was determined to carry out erosion tests using a shot blasting machine to propel the aluminium balls to impact the specimens. The results are presented here with possible reasons for wear mechanism behaviour.

6.2 Experimental Details

Erosion tests were carried out by a shot blasting machine with a nozzle of internal diameter 10 mm and length 50 mm. The target materials employed to carry out the tests were H13 steel with hardness 350 H_{V20}. H13 steel was used as a target material due to its wide use for aluminium, magnesium, and zinc die casting dies where resistance to thermal fatigue due to alternated heating and cooling cycles is of primary importance. [92-94]. Table 6.1 shows the chemical composition (wt. percent) of the H13 steel was used.

Table 6.1 Chemical composition of H13 steel

Composition	C	Si	Mn	P	S	Cr	Mo	V
Wt%	0.37	0.89	0.45	0.011	0.001	5.12	1.25	0.88

The average roughness of each specimen before testing was 0.587 µm, and their dimensions were 40 X 40 mm X 10 mm in thickness. 6061 aluminium alloy balls were used as the erodent. The balls had a diameter of 3 mm and were 0.04 g in weight.

6.2.1 Test Method

The impact experiments were carried out with the impulse-flow balls/air mixture controlled by the pedal at the bottom of the blast machine (as described in Chapter 5). The erodent particles (aluminium balls) were carried down the hopper mounted at the bottom of the cabinet of the blast machine. The system was very quick to operate, allowing a great many ball impacts to be carried out in the time scale of the pulse. Aluminium ball velocities were controlled by four different air pressures, 20, 40, 60 and 80psi giving velocities of 9.19, 15.2, 18.4 and 20 m/s respectively. In addition, three impacted angles on the target surface were used, 30°, 60° and 90°. When measuring the time between the first aluminium ball striking the surface and the time of the last ball strike on the surface (in the high speed video), it was found out the duration time of the pulsed shot was equal to 1.5 second for each shot.

The total shots in every test was 7200, although the specimen was removed every 1200 shots to measure the mass loss. The specimens were weighed using an analytical balance with an accuracy of ±0.00001g, before the beginning of the each test and removed every 1200 shots, cleaned and reweighed to find the mass loss. Aluminium balls were fired from a height of 30 mm. Erodent particles were changed each 7200 shots for all tests.

6.3 Results and Discussion

6.3.1 Wear Scars

The first stage, of tests was carried out using the flat surface of H13 steel specimens. The specimen characteristic surface feature after being impacted at each different velocity and impact angle were examined using an optical microscope and two methods were used to quantify surface topography, a 2D profilometer and a 3D. The wear scar was split up into three sections: top, central and bottom with respect to the position that it held in the specimen holder during the testing time. This was done to show the difference in each one of the impact zones. Higher damage was seen in the central part, but also slight damage was observed in the top and bottom part of the erosive scar. Figure 6.1 shows a typical erosive wear scar obtained when impacted at an angle of 30° and the three zones.
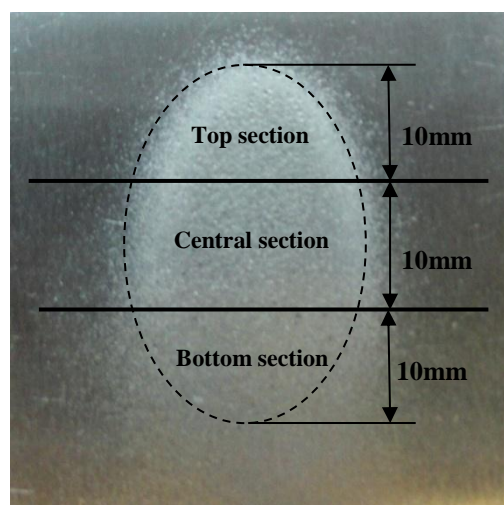
Figure 6.1 Wear scar zones.

6.3.2 Surface Morphology

Figure 6.2 shows the images of erosive scars inflicted on a specimen surface when impacted at an angle of 30°. It is possible to observe the damage inflicted on each of the specimen surfaces is dependent on the different velocities of the aluminium balls. All wear scars were shallow elongated craters with an elliptical shape. The erosive scar was larger with higher velocity. The surfaces of the specimens were examined with an optical microscope and infinite focus microscope, which characterized the erosive wear damage features. The images are presented in the three sections of the erosive scars (see Figure 6.2).

9.19 m/s	15.2 m/s
16mm	17mm
18.4 m/s	20m/s
20mm	22mm
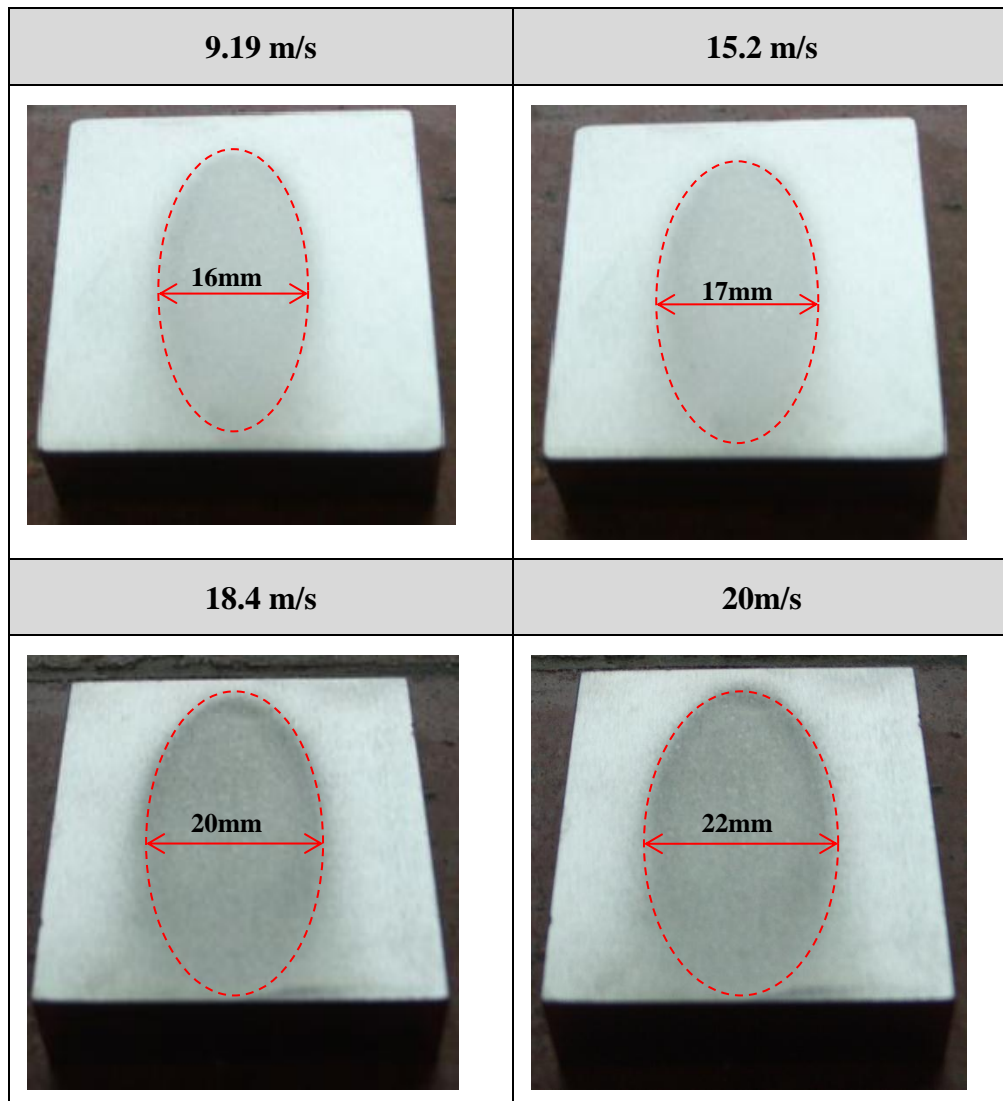
Figure 6.2 Wear scars at an impact angle for 30°.

The images in Figure 6.3 are from the top section, which were characterized by tiny pits spread on the surface of the specimen, a few shallow round and elliptical craters, irregular indentation lines and small cracks. The size of the indents grew as the velocity increased. Table 6.2 presents the size of craters on the surface at an impact angle of 30°.
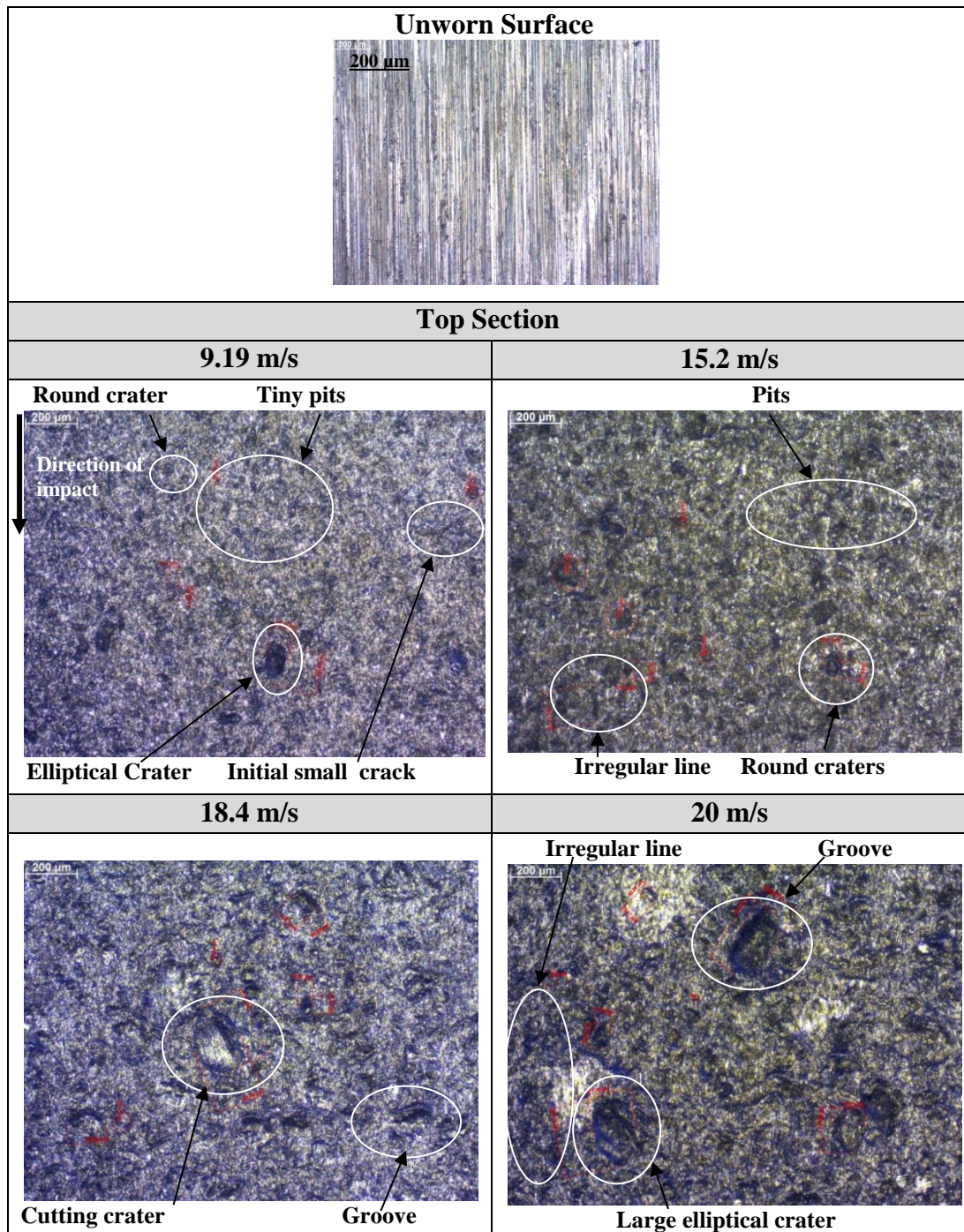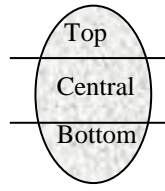
Figure 6.3 Erosion damage at top section 30° impact angle.

Table 6.2 Average size of round (RC) and elliptical craters (EC) at an impact angle of 30°

Velocity (m/s)	Average Crater Size (µm)					
	Top		Central		Bottom	
	RC	EC	RC	EC	RC	EC
9.19	37	113	40	151	30	84
15.2	46	127	66	162	37	97
18.4	85	162	129	273	43	112
20	125	204	153	283	66	115

In the central section, pits and craters produced due to impact of balls were larger than those at the top or the bottom section and increased with rising ball velocity. Damage at the central part of the specimen has been significantly increased by subsequent balls striking with high kinetic energy later in the pulse where the balls had no friction with the inside wall of the nozzle to slow them down. In addition, most of the balls struck in the central part of the specimen. The erosion damage was characterized by pits, round and elliptical craters (see Table 6.2), irregular indentation lines and grooves as shown in Figure 6.4. Finally, at a velocity of 20 m/s, the wear damage showed more irregular grooves and irregular zigzag indentations.

Central Section	
9.19 m/s	**15.2 m/s**
18.4 m/s	**20 m/s**
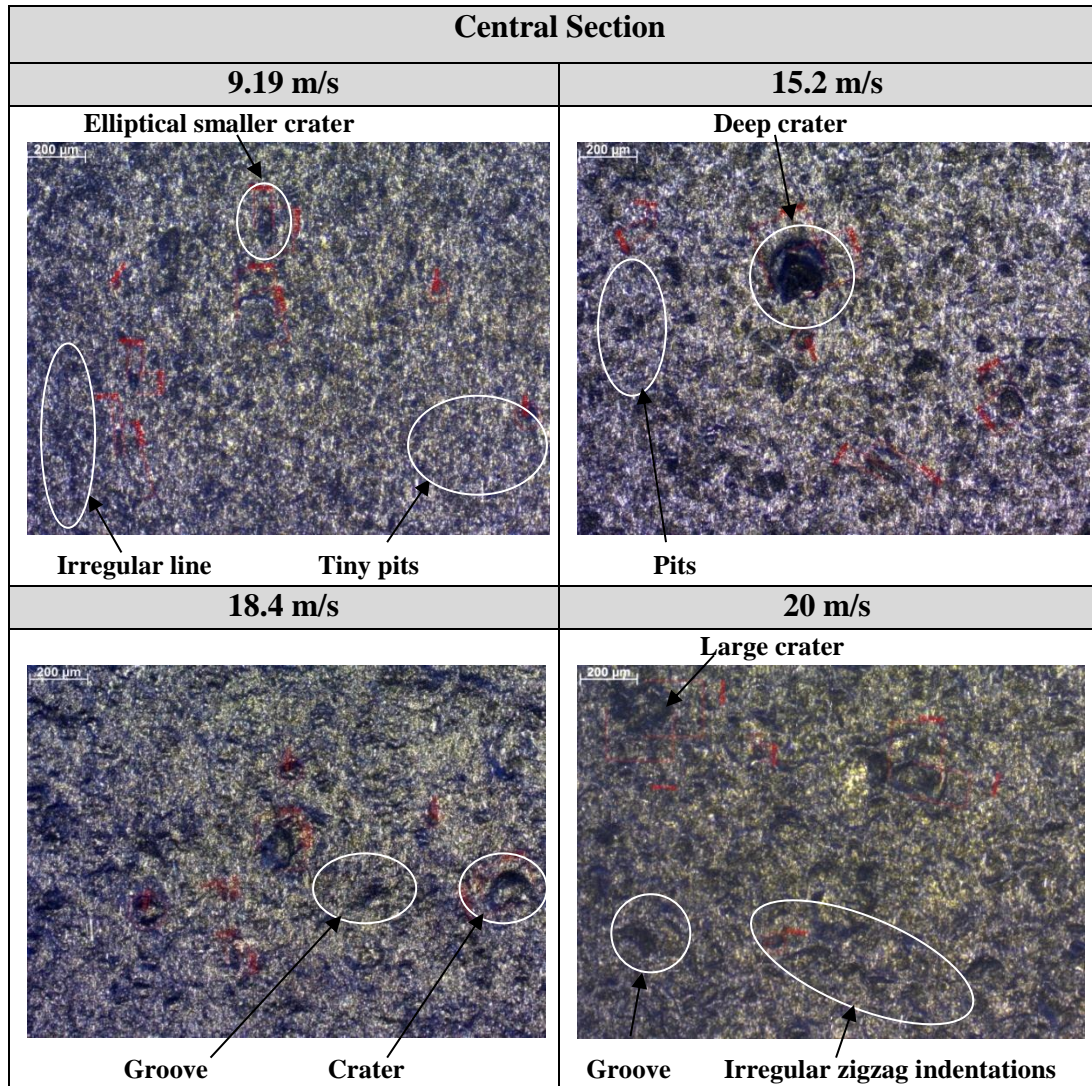
Figure 6.4 Erosion damage at central section 30° impact angle.

The wear mechanisms which cause the material loss from the bottom of the scar are ploughing and cutting, see Figure 6.5. In addition, it is seen that most damage on the surface of the specimens was incurred here as most material was removed by balls acting with different orientations, so some cut material as a chip and others slid along the surface downwards after the first impact, raising prominent lips.

In all cases, it is supposed that material was removed by a cutting action similar to cutting tool in a grinding process so more random irregular indentations are observed in the micrographs. In addition, the bottom section showed evidence of irregular indentations similar to scratches that could have been inflicted by sliding of the balls after the first contact with the surface. In addition, elliptical pits and craters similar to the case of the top section occurred with varied size (see Table 6.2).
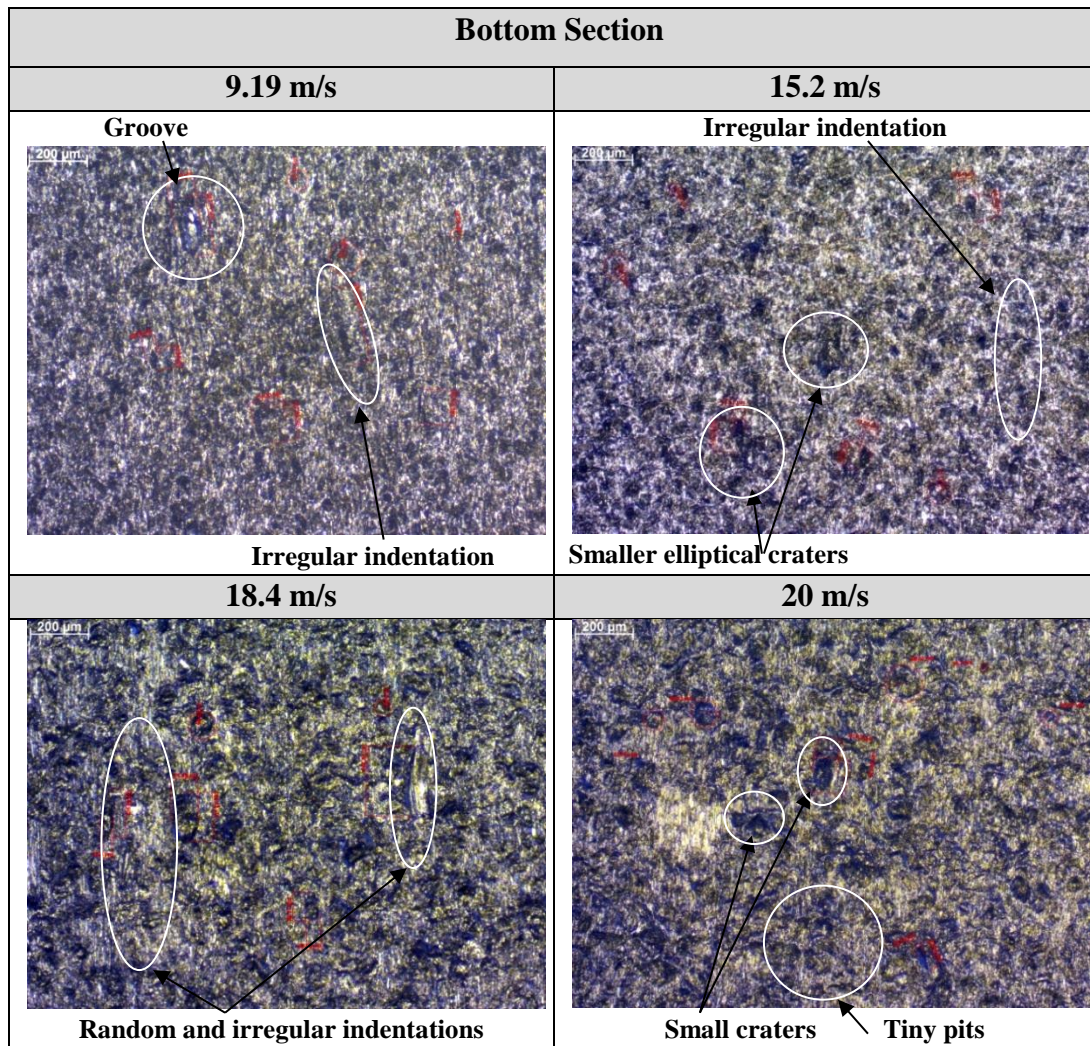
Figure 6.5 Erosion damage at bottom section 30° impact angle.

The damage on the surfaces when they were impacted at an angle of 60° is shown in Figure 6.6. It is possible to observe that the wear scar was rounder in shape than at 30°. However, the erosion damage was characterized by a higher depth than that observed at 30°. This will be confirmed in the profile measurements carried out with a profilometer. In addition, the wear scars became larger when the velocity of the aluminium balls in the system was increased. At a 60° angle more aluminium balls rebounded straight back and then impacted incoming balls. This partly protected the surface and meant that the scars were diminished and concentrated in one spot. These wear scars were similar to those observed in previous erosion studies using a 60° impact angle [95-96].

9.19 m/s	15.2 m/s
19 mm	22 mm
18.4 m/s	**20m/s**
24 mm	27 mm
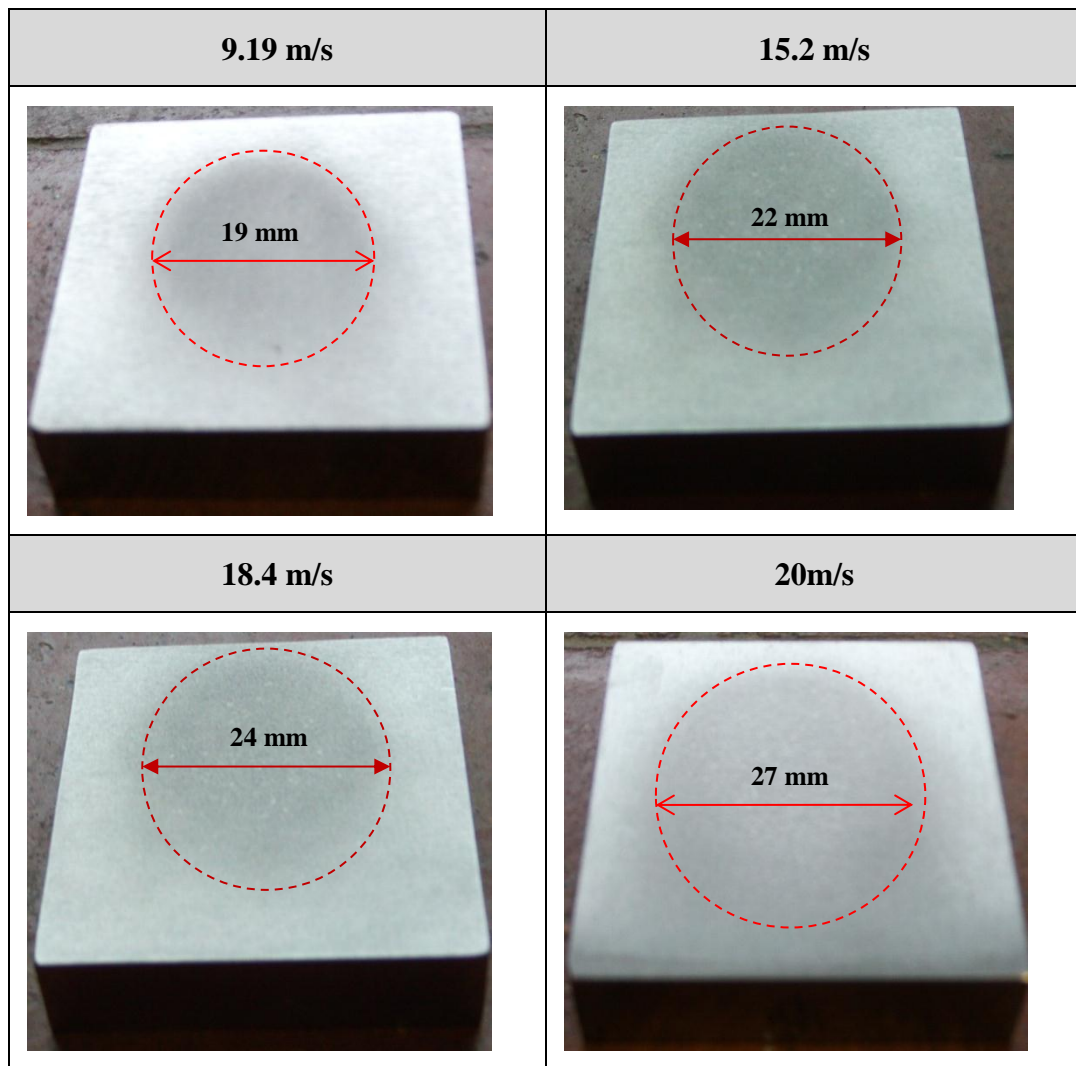
Figure 6.6 Wear scars at an impact angle of 60°.

Figure 6.7 shows the wear damage produced at the top section of the 60° scar. As mentioned for impact at an angle of 30°, the erosion damage was characterized by tiny pits spread on the surface, round and elliptical craters are shown in Figure 6.7, a few grooves, and more in irregular zigzag indentations, especially with velocities of 18.4 and 20 m/s. The pitting is more intense than that seen at 30°. Table 6.3 shows the size of craters on the surfaces.
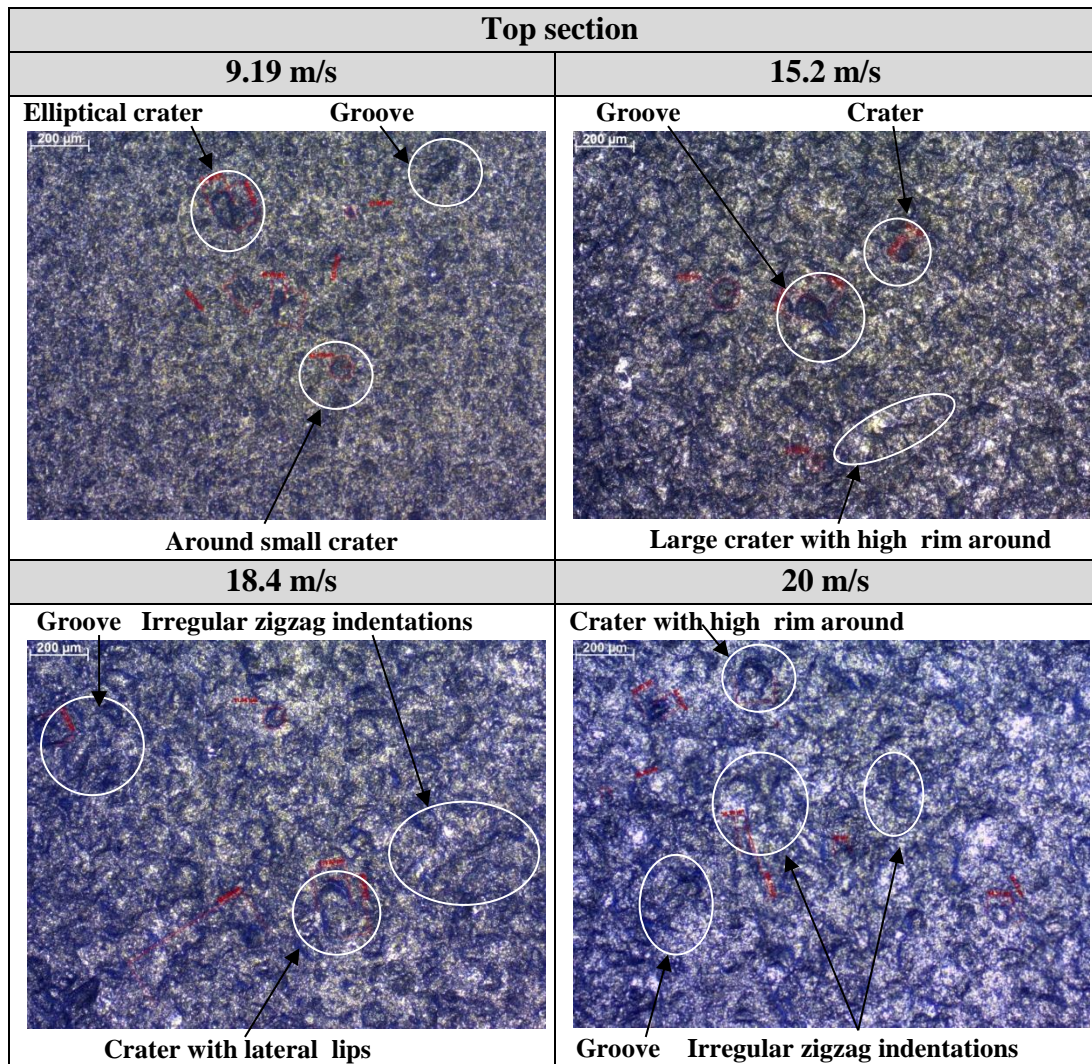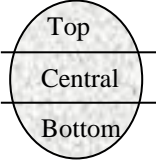
Figure 6.7 Erosion damage at top section 60° impact angle.

Table 6.3 Average size of round (RC) and elliptical craters (EC) at an impact angle of 60°

Velocity (m/s)	Average Crater Size (µm)					
	Top		Central		Bottom	
	RC ⊖	EC ⊖	RC ⊖	EC ⊖	RC ⊖	EC ⊖
9.19	42	34	45	81	74	70
15.2	60	58	67	118	116	95
18.4	85	87	82	164	128	126
20	111	96	125	233	144	134

Top
Central
Bottom

The examination of the specimen surfaces after being impacted at an angle of 60° showed that deformation wear mechanisms coexist, and compete more than cutting or ploughing which is vice versa at an angle 30°. Cutting erosion dominates at lower impinging angles and deformation at higher impinging angles. Cutting exists when the ball rolls, indenting the surface and raising material into a prominent lip, which is vulnerable to removal by subsequent nearby impacts. Ploughing causes formation of a lip in front of the particle [97, 98]. The initial stage is the formation of a lip at the exit end of the crater by shearing of the surface layers. This lip detaches from the surface by the propagation of ruptures at the base of the lip.

Deformation wear occurred when the target surface was repeatedly deformed by impacting particles which caused extrusion into side ridges or lips, subsequently removed as more particles impact on the same area. Comparing the texture at an impact angle of 30°, craters are deeper and there are fewer irregular indentations.

Figure 6.8 shows the damage at the cerntral section when an angle 60° was used to impact the specimen surface. In this case, the surface was more highly deformed than that at the top or bottom section. It is possible to observe that the scar presented tiny pits, some round and elliptical deep craters as shown in Figure 6.8, a few grooves and irregular zigzag indentations especially at velocities of 18.4 and 20 m/s.

Central Section	
9.19 m/s	**15.2 m/s**
18.4 m/s	**20 m/s**
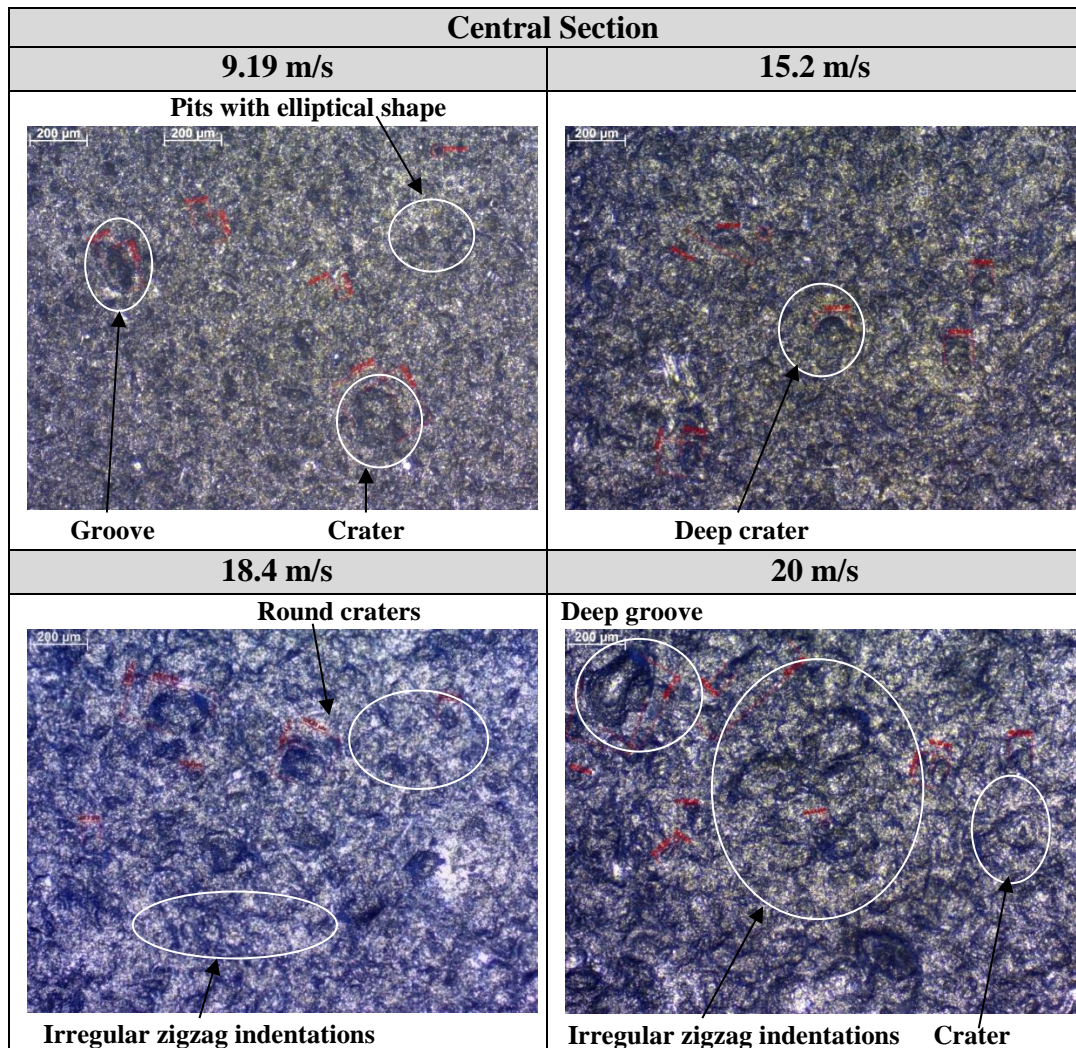
Fig. 6.8 Erosion damage at central section impact angle 60°.

The damage produced in the bottom section was more characteristic of sliding of aluminium balls after they impacted the surface. The elliptical craters are larger in the bottom section which can be related to sliding with impact for balls on the surface. Cutting and ploughing mechanisms are involved in the damage incurred here as most material was removed by balls acting with different orientations. In Figure 6.9, it is possible to see that the damage inflicted on surfaces from erosion testing showed some similar features to the damage at the top section of the surface specimen.

As mentioned in previous cases, the surface presented tiny pits spread on the surface, some round and elliptical craters are presented in Figure 6.9, a few grooves, irregular lines and higher in irregular zigzag indentation especially at velocities of 18.4 and 20 m/s.
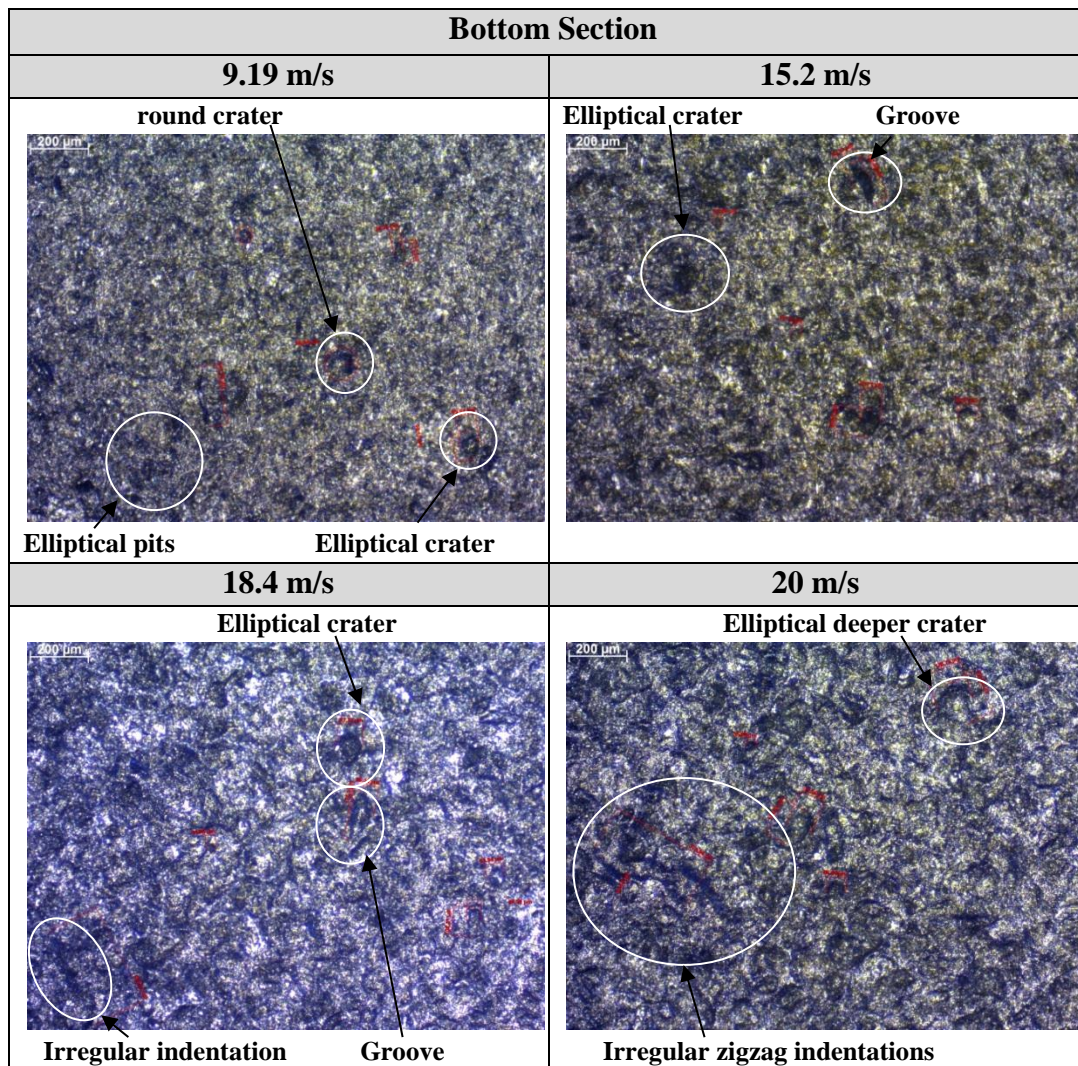
Figure 6.9 Erosion damage at bottom section impact angle 60°.

It is possible to see from Figure 6.10 that the wear scars were larger as the aluminium ball velocity was increased for impacts at 90°. Also it shows that the erosive scars had a circular shape approximately similar to that obtained in tests at 60°, however, these wear scars presented greater depths than those at 30° and 60°. In addition, it is clearly seen that the erosion damaged area had no clear edges.

As previously explained in the motion analysis of aluminium balls at an impact angle 90° a lot of aluminium balls would rebound from the surface of the specimen and very few slide which means that the rebounding aluminium balls would crash into the other aluminium balls moving downwards from the nozzle and could then deflect and hit the surface of the specimen at wider position. This could explain the blurring of the scar edges. This phenomenon is more pronounced on the wear scar area of the impact at 90° than that at impacted angles 30° and 60°.
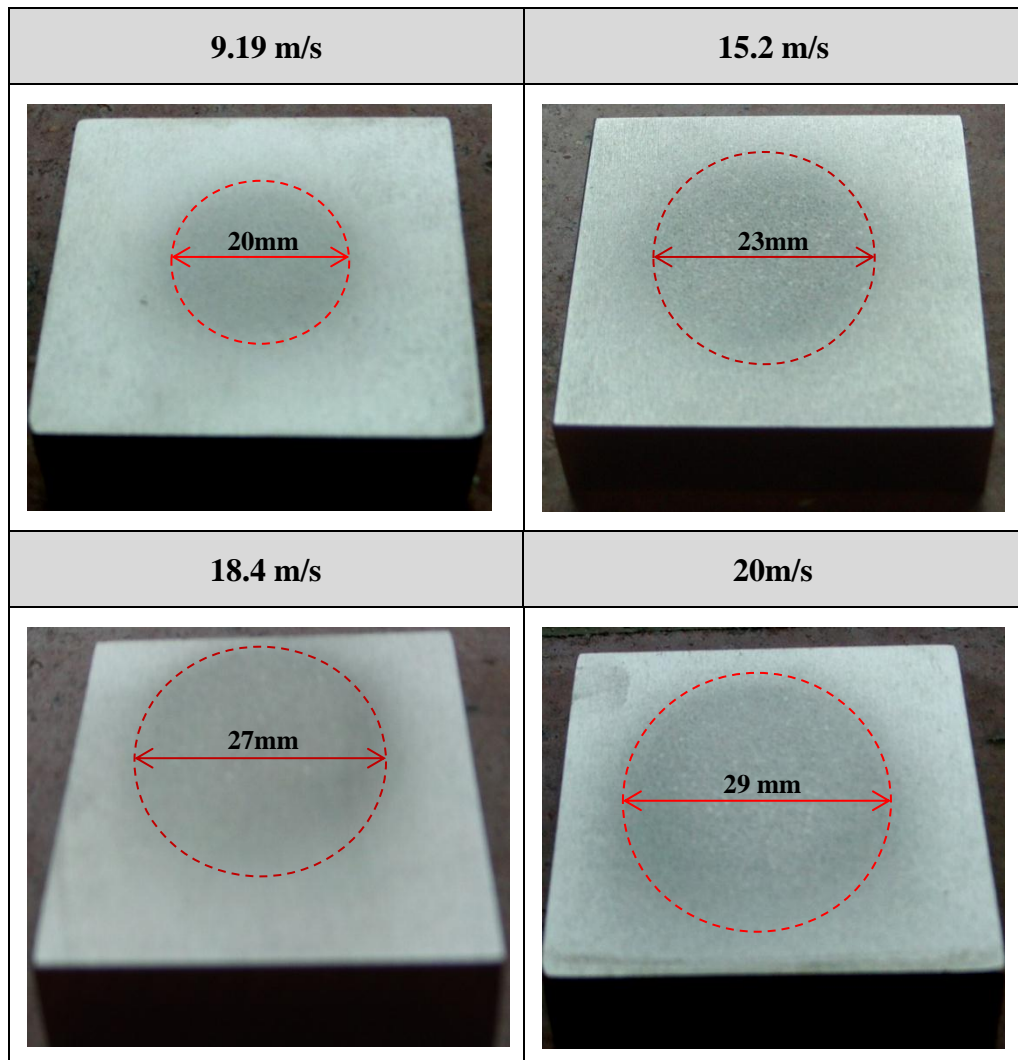
Figure 6.10 Wear scars at an impact angle of 90°.

As mentioned in the cases at angles 30° and 60°, the erosion damage on the specimens surfaces were characterized by tiny pits, round craters, a few grooves, and irregular lines. Figure 6.11 shows the wear damage produced at the top section of the surface specimens inflicted at an angle 90°. In this case the surfaces were highly impacted and deformed with low evidence of sliding. The craters are nearly round with higher in depth than those seen at impact angles of 30° and 60°. Normal impact causes higher work hardening, which led to lower erosion rate and then to steady state erosion with a continuous mass loss of the specimen due to plastic deformation and platelet formation around the indentations formed by impacts of individual aluminium balls were removed by subsequent impacts (erosion rate is discussed later in section). However, Table 6.4 presents the size of round craters on surface at an impact angle of 90°.

Top Section	
9.19 m/s	**15.2 m/s**
Groove Small crater	Larg deep craters Smaller craters lateral lips
18.4 m/s	**20 m/s**
Irregular zigzag indentations Crater Groove	Irregular zigzag indentations Crater with high lips round
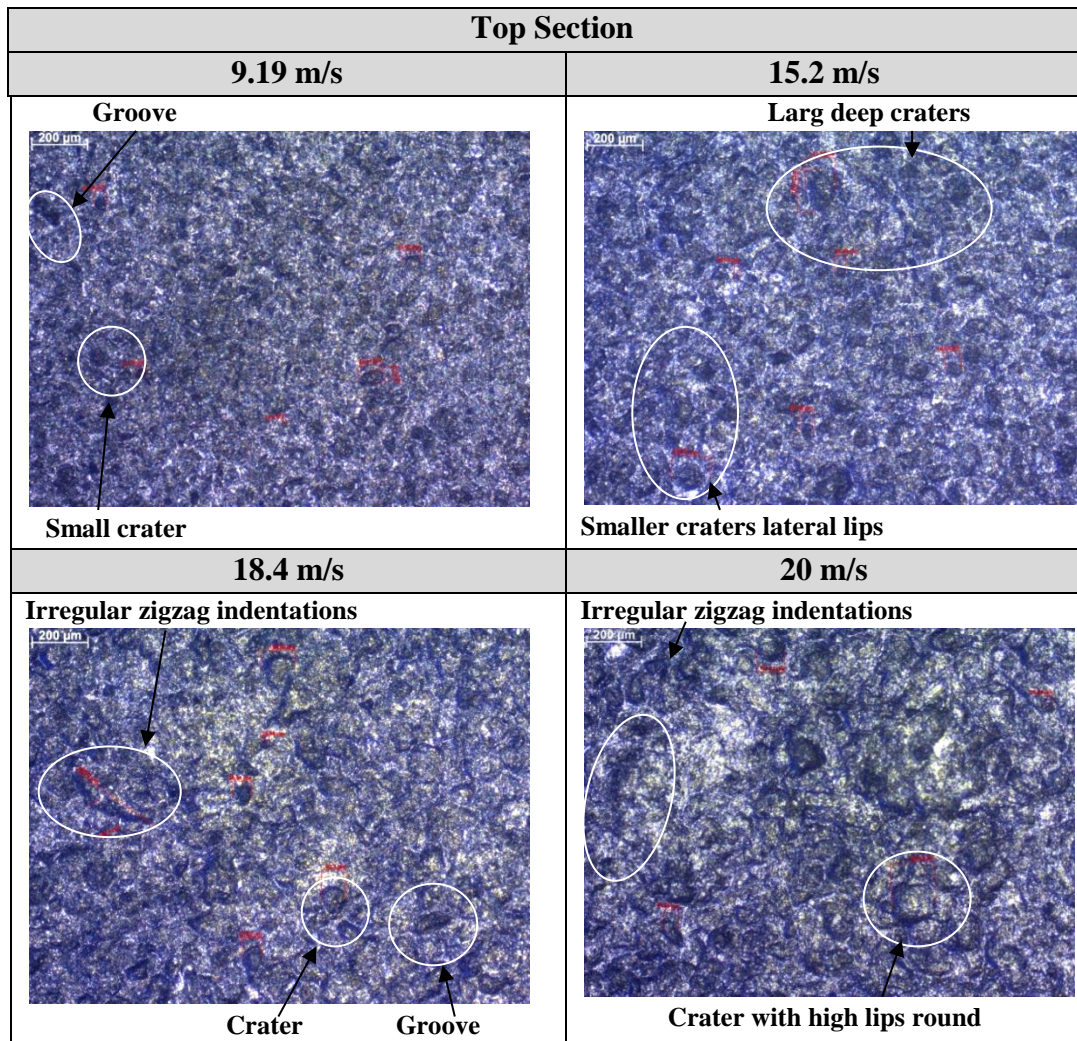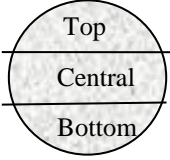
Figure 6.11 Erosion damage at top section impact angle 90°.

Table 6.4 Average size of round craters (RC) at an impact angle of 90°

Velocity (m/s)	Average Crater Size (μm)		
	Top RC $\ominus$	Central RC $\ominus$	Bottom RC $\ominus$
9.19	37	40	30
15.2	46	66	37
18.4	85	129	43
20	125	153	66

Figure 6.12 shows the images of the erosion damage produced in the central section of the surfaces of the specimens impacted at 90°. Larger craters are seen than those seen on the top section (see Table 6.4). There is also higher grooving in all cases. It is possible to observe that a few of the craters had elliptical shapes which meant sliding could be happening with impacting. In addition, it is clearly seen that the increase of the erosion damage is related to the aluminium ball velocity effect.

Unworn Surface

200 µm

Central Section

9.19 m/s	15.2 m/s

Round crater

200 µm

200 µm

Round small and large craters

18.4 m/s	20 m/s

Crater   **Irregular zigzag indentation**   **Crater**

200 µm

200 µm

Large crater with higher lips around   **Groove**
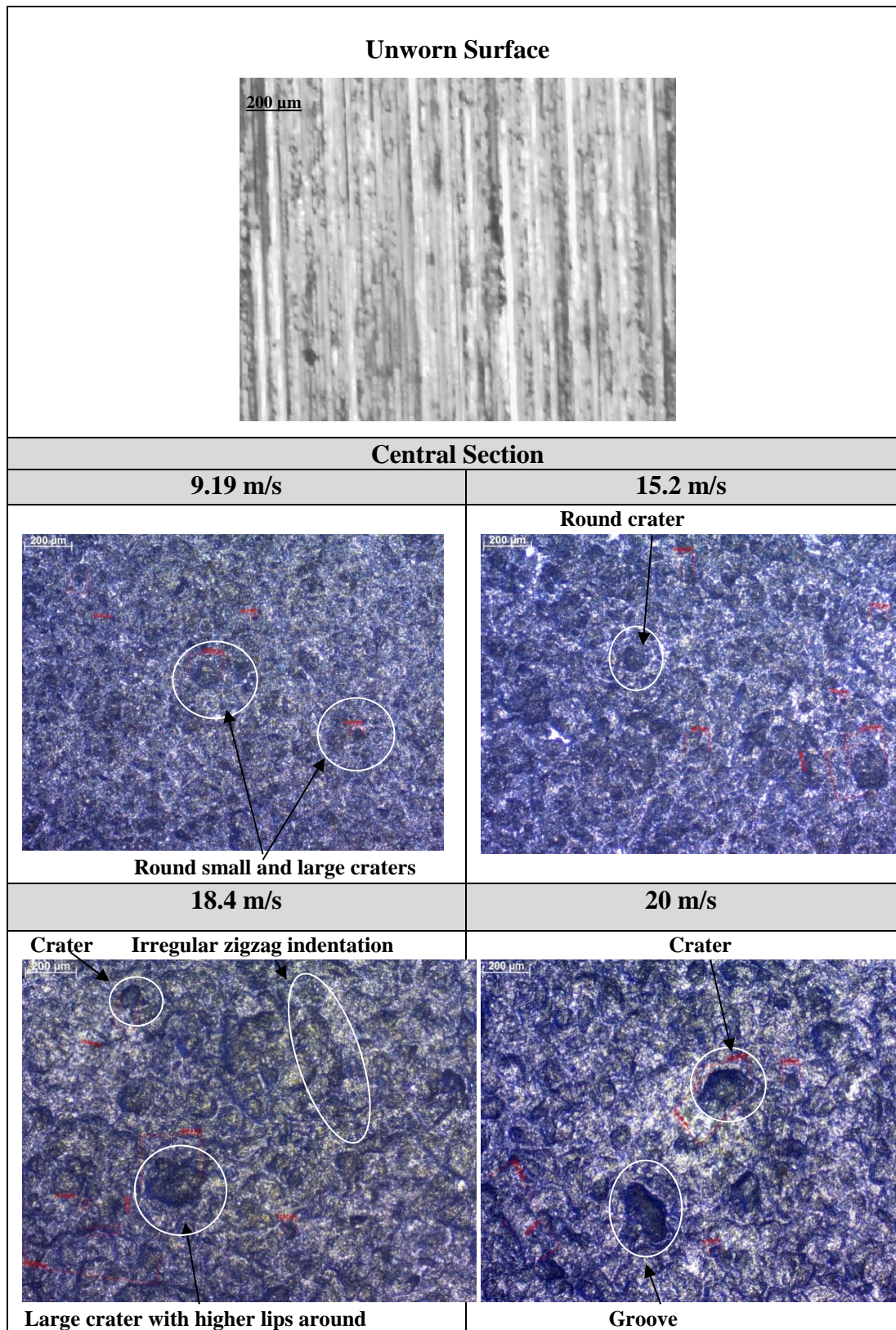
Figure 6.12 Erosion damage at central section impact angle 90°.

Erosion damage at the bottom section of the specimen surface was similar to that at the top and central sections. In this case the surface had craters with a smaller size than at the centre (see Table 6.4). In addition, it is assumed that the loss of material from the specimen surface appears to occur due to successive impacts of a large number of aluminium balls, which form a plastically deformed layer. Also the erosion damage was increased as the aluminium ball velocity was increased, as shown in Figure 6.13.

Figure 6.13 Erosion damage at bottom section impact angle 90°.

6.3.3 Profilometery

Analysis of eroded surfaces was carried out to characterise the roughness and morphology for different impact velocities and angles. A 3D profilometer which can acquire a 3D-height map and Ra parameter was used to quantify features. A 3D profilometer seems to be the more appropriate to obtain a more precise picture of the surface. In addition, images were taken by the 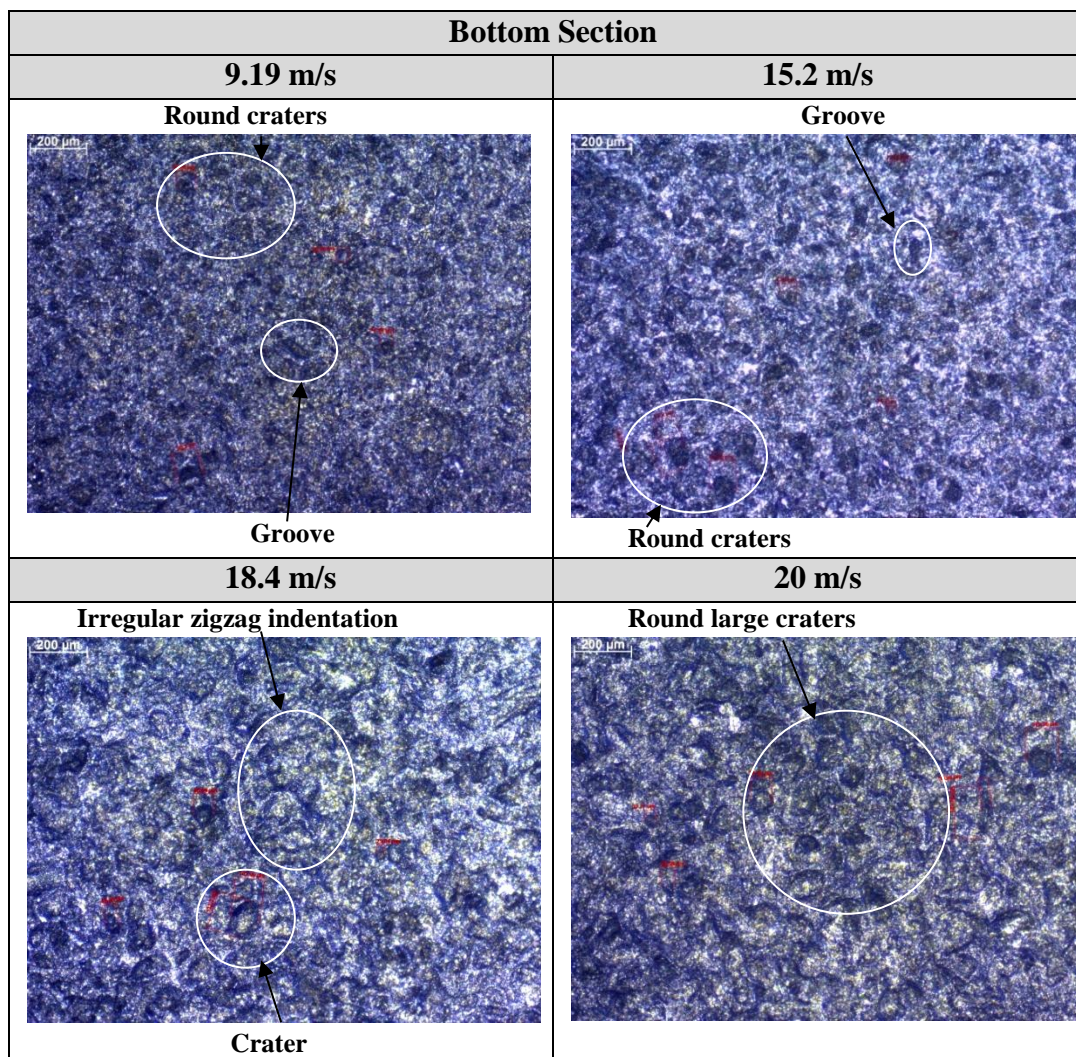same device which gave more help to understand more completely the process of formation of the surface roughness. Figure 6.14 shows the erosion damage in the middle section of scars when the surface was impacted at an angle 60°, and 18.4 m/s for 7200 pulses. The main characteristic, it has different size, height of craters and pits across the area examined. It is possible to observe readily that the difference between the highest points (tip peak), as presented in an orange colour, and the lowest points (valley), as presented in pink colour, is 24 μm. Also it is possible to register the depths of the craters and grooves as presented in colours across the surface damage, which indicates that the information in the 3D micrograph is very useful for the accurate characterization of surface features.
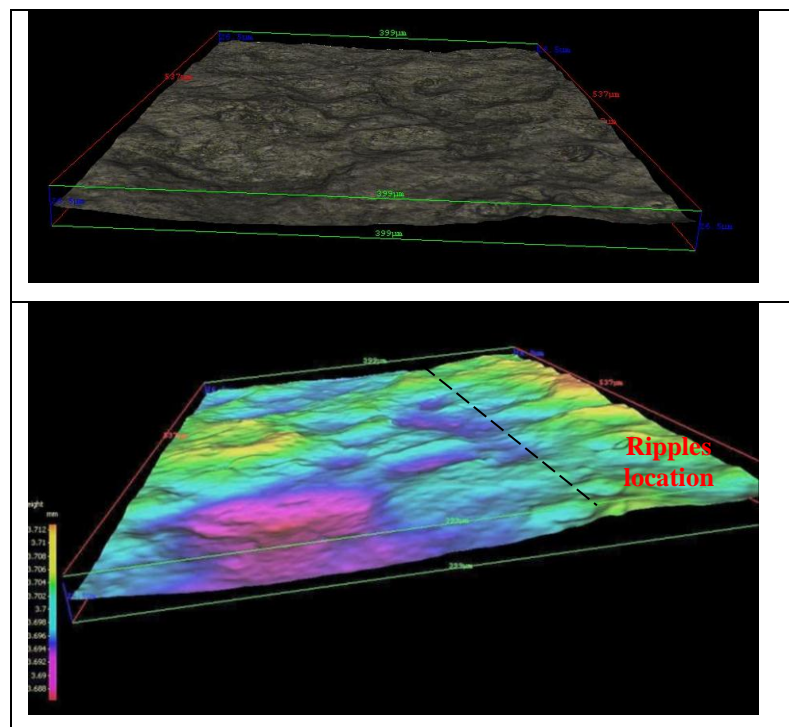
Figure 6.14 - 3D profilometer height map (399 μm X 537 μm), showing how worn specimen surface in central zone at 60° and 18.4 m/s.

A further 3D profilometer height map (286 µm X 537 µm) is presented in Figure 6.15, which shows the damage produced in the central part of the surface at, an impact angle 60°, and particle velocity of 15.2 m/s.
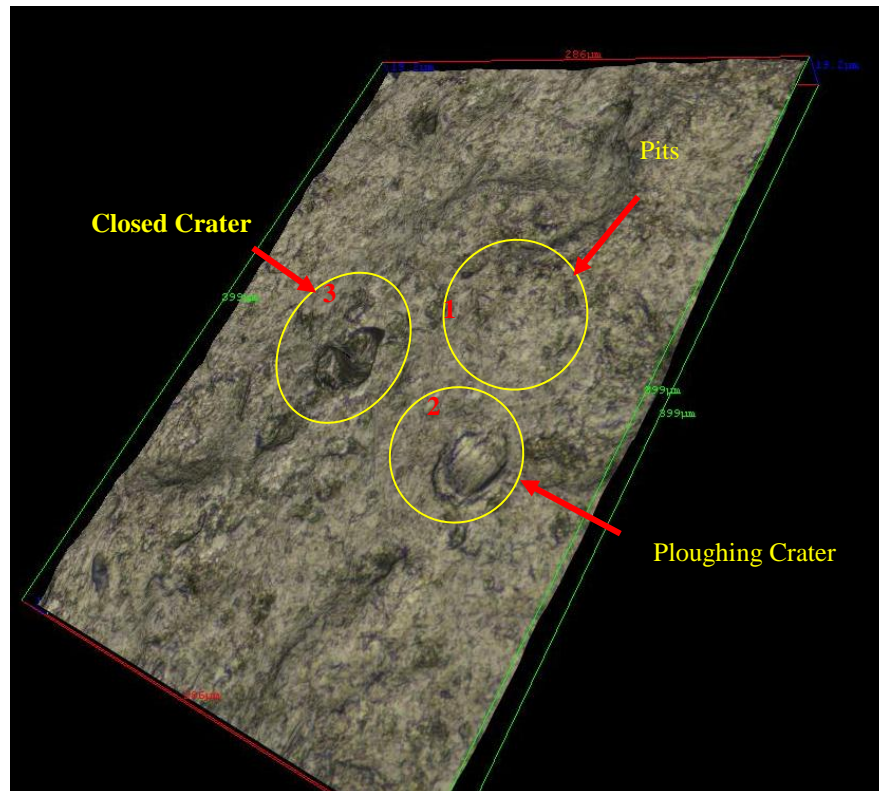
Figure 6.15 - 3D profilometer height map (399 µm X 537 µm), shows types of craters.

In zone 1, of the wear scar, there is evidence of intense pitting. It may suggest two ways that tiny pits form on the surface material during impact.

In the first, tiny pieces of material are removed through impact or impact with sliding also causes fatiguing of material close to surface especially at grain boundaries. In the second way, the materials with weakened grain boundaries are plucked from the surface as a platelet. The release of a platelet wear particle from the surface cause pits, the mechanism by which this would happen is illustrated in a schematic shown in Figure 6.16. Wear mechanisms of removal material seen in the micrographs are similar to those seen in previous studies [99-102].

<div align="center">(a)   (b)</div>
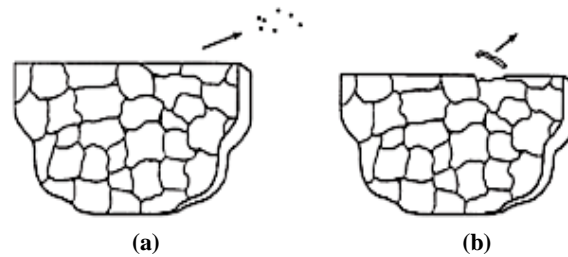
Figure 6.16 Schematic diagram shows formation the pits, (a) material removal, (b) remnants of a grain are plucked from surface as a platelet.

In addition, it is clearly seen that the worn surface presents three types of craters. The craters always are smaller than the particle that causes them as a portion of a particle enters and forms an impact crater. These types of craters are as follows;

- Indentation or deformed craters, show some evidence in Figure 6.17 that the initial surface had been depressed into their walls and the crater has some plastically deformed material raised above the initial plane of the surface called a hump on the forward exit side of crater.
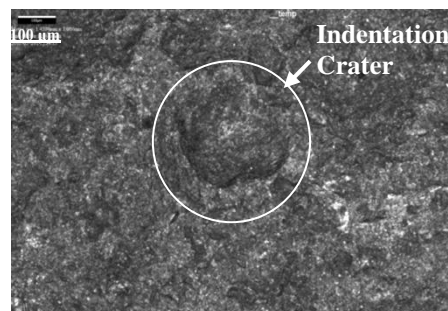
Figure 6.17 Showing deformed crater in central zone at 60° and 18.4 m/s.

- Ploughing craters (at zone 2) occurred when particles deform the surface by ploughing, displacing material to the side and in front of the particle due to a particle forces its way deeply into the surface and then translates along the surface for a distance. Subsequent impacts lead to the detachment of material from the rim of the crater. The majority of ploughing craters occur by rounded particles striking on surface material [103], Figure 6.18 shows an evidence for the formation of a ploughing crater with simple schematic.
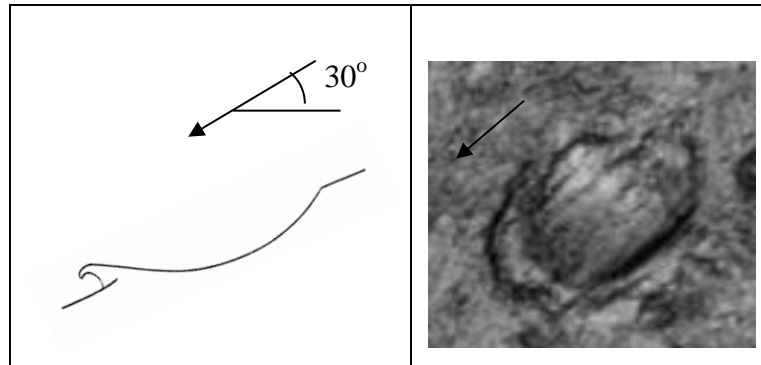
**Fig. 6.18 Shows ploughing crater formation, (a) schematic diagram,
(b) evidence ploughing crater.**

- Sheared craters in Figure 6.19 or cutting wear occurred when a portion of erodent particles damaged the surface of the material in a shallow depth and involved a ridge of plastic deformed material. The ridge may be strongly or weakly attached to the surrounding metal. Shearing or cutting wear could push the surface material to the exit side. Usually deformation wear appeared at the initial stage of erosion and transformation to cutting wear which it meant that cutting wear predominated at advanced stages in all erosion zones which agreed with some earlier normal impingement studies [104-106].
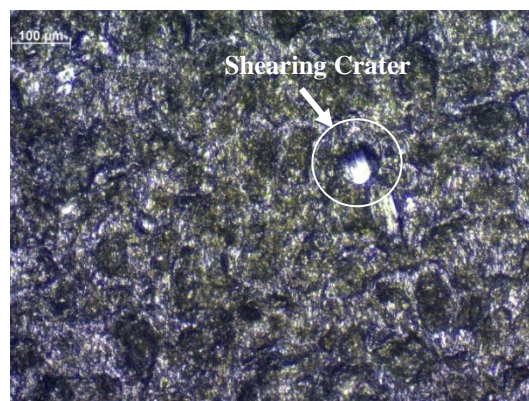
Figure 6.19 Showing shearing or cutting crater in bottom zone at 60° and 18.4 m/s.

Also, it is possible to observe the effect of plastic deformation at a crater seen in zone 3. This shows a crater closing Figure 6.20. From the micrograph, it can be seen the sharp tip of the crater is pushed deeply into the material surface which means no volume removal of material. Rather there was an extensive redistribution of the surface by plastic deformation.
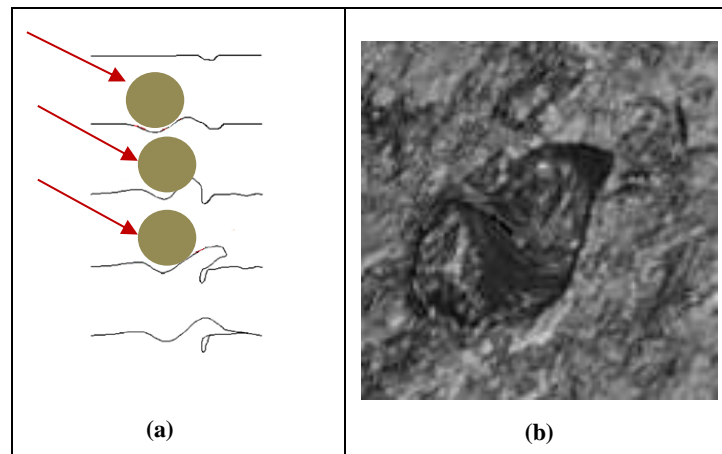
**Figure 6.20 Shows evidence crater closing, (a) Schematic diagram,
(b) Evidence of crater closing.**

In Figure 6.14 topography at some locations looks similar in appearance to ripples. Ripple formation can occur in all types of material whether they are brittle or ductile such as (stainless steels and copper-based alloys) when eroded. The formation of ripples can occur by solid particle erosion in a gas or liquid medium containing solid particles due to the tangential velocity [106-109].

Previous attempts to explain the formation of erosion ripples using Scanning Electron Microscope (SEM), optical microscopy and a profilometer to study the morphology of impacted surfaces eroded surfaces are briefly discussed below and discrepancies are presented and highlighted.

Carter et al. [110] observed ripple formation in copper eroded by sandblasting. They suggested that the ripple formation is related to the morphology of individual impact craters and plastic flow. Griffin & Macmillan [108] carried out a study related to ripple formation on lead. They concluded that the ripples run parallel to the tangential component of impact velocity. The mechanism responsible for the ripple formation is related to the formation of raised lips of material at individual impact craters. Additional impacts immediately around the craters can widen and deepen them, so that as a fraction of material develops into the lips, a peak and valley structure is formed. In the next stage, the displacement and removal of material by plastic flow keeps advancing downstream until the individual peaks and valleys meet. It could be suitable to explain for the ripples in term of dunes in sand deserts and ripples formed in river beds as a result of the wave action of overlying wind or water [111]. It is possible to observe that the sequence of impacting aluminium balls displaces materials from the surface. The accumulation and coalescence of the individual erosion craters and plastic flow are assumed to result in the formation of the ripple shape.

6.3.4 Roughness

It is considered that the first and most important task in the classification of cast roughness surface is to extract features that characterize the surface roughness of varying products [112]. In this section results of investigations related the surface roughness, wear behaviour, impact angles and the velocity of erodent particles are presented. The results show that the surface of the samples was gradually roughened by impacting particles. The results for Ra, where Ra is the arithmetic average deviation of the surface valleys and peaks, were determined from specimens using a Mitutoyo Surftest Profilometer. The parameters used to conduct the measurements were a sample length of 30 mm and a speed of 0.5 mm/s. The profiles obtained in the central part of the wear scar after impact by 7200 pulses are observed in Figure 6.21 for impact angles of 30°, 60° and 90°, and a velocity of impact of 20 m/s.

From these, it is possible to notice that an impact angle of 30° presents a smoother profile than that at 60° and 90°. Negative correlation between roughness and wear was observed, higher roughness with lower wear. It is interesting to note that with higher material loss the roughness is lower, which meant different wear mechanisms caused material loss from the surface.

Rq = 3.617 μm
Ry = 18.626 μm

(a)

Rq = 6.778 μm
Ry = 44.640 μm

(b)

(c)
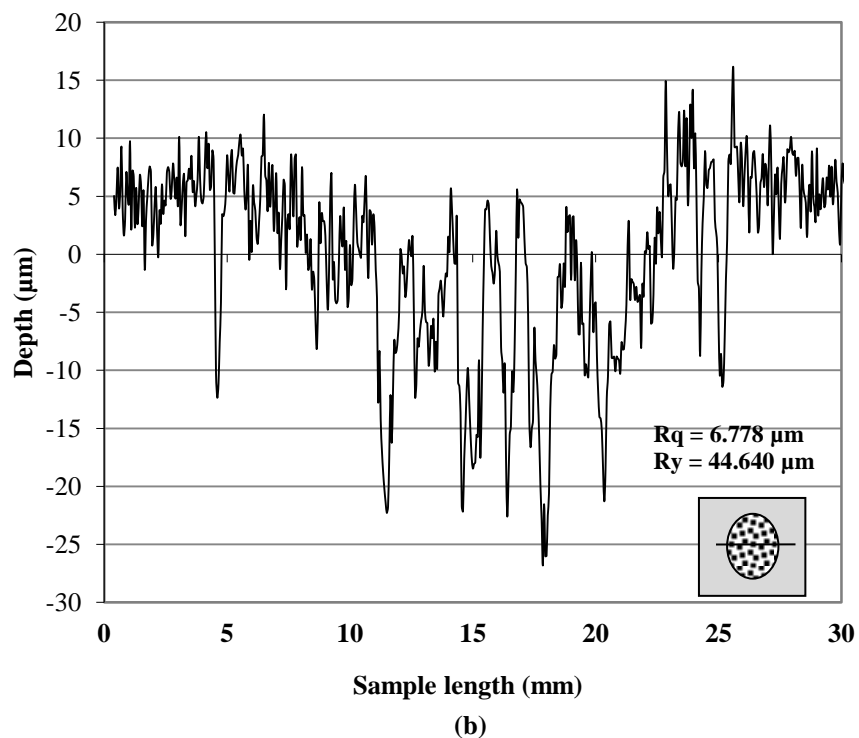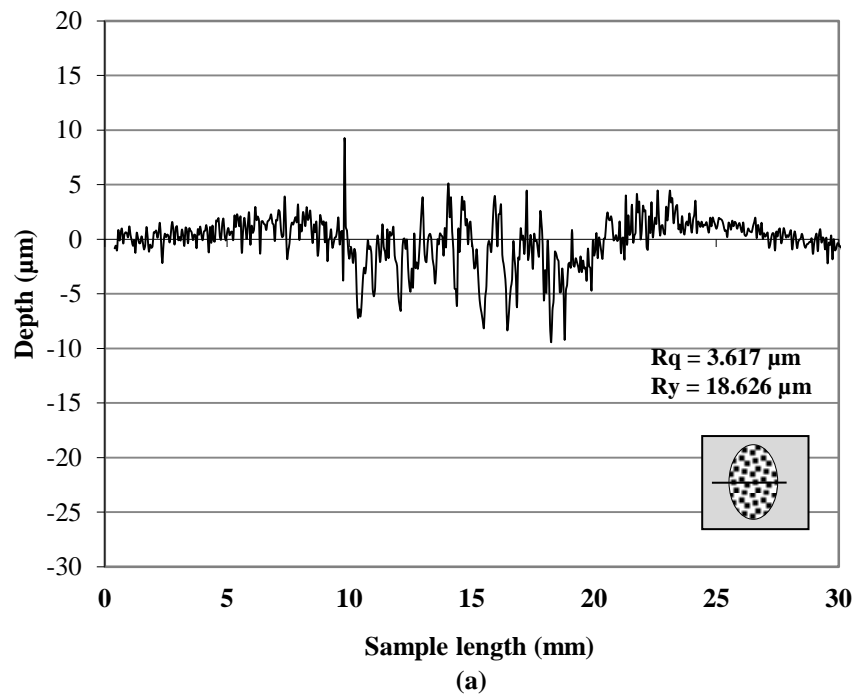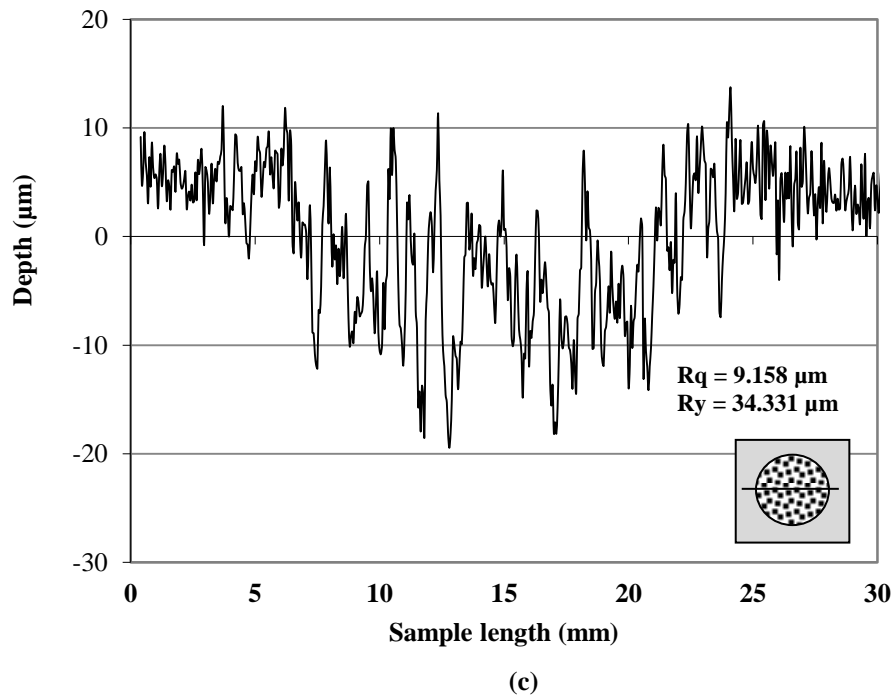
Figure 6.21 Profile obtained at impact angle, (a) 30°, (b) 60°, (c) 90°.

The same procedure was carried out to show the variations in profile between the top and bottom sections of the wear scars. For example, the profiles obtained for specimen impacted by 7200 pulses at impact angles of 60° and a velocity 20 m/s. The results are presented in Figure 6.22, and show smoother profiles at the top and bottom parts than at the central part.
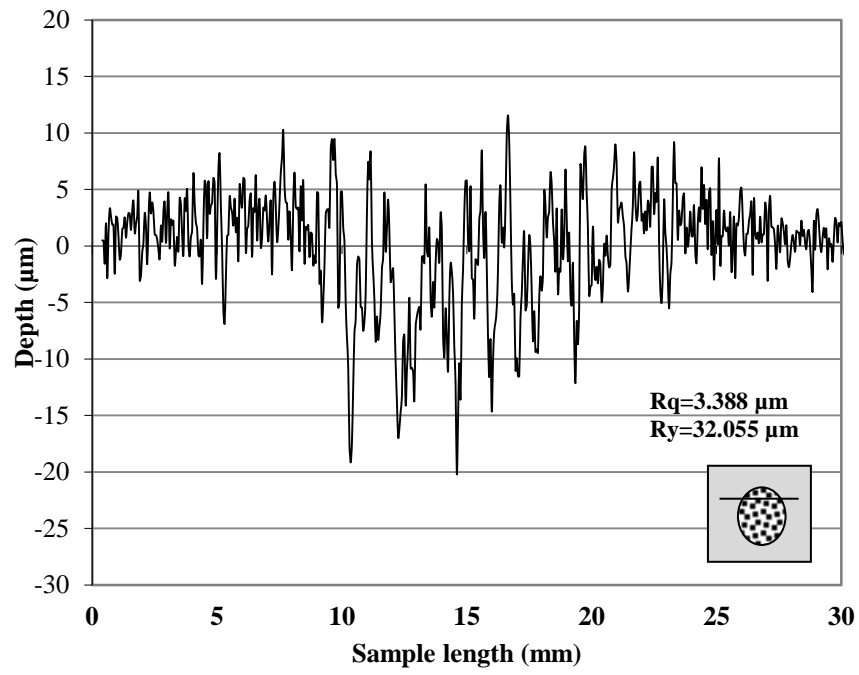
(a)
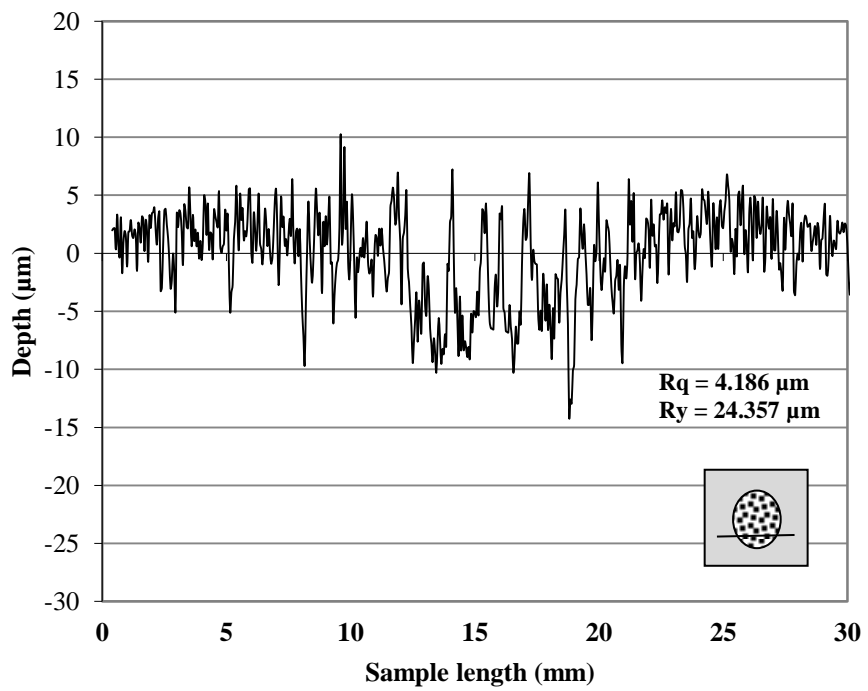
(b)

Figure 6.22 Profile obtained at an impact angle 60° in section, (a) top, (b) bottom.

As a complement, the Ra results obtained from erosion tests are presented in Figure 6.23. It can clearly be seen that the roughness is lower at low impact angle and velocity and increases with these parameters. In addition in Figure 6.24 the values of surface roughness for three samples impacted at angles of 30°, 60° and 90° and a velocity of 20m/s are presented. From the results, it was concluded that the criteria of Ra or roughness surface at central part was higher than at the top or bottom sections, which meant that the surface at central section was more highly deformed than at top or bottom section due to accumulate and large number of aluminium balls impacting here. The determination of Ra is very important for the following reasons [113].

- A hot molten material fills a die cavity during the die casting process, which then cools and solidifies. As the material cools and solidifies, it will shrink. The shrinkage of castings will result in casting distortion, the shape and size of castings deviating from the desired and nominal dimensions. For some casting features where normal shrinkage cannot take place due to resistance of the die wall, non-uniform shrinkage will be developed.

- During the ejection operation of die casting process. The ejection load creates an ejection resistance with increased roughness of a die.
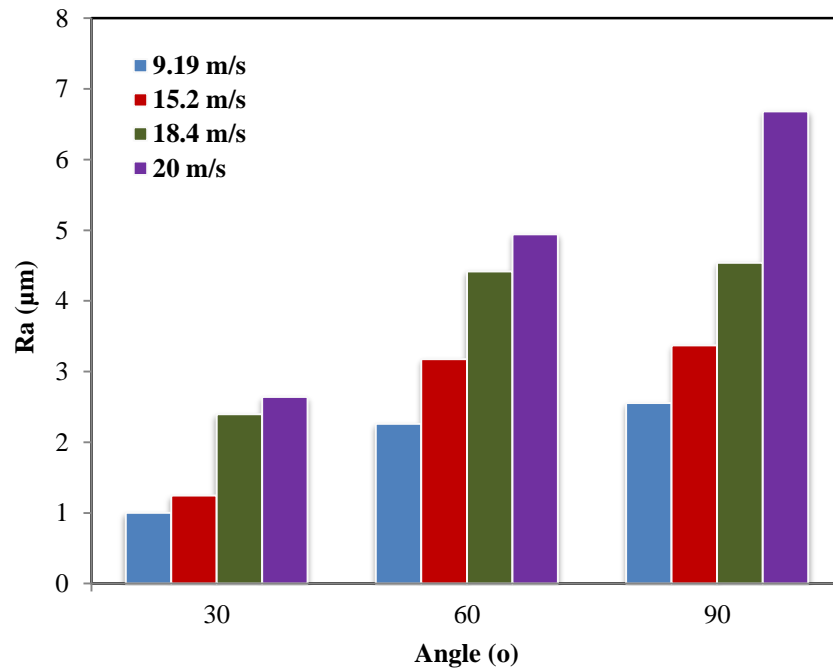
Figure 6.23 Comparison of Ra values obtained at impact angles of 30°, 60° and 90°, for all velocities used in tests.
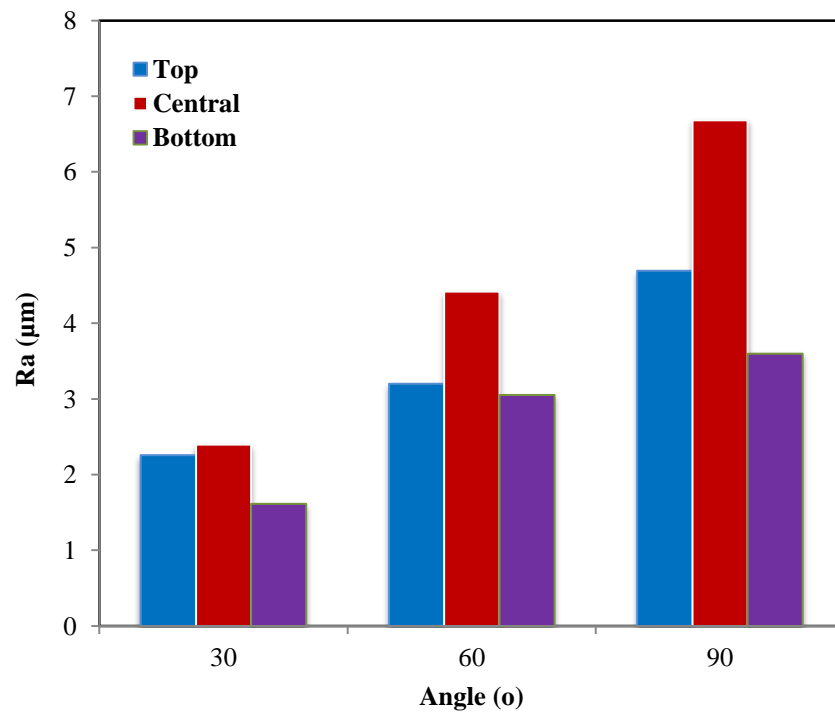
Figure 6.24 Comparison of Ra values obtained at impact angles of 30°, 60° and 90°, in top, central, bottom sections.

6.3.5 Wear Rates

The erosion damage was characterized by total mass loss and erosion rate. To compare the wear loss of the specimen, each specimen was weighed before and after a test. Then, the mass loss was calculated by the difference between the initial weight (Wi) and the weight after every 1200 shots (Wn) as follows,

$$\text{Mass Loss} = \text{Wi} - \text{Wn} \qquad\qquad 6.1$$

The erosion rate was obtained dividing the mass loss generated every 1200 shots by the cumulative mass of the impacting balls. The following equation was used for carrying out the calculations:

$$\text{Erosion Rate} = \frac{\text{Removed Mass (g)}}{\text{Mass of aluminium balls striking the surface (g)}} \qquad 6.2$$

Recent publications [36-39] carried out on cavitation erosion, liquid erosion and solid particle erosion of ductile materials highlighted the effect of exposure time on erosion rate. This relationship was divided into four periods, as shown in the Figure 6.25 incubation period, acceleration or accumulation period, deceleration period and steady-state period.
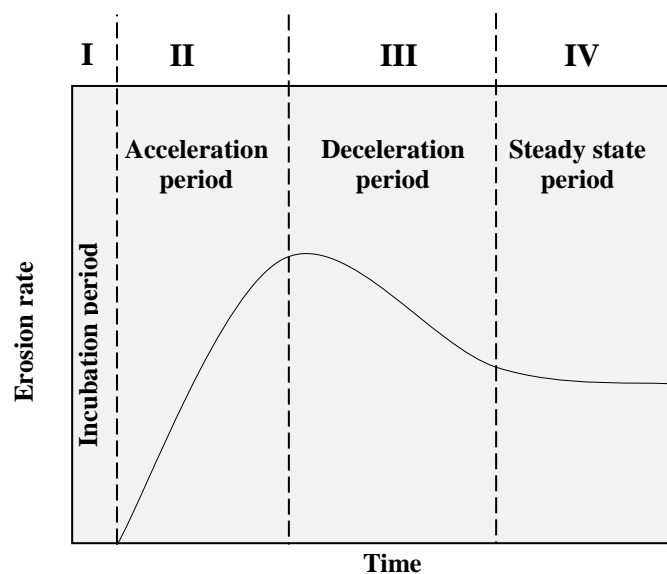
Figure 6.25 Effect of time on erosion rate.

The mass loss data are presented for the case of an impact angle of 30° in Figure 6.26. Measurements of mass loss were conducted for four different air pressures used in the system and hence four velocities of aluminium balls obtained. From these graphs, it is possible to confirm that as the velocity is increased, the mass loss and erosion rate are higher.

At 30° the incubation and acceleration periods were characterized by a short time or shot numbers less than 1200 shots. This can be explained by the fact that there are three major erosion mechanisms causing the mass loss from the surface, cutting, ploughing and deformation erosion, and their portions depend on impact angle. The lower impinging angle has cutting and ploughing erosion and higher impinging angle has deformation erosion, their effects share a specific portion. The higher the impinging angle, the larger is the portion of deformation erosion and vice versa. Deformation gives less material removal than cutting and ploughing.

This meant that the mass loss is strongly dependent on impact angle, and then the periods are different from one curve to another. After these first 1200 shots the mass loss tends to decrease, the hardness of the surface material will increase with increased shot numbers or exposure time. This increase is more effective for the layers located near the surface. The magnitude of erosion rate was decreased which caused the deceleration period on the curve between 1200 and 3600 shots and decreased with increased particle velocity. Finally, after the deceleration period, steady state erosion is reached, characterized by an approximately straight line as shown in the curves. Compressive stress is directly related with hardness and increases in the sub-surface with the increase the shot numbers, the thickness of the compressive layer is a function of the number of shots.
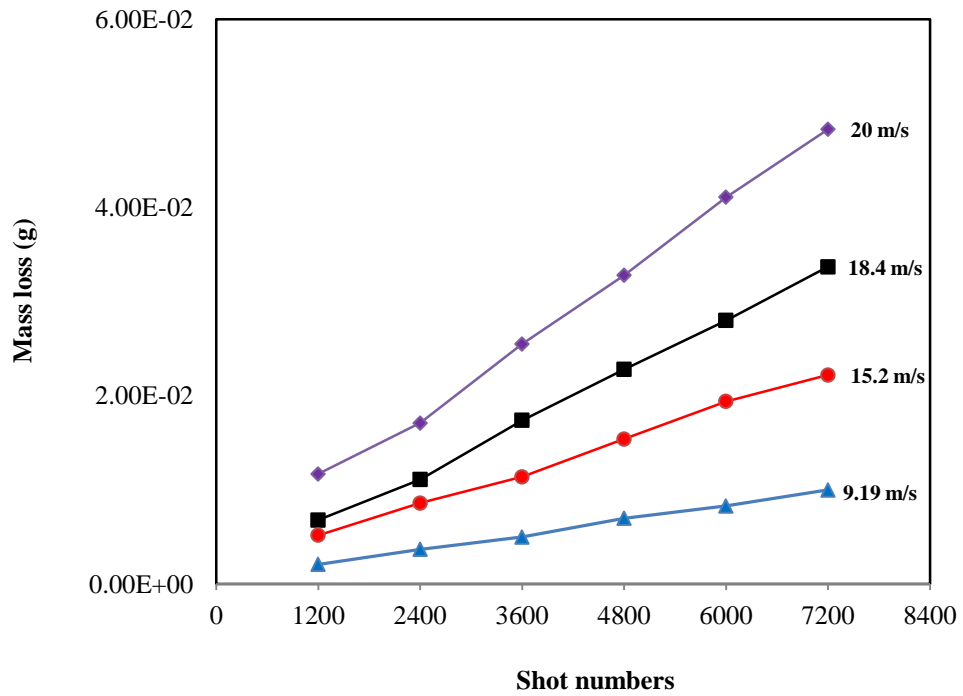
(a)
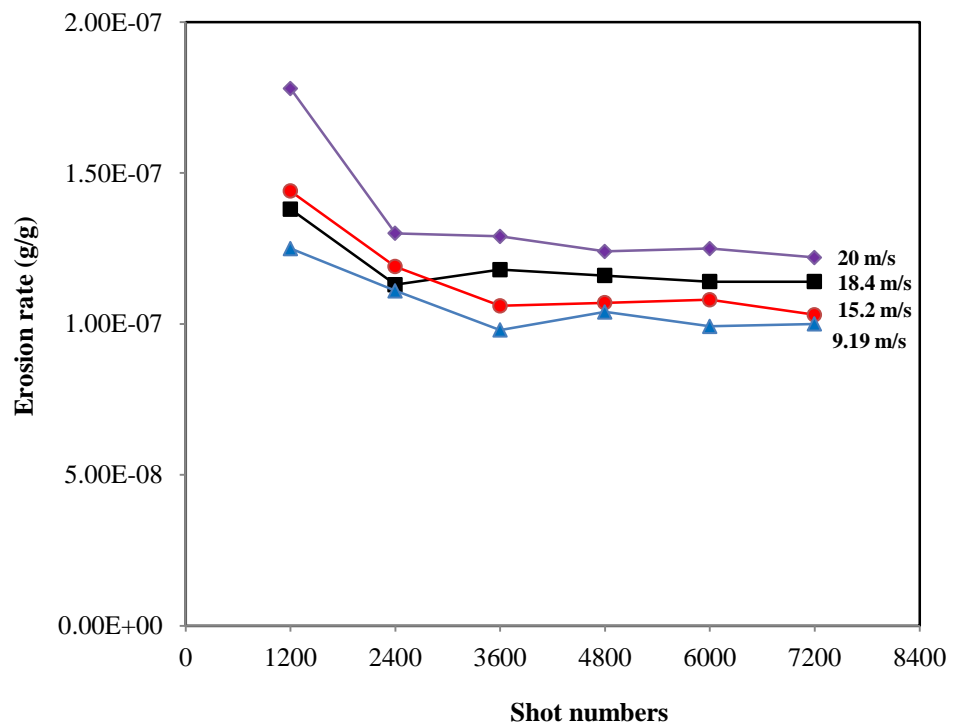
(b)

Figure 6.26 - (a) Mass loss against shot numbers, (b) Erosion rate against shot numbers at 30° impact angle, effect of particle velocity (9.19, 15.2, 18.4, 20 m/s).

The experimental results of cumulative mass loss and erosion rate versus the numbers of shot are presented in Figure 6.27 for an impact angle of 60°. It seems clear that the erosion curves may be divided into four major periods:

- **Incubation period**, it is clearly seen from the curves that the incubation period at an impact angle 60° is higher than that at an impact angle of 30°, It is thought that at 60°, this incubation period is higher due to a reduction of the cutting erosion effects or sliding action of the aluminium balls on the target. It lasted until 1200 shots as shown. Small damage during the early shots during which the material undergoes permanent changes due to the repeated impact. During this period no mass loss is seen or very little which means no damage resulting in material loss will occur on the surface material specimen under impulse loading.

- **Acceleration period**, from the erosion curves, it is seen that after the incubation period, the mass loss became higher when the velocity and number of shots were increased. It lasted until the first 3600 shots, as shown. The loss of metal from an eroding surface was observed to occur primarily by a ploughing mechanism at all particle-impact angles. The evidence indicates that the platelets are initially extruded from shallow craters made by particle impacts. Once formed, they are forged into the distressed condition in which condition they or parts of them are vulnerable to being knocked off the surface by subsequent particle impacts.

- **Deceleration period**, for this period, it is clearly seen from the graphs that the mass loss was reducing this in turn leads to a lowering magnitude of erosion rate. As seen from erosion rate curves, the deceleration period is limited between 2400 to 4800 shots, it seems to be agreement with the literature review where it is possible to state that the hardness will increase with increases shot numbers. Hardness increase is more effective for the layers located near the surface, residual stresses after impact induces compressive stresses in the sub-surface, the thickness of the compressive layer is a function of the number of shots intensity, increased in magnitude of compressive stress could be a factor leading to the decrease in the mass loss and erosion rates.

- **Steady state period**, it is shown that the steady state erosion starts approximately from 4800 shots and at this period the rate of erosion becomes very nearly independent of the number of shots. This could be a result of work hardening. Also repeated impacts may cause the closing of craters lips or ridges as previously explained.

(a)

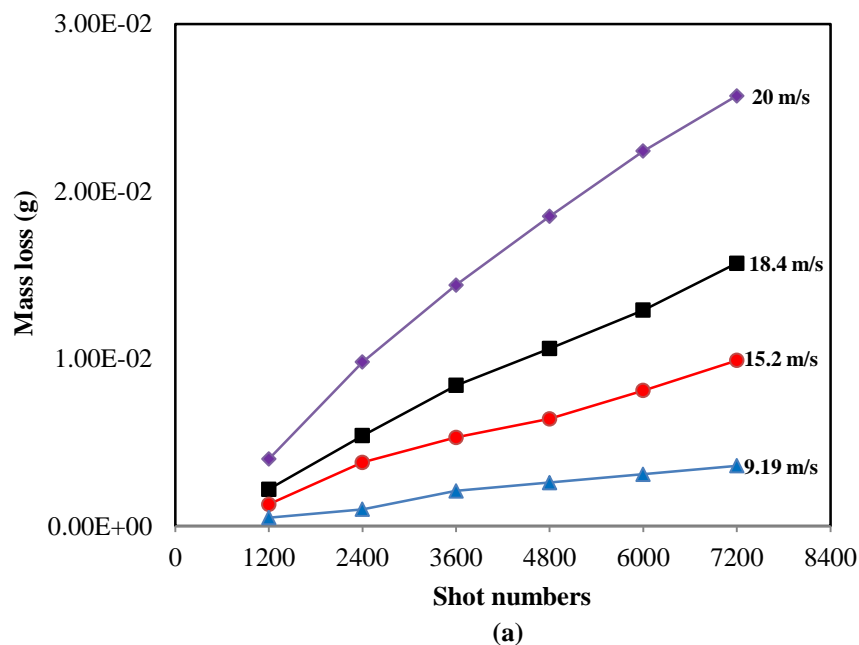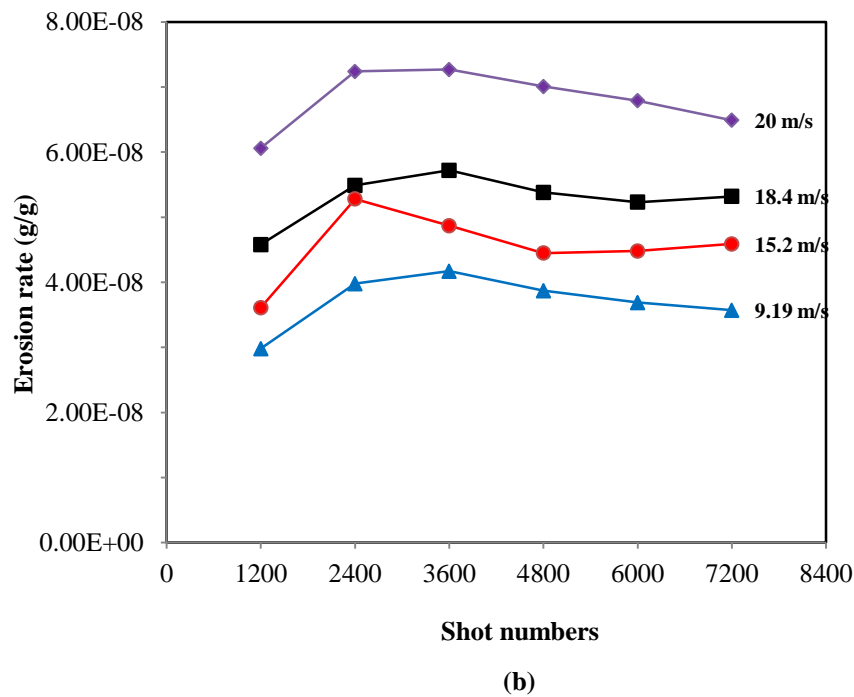**(b)**

**Figure 6.27- (a) Mass loss against shot numbers, (b) Erosion rate against shot numbers at 60°
impact angle, effect of particle velocity (9.19, 15.2, 18.4, 20 m/s).**

It was possible to observe that the results at an impact angle 90° had a similar behaviour with previous results at an impact angle 60°, on the other hand, being lower than the results at an impact angle of 30°, which meant that the behaviour of wear mechanism at normal impact was different from 30°, approaching those at 60°. In this, it is possible to observe that the values showed a decrease with respect to the data exhibited in former cases (30° and 60°). It seems to be in agreement with the literature review where it is possible to state that for ductile materials this impact angle is supposed to inflict the lowest erosion rate [114, 115].

It is observed that the surface damage in ductile materials caused by the sum of two wear mechanisms, cutting wear which is increasing at a shallow angle of incidence (typically 20°-30° from the plane of the surface), and deformation wear which is increased at normal impact, while deformation wear occurred when the target surface was repeatedly deformed by impacting particles which caused the surface to work-harden and crack. Spreading and propagation of the cracks caused the material removal. The results in this study seem to disagree with the previous studies where it is supposed to state that for ductile materials when spherical particles are used as the erodent instead of angular particles, the erosion rate exhibits a maximum at 90° even in the case of ductile materials such as copper and mild steel, which meant that the erosive wear is only dependent on fatiguing. The cutting action was not considered the main wear mechanism causing material removal from the target surface.

Figure 6.28 shows the same tendency with previous curves. As the shot numbers increased the mass loss was increased. Also it was observed that steady state erosion was reached from 3600 shot numbers at a velocity of 18.4 and 20 m/s, while it was reached from 4800 shots number at a velocity 15.2 m/s. As in the latter case at 60°, work hardening of the material could be a factor as this is more severe at normal incidence. In this case, the mass loss and erosion rate curves indicate that the incubation period at a velocity of 9.19 m/s was extended more with respect to the incubation period at 60°, since a slight loss of material is observed in this duration. Then, the curve is different for high velocities as the four periods of erosion rates are clearly demonstrated. However, comparing the effects of time on erosion rate for different impact angles for surface materials and different impact velocities for erodent particles it seems the data is in agreement with previous studies of solid-particle erosion or liquid-erosion by using the relationship between exposure time and erosion rate. To obtain extra results to evaluate the erosive wear resistance for materials or coating surfaces, micrographs were taken by using optical microscope and optical (3D measurement and inspection with infinite focus) equipment, then used for further discussion and explaination of wear mechanisms actually happened on the surface material [116, 117].
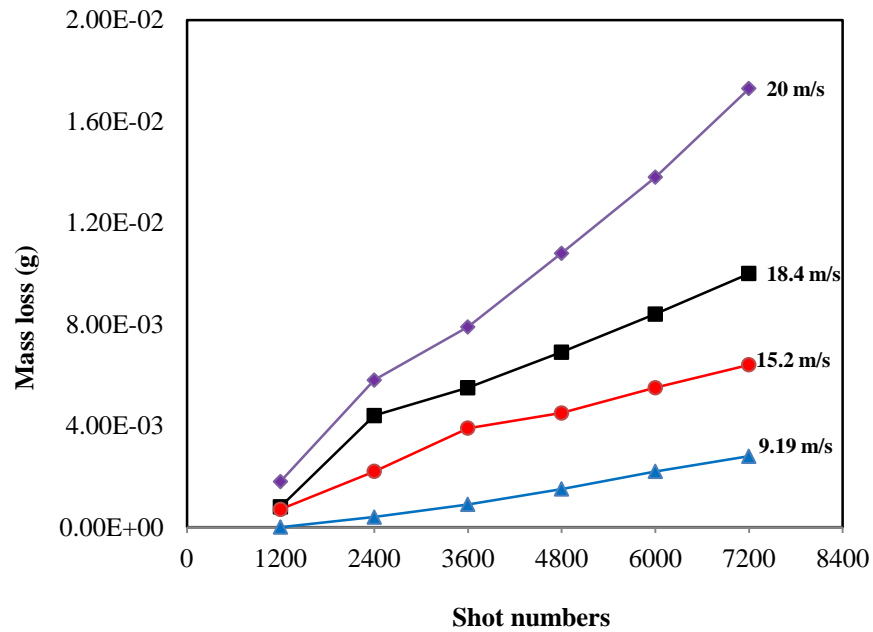
(a)

(b)

Figure 6.28 - (a) Mass loss against shot numbers, (b) Erosion rate against shot numbers at 90° impact angle, effect of particle velocity (9.19, 15.2, 18.4, 20 m/s).
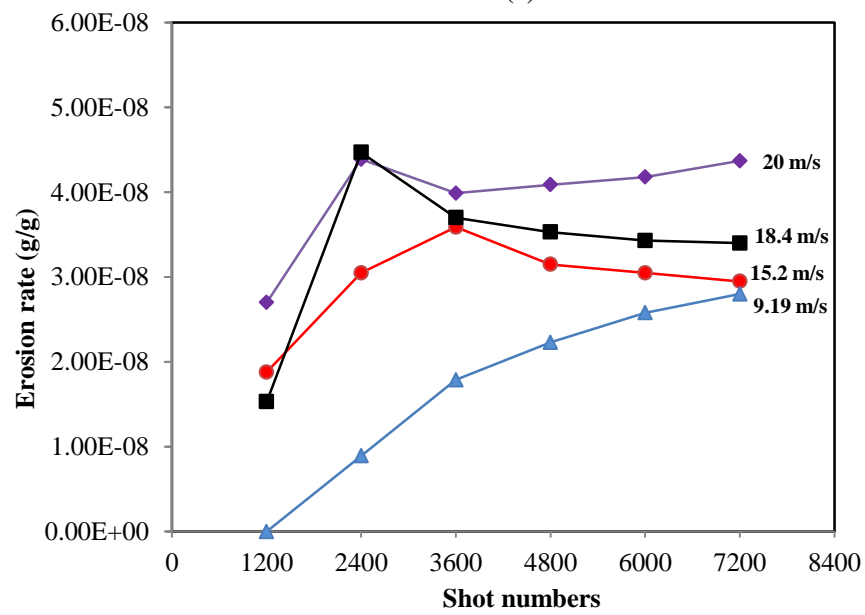
The data obtained from the tests are compared with the results from the known erosion rate to evaluate the wear resistance of surface material for different inclined angles. Figure 6.29 illustrates the erosion rates of four different impact velocities against the angle of impact. Angle effects have been observed and have been related to a change in the erosion mechanism. It has been found that at high angles of impact, 90° and 60°, material removal occurs through the formation of lateral fracture of lips and ridges, also formation and removal of chips from the surface. While at the lower angle of impact 30° damage caused plastic flow in surface material. Material removal occurred by micro-cutting and micro-ploughing. In addition, it is possible to conclude that the mass loss and erosion rate were higher as the particle velocity was increased. Finally, ductile materials such as H13 steel shows higher erosion rate at impact angle of 30° and lowest at 90°. This is in good agreement with data obtained by other authors [118, 119].
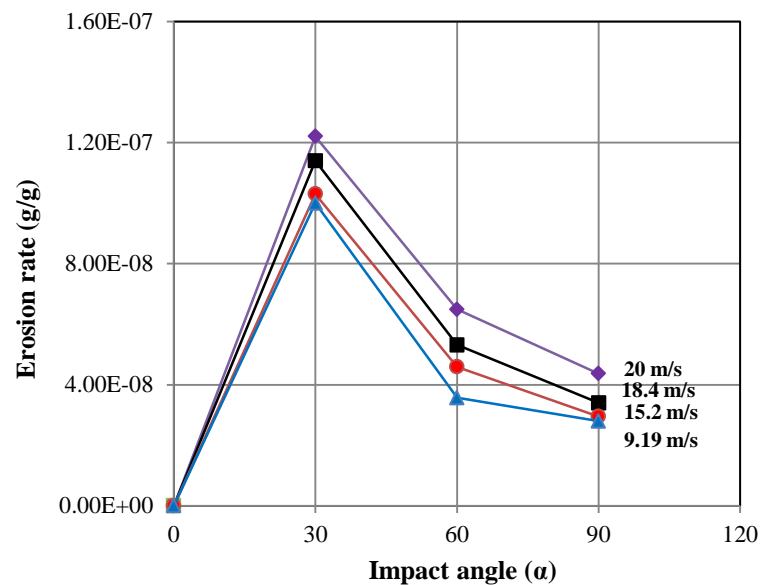
Figure 6.29 Erosion rate curves against impact angle.

6.3.6 Effect of impact velocity on erosion rate

One of the parameters remarkably influencing erosion is impact velocity. In Figure 6.30 shows the relationship between the impact velocity and the erosion rate, where it has been shown that as the particle velocity is higher the erosion rate is constantly increased. Increasing the impact velocity increases the impact energy on the surface material and more aggressive damage. It has been seen before that if the particle velocity increases 10 times the erosion rate increase between 100 and 1000 times [120]. It seems the result obtained in this study agree with previous literature results that show increase that on the impact velocity may cause more severe wear of surface material [121, 122].
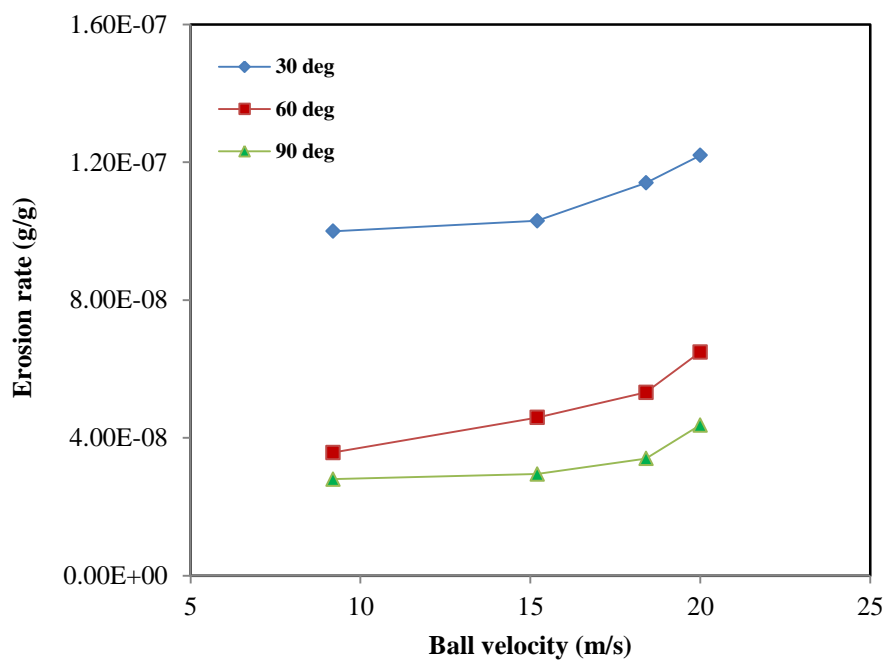
Figure 6.30 Erosion rate dependence on impact velocity.

In addition, it is important to mention that the mass loss is strongly dependent on the impacted angles more than on impact velocity [see Figure 6.29] which explains why the result obtained for the factor n in equation $E = \text{Constant } V^n$ [66] is in disagreement with previous studies. The calculated factor n of an impact angle of 60°; has been found from the equation in Figure 6.31.

$$E = \text{Constant } V^n \qquad\qquad 6.3$$

Then:

$\text{Log } E = \text{Log C x } V^n$

You can simplify this to give the final equation:

$\text{Log } E = \text{Log C} + n \text{ Log } V$
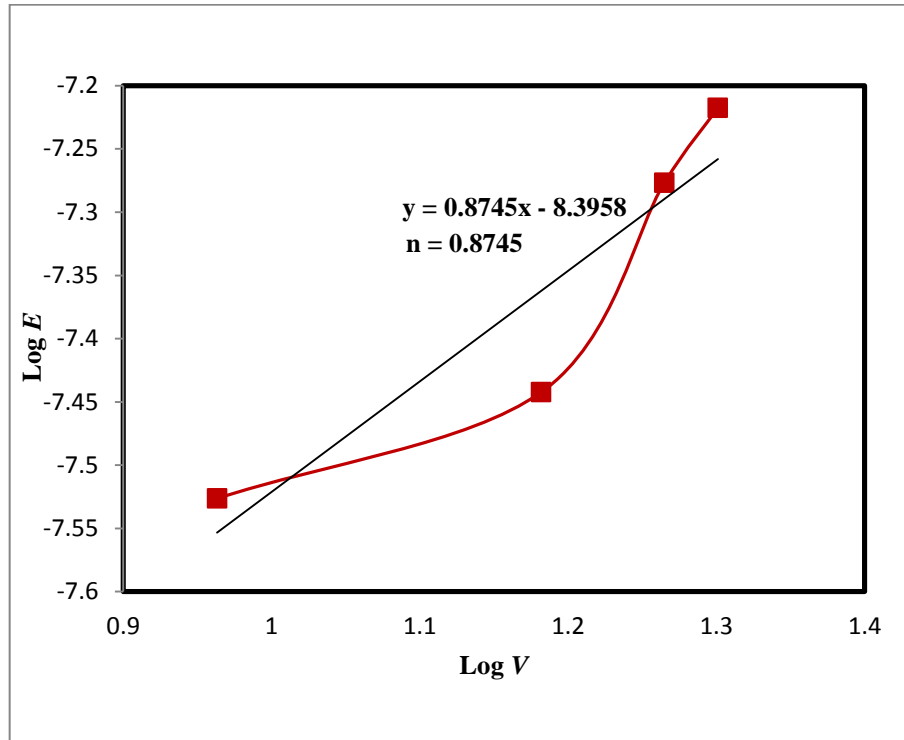
Figure 6.31 The value of n factor.

6.4 Conclusions

The erosion tests have shown that the material can be removed from a surface of H13 steel specimens impacted at normal and obliquely by spherical particles such as aluminium balls. The mechanisms of material removal for ductile materials are cutting, and ploughing wear which is increasing at a lower impact angle (30°) and deformation wear which is increased at a normal impact angle of 90°. The wear scar in this case had an elliptical shape at an impact angle of 30° and semi circular at impact angles of 60° and 90°. In respect to 60° and 90°, less damage was seen on the surface. However, that erosion rate is dependent on particle velocity.

The erosion rate curves at impact angles of 60° and 90° show a similar behaviour with previous experimental data, in which the periods of erosion rate are based to recognize and highlight the mainly exploration of this concept of erosion research on liquid impacts [40-41].

7

Erosion Testing on Cylindrical Surfaces

7.1 Introduction

Erosion tests on cylindrical specimens of H13 steel were carried out. In the experimentation, two particle velocities 15.2 m/s and 20 m/s, were used to impact the specimens in two cases: central impact and eccentric impact to illustrate the impact that could occur as molten aluminium enters a die. Two methods to quantify surface features and the topography of the surface were used, 2D profilometry and 3D profilometry

7.2 Erosion Testing

7.2.1 Test Apparatus

Erosion tests were carried out by a shot blasting machine with a nozzle of internal diameter 10 mm and length 50 mm. A schematic drawing of the experimental apparatus used for this experimentation is shown in Figure 7.1.
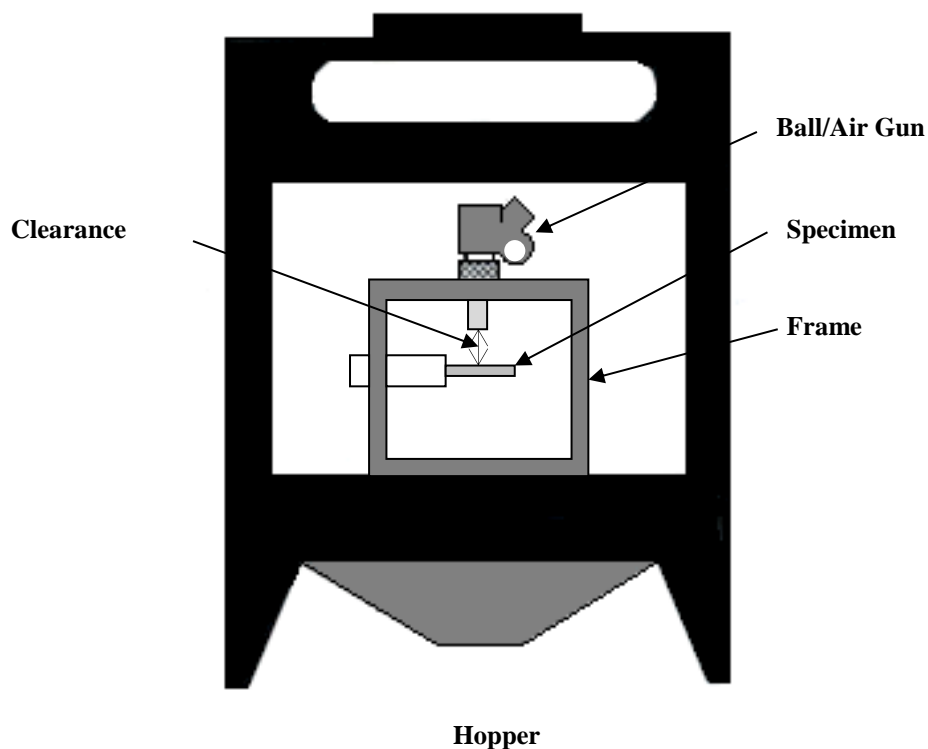
Figure 7.1 Schematic drawing of test apparatus.

7.2.2 Specimens and Tests Method

The target materials employed to carry out the tests were H13 steel with a hardness of 300 H_{V20}. The test surfaces were not treated. The average roughness of each specimen before testing was 0.5 µm (R_a), and their dimensions were as follows: 10mm in diameter and 70mm in length. The total number of shots for every test was 7200, although the specimen was removed every 1200 shots to measure the mass loss (after cleaning). The specimens were weighed using an analytical balance with an accuracy of ±0.00001g.

Tests on cylindrical H13 steel samples were carried out using different conditions. Two air pressures were used to conduct the tests, 40 and 80 psi giving velocities of 15.2 m/s and 20 m/s. Table 7.1 presents all the testing conditions used.

Table 7.1 Erosion testing conditions.

Testing Conditions	
Specimen (H13 steel)	Cylinder 10 mm in diameter and 70 mm in length Roughness: 0.5 µm (R_a) Hardness: 300 H_{V20}
Erodent particle (Aluminium ball)	Type: 6061 Aluminum alloy Basic diameter: 3 mm Weight : 0.04 g
Air pressure (psi)	40, 80
Impact locations	Central, Eccentric
Abrasive pulse flow rate (g/shot)	30, 55
Particle velocity (m/s)	15.2, 20
Testing cycle exposure	Mass loss measured every 1200 shots until 7200
Nozzle to specimen distance (mm)	30

7.3 Results

7.3.1 Wear Scar

In Figure 7.2, the erosion damage inflicted on each one of the H13 steel samples is clearly seen. Two samples were used for each case. In the first case, the sample was mounted at a central position to allow particles to strike the cylinder surface material in the middle of the sample. The wear scar produced had an elliptical shape with diagonals of 15 and 20mm when the surface was fired at 15.2 m/s, while for an impact of velocity 20m/s, the wear scar had a similar shape, elliptical with diagonals 16 and 22mm. Most of particles impacting at the edges of wear scar will slide down in a radial direction after impact. It undoubtedly could contribute to a larger area being covered with increased sliding. With a higher velocity the balls spread further from the nozzle and hence a larger wear scar was seen. The wear scar was split up into twelve sections, divided by angles or zones with respect to the position that it held on the specimen holder during the testing. It was observed that most of the balls struck in the central section between the angles, 75 and 120 or zones, 5 to 7, but also slight erosive damage was observed on both sides.

In the second case, the sample was mounted at an eccentric position to allow for particles to strike the cylinder surface material at the top and side of the sample. It is possible to observe the wear scar became smaller. The erosive scar is a half elliptical shape shown in Figure 7.2b, also the wear scar was larger as the particle velocity was increased, 17 mm by for an impact velocity of 15 m/s and, 19 mm by for an impact velocity of 20 m/s.
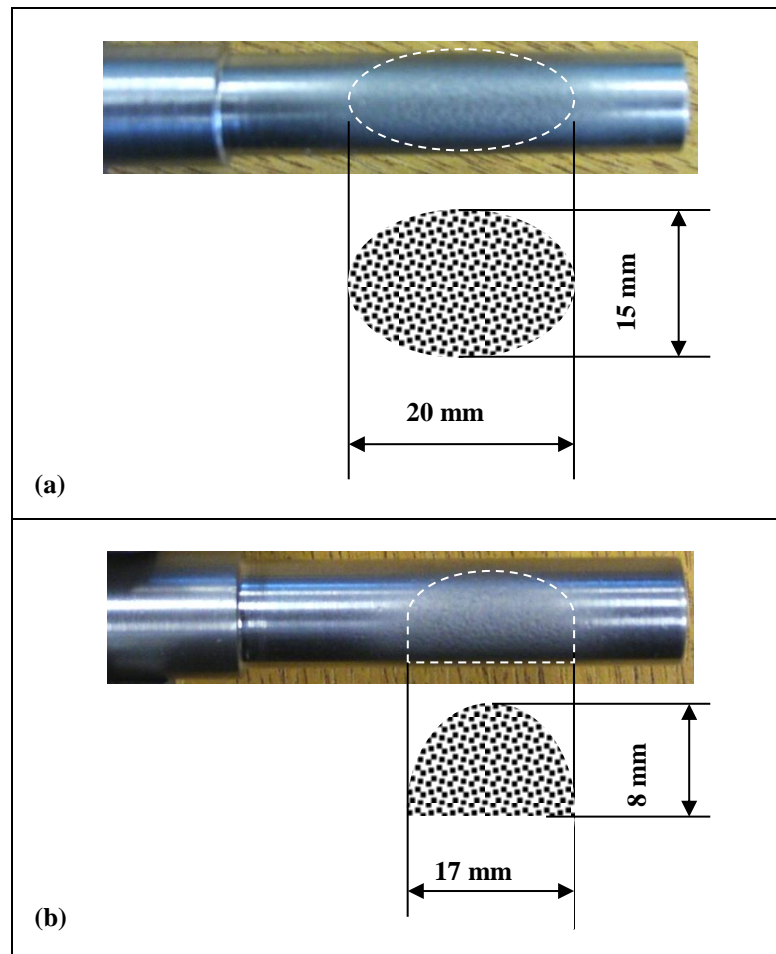
Figure 7.2 Wear scar at: (a) central position, (b) eccentric position.

7.3.2 Wear Surface Morphology

The erosion damage produced in the samples surfaces was characterized in two cases: the first case, the sample mounted at the central position as mentioned in previous sections. The examination of the erosion damage was carried out for sample surface presented after inflicted by tiny pits spread on the surface, different craters in shape and size depending on the wear mechanisms actually happening in the surface and indentation lines depending on the location of impact on the sample surface.

Erosion damage was analysed by optical microscopy and an Optical 3D measurement and inspection system with an infinite focus to help to understand the wear mechanisms. The micrographs are presented in three parts for the erosive scars. It is important to make an evaluation of how the aluminium balls are striking the cylinder surface and what types of wear mechanisms could occur on it. This means wear in each part depended on the regime of particle behaviour. The first part consists of zones 0-2 and, 10-12 or angles from, 0° to 30° and, 165° to 180°. In this case, it was observed the particles had slid on the material surface.

Figure 7.3 present the damage for both sides, which characterized the erosion damage by severe shallow elongated craters with varied sizes from 43 µm in width, 99 µm in length to and 76 µm in width, 105 µm in length for an impact velocity of 15.2 m/s, while craters sizes for an impact velocity 20 m/s were registered as smaller craters, 44 µm in width, and 102 µm in length to 132 µm in width, and 185 µm in length for larger craters. Also with an impact velocity of 15.2 m/s, large indentation lines were seen of 26 µm width, and 236 µm length. Ploughing mechanisms are involved in the damage incurred here as most material was removed by particles acting with one direction along the surface downwards after the first impact. For this instance, both sides for the sample held in the central position, larger lips were extruded in some craters and forward edges which can be related to a ploughing and greater plastic deformation. In addition, the damage on the surface increased when the particle velocity in the system was higher.
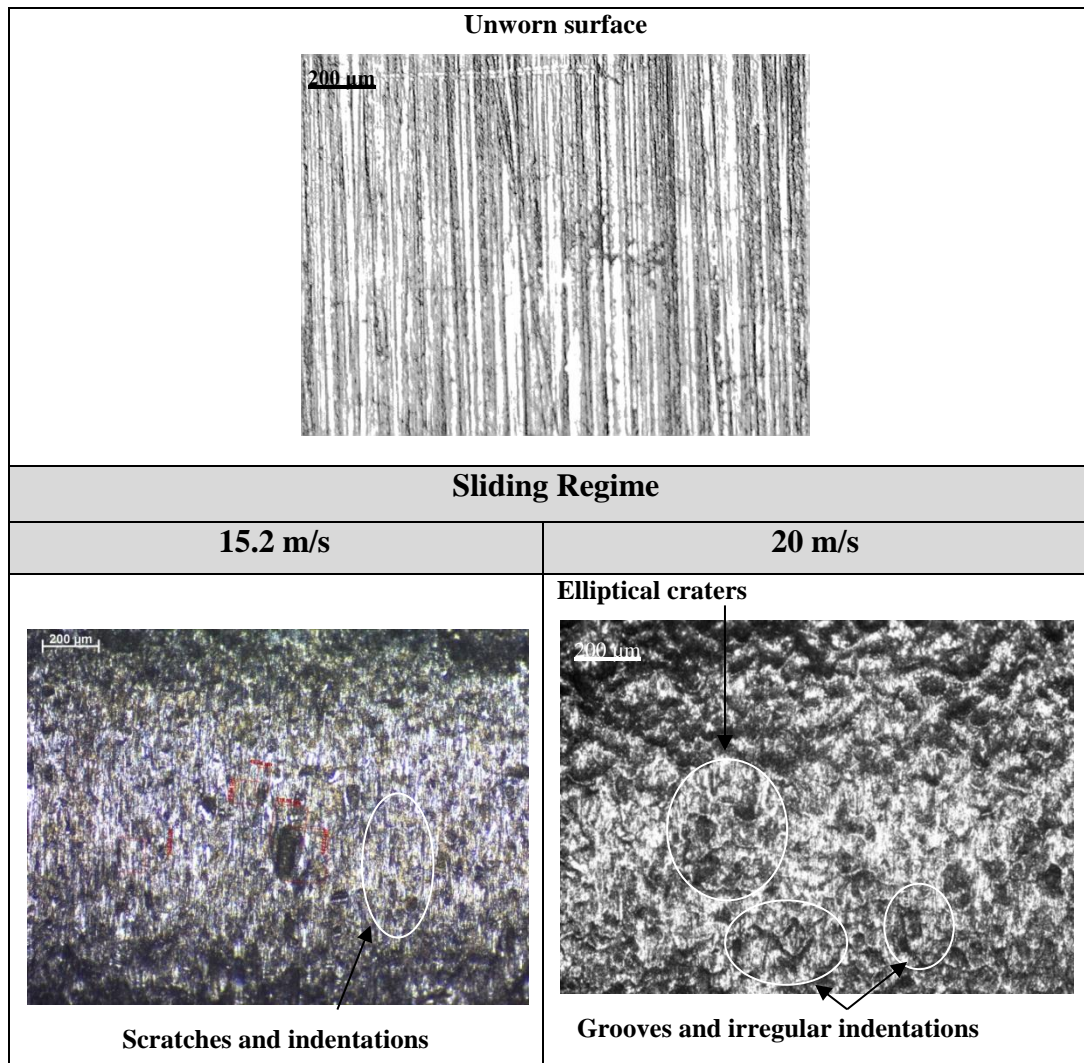
Figure 7.3 Erosion damage for central sample at the side section.

In figure 7.4 shows the wear damage produced in the middle sections of the specimens impacted at a central position more tiny pits are spread on the surface, less elongated craters. Sizes for small craters ranged from 76 μm in width, 92 μm in length to 123 μm in width, and 162 μm in length for larger craters.

In the case of higher velocity 20m/s, the craters on the surface were larger and elongated with sizes of 160 μm in width, and 234 μm in length, but also some indentation lines were seen around them. In this instance, also larger lips were extruded in most of craters in their sides and forward edges due to ploughing mechanisms which happened intensively in this part with great plastic deformation.

Impact and sliding part	
15.2 m/s	20 m/s
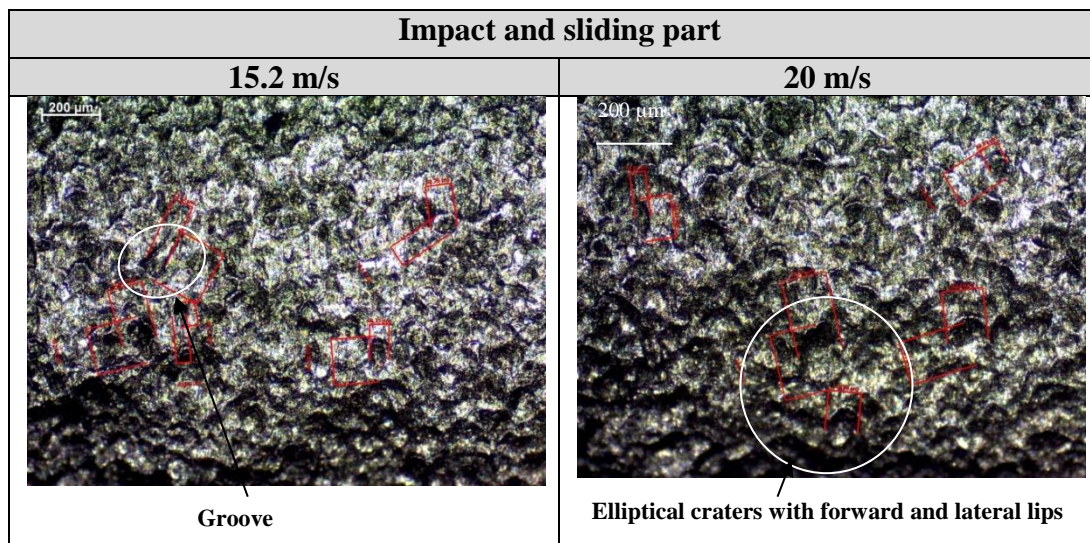
Figure 7.4 Erosion damage for central sample at the middle section.

As for the centre section when material surface was impacted at range area between the angles, 75° to 120° or radial zones from, 8 to 10. The damage produced in the centre section was the highest on the sample. It was increased due to intense numbers of balls striking at this part with high kinetic energy as they had a shorter path between the tip of the nozzle and the material surface also the particles had less friction with the inside wall of the nozzle.

A darker part at normal impact zone is observed which can be related to a greater plastic deformation due to normal impact and ploughing mechanisms being involved in the damage incurred here as most material was removed by particles acting. A characteristic feature of this is deeper round craters with higher lips. The specimens that were impacted at velocities of 15.2 and 20 m/s showed craters with diameters round from (41 µm to 108 µm) as shown in Figure 7.5.

Impact part	
15.2 m/s	**20 m/s**

Craters with round lips (15.2 m/s)   **Craters with round lips** (20 m/s)
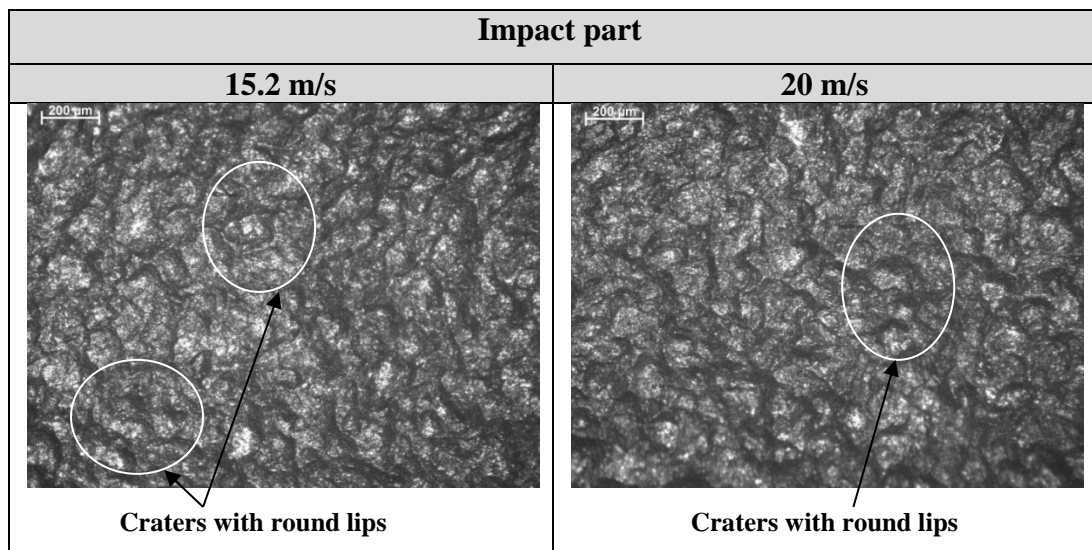
Figure 7.5 Erosion damage for central sample at the centre section.

In the second case, for wear damage inflicted at an eccentric position, the erosion damage was characterized as mentioned in the previous case (at a central position) by craters with various sizes, tiny pits, scratches and indention lines. Larger craters were registered at the impact section (central zone in Figure 5.4, Chapter 5) whereas elongated craters were presented at the impact and sliding section (middle section in Figure 5.4, Chapter 5). Longer and more intense in scratch lines were registered at the sliding section (side section in Figure 5.4, Chapter 5).

The micrographs in Figure 7.6 show the damage presented in the sliding part between angles 0° to 30° or radial zones 0 to 2 which registered a higher number of scratches and indentation lines caused by ploughing, cutting and sliding action. The samples exhibited scratches and indentation lines sizes from 63 µm in width, and 252 µm in length.

Sliding Regime	
15.2 m/s	20 m/s
Scratches and indentations	Elliptical craters with lips removed and irregular indentations
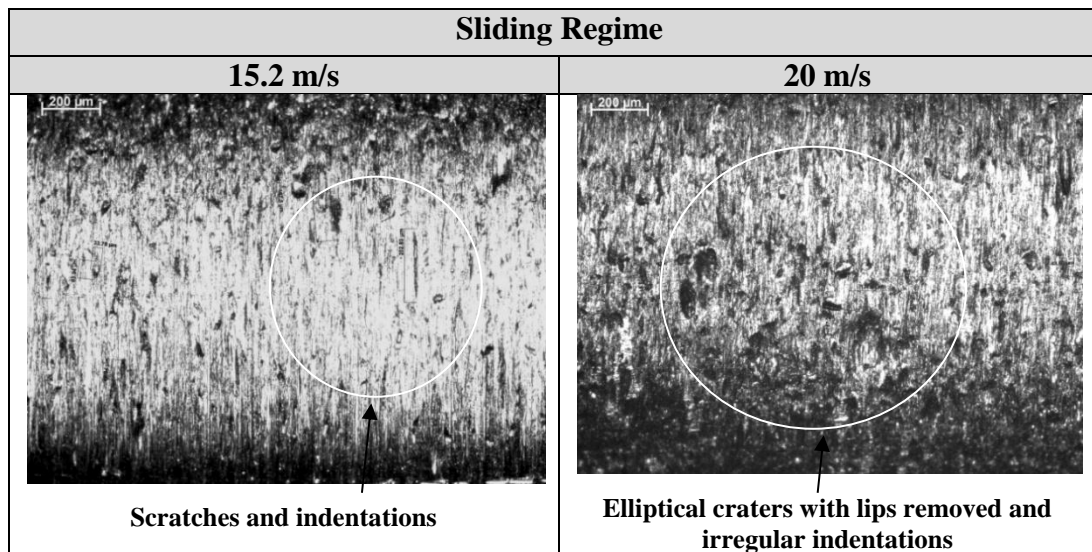
Figure 7.6. Erosion damage for central sample at the centre section.

In the impact and sliding section, elliptical shallow craters were seen in the area between the angles 30° to 75° or radial zones 2 to 4. The erosion damage exhibited elongated craters caused by a ploughing action as the particles slid downwards after impacting the material surface, as shown in Figure 7.7. This damage was intense since a higher number of balls acted here.

For this instance, larger lips were extruded in some craters in their sides and forward edges. The crater size fluctuated between 45 µm in width, 64 µm in length, and 78 µm in width, 112 µm in length, also grooves were observed at velocities of 15.2 and 20 m/s respectively.

Impact and sliding part	
15.2 m/s	**20 m/s**
Irregular indentations	**Elliptical craters with forward lips**
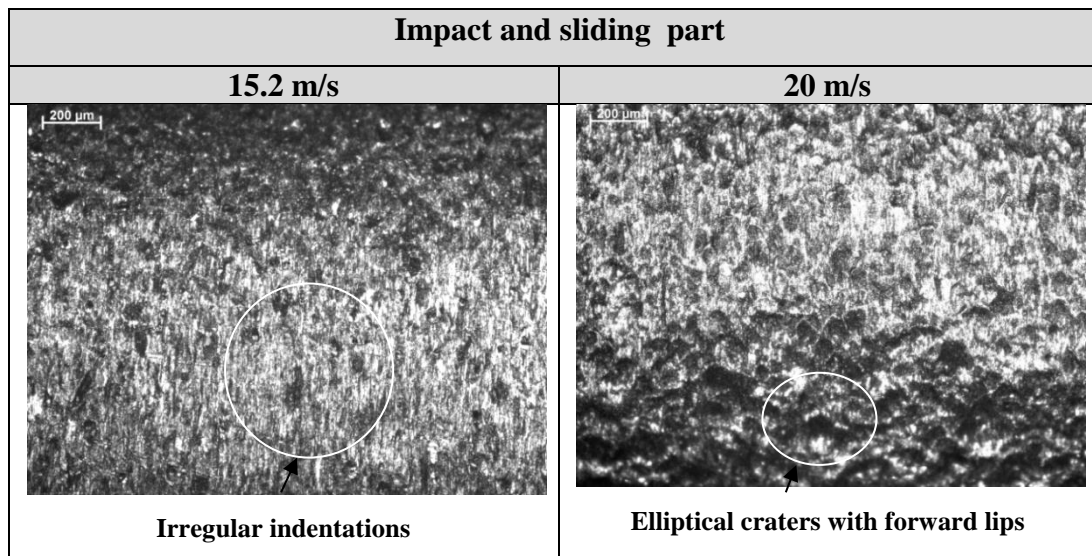
Figure 7.7 Erosion damage for eccentric sample at the impact and sliding section.

Figure 7.8 shows the damage presented in the impact part between angles 75° to 90° or zones 4 to 6 which was higher, with round craters with lips in front and sides. The loss of material from eroded surfaces appears to be due to successive impact of a large number of particles, which form a plastically deformed surface layer. It is supposed that a normal impact caused a higher deformation at this section. The specimens that were impacted at velocities of 15.2 and 20 m/s showed craters with diameters around 55 µm and 99 µm respectively.

Impact part	
15.2 m/s	**20 m/s**
Craters with round lips	**Craters with round lips**
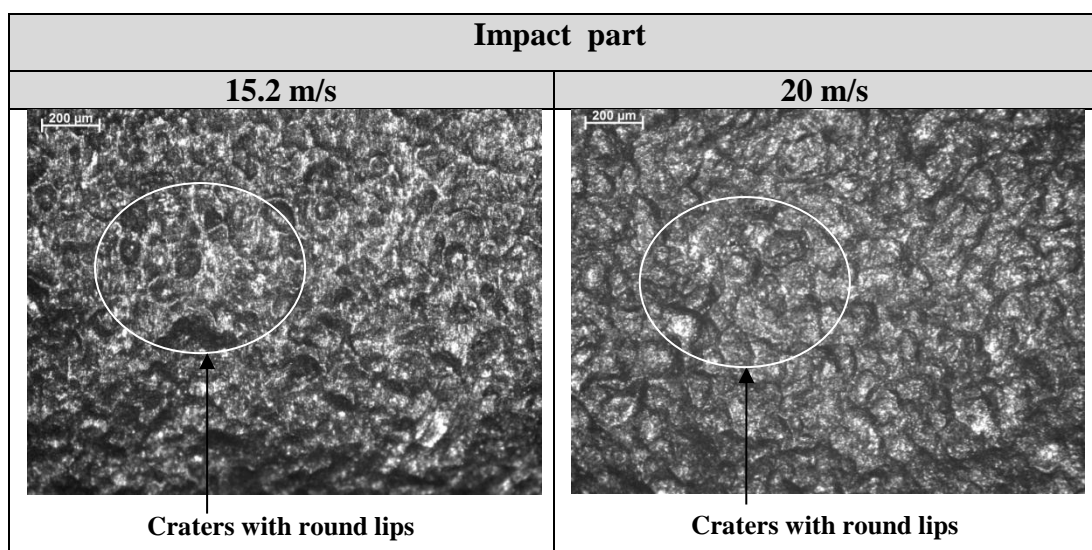
Figure 7.8 Erosion damage for eccentric sample at the impact section.

7.4.3 Profilometer Surface Map

A 3D micrograph is often required for the accurate characterization of surface features. Figure 7.9 shows another factor to consider is the effect observed when a particle strikes the at impact section for each position, central and eccentric. The scars were taken for the samples at impact velocities of 15.2 and 20 m/s. In this case, lips could be one more contribution to changes in mass loss. As mentioned in Chapter 6, where the different types of craters were defined, these seen here are "deformed craters", where the surface has been depressed into their walls and the crater has some plastically deformed material that has risen to the sides and the forward part in relation to the impact direction of the particle. It meant that the difference in the damage inflicted in each section was analysed where the deformation action represented the main cause of damage at angles between 75° and 120° for the central sample and 75° to 90° for eccentric sample.
The examination was carried out of the eroded surfaces at central and eccentric location in the impact section.

From the images it was seen that for both surfaces indentation craters were formed with different sizes. It is possible to see in Figure 7.9 that the eroded surface impacted at the central position has deeper craters with a higher lip height than those at the eccentric position, shown in Figure 7.10. It was seen that the highest higher between valley and the tip of lips of craters are 30 µm, while at eccentric position it was 20 µm.
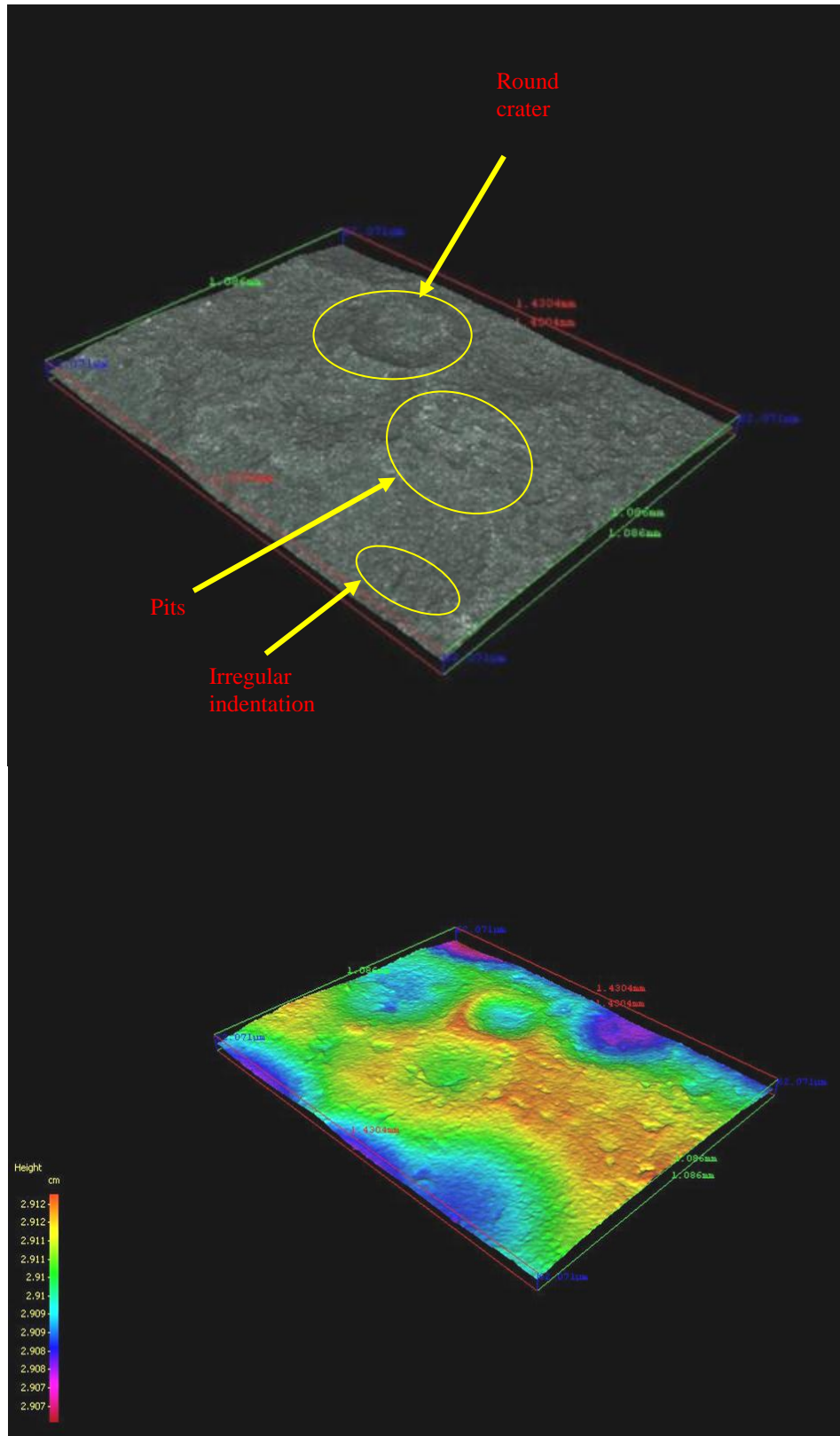
Figure 7.9 - 3D profilometer surface map (1.086 mm x 1.43 mm) of erosion damage for central sample at the impact section.
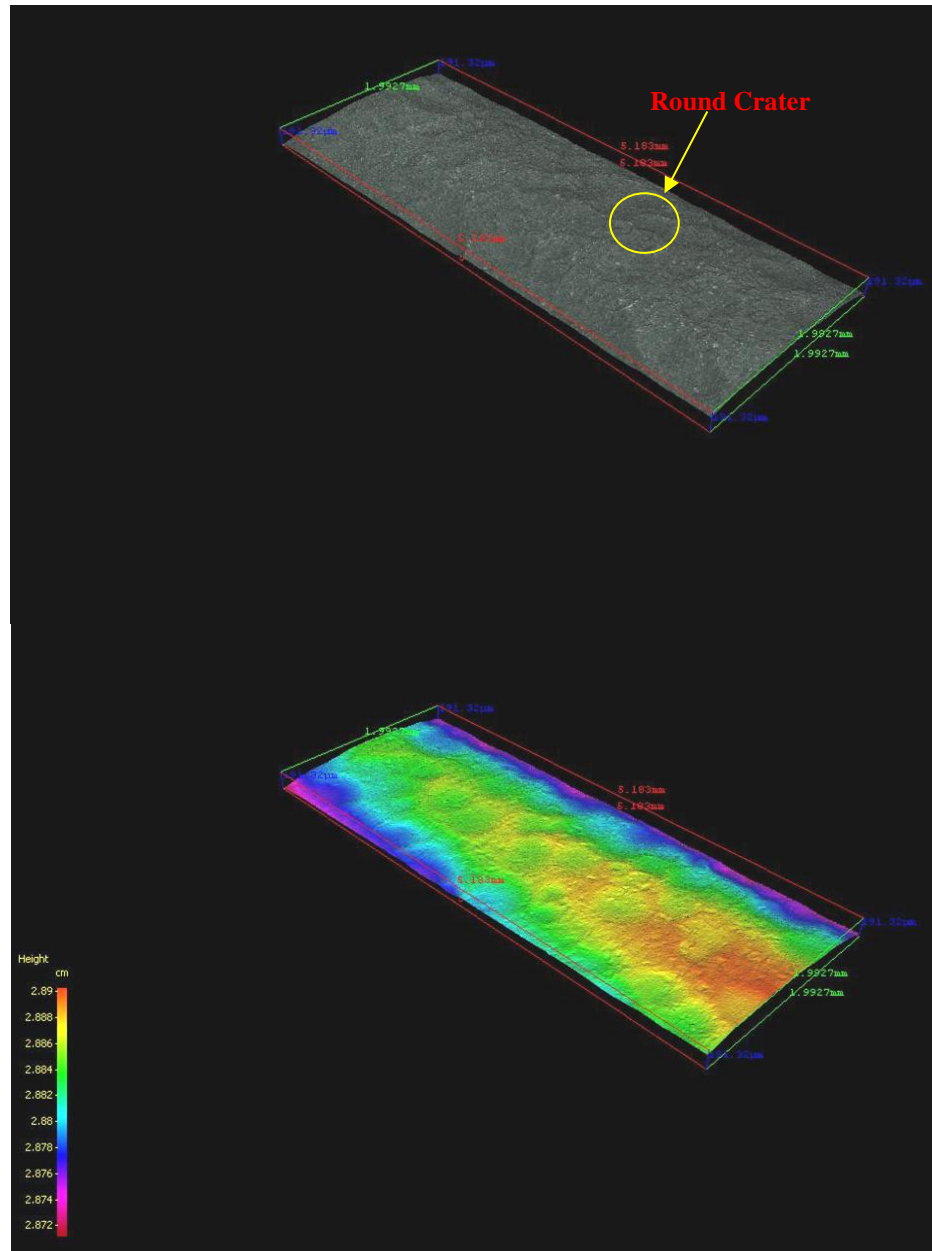
Figure 7.10 - 3D profilometer surface map (1.99 mm x 5.18 mm) of erosion damage for eccentric sample at the impact section.

Different wear mechanisms were observed in Figure 7.11, where the surface was inflicted at the eccentric position. A deformation, cutting and ploughing action was present on the eroded surface. It is evidence to display the regimes of the impact on material surface collected in one image.
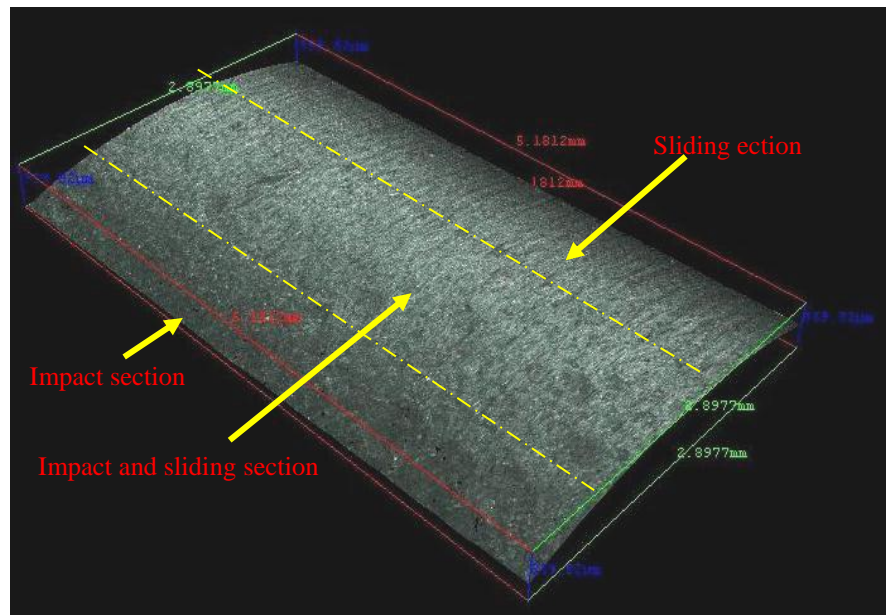
Figure 7.11 - 3D profilometer height image (2.89 mm x 5.18 mm) of erosion damage for eccentric sample, in impact and sliding section.

7.4.4 Roughness

The Ra measurements obtained from erosion tests at an impact velocity of 20 m/s are presented for central and eccentric impact locations. The measurements were carried out using a Mitutoyo Surftest Profilometer, where a stylus was dragged steadily across each radial zone on the surface under examination. The parameters used to conduct the measurements were a sample length of 30mm and a speed of 0.5 mm/s. The data obtained in the two cases, for central and eccentric impact, are presented in Figure 7.12. From this, it is possible to notice that the location areas between angles 75° and 120° for centric impact and 75° to 90° for eccentric impact have a roughness profile otherwise the area out of these angles they have a smooth profile at (original surface roughness). It is possible to state the area with highest roughness is at the centre of the impact outside this area, which could be originated by impact with sliding and sliding having lower roughness than impact alone. As cutting and ploughing mechanisms present shallow craters.
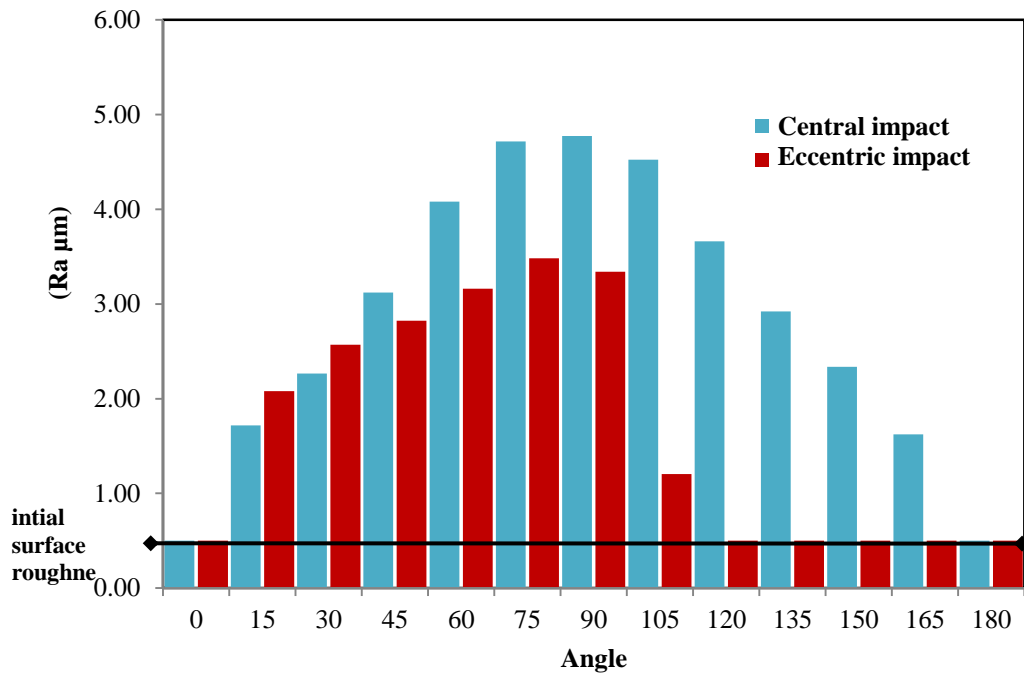
Fig. 7.12 - Ra Data obtained for central and eccentric impact.

7.4.5 Erosion Rate

The erosion damage was characterized by mass loss from which an erosion rate was calculated. Each specimen was weighed before and after tests for different impact locations and particle velocities. Then, the mass loss was calculated by the difference between the initial weight (Wi) and the weight after every 1200 shots (Wn) until 7200 shots as follows:

$$\text{Mass Loss} = Wi - Wn \qquad\qquad 7.1$$

Erosion rate was obtained by dividing the mass loss generated every 1200 shots until 7200 shots, the cumulative mass of the impact balls used every 1200 shots to cause the total mass loss for 7200 shots. The following equation was used for carrying out the calculations:

$$\text{Erosion Rate} = \frac{\text{Removed Mass (g)}}{\text{Mass of aluminium balls striking the surface}} \qquad 7.2$$
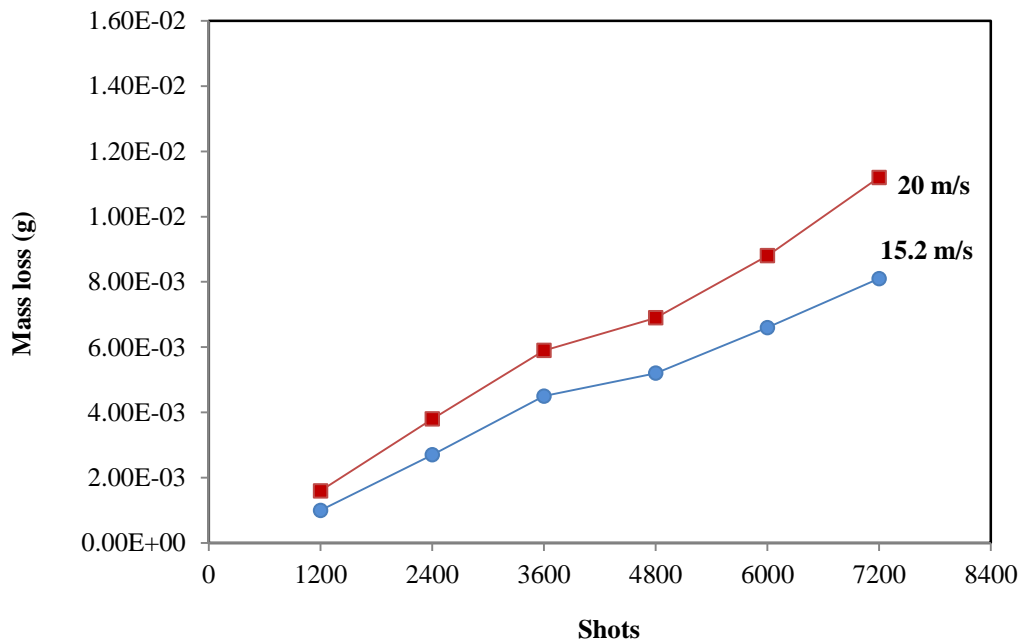
(a)
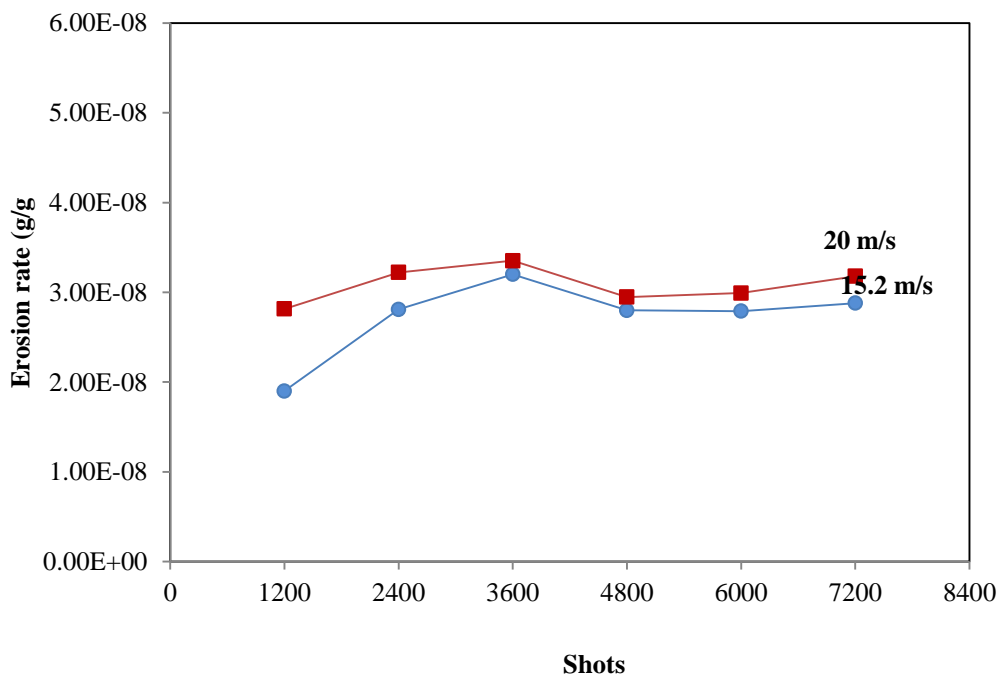
(b)

Figure 7.11 - (a) Mass Loss, (b) Erosion rate curves against shots at a central position.
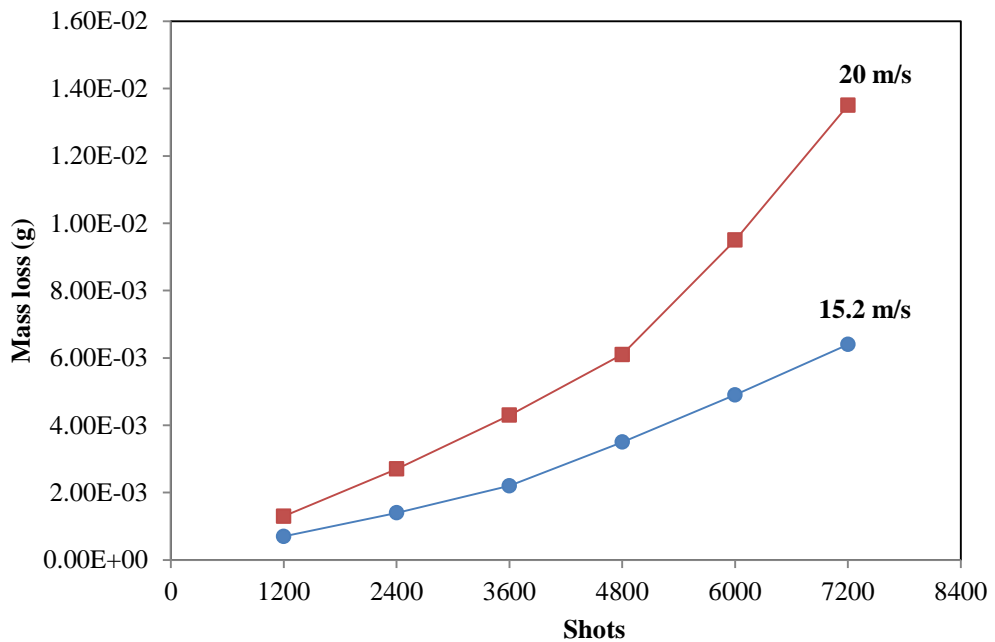
(a)
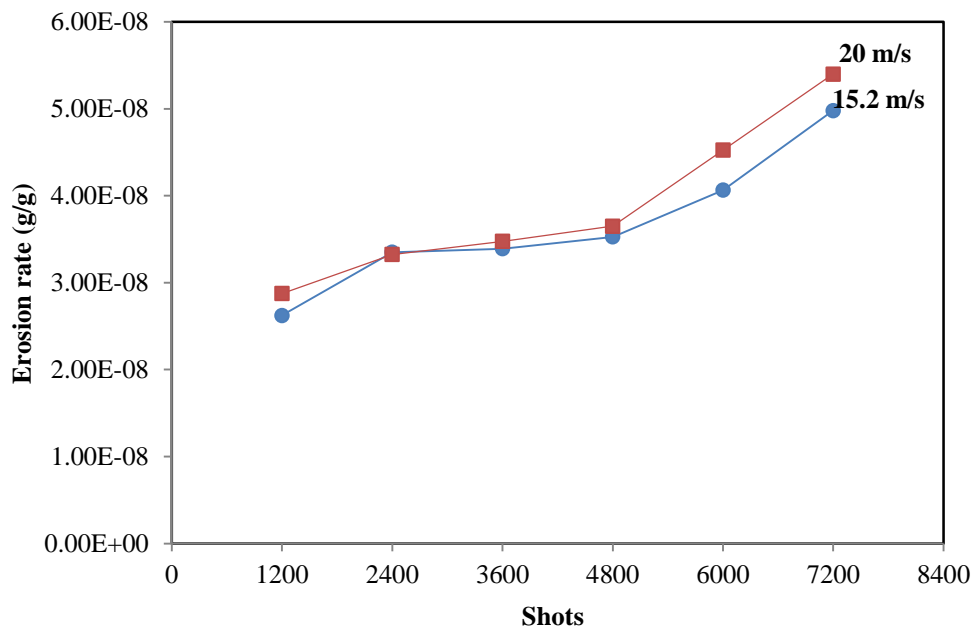
(b)

Figure 7.12 - (a) Mass Loss, (b) Erosion rate curves against shots at an eccentric position.

The results for mass loss and erosion rate obtained for impact at the central position are displayed in Figures 7.11a and b. It is possible to observe that the mass loss and erosion rate were higher at increased velocity.

In this case, the curve tendency showed a similar behaviour to that observed for flat surfaces (see Figure 6.28). Again four stages; incubation period, acceleration or accumulation period, deceleration period and steady-state period are seen.

Figure 7.12 shows the results of mass loss and erosion rate for samples impacted at the eccentric position. It is possible to conclude that the results follow the same trend of erosive wear to those presented in the literature review [49], where it is possible to observe that the erosion rate was getting higher when the shots and velocity were increased at first till around 2400 shots, then wear rate flattened. After 4800 shots the wear rate increased again due to fatigue processes in the upper layers causing material loss. In addition, the material surface was more piled up as the continuous ploughing action increased the micromachining. Finally, it can be noticed that for the central location the wear rate initially had a high value and then decreased due to increasing hardening of the surface, otherwise, at eccentric position the wear rate had low-steady wear and was raised due to ploughing and micromachining.

7.4 Conclusions

Erosion tests have been carried out using cylindrical H13 surfaces, specimens mounted in two positions; central to and offset from the particle flow. The results showed four regimes of particle behaviour, impact only, impact and sliding, sliding only and pressed only. A different wear mechanism was observed in each position. It is described by a difference in shapes and sizes for craters whereas a circular shape is observed at a central position, an eccentric position shows an elliptical shape and lower depth craters compared to that seen at the central position.

In addition, different wear mechanisms were observed at each position. Plastic deformation was higher at central position compared with an eccentric position. On the other hand, ploughing and micromachining action were more presented in the eroded surface at an eccentric position.

8

Effects of Temperature on the Erosion Behaviour

8.1 Introduction

In this chapter tests are outlined that were carried out to study the effects of temperature on the erosion behaviour of H13 steel. Temperatures of 200°C which represents the injection temperature of a semi-solid aluminium into the die, and a temperature of 400°C which represents the temperature of molten aluminium injected to a die. Also incremental tests were carried out in which the temperature varied from 50°C to 400°C, in steps of 50°C where it is possible to observe the full behaviour of erosion rate with temperature.

8.2 Experimental Details and Procedure

8.2.1 Tests Apparatus

Experiments were performed using the erosion test apparatus outlined in Chapter 5, for this testing a cartridge heater was incorporated with the specimens to apply heat as shown in Figure 8.1.
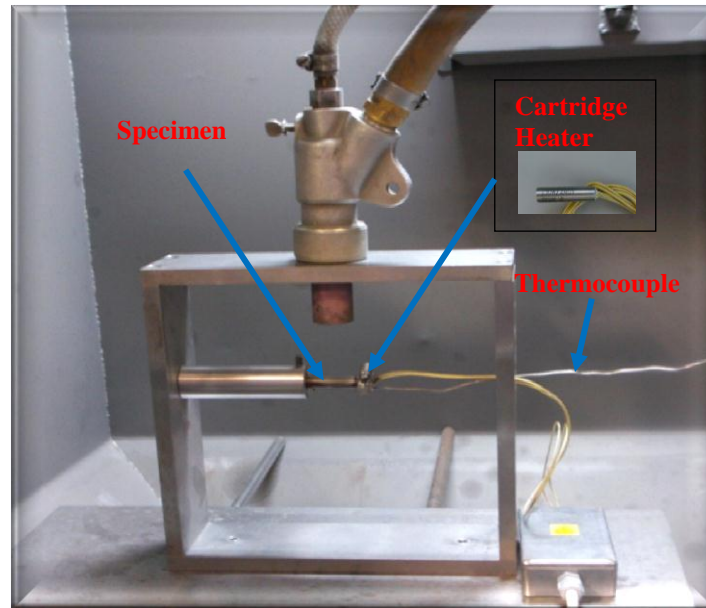
Figure 8.1 Cartridge heater and the thermocouple location in the frame.

A description of the cartridge heater employed to conduct the experimentation is shown in Table 8.1.

Table 8.1 Cartridge heater details.

Cartridge Heater Details	
Insulation	Magnesium Oxide Powder
Diameter Ø (mm)	6
Length (mm)	30
Maximum Temperature (°C)	750
Voltage Supply (V)	Any voltage up to a maximum of 480

Temperature control was a described using a CAL 3300 and 9300 Auto-tune temperature controller as shown in Figure 8.2. Feedback control was to regulate using a TJ36 type thermocouple mounted on the specimen.
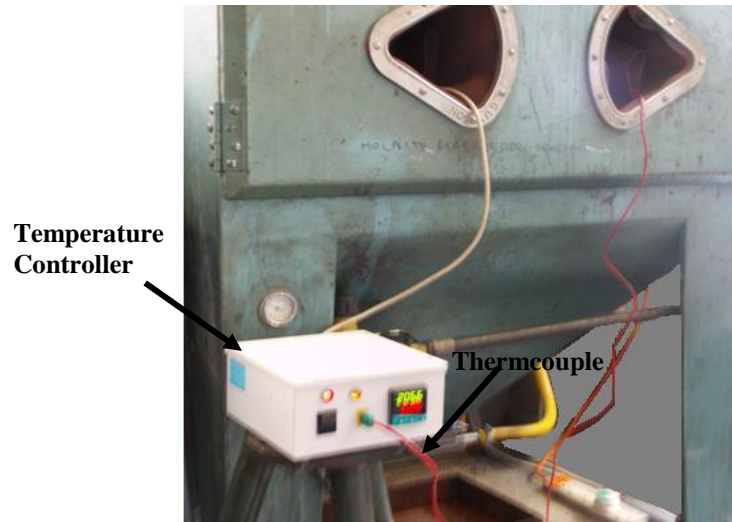
Figure 8.2 Temperature Controller (model CAL 3300).

To evaluate the heating rate and temperature, stability trials were run in which the specimen temperature was taken to 200°C and 400°C. The data is shown in Figure 8.3. The time to reach stability at the required temperature was good.
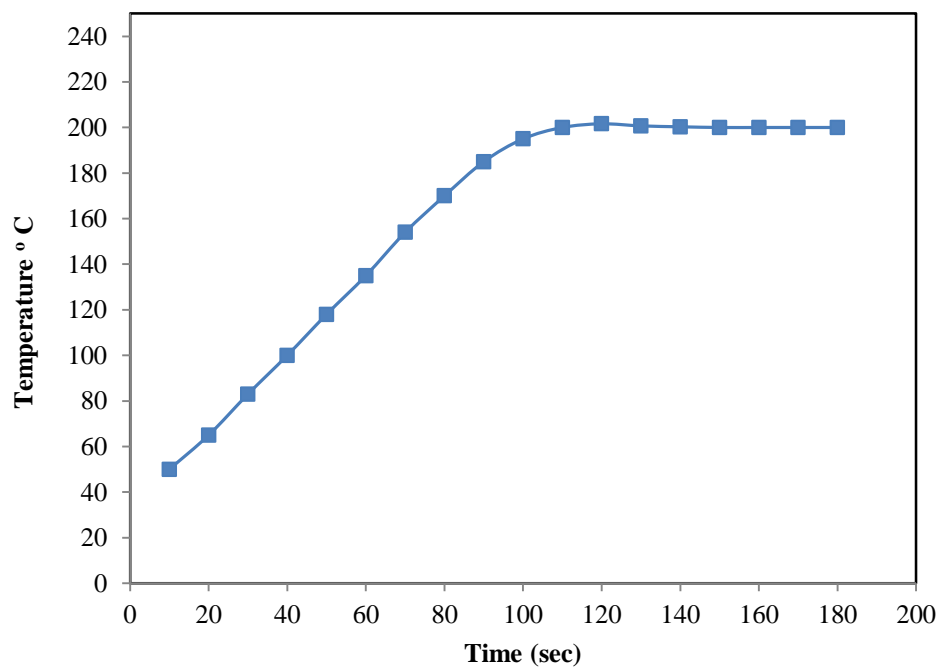
(a)
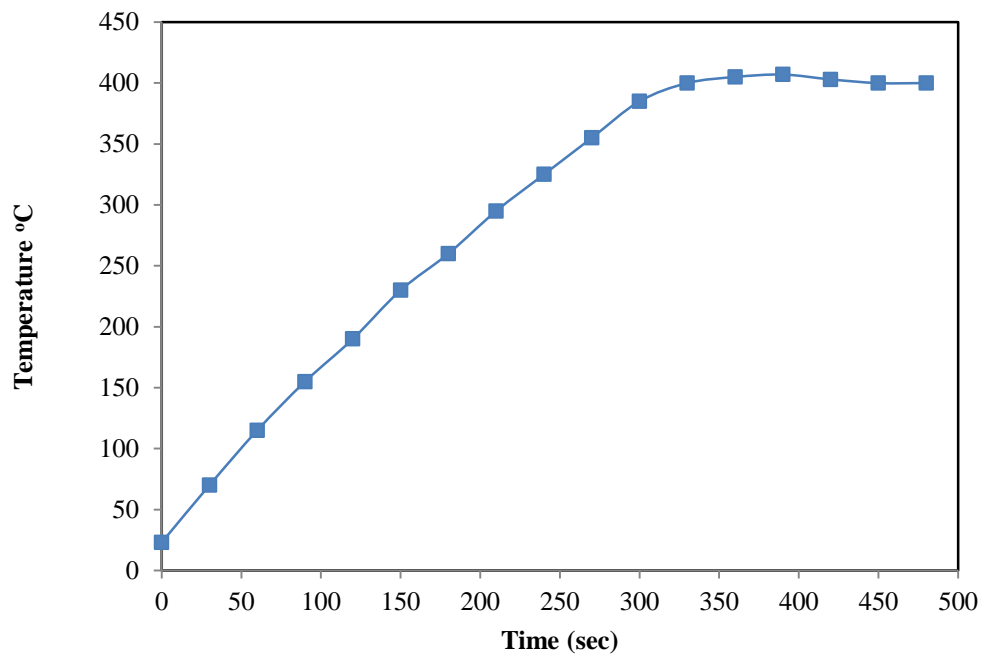
(b)

Figure 8.3 Time to reach required temperature, (a) 200 ^{o}C, (b) 400 ^{o}C.

8.2.2 Specimens and Test Method

The target material employed to carry out the tests was H13 steel with hardness 300H$_{V20}$. One air pressure was employed for all tests and hence the velocity of the particle was 15.2 m/s. The test surfaces were without treatment. The average roughness of each specimen before testing was 0.5 µm, and their dimensions were: 10mm diameter and 70mm length. The total number of shots for at 200°C and 400°C was 7200 shots, although the specimen was removed every 1200 shots to measure the mass loss. The specimens were weighed using an analytical balance with an accuracy of ±0.00001g, before the beginning of every test and removed every 1200 shots, cleaned and reweighed to find the mass loss. A test was also carried in which the temperature was increased incrementally every 1200 shots to study how temperature affects wear across the full temperature range.

8.3 Results and Discussion

8.3.1 Wear Rates

The wear scars obtained with elevated specimen temperature are shown in Figure 8.4. The wear scars were larger and deeper than those at room temperature (see Figure 7.6 from the previous Chapter 7).
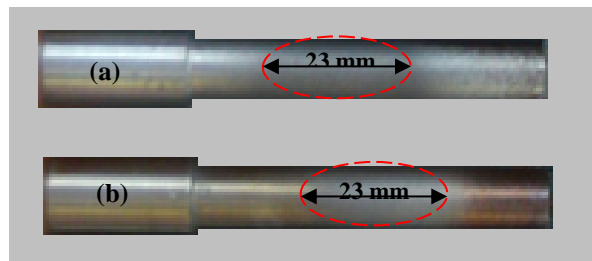
Figure 8.4 Wear scar at temperature, (a) 200°C, (b) 400°C.

Cumulative weight loss and erosion rate versus the shot number are presented in Figure 8.5. Results show the dependence of mass loss and erosion rate on temperature. From these graphs, it is possible to confirm that as the temperature is increased in the system, the mass loss and the erosion rate are higher. In addition, an incubation period characterized by no mass loss rate is observed at the start of the tests. It lasts until 1200 pulses have been applied. The mechanical properties of metals are highly dependent on temperature. The modulus of elasticity of metals decreases as the temperature increases [123]. Which may explain the wear behaviour seen here. The high temperature will have caused a decrease in the hardness of steel and contributed to the erosion rate increase with the increase in temperature. Ploughing mechanisms caused the material removal from the material surface as particles impacted and slid along the surface. A large amount of plastic strain caused material pile up along the edges of the indents which is fragile and therefore becomes damaged during subsequent impacts. Also, some oxidation of the specimens did occur, especially at the highest temperatures.

The contribution of oxidation to the increase in the mass loss at elevated temperature is governed by the nature of interaction between material surface and oxidation, i.e., the thickness, morphology and adherence to the surface of the oxide scales that form in these materials [124, 125]. The erosion rate curves indicated that the erosion rate at room temperature increased until 3600 pulses and they levelled off after a slight decline for tests at higher temperatures, the erosion rate dropped from 1200 pulses. It is probable that an increase would have been seen if measurements had been taken at shorter intervals up to 1200 pulses. A similar behaviour for erosion curves was seen shown with those previously in Chapter 6. Four stages area again have shown for erosion rate. The eventual steady state erosion for the samples at room temperature could be a result of work- hardening. Also repeated impact may occur closing craters lips or ridges as previously explained. It was seen that the steady state erosion for the sample was impacted at 200°C was from 3600 pulses. On the other hand, for the sample impacted at 400°C temperature showed that the work-hardening was decreased which caused an increase in the erosion rate from around 4800 pulses.

Once more, it is necessary to consider several fundamental metallurgical processes to facilitate the understanding of the erosion-temperature relation such as, mechanical strength, tensile or yield stresses are lower at elevated temperatures of the samples, which cause a decrease in the total energy required to remove a certain amount of material as the temperature increases.
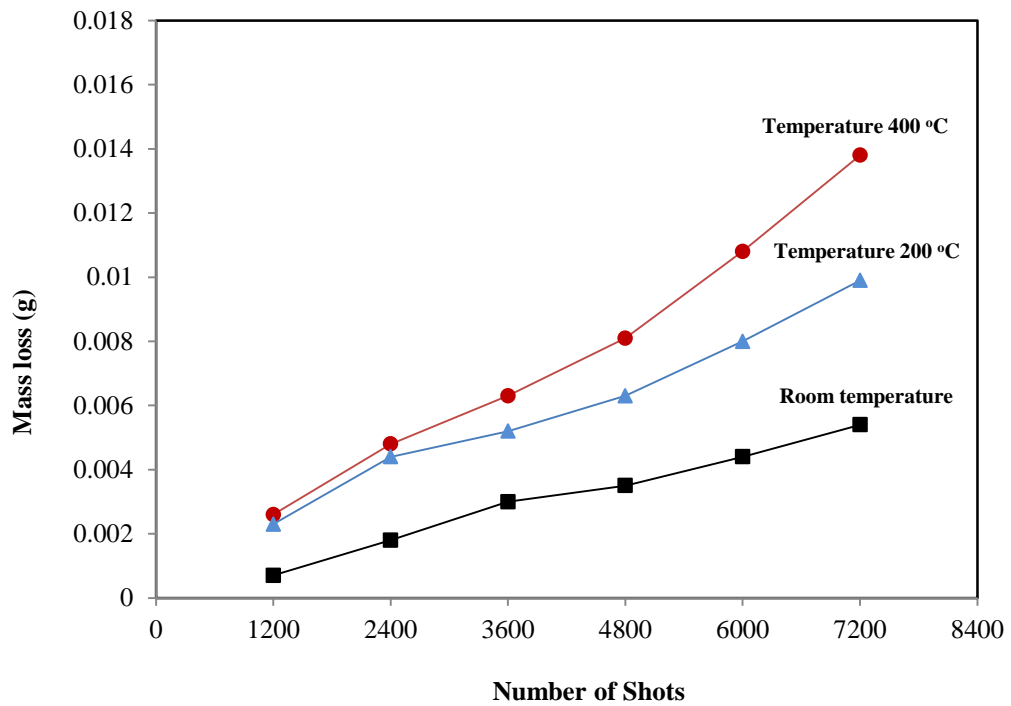
(a)
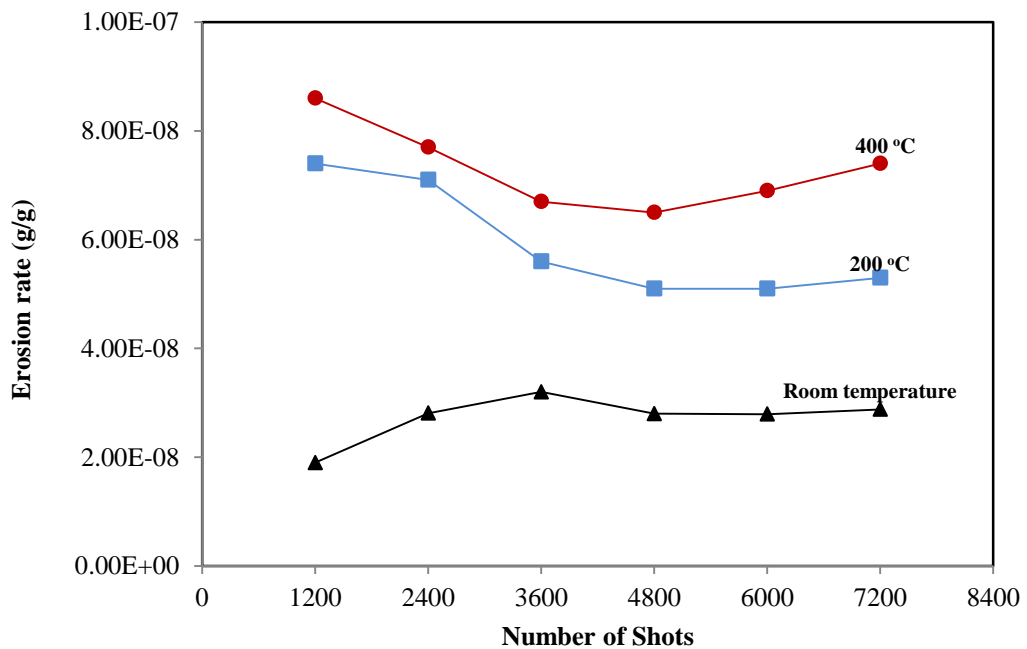
(b)

Figure 8.5 - (a) Mass Loss, (b) Erosion rate curves against shots at particle velocity 15.2 m/s.

Figure 8.6 shows the erosion-temperature relationship determined from the aforementioned. It is possible to observe the tendency observed in the former case where the erosion rate was getting higher at elevated temperature in the sample. The result was obtained when an impact velocity 15.2 m/s was used to impact a sample of H13 steel at a central location. In this case, the values of erosion rate were higher as the primary effect of temperature is to soften the inflicted material and increase erosion rate [126]. The rate and mechanism of erosive wear are influenced by temperature. When a higher temperature is used the material surface can oxidize and corrosion can take place and further accelerate the erosion rate. The thickness of oxidation can be more effective on wear mechanisms as the material is removed from the eroding surface as a relatively brittle oxide and this process of wear could be transmitted incrementally to erosion of brittle material [127].

It is also thought, at sufficiently high temperature, the metal underlying surface does not come into contact with the impacting particles because of the thickness of oxide layer may prevent direct contact. In addition, the curve showing the changing gradiant of erosion rate at 200 $^{\circ}$C. It is thought that could be increased the compression stresses when softened the material with repetitive impacting especially at central section causing deceleration in erosion rate.
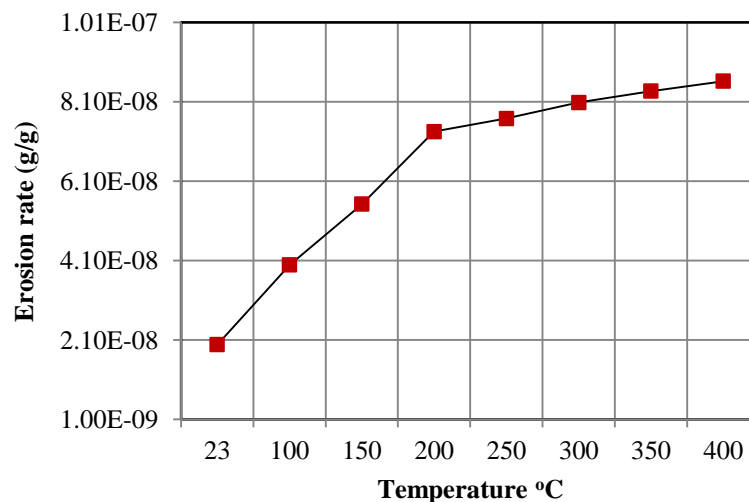
Figure 8.6 Erosion-temperature relation at impact velocity 15.2 m/s.

Figure 8.7, shows the values of the hardness of the H13 steel that was used in tests when it was at elevated temperature. The values showed a decrease 200 H_{V20} at a temperature of $400^{\circ}C$, which it meant that the hardness of sample decreased to 66% of its original value at room temperature. However, the testing temperature is becoming an important factor to be considered in wear studies, since ductile-to-brittle transitions in mechanical behaviour can affect the mechanisms of mass removal from the surface. When the temperature is increased in a system, ductile mechanisms like cutting, ploughing and plastic deformation become less significant and the corrosion processes at the surface are intensified.
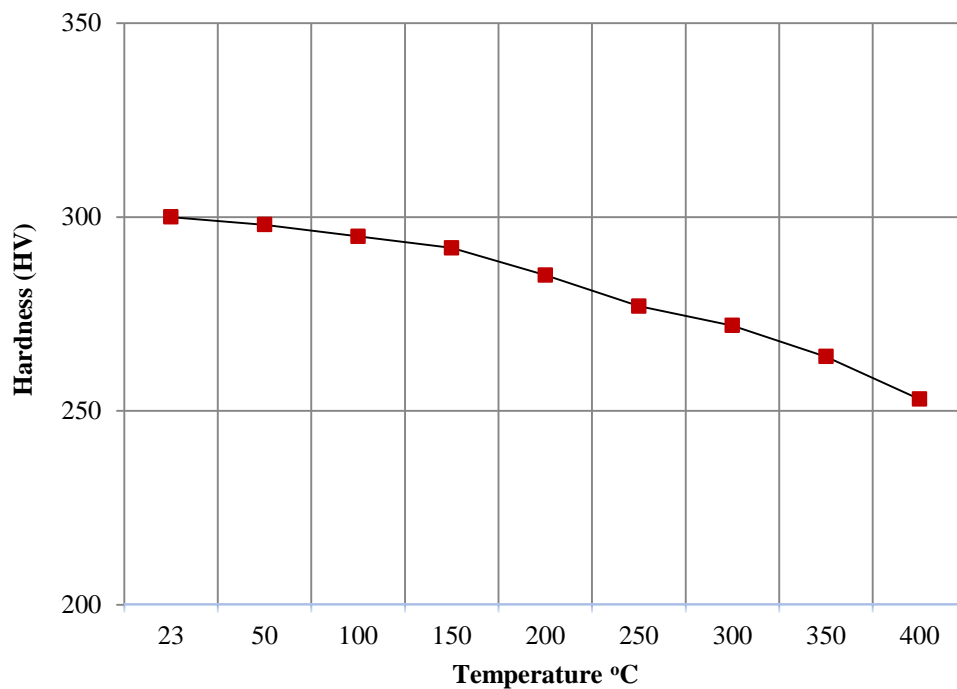
Figure 8.7 Hardness-Temperature Relationship.

8.3.2 Surface Morphology

Erosion mechanisms and morphological features of the eroded craters were analyzed by optical microscopy and profilometery.

In Figure 8.8b it can be seen that the sample eroded at 400°C predominantly exhibited craters with high depth and size than sample eroded at 200°C. It is clearly seen from the profilometer that the craters were in the range of 4 to 8 µm in depth for the sample elevated temperature to 200°C, whilst they were 5 to 15 µm in depth for the sample elevated to 400°C.
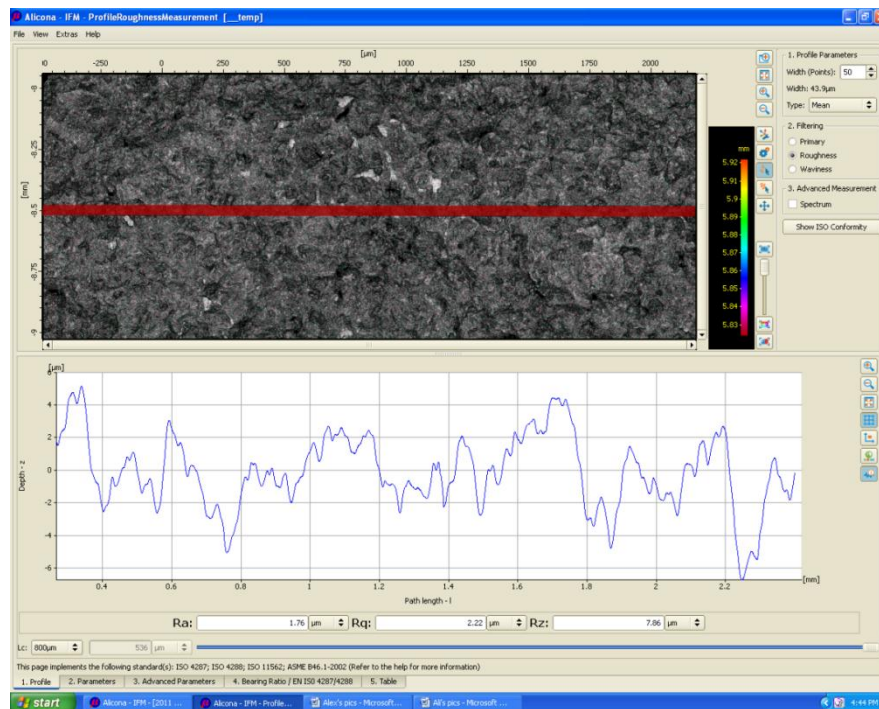
(a)
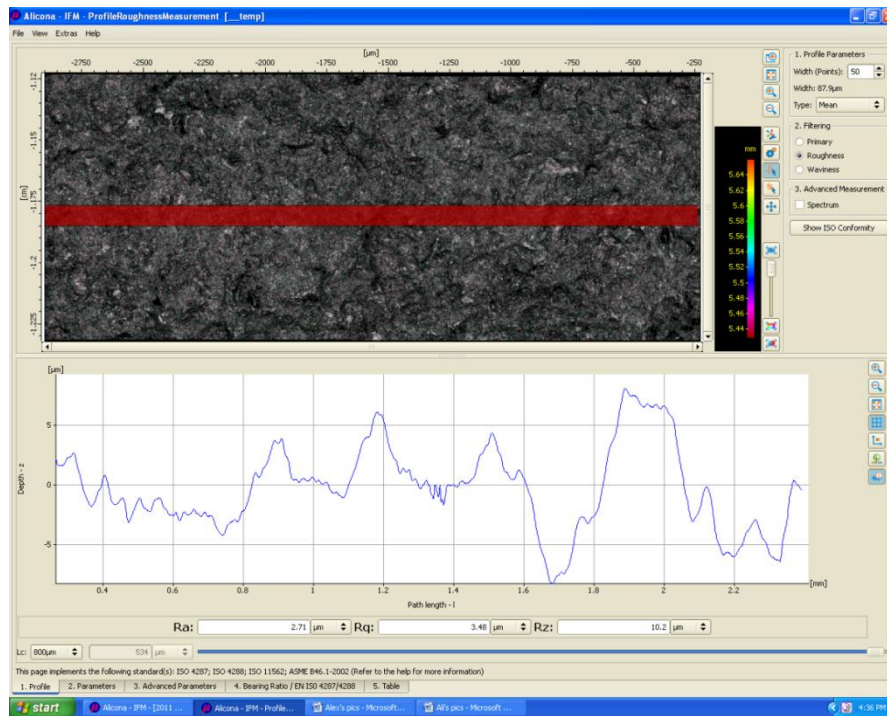
(b)

Figure 8.8 Roughness parameters at temperatures of: (a) 200 ºC, (b) 400 ºC.

The micrograph presented in Figure 8.9 shows a 3D profilometer height map when it was subjected to repeated impacts of aluminium balls at the centre section for the sample elevated temperature to 400ºC. The damage produced in the central part of the material surface showed two types of craters, ploughing and indentation craters with high lips which it meant that ploughing and deformation are the main wear mechanisms. It appears that as the test temperature increases, the size of the shallow craters and platelets that are formed increases. This relates to the increase in subsurface ductility and the decreasing hardness and effectiveness of the subsurface work-hardened zone. In addition, it was possible to observe that the indentation craters had high plastically deformed material that had risen to the sides and the forward part in relation to the impact direction of the particle.
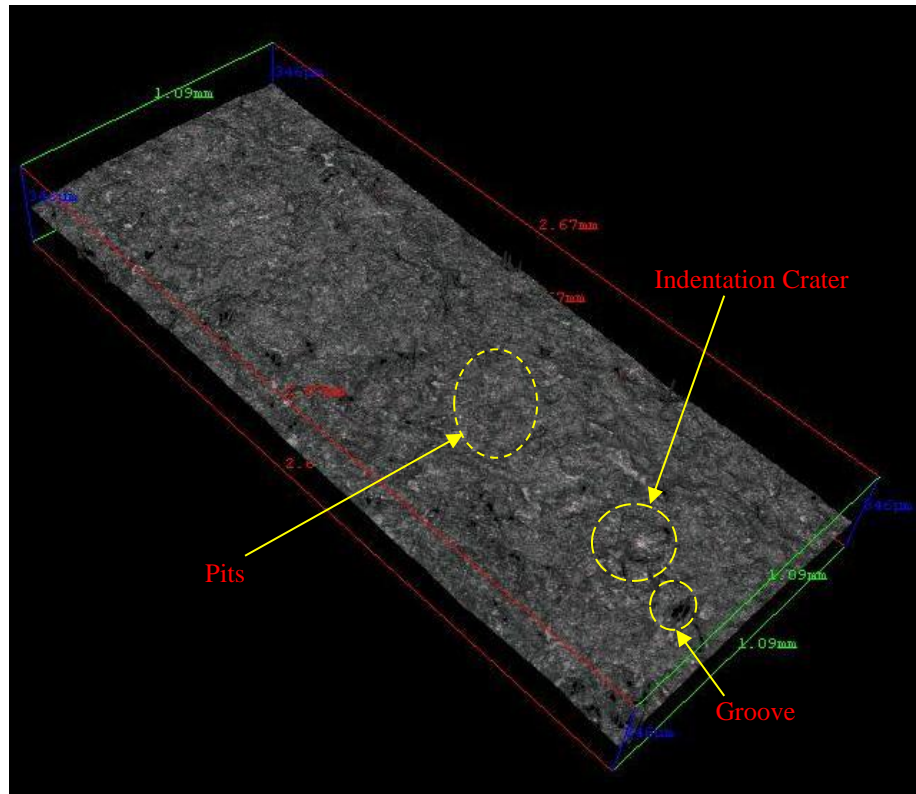
Figure 8.9 - 3D profilometer image (1.09 mm X 2.67 mm) for damage sample elevated to temperature 400°C.

Finally, the micrograph presented in Figure 8.10 shows the phenomenon of rippling which indicated that the material was softened by high temperature. The mechanism responsible for the ripple formation is related to the formation of raising lips of material at individual impact craters. Additional impacts immediately around the craters can widen and deepen them. In the next stage, the displacement and removal of material by plastic flow keeps advancing downstream until the individual peaks and valleys meet [108].

<div align="center">(a)   (b)</div>
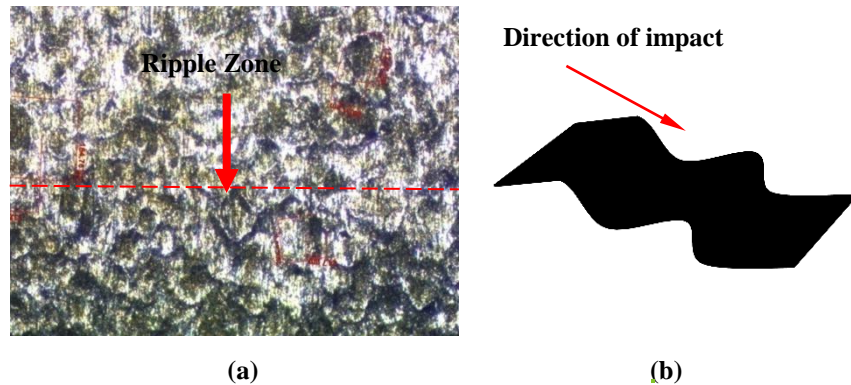
Figure 8.10 Shows the ripple phenomenon, (a) in the sample, (b) schematic ripple pattern.

8.4 Conclusions

The resistance to erosion damage in the samples was decreased when the sample temperature was elevated, although at high temperature the material was softened by high temperature, which led to cutting wear, especially at sections where sliding occurred with impact. High temperature hardness tests indicated that an increase in the erosion rate of the specimens was related to a decrease the hardness.

In addition, the erosion testing displayed an important factor to be considered when elevating the temperature of the samples was oxidation formed on the surface that could affect to the transition from ductile-to-brittle properties. Oxide formation could not protect the surface due to softening and affect material removal from the surface. Finally, micrographs displayed ripple patterns lying transverse to impact direction of the erodent for all tests which indicated that the material was softened at high temperature.

9

Nanoindentation Testing

9.1 Introduction

This chapter presents the results of tests carried out to measure the hardness and elastic modulus by indentation for an untreated surface of a cylindrical H13 steel specimen after being struck by aluminium balls at a central position and an impact velocity of 20 m/s.

9.2 Test Apparatus

The Experiments were performed using a depth-sensing indentation device (Zwick ZHU 2.5) with a Vickers indenter tip as per EN ISO 14577-1 standard, as shown in Figure 9.1. Software was used to compute the elastic modulus by using the slope of the unloading cycle.
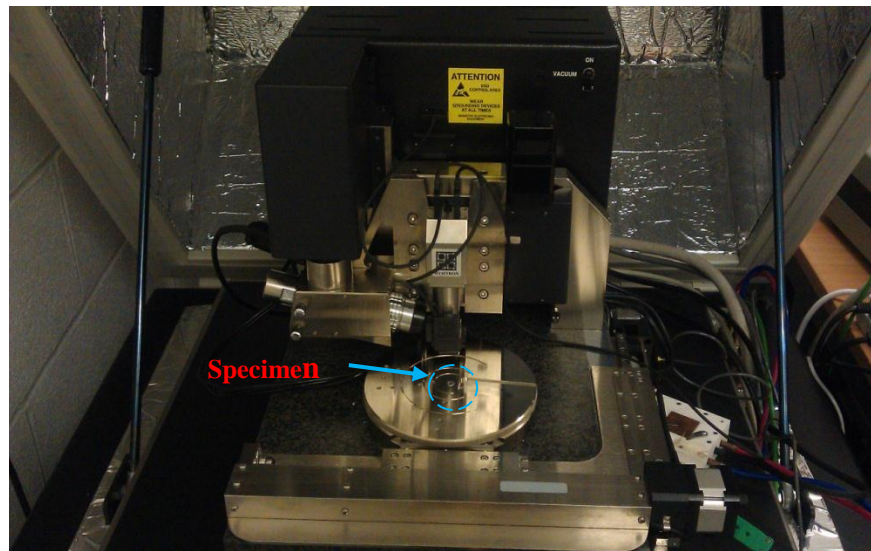
Figure 9.1 Photograph of typical apparatus.

9.3 Nano-indentation Data Analysis

There are several methods for nano-indentation data analysis to measure the hardness and elastic modulus of a material. In general, the basic principle method is to measure the hardness and elastic modulus of a material from indentation load/displacement data obtained during one cycle of loading and unloading, a schematic drawing in Figure 9.2 shows how the shape of the unloading curve provides a measure of elastic modulus [128-132].
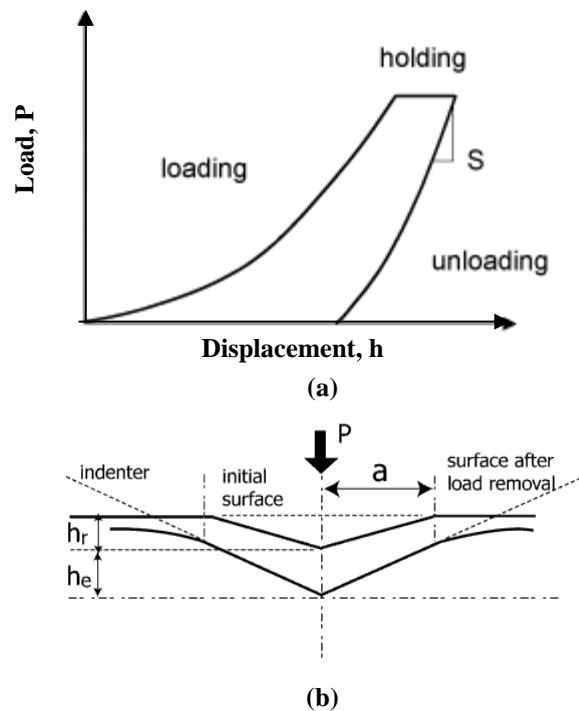
Figure 9.2 Schematic diagram for, (a) *P–h* curve, (b) hardness impression [130].

The basic principles for analysis of the nano-indentation load–displacement curves are:

- **P**: applied load

- **h**: indenter displacement

- **h_r**: plastic deformation after load removal

- **h_e**: surface displacement at the contact perimeter

As the force is applied to the indenter, the depth of penetration is measured. The area of contact at full load is determined by the depth of the impression and the known angle of the indenter.

The hardness is found by dividing the load (as observed in the data) by the projected area of the indentation.

The hardness is estimated from [128]:

$$H = \frac{P_{max}}{A}$$

9.1

where, P_{max} is the peak indentation load and A is the projected area of the hardness impression, A is the contact area.

The basic shape of a load/displacement curve depends on a combination of properties of the materials, particularly elasticity and plasticity and can reveal which type of material was used, as shown in Figure 9.3, where examples of different materials with different elastic modulus and yield stresses are illustrated.
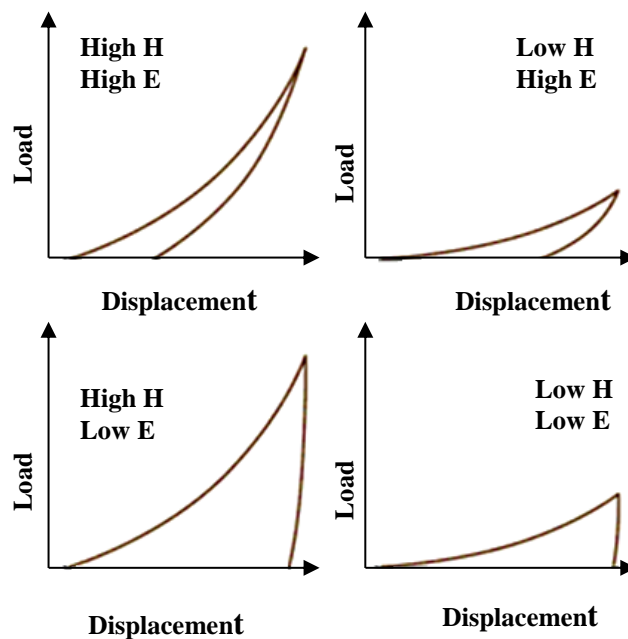
Figure 9.3 An example of load/displacement curves for idealized materials with a range of hardness and elastic properties.

The analysis method used in this to determine the hardness, H and elastic modulus, E was given by the Oliver and Pharr analytical model [128, 129]. As shown in Figure 9.4, there are three important quantities measured from the P–h curves: the maximum load P_{max}, the maximum displacement, h_{max}, and the elastic unloading stiffness, $S = dP/dh$ is the experimentally measured stiffness of the upper portion of the unloading data.
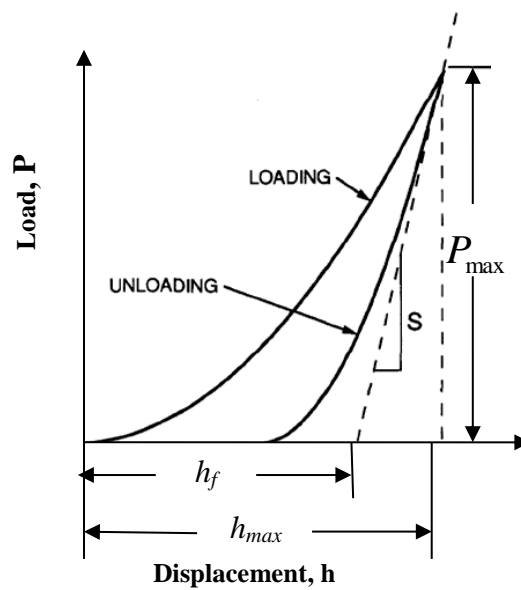
Figure 9.4 Schematic representation of load versus indenter displacement data for an indentation experiment.

9.4 Sample Preparation

The steps of preparation for the sample are briefly described as follows:

- Sectioning: Cutting is accomplished by an electric discharge Machining

- Mounting: Bakelite was used for small samples, which is a relatively hard thermosetting polymer.

- Coarse and Fine Grinding: To remove damage introduced by sectioning. Typical grit sequence used was 400, 600, 800 and 1200 mesh. Each step typically took 1-2 minutes.

- Polishing: 6 micron diamond paste and 1 micron diamond were used. After each step the specimen was placed under running water and was hand rinsed with alcohol

- Etching: Using Nital 5% (composition 5cc HNO3+95ccEthyl alcohol), immersing the sample for 20 seconds.

In Figure 9.5, it can be seen that the microstructure of the sample consists of pearlite and ferrite. The pearlite phase has a typical lamella structure consisting of sheets of cementite embedded into a matrix of ferrite. The white grains correspond to ferrite phase, while the dark grains to pearlite.
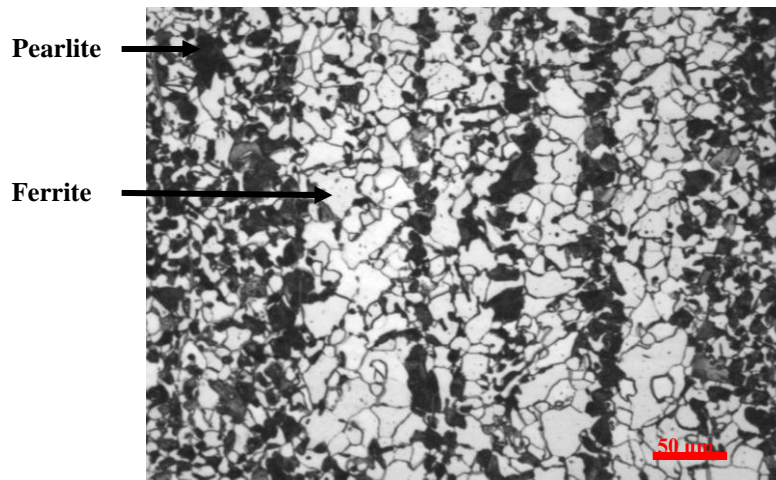
Figure 9.5 Microstructure of the H13 sample.

9.5 Test Procedures and Results

In the first set of tests, nanoindentation was performed at 50 µm beneath the wear scar surface at six positions to cover the whole area of the wear scar on the specimen. H13 steel impacted by aluminium balls at a velocity 20 m/s in a central position as shown in Figure 9.6. Sixteen indentations were made at each position. Four indentations in the X and four in the Y direction, the distance between each indent on the X and Y axis was 4µm as shown in Figure 9.7.
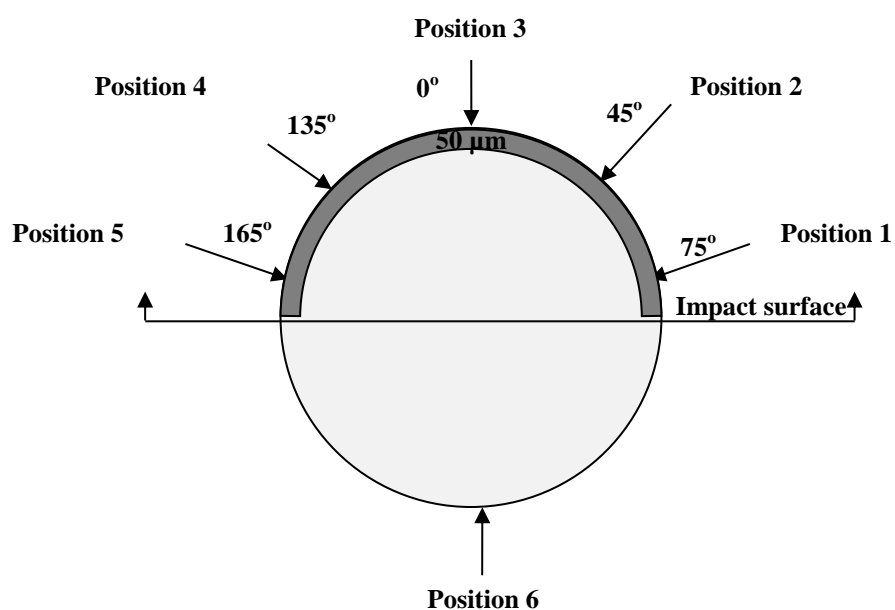
Figure 9.6 Schematic diagram for location of tests in the sample.
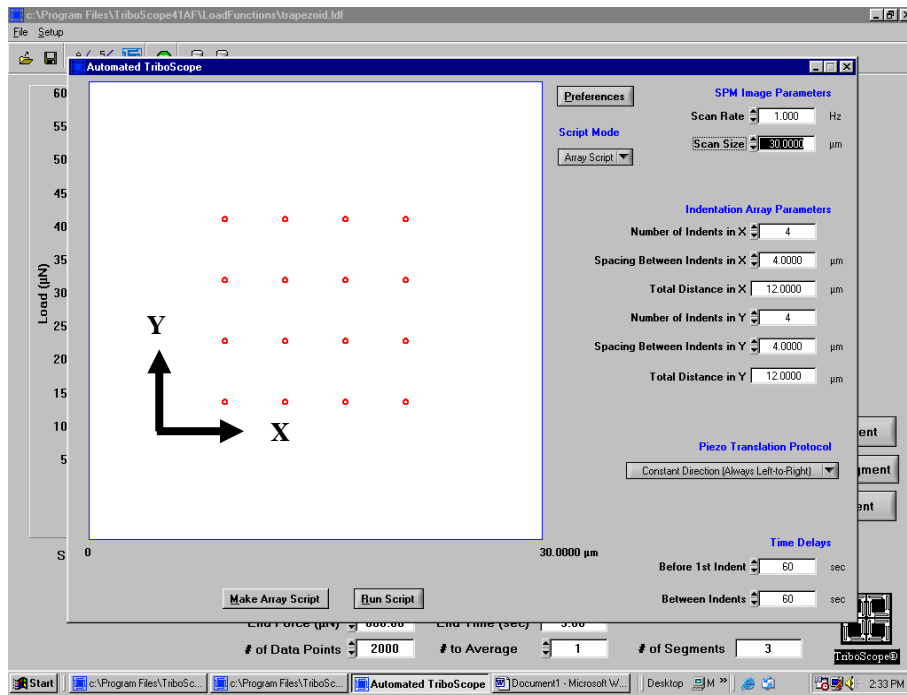
(a)
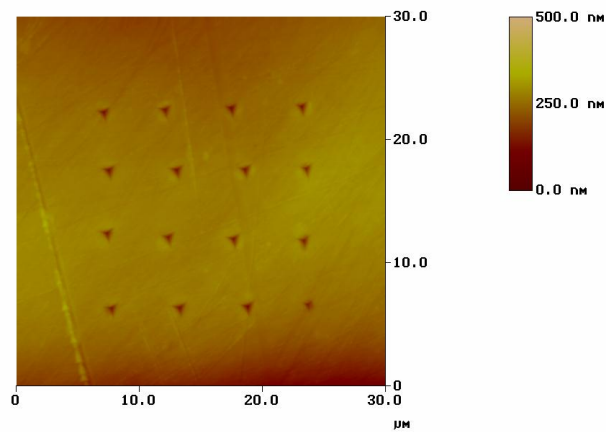
(b)

Figure 9.7 Experimental evidence for each position indents in X and Y in, (a) software, (b) indenter tip in material.

A prescribed load was applied to the indenter in contact with the specimen at positions from 1-9 (see Figure 9.6). This is only example data for one graph from the sixteen graphs for each position is shown in Figure 9.8. The depth of penetration was measured for each position at full load. The area of contact was determined by the depth of the impression and the known angle of the indenter.
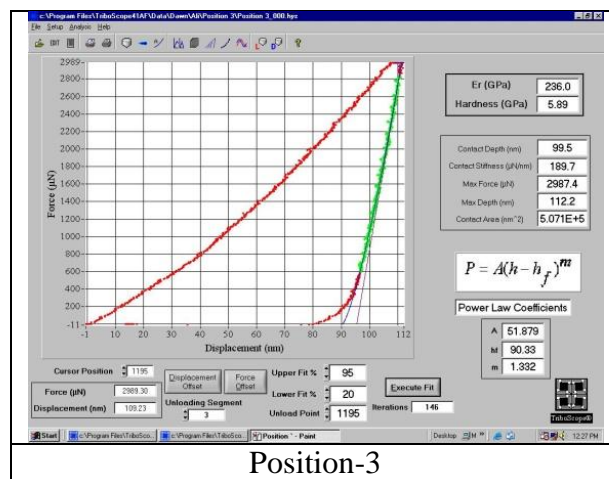
Figure 9.8 Load/displacement (*P–h*) curves for nanoindenation tests for the position 3.

In Figure 9.9, it is possible to observe all the load–displacement (*P–h*) curves obtained during nanoidentation testing at sixteen points for position 3 as an example to illustrate the typical calculations. Table 9.1 summarizes the minimum, maximum, mean value and the standard deviation of the sixteen data points on the penetration depth, explained above, h_{max} measured at each peak load P_{max}. The results obtained have different values, which indicated that these *P–h* curves were obtained by indenting at the different positions at specimen surface.
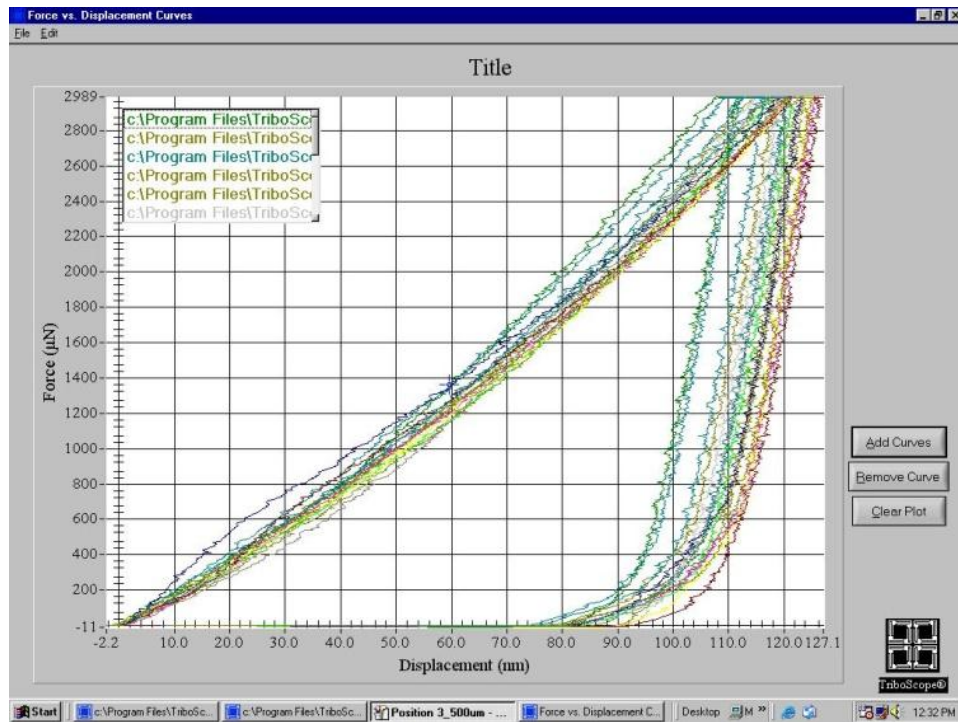
Figure 9.9 All (*P–h*) curves for position 3.

Table 9.1 Summarizes for minimum, maximum, mean value and the standard deviation data on the penetration for position 3.

Number of Data Points = 15

File	hc(nm)	Pmax(♯N)	S(♯N/nm)	A(nm^2)	hmax(nm)	heff(nm)	Er(GPa)	H(GPa)	A	hf(nm)	m	X(mm)	Y(mm)
Position 3_000.h	99.4906	2987.444	189.7038	507120.8	112.1849	111.3016	236.0234	5.890992	51.87948	90.32743	1.331865		
Position 3_001.h	106.7908	2986.277	195.6184	561094.8	118.9321	118.2402	231.3803	5.322233	50.99314	97.68684	1.346364		
Position 3_002.h	100.8932	2986.445	205.444	517302.5	112.7779	111.7956	253.0789	5.773111	41.8014	91.26164	1.412574		
Position 3_003.h	113.0033	2983.88	215.7756	608936.7	124.4659	123.3748	244.9915	4.900149	20.02928	101.0837	1.611948		
Position 3_004.h	112.8222	2985.396	242.1698	607517.3	122.7109	122.068	275.2805	4.914092	8.052921	98.8729	1.881541		
Position 3_005.h	108.7058	2985.206	216.211	575654.2	119.8618	119.061	252.4827	5.185763	16.7878	96.20273	1.655563		
Position 3_006.h	110.87	2984.911	213.3914	592309.9	122.1064	121.3609	245.6616	5.039441	36.15986	100.9069	1.462263		
Position 3_007.h	105.8424	2985.293	216.556	553945.6	117.0723	116.1814	257.7932	5.389144	26.66847	94.90893	1.543125		
Position 3_008.h	115.1289	2983.785	221.3314	625710	126.1855	125.2397	247.9084	4.768638	22.70342	103.7881	1.591242		
Position 3_009.h	114.9213	2984.324	228.4855	624062.5	125.6571	124.7173	256.2592	4.782092	37.22123	105.3834	1.480236		
Position 3_010.h	109.9747	2986.727	209.8673	585394	121.6087	120.6483	243.0275	5.10208	28.39274	99.07562	1.515842		
Position 3_011.h	113.5912	2984.149	248.6384	613555.6	123.6248	122.5927	281.2394	4.863698	0.409642	91.52814	2.588291		
Position 3_013.h	116.7181	2984.51	238.3512	638385	127.1064	126.1093	264.3083	4.675093	5.663437	101.5839	1.958666		
Position 3_014.h	109.5898	2984.72	212.2011	582432.3	120.7911	120.139	246.3541	5.124579	42.93512	100.2028	1.417382		
Position 3_015.h	115.3171	2984.101	236.4001	627204.4	125.9149	124.7844	264.4709	4.757781	3.359203	98.55162	2.078155		
AVERAGE							**253.4**	**5.1**					
MEAN							**252.5**	**5.0**					
STD DEV							**13.7**	**0.4**					

162

The hardness *(H)* and Young's modulus (*E*) were calculated using the method developed by Oliver and Pharr [128, 129]. The nanoindentation data for the first case is presented in Table 9.2.

Table 9.2 Average nanoindentation data for *E* and *H*.

Position	*E* (GPa)	*H* (GPa)
1	220.6	4.2
2	233.8	4.3
3	253.4	5.1
4	212.5	4.3
5	206.9	3.6
6	183.3	3.4

A second set of tests was carried out using two lines of indentations at position 3, moving deeper towards the centre of the sample. Measurements were performed at thirty one positions inside the bulk of the sample, a distance 6 μm was taken between each position, as shown in the schematic drawing in Figure 9.10. The test conditions and calculations were exactly similar to the first set of tests except that only one indentation was performed at each position.

Position 3

6 μm

Impact area
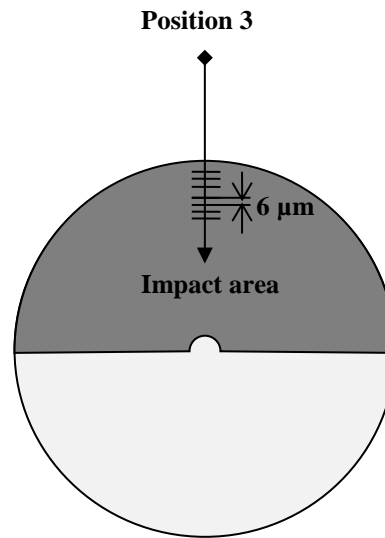
Figure 9.10 Schematic diagram for location of tests in the sample.

9.5.1 Analysis of the Loading Curves

The nanoindentation test has been established as an important tool for the mechanical characterization of materials on the submicron scale. Such a test is usually conducted using instrumented machines with which an indenter load, *P*, and indenter displacement, *h*, can be continuously and simultaneously recorded during indenter loading and unloading.

The unloading data are then analysed to yield the hardness, *H*, and the Young's modulus, *E*. The measurements of hardness and elastic modulus by instrumented indentation techniques has widely been adopted and used in the characterization of the mechanical behaviour of materials at small scales. Mechanical properties can be determined directly from indentation load and displacement measurements without the need to image the hardness impression [133-135]. The differences in the measured *P–h* curve for the differences positions may be attributed to differences between the local microstructural features in the vicinity of each indentation position.

In other words, the experimental facts shown in Table 9.1 seem to indicate that the measured *P–h* curve may depend strongly on the local microstructural features and, as a result, the mechanical properties deduced from the analysis of the *P–h* curve are only the more local, rather than the bulk, properties of the test material. However, during unloading the effect of microstructural inhomogeneity of the load–displacement curve may also be examined, from the quantitative analyses of the unloading data on the position 3. It was possible to observe that the unloading behaviour also may be attributed to differences between the local microstructural features in the vicinity of each indentation position. In the most commonly employed Oliver–Pharr method for analysing the nanoindentation data, an empirical power law is selected to describe the unloading data [128, 129].

$$P = \alpha(h - h_f)^m \qquad\qquad 9.2$$

where *α* and *m* are empirically determined fitting parameters and h_f is the final displacement after complete unloading and also determined by curve fitting. It should be pointed out that a basic assumption for using Eq. (9.2) to describe the nanoindentation unloading behaviour is that the unloading is pure elastic, i.e. The unloading curve and the corresponding reloading curve should overlap with each other. The hardness and Young's modulus data from tests for the six positions is plotted in Figure 9.11. As described above the positions were measured at 50 μ m beneath the surface of the specimen. Clearly, it can be seen the values of hardness and modulus elasticity were increased at position 3 and recorded to 5.1 GPa for hardness, *H*, and 253.4 GPa for elastic modulus, *E*, compared to the base material hardness, *H*, of 3.3 GPa and modulus elasticity, *E*, of 183.3 GPa respectively, at the position 6. At this position significant work has clearly occurred.
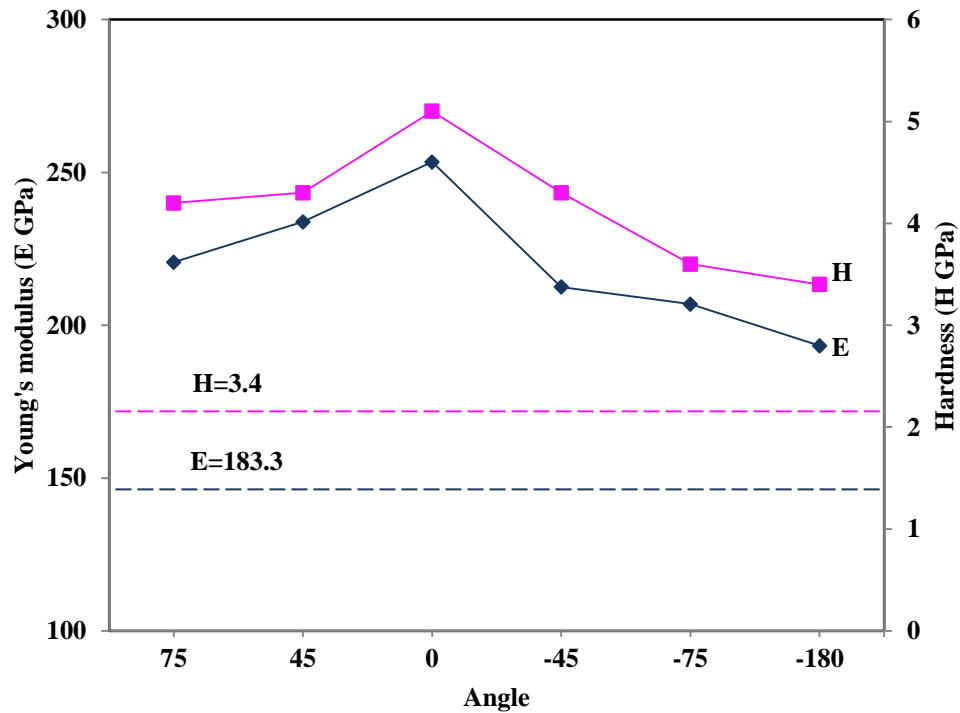
Figure 9.11 Position against Young's modulus and hardness.

9.5.2 Variation Property with depth

Figure 9.12 shows the data from a nanodentation tests carried out deeper towards the bulk centre of the sample. Two lines of indentations towards the centre of the sample were carried out. The hardness measurements reveal different hardening distribution in different scales. That is to say, not only the metallic matrix is hardened by the impact behaviour, but also the particles are re-distributed and broken and residual stresses build up between them. In addition, the results show that the values of hardness got lower below the 50 μm depth used in the first set of measurements. The graph in Figure 9.12a shows that work hardening occurred till a depth of 50 μm in the material due to cold deformation that caused dislocation movements in the crystal texture.

(a)

(b)
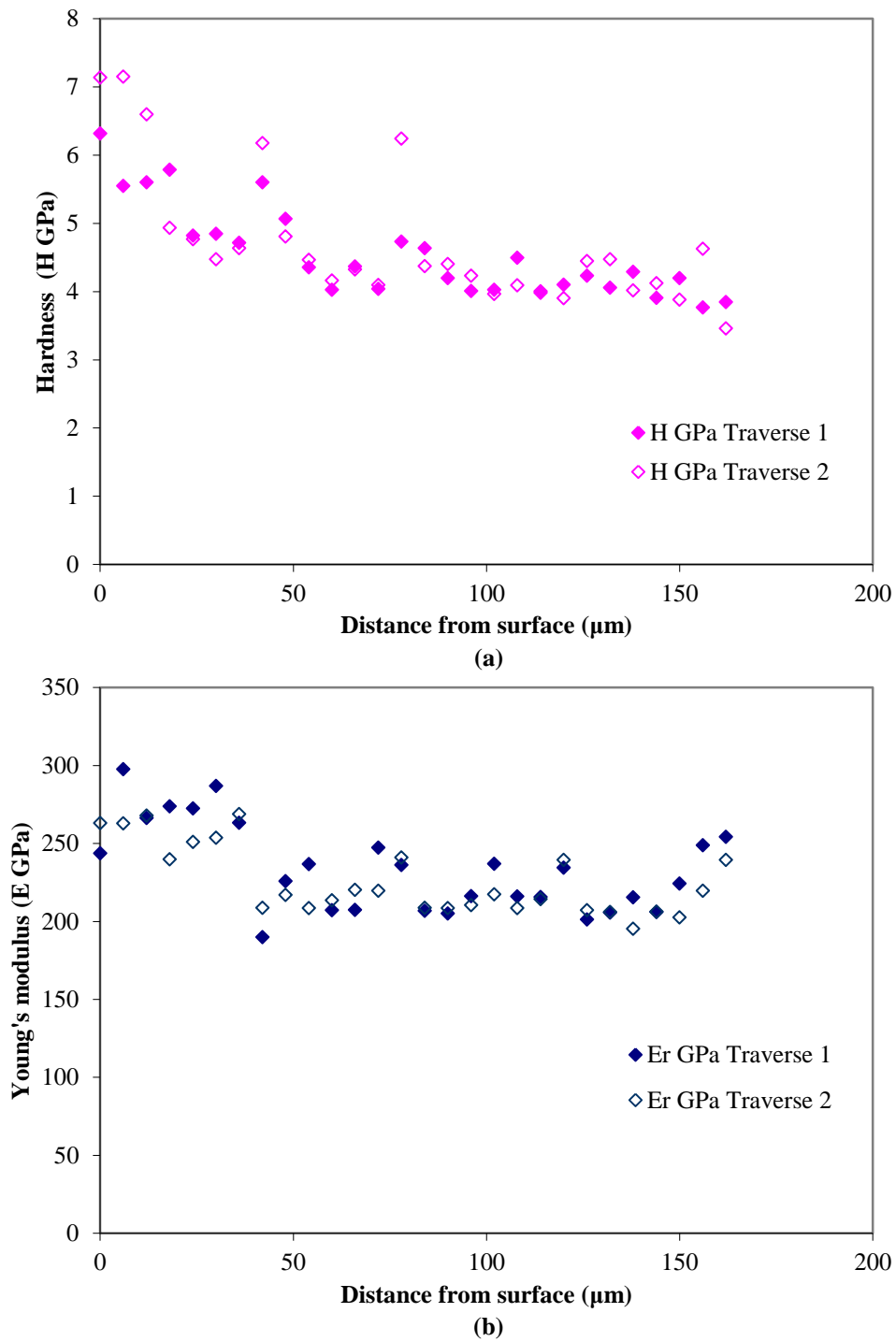
Figure 9.12 Distance from surface against, (a) hardness, (b) Young's modulus.

9.6 Conclusions

Nano-hardness testing was carried out using two ways, 50 μm beneath the damage surface and deeper inside the bulk material. The results showed that work hardening uses more significant at the central points where most particles impacted and that H and E were affected to a depth of 50 μm (see the steady state wear rate at curves in Chapter 7).

10

Erosion Testing on Surface Treatments

10.1 Introduction

This chapter outlines erosion tests on heat treated and then coated cylindrical H13 steel samples. Commonly used coatings to protect tools in die casting were used. A heat treatment and then surface coating can have a large effect on erosion damage. Samples have been tested to evaluate their resistances to erosive wear and to assess how this compares with behaviour seen for untreated material in Chapter 7. Eight commercial coatings have been evaluated for their wear resistance and roughness. The objective was to permit an optimized selection of coatings to be used to give good resistance to erosive wear. In the experiments, only one particle velocity was used to impact the samples at a central position since it was considered enough to study the erosion damage in this case.

10.2 Experimental Details

10.2.1 Specimens

H13 steel samples were heat treated before the surface was coated to increase the hardness of samples from (300 to 550 H_{V20}). Samples were subjected to successive impacts of aluminium balls to total shots (14400) for every test to find out the performance with solid particle erosion of these surface treatments. The sample was removed every (2400) shots to measure the mass loss. The dimensions of the cylindrical samples were 10 mm in diameter and 70 mm in length. The samples were mounted in the centric position where aluminium balls are intensively impacted onto the central zone of the samples. Impact velocity 20 m/s was employed for all tests. Tables 10.1 and 10.2 show the details of coating materials and coating processes.

Table 10.1 Properties of coating materials supplied by *TTI Group Ltd in the UK*.

Coating material (PVD)	Micro-hardness HV0.05	Max. Working temperature
Titanium Nitride (TiN)	2300 ± 200	600 ^{o} C 1100 ^{o} F
Titanium Aluminum Carbo-Nitride (TiAlCN)	3500 ± 500	800 ^{o} C 1470 ^{o} F
Chromium Nitride (CrN)	1800	700 ^{o} C 1300 ^{o} F

Table 10.2 Coating processes supplied by *TTI Group Ltd in the UK.*

Coating material	Coating process
Titanium Nitride (TiN)	Physical Vapor Deposition (PVD) Plasma Nitrided + Titanium Nitride (PN + TiN) Plasma Nitrided + post polish + Titanium nitride (PN + Polish + TiN) Duplex Titanium Nitride (TiN X 2)
Titanium Aluminum Carbo-Nitride (TiAlCN)	Physical Vapor Deposition (PVD) Plasma Nitrided + Titanium Aluminum Carbo-Nitride (PN + TiAlCN)
Chromium Nitride (CrN)	Physical Vapor Deposition (PVD). Plasma Nitrided + Chromium Nitride (PN + CrN)

Erosion tests were carried out on H13 steel samples have been hardened and tempered. Hardening was done at 1020°C and tempered twice at 540°C to give hardness 500-550 H_v. The controlled processes of heating and cooling leads to change the microstructure of the material, thus improving its mechanical properties.

An industrial collaboration was established to obtain the sample coatings. The industrial participation was in terms of providing, sample coatings, heat treatment services etc. An important objective for candidate coatings that were used in the testing phase of the program was that these coatings had excellent wear resistance, adequate adhesion to the surface material, good mechanical properties (hardness, ductility, fatigue strength, shear strength and ultimate tensile strength), corrosion and oxidation resistance. In addition:

- Application of coating is easy and lower cost.

- The coatings and dies are easier to repair.

10.2.2 Test Method

Tests were carried out in line with the approach described in chapter 7 for cylindrical specimens aligned central to the flow of aluminium balls. Table 10.3 presents the experimental conditions used in the tests.

Table 10.3 Erosion testing conditions.

Testing Conditions	
Specimen (H13 steel)	Cylinder 10 mm in diameter and 70 mm in length Roughness: 0.1-0.2 μm (R_a) Hardness: 550 H_{V20}
Erodent particle (Aluminum ball)	Type: 6061 Aluminum alloys Basic diameter: 3 mm Weight : 0.04 g
Air pressure (psi)	80
Impact location	Central
Abrasive pulse flow rate (g/shot)	55
Particle velocity (m/s)	20
Testing cycle exposure	Mass loss measured every 2400 shots until 14400 shots
Nozzle to specimen distance (mm)	30

10.3 Coating Technology Processes

10.3.1 PVD Coating Process

The Physical Vapor Deposition (PVD) process shown in Figure 10.1 is a method of single or multi-layer coating application used to describe a wide range of coating techniques whose coating is carried out under vacuum. It can be used to deposit Carbides, Nitrides, Oxides and Carbonitrides. There are two fundamental PVD processes, namely evaporation and sputtering and these processes may be assisted by the action of a glow discharge or plasma, in which case the process is referred to as Plasma Assisted Physical Vapor Deposition (PAPVD) [136, 137].
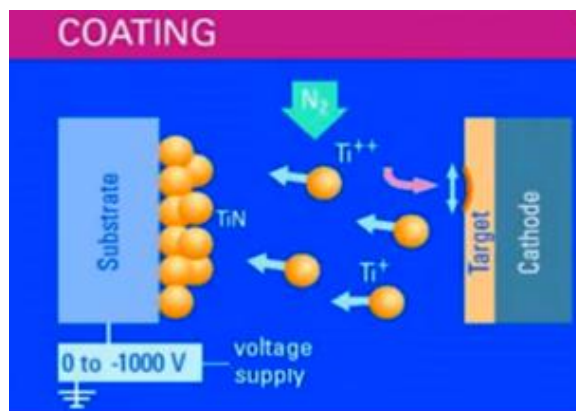
Figure 10.1 Physical Vapor Deposition (PVD) process [136].

10.3.2 Plasma nitriding

Plasma nitriding is a process of fast nitrogen diffusion into a metal surface for formation of hard nitrides. The efficiency of plasma nitriding does not depend on the temperature, usually the range of temperature to achieve the plasma nitriding is from 260 °C to more than 600 °C [138].

10.4 Results

Figure 10.2 shows the examination of erosive scars on the hardened and tempered specimen. The wear damage produced was characterized by pits and around craters with large angles of impact, whilst at low impact angles, grooves and scratches were present due to the ploughing and cutting action, which were carried out by the particles that sliding along the surface after impact, although they could have been caused by particles that impacted the surface with different orientations making it easier for them to slide on the surface. However, the hardened and tempered sample had the capability to enhance wear resistance of H13 steel compared with untreated samples, (previously shown in Chapter 7). Since the craters that were presented on the worn surface were smaller. Table 10.3 presents the data of damage erosion on the untreated sample and heat treated sample were impacted at the central zone with an impact velocity 20m/s.

Table 10.3 Size of craters.

Size of craters (μ m)	Untreated sample	Heat treated sample
Smaller elliptical crater diagonals	55, 112	28, 43
Larger elliptical crater diagonals	78, 168	34, 61
Round crater diameter	55-99	20-40

Unworn Surface

Central zone (High impact angles)	Side zone (Low impact angles)
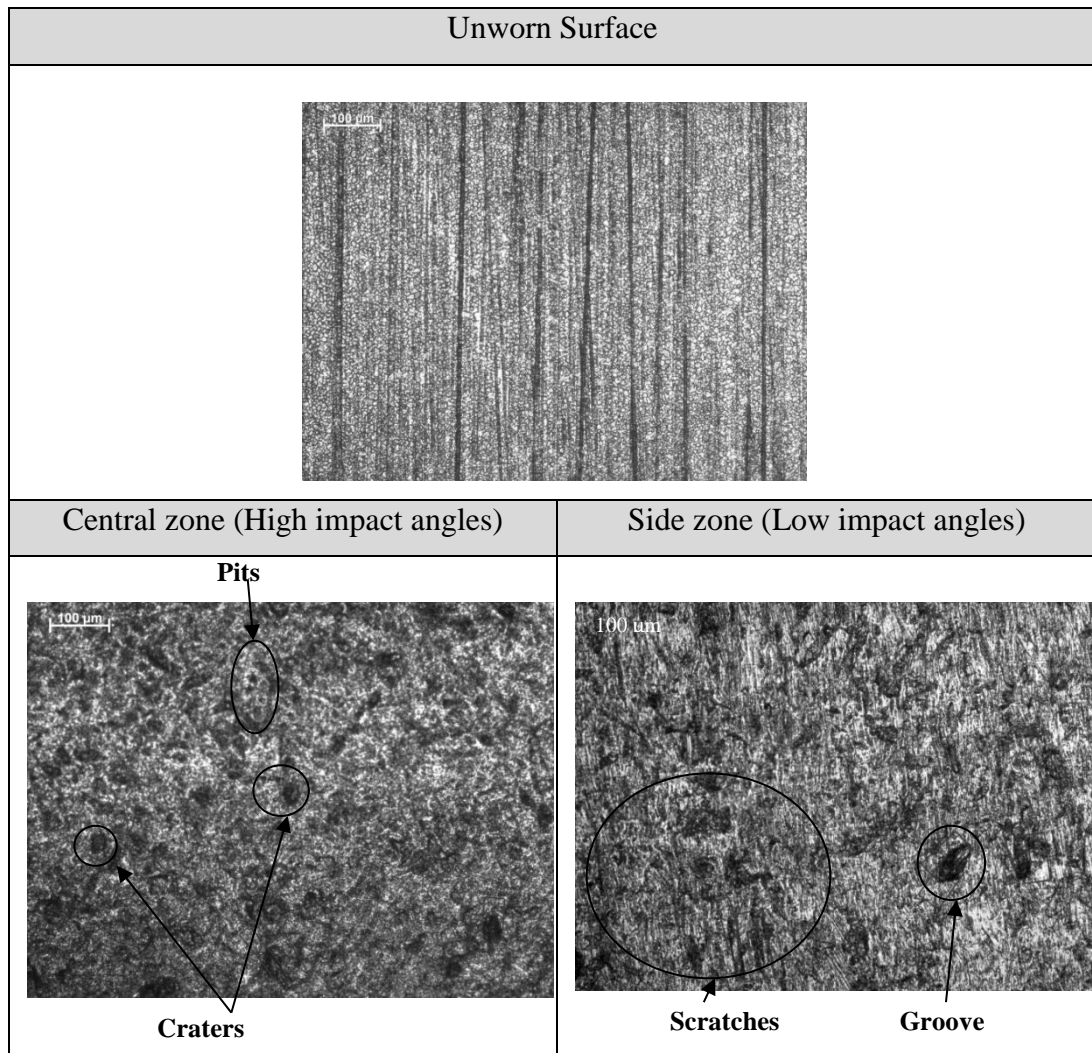
Figure 10.2 Erosion damage on hardened and tempered sample.

10.5 Wear Scars in TiN Coated Samples

Figure 10.3 shows the damage inflicted on cylindrical H13 steel samples coated with TiN using different methods. The wear scar for the high erosion resistance samples (with Plasma Nitriding) was not visible at this scale. Samples coated without Plasma Nitriding showed lower resistance to erosion wear. It is clearly seen the erosive wear has caused an elliptical scar to form (as seen in previous testing, see Chapter 7).
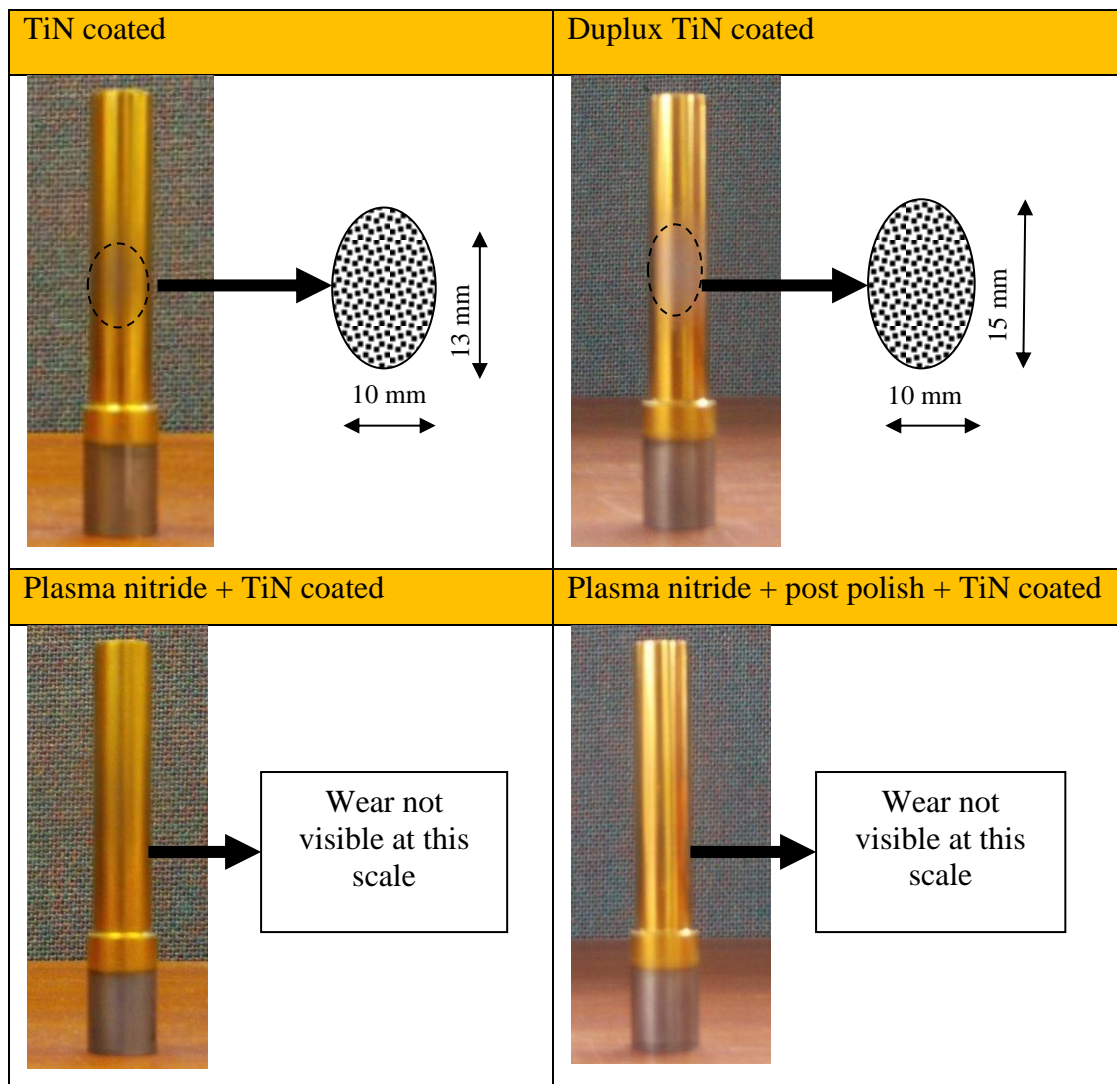
Figure 10.3 Wear scars on (TiN) coated samples.

10.6 Micrographs of Eroded Surfaces

10.6.1 (TiN) Coating

The surface images obtained for TiN specimens are shown in Figure 10.4. The damage produced was dependent on the impact angle, at a normal impact angle the coating removal is higher than at low impact angles. It might be noted that at low impact angles the removal of coating material resulted more in scratches, grooves and elliptical craters at the eroded surface due to the micro-cutting. However, in view of the results obtained by examination of eroded coating surface at high impact angles can be deduced that the erosion processes combined form, indentation of particles, cutting action and microcracks which consisted of several stages. The first is based on the fact that some of the impinging particles will cause local microcracks in the coating material. Secondly, progression and intersection of microcracks resulting in formation of fragments of coatings. Thirdly, multiple particle impacts on the surface will result in detachment of these fragments from the substrate. Finally, in result severe of coating fragmentation and removal of coating from local eroded areas.

Further, removal of coating layer caused the damage transmitted to the origin sample surface which meant evidence for deep craters and grooves as seen in erosion cylindrical surface in Chapter 7. At this stage higher in coating removal due to formed of indentation craters led to a pile up material around the crater and caused vertical cracks in the coating layer resulting in severe coating fragmentation and removal. It is clearly seen in the next section, where SEM images are shown for cross section through the coating layer.

Unworn surface

Central zone (High impact angles)	Side zone (Low impact angles)
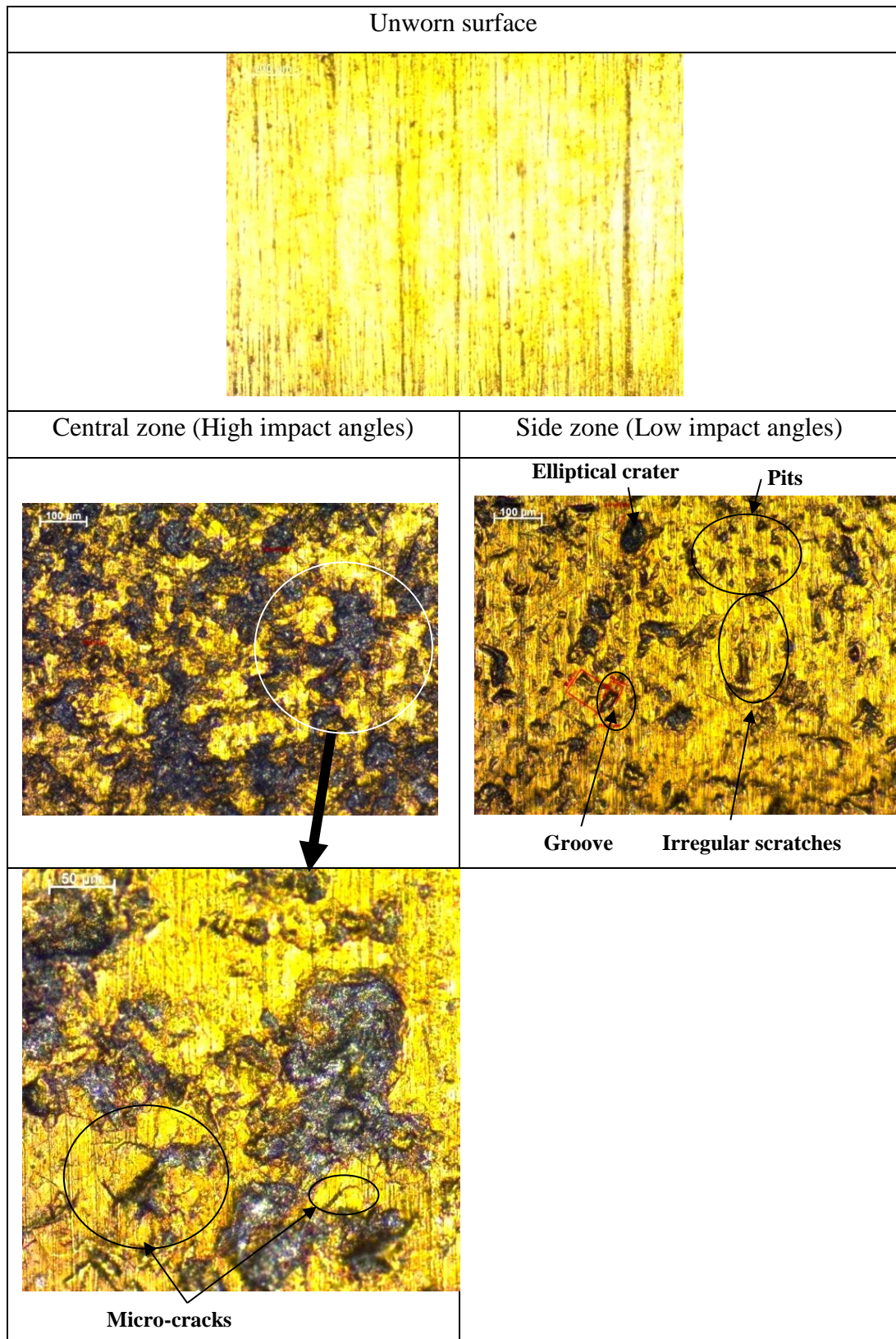
Figure 10.4 Erosion damage on Titanium Nitride (TiN).

10.6.2 Duplex (TiN X 2) Coating

In Figure 10.5, it is possible to observe similar damage in the duplex TiN coating in all regions to the TiN coated sample due to severe deformation and plastic straining of the surface material. Multiple particle impacts on the surface will result in high compressive and shear stress caused by the normal indentation of the aluminium balls on the surface, that local microcracks were formed, propagated and intersected each other causing the formation of local coating fragments which the fragment removed from the eroded surface depended on the quality of the adhesion between the coatings and the substrate.

For the Duplex coating if the adhesion between layers is not sufficient, the initial failure will cause delamination of the top layer of TiN. This is evident in Figure 10.4. Damage appears greater in the central zone again with large numbers of craters formed in the side zone caused more original surface is visible.

Unworn surface	**Detachment first coating layer**
Centric zone(High impact angles)	Side zone(Low impact angles)
Detachment fragments coating **Crater**	 **Irregular indentations**
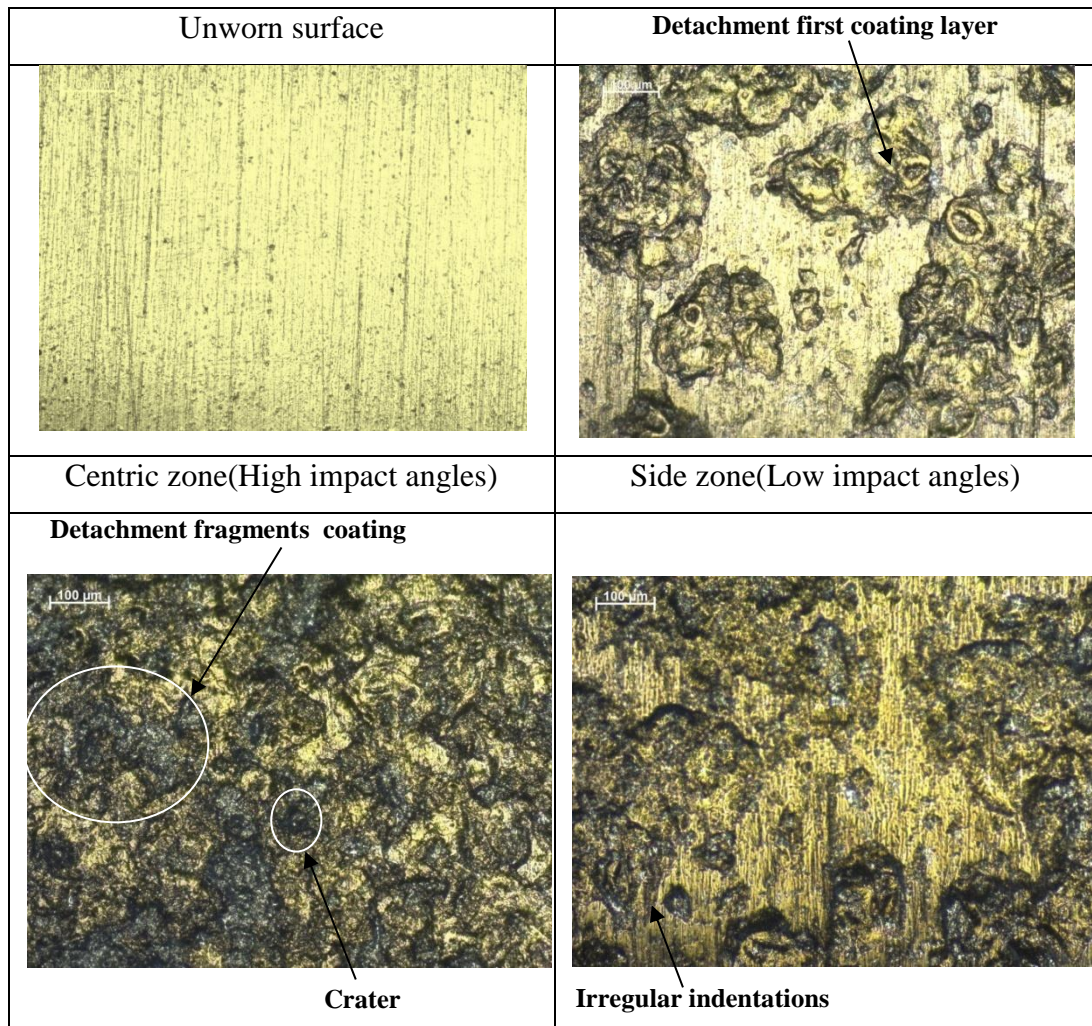
Figure 10.5 Erosion damage on duplex Titanium Nitride (TiNX2).

10.6.3 (PN + TiN) Coating

The micrographs in Figure 10.6 show the damage caused when a Plasma nitrided + Titanium Nitride (PN+ TiN) coating was used. The wear scar obtained after impact is not clear due to the high wear resistance and low mass loss. The sample only suffered slight damage. The wear damage produced was characterised by very small of pits and indentations craters probably caused by fatiging of the coating layer close to surface especially at grain boundaries. Continuous impacting of coating materials causes weakened grains to be plucked from the surface as a chip. Impinging particles also act as single pass cutting edges; each impact removing very small amount of coating material. The cutting action in the low impact angle areas also caused a few grooves and scratches to occur on the surface.

Unworn surface

Central zone (High impact angles)	Side zone (Low impact angles)
Indentation craters	**Groove** **Pits**
	Scratches
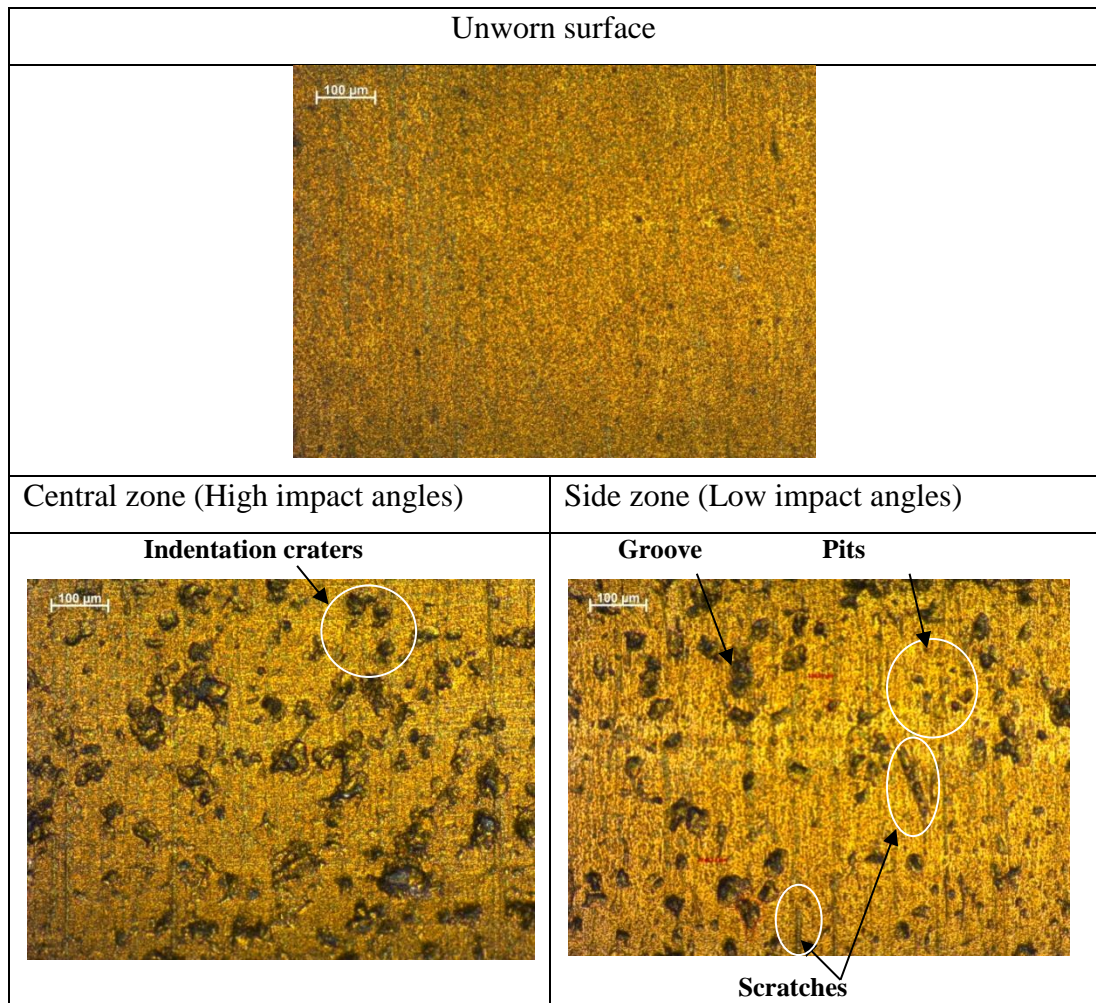
Figure 10.6 Erosion damage on Titanium Nitride with Plasma Nitride (PN + TiN).

10.6.4 (PN + Polish + TiN) Coating

In Figure 10.7, it is possible to observe similar damage for PN + Polish + TiN in all regions with the surface damage for the (PN + TiN) coated sample. The material removal was observed to occur as a combination of fatiguing and cutting action leading to small chunks of material being removed. The PN has given much better hardness to the TiN has led to less deformation and less coating delamination and hence less wear.

Unworn surface	
Central zone (High impact angles)	Side zone (Low impact angles)
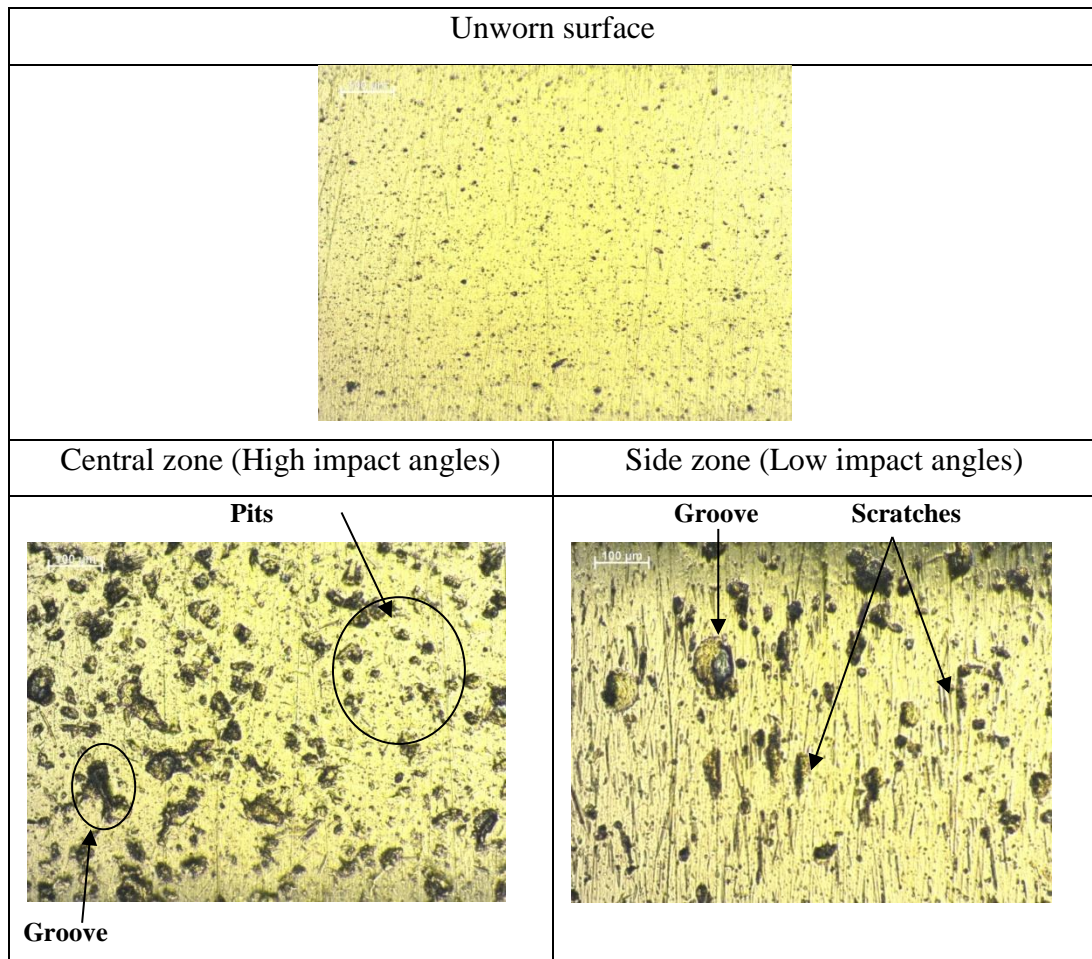
Figure 10.7 Erosion damage on (PN + post polish + TiN).

10.6.5 SEM Images

A final examination was carried out of the eroded coated surface using SEM for the TiN coated sample as it had higher surface damage compared with the other coated samples. The fragments dispatched from the surface are clearly seen in Figure 10.8. The lower erosion resistance is clearly caused by the poor adhesion of the coating layer with the substrate.

In addition, it was possible to observe that the increase of the erosion damage is related to plastic deformation. The damage area had deep craters due to the impact and indentation of the aluminium balls on the surface material. These craters are similar to those obtained in tests for untreated materials. It is assumed that the fragmentation of the coating material played an important role in the damage observed in all impact angles.
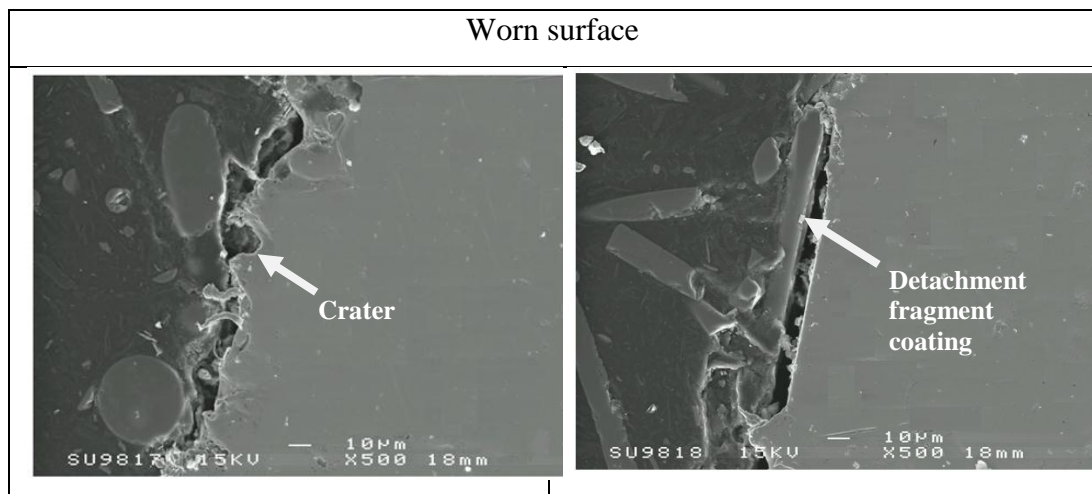
Figure 10.8 Damage of Titanium Nitride (TiN) coated.

Optical microscopy and SEM analysis showed that TiN coated was completely worn after 14400 shots compared with Plasma Nitride treatment that showed very light surface damage. Depth and distribution of damage for coating layer indicated that among other things, the efficiency of a PVD hard coating depends on the adhesion to the substrate and indirectly on the properties of the substrate-coating interfacial region. The dominant coating failure mechanisms indicated that the impact leads to a maximum stress, higher than the coating endurance stress limit, fracture occurs in the coating layer, and material is removed. The well-adhered coating withstands the impact much better and has lowered a removal propagation rate, compared to the poorly-adhered.

10.7 Wear Scar in TiAlCN Coated Samples

The results obtained when TiAlCN coated and PN+ TiAlCN coated were used are shown in Figure 10.9. It is possible to observe that the TiAlCN coating presented more damage with chunks of coating materials being removed from the surface, than that with the PN+ TiAlCN coating. The TiAlCN coating displayed an elliptical area scar, with PN added the damage was not visible at this scale.

TiAlCN coated	PN+ TiAlCN coated
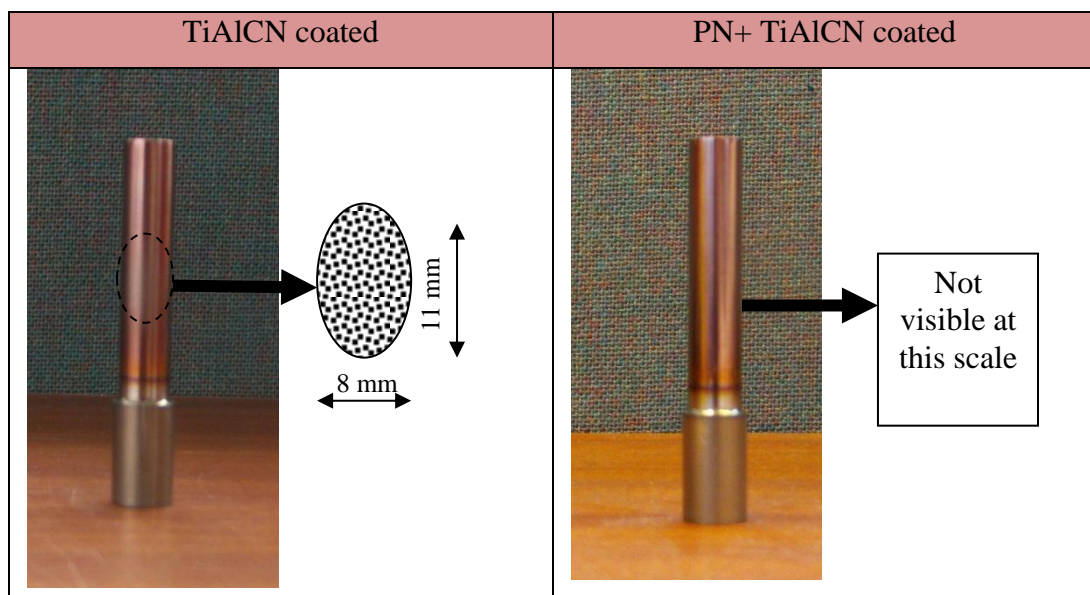
Figure 10.9 Wear scars on (TiAlCN) coated samples.

10.8 Micrographs of Eroded surfaces

10.8.1 (TiAlCN) coating

The wear damage on the TiAlCN coated sample surface is shown in Figure 10.10. Coating removal was observed to occur in combination with indentation and cutting action leading to small chunks of material being removed. The size of the damage area might increase due to continual impingement of particles that might lead to single pass cutting of previous crater and pits edges, hence the sizes of craters and pits will increase.

Unworn surface	
Centric zone (High impact angles)	Side zone (Low impact angles)
Craters and pits **Detachment fragments coating**	**Groove** **Indentation**
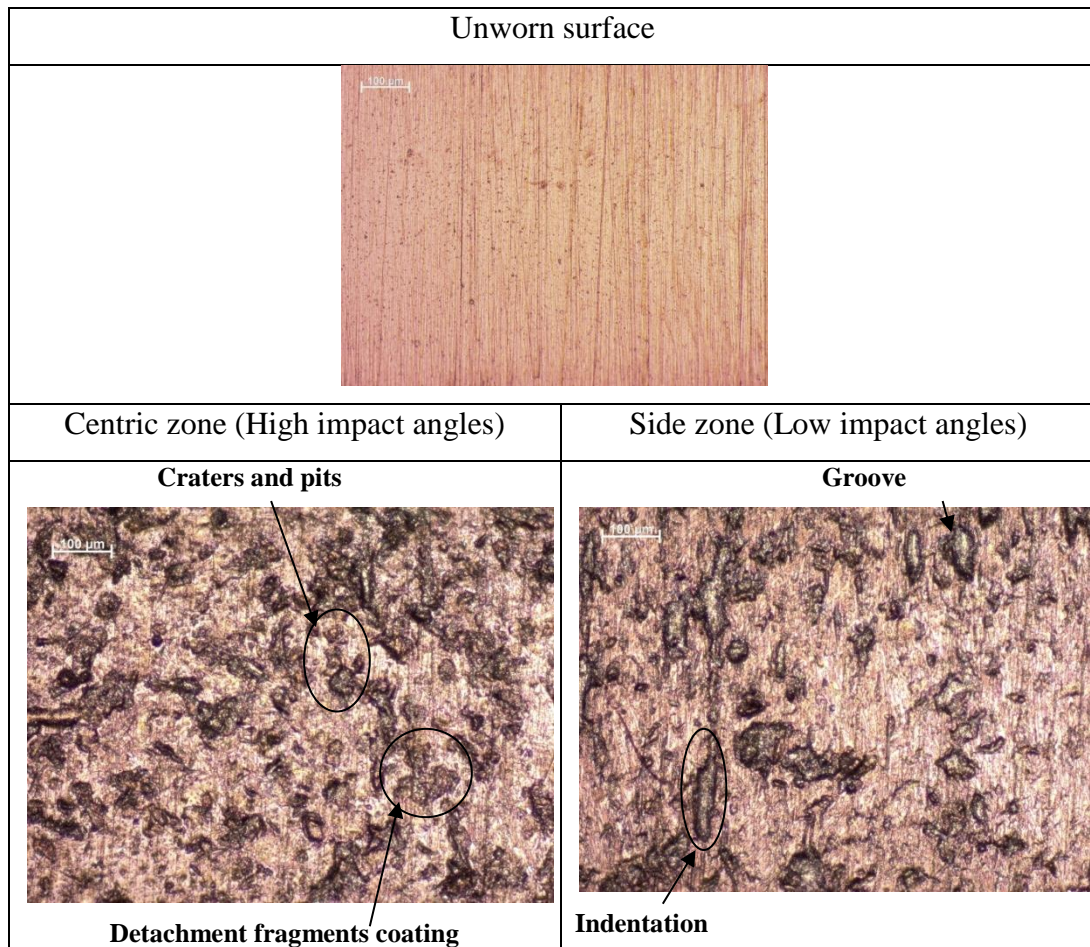
Figure 10.10 Erosion damage on (TiAlCN).

10.8.2 (PN + TiAlCN) coating

In Figure 10.11, it is possible to observe similar damage for PN + TiAlCN in all regions with the surface damage for (PN + TiN) coated sample**.** The material removal was also dependent on the impact angles as explained previously. Fatiguing and cutting action leading to small chunks of material being removed at the high impact angles zone. The damage was much lower than the previous case with no PN. In addition, it is clearly seen from the enlarged image for the damaged area that microcracks propagated at the edges of the grooves or craters. Continuous impacts cause chunks plucked out. This process could be increasing the area damaged and coating layer to be removal.
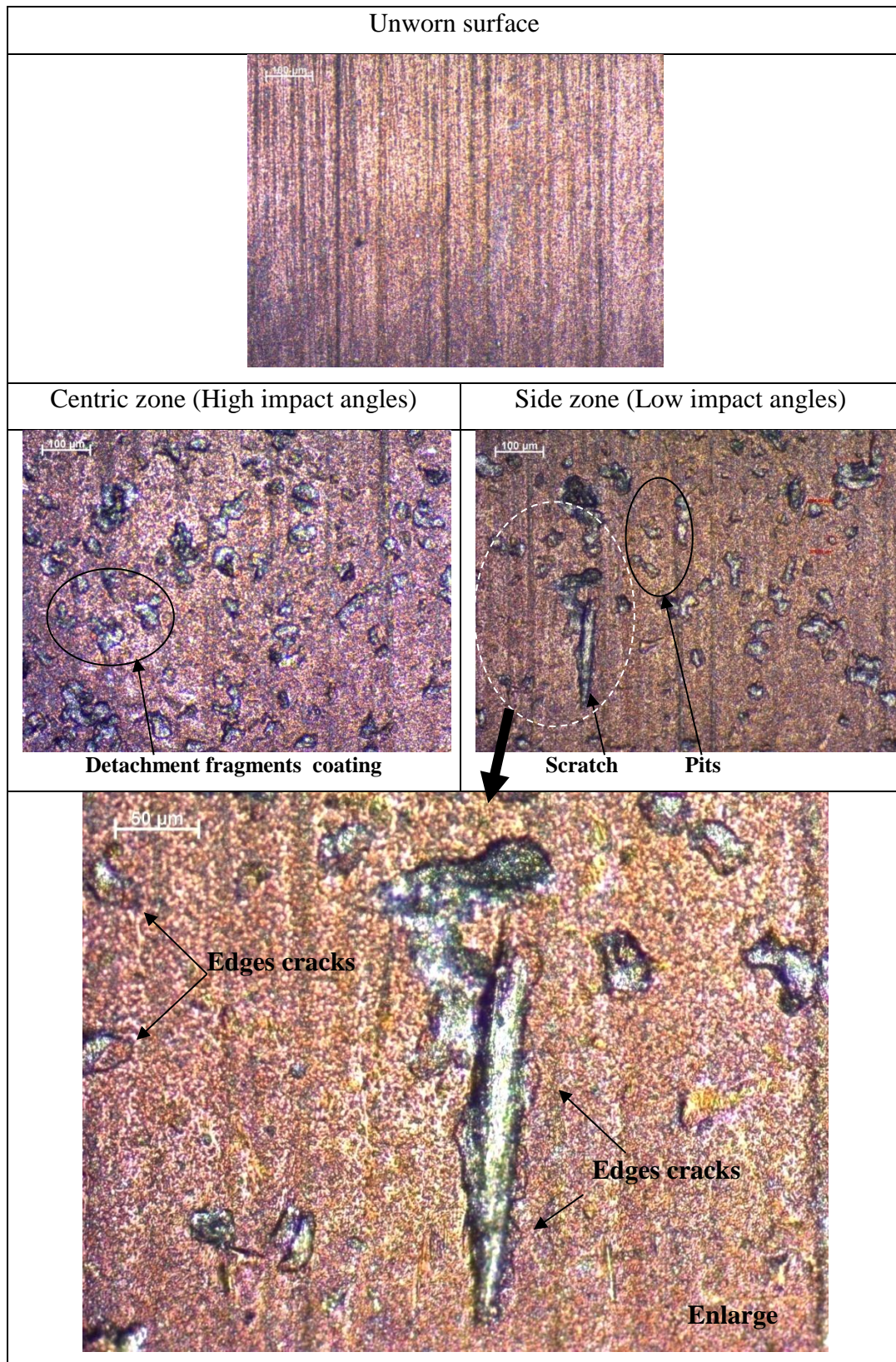
Figure 10.11 Erosion damage on (PN+AlTiCN).

10.8.3 SEM images

Figure 10.12 shows the cross-sectional SEM micrographs at lower magnification of the eroded surface coated with PN + TiAlCN after striking by 14400 shots of aluminium balls at central location. Figure 10.12b reveals partial coating removal as pits probably caused by fatiguing and micro-cutting described in previous section 10.7.3 for (PN + TiN) Coating. However, examination of the eroded wear track of the PN + TiAlCN coated surface showed high wear resistance.
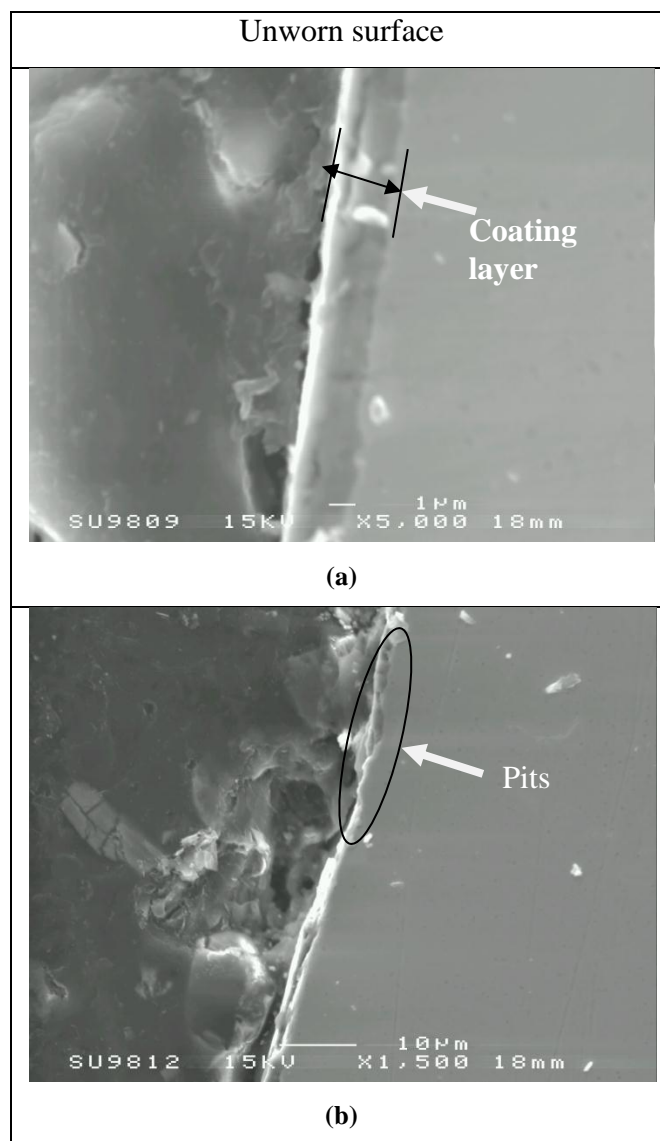
Figure 10.12 Damage of (PN + TiAlCN) coated.

10.9 Wear Scar in CrN Coated Samples

Figure 10.13, shows the wear damage produced on the CrN coated specimens. As in the previous cases, the difference between CrN coated and PN+ CrN was the significant. The CrN coated sample presented a visible elliptical shape damage whilst the PN+ CrN coated sample presented surface damage not visible at this scale.

| CrN coated	PN+ CrN coated
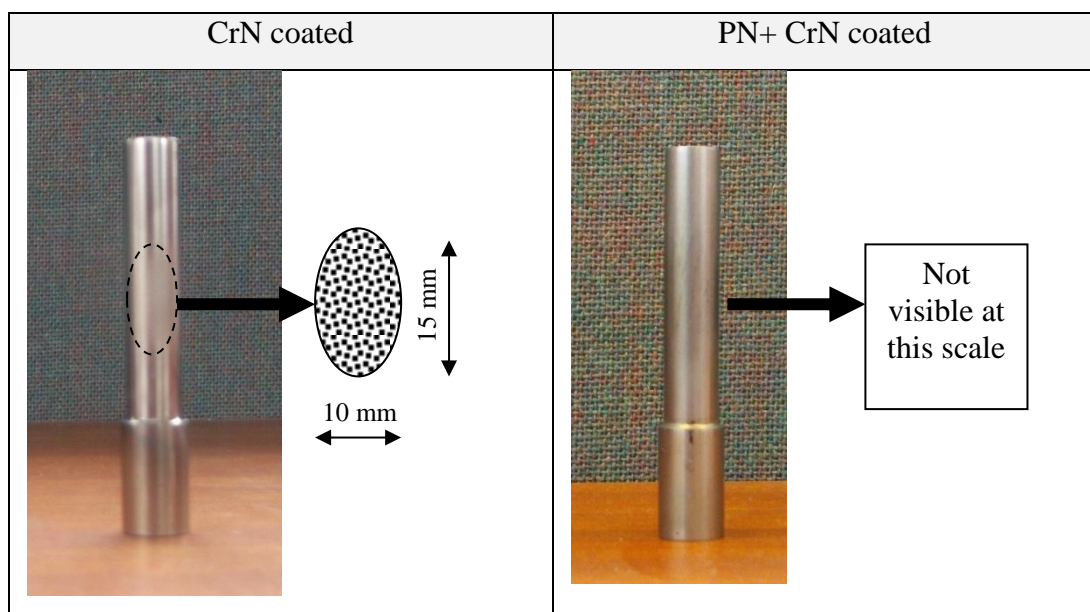
Figure 10.13 Wear scars on (CrN) coated samples.

10.10. Micrographs of Eroded Surfaces

10.10.1 (PN + CrN) Coating

The wear damage on the sample coated by (Plasma nitrided + CrN) is shown in Figure 10.14. It is very similar to that shown in samples coated by (PN+ AlTiCN), and (PN + TiN). Higher damage was seen in the central part, whilst little damage occurred on both sides of the sample. The central zone surface encountered cohesive failure, due to the occurring more intense stress field. At the central zone the dominant wear mechanisms were identified as a combination of plastic deformation inflicted by the indentation of the solid particles with resulting indentation craters, and cutting erosion.

The removal of coating material from the side section resulted from cutting erosion, evidenced by more scratches being seen on the material surface.

Unworn surface	
Central zone (High impact angles)	Side zone (Low impact angles)
Craters **Pits**	**Crater** **Scratches**
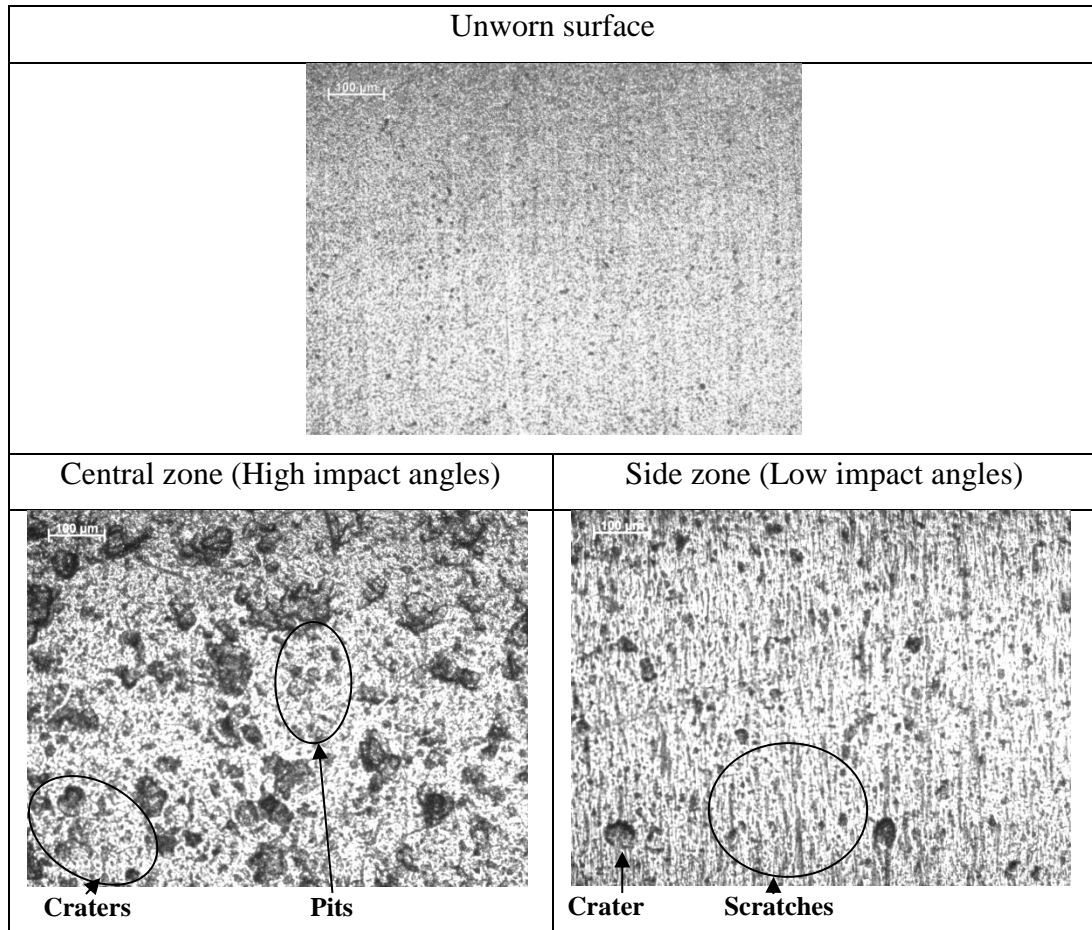
Figure 10.14 Erosion damage to (PN + CrN) coating.

10.10.2 (CrN) Coating

The damage produced in the CrN coated sample is shown in Figure 10.15. Damage is similar to that seen in the other coatings with no PN.

Unworn surface	
Central zone (High impact angles)	Side zone (Low impact angles)
 Detachment fragments coating	 **Detachment fragments coating**
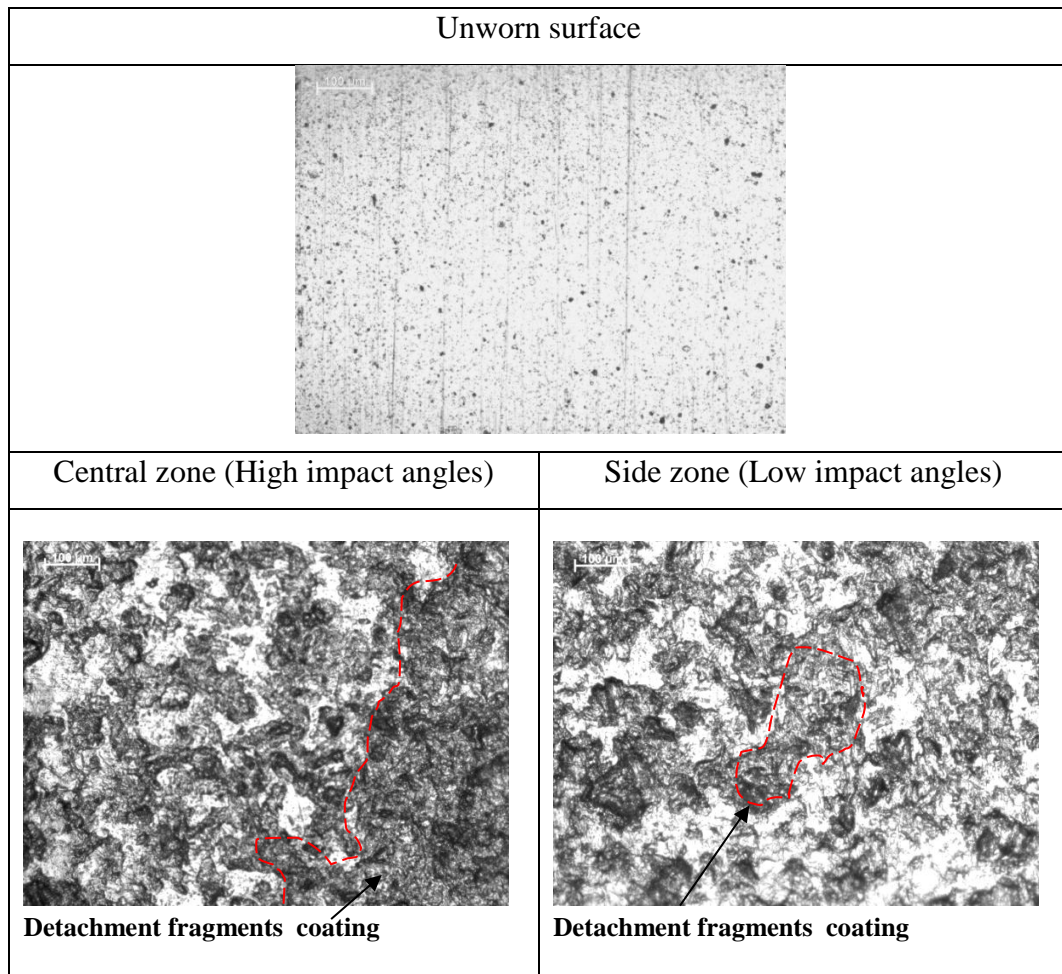
Figure 10.15 Erosion damage to (CrN) coating.

10.10.3 SEM Images

Figure 10.16 shows the SEM cross section for (PN +CrN) coated damage caused by the aluminium ball impingement. There was partial coating removed. Fragmentation and a gap between coating layer and substrate was starting to lead to easily the coating removal.

Unworn surface
Coating layer **Sample material**
Worn surface
Starting a gap between coating layer and substrate
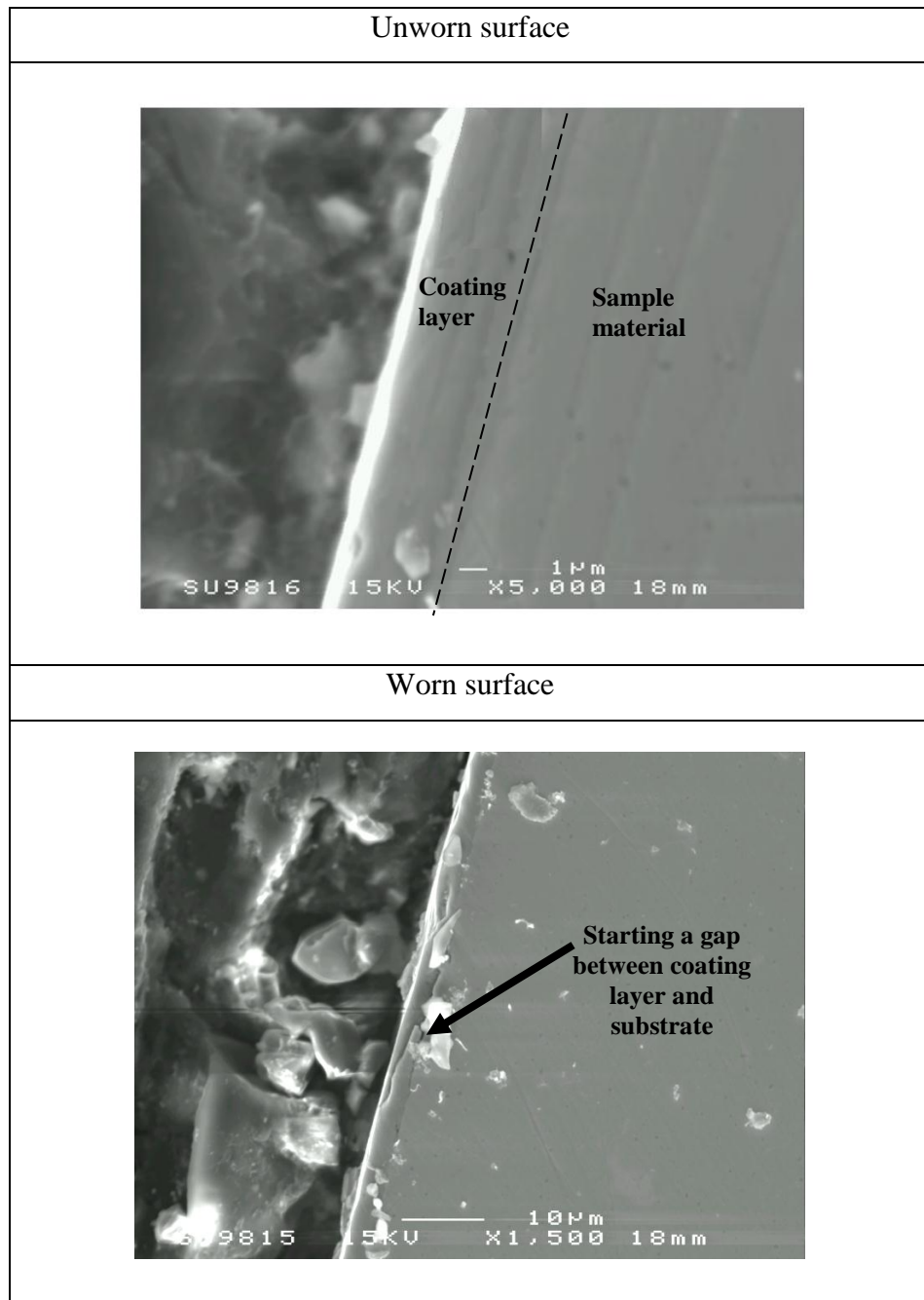
Figure 10.16 Removal the coating (PN + CrN) from the substrate.

10.11 Roughness Measurements

The study showed that the surface roughness increased as wear damage on the surface material increased. The results show that the coated surface of the samples was gradually roughened by continuous particles impact.

The Ra results obtained for coated samples impacted by 14400 shots at an impact velocity of 20 m/s, are presented in Figure 10.17. This shows a higher roughness for coated samples without plasma Nitrided treated (PN) for all coating materials, which registered a range of Ra from 0.539 to 1.645 µm. This ties in with the surface images of worn surfaces.
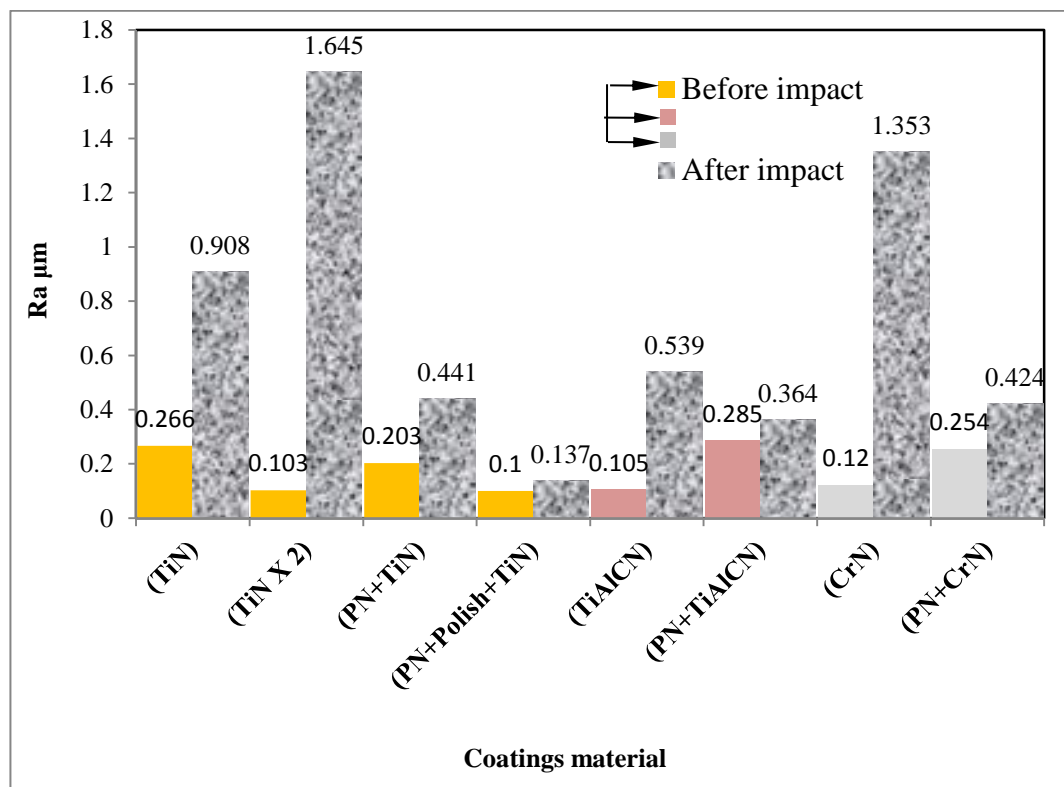
Figure 10.17 - (Ra) roughness for coating material before and after impacts.

In addition, The results of mass loss obtained from the tests after 14400 shots were subjected to comparison with roughness as observed in Figure 10.18. It is possible to see the effect of roughness on mass loss.
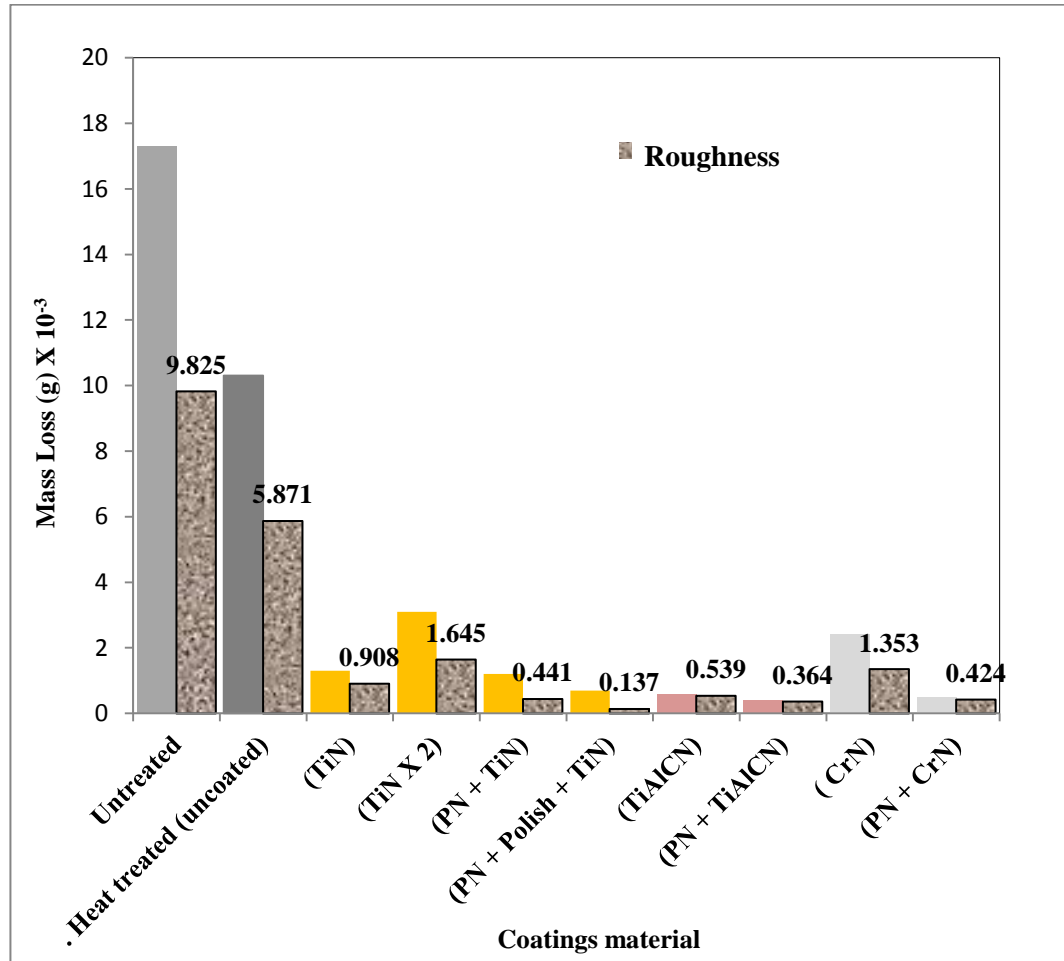
Figure 10.18 - (Ra) roughnes against mass loss..

10.12 Mass Loss and Erosion Rates

The erosion damage was characterized by the mass loss and the erosion rate. The samples were weighed before tests using a balance with a precision of ± 0.00001g. After that they were reweighed every 2400 shots. Mass loss and erosion rate were calculated by using equations 7.1 and 7.2.

The results of mass loss obtained from the tests after 14400 shots were subjected to comparison as observed in Figure 10.19. It is possible to see the effect of coating and the method of coating on mass loss. Samples treated with Plasma nitrided (PN) for all cases of coating material display a lower mass loss than those coated without Plasma nitrided (PN) treatment.
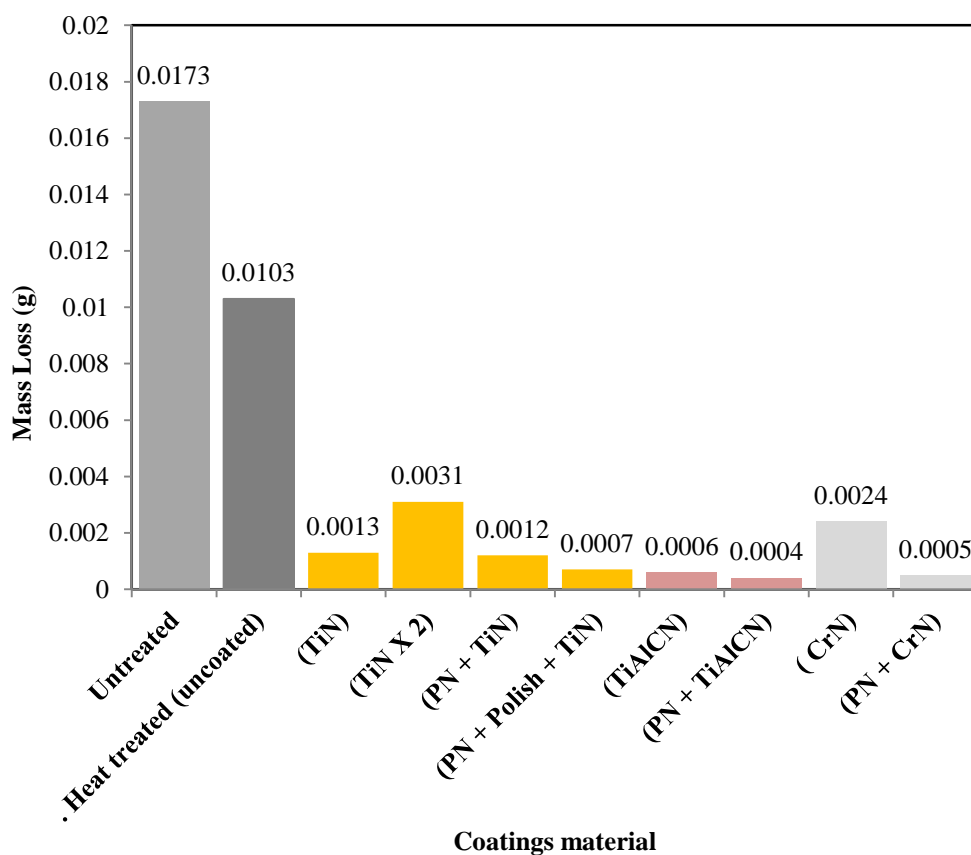
Figure 10.19 Mass loss comparison.

The erosion rates obtained from the tests were subjected to comparison as observed in Figure 10.20. It is possible to see the effect of Plasma nitride (PN) on erosion rate. Samples not with no Plasma nitride (PN) display a similar behaviour and showed the same tendency mentioned previously in Chapter 7 with uncoated surfaces, but with a difference in magnitude of wear they had higher wear resistance to erosion in comparison with those uncoated samples. The erosion curves related to (TiN, CrN and TiNX2) coatings indicated three possible stages in the erosion process.

The first stage, which extends up to 4800 shots, can be called the acceleration period since the erosion rate limit and rising with number of impacts. The loss of material from the coated surface was observed to occur primarily by the progression and the intersection of microcracks resulting in formation of fragments of coatings. Consequently, particle impacts on the surface will result in detachment of these fragments from the substrate and removal of fragments from locally eroded areas. Then, a deceleration period occurs in which erosion rate decreases. From curves the deceleration period was extended up to 9600 shots. This agrees with the literature review where it is possible to state that the hardness will increase with increase in shot numbers. Hardness increase is more effective for the layers located near the surface, residual stresses after impact induces compressive stresses in the sub-surface, the thickness of the compressive layer is a function of the number of shots, so increase in the magnitude of compressive stress could be a factor for decreasing the mass loss and erosion rate. There could also be some material from aluminium balls smeared on the surface of the specimen which could reduce the effect of impact forces on the eroded surface this happens in actual dies as explained in chapter 3. The final stage presents a steady state. It comprises shots between 9600 t0 14400 shots with wear curves nearly flat.

All erosion curves for the coatings with PN had a similar behaviour. No initial climb occurred on the wear rate (this may have been apparent if measurements had been taken before 2400 cycles). Although the incubation period and acceleration period might occur before 2400 shots with a lower amount of mass loss due to the good adherent coating material. However, the plots after 9600 shots show a steady state erosion rate. It is shown that the steady state erosion starts approximately from 4800 shots.
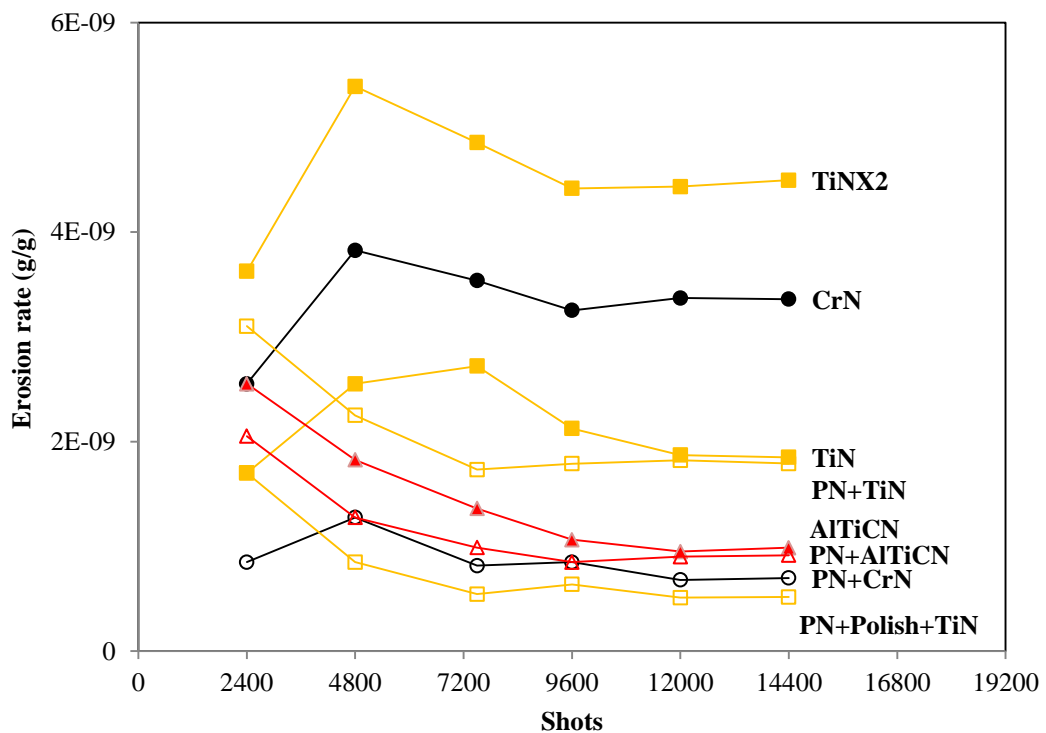
Figure 10.20 Erosion rate comparison.

10.13 Conclusions

Three coatings materials with different coating processes have been evaluated for their wear resistance and roughness. It was found that the Plasma nitride (PN) with coated material was the surface treatment with the best resistance to erosion. The coating material with the lower performance were Titanium nitride (TiN), duplex Titanium nitride (TiN X 2) and Titanium aluminium Carbo-nitrided (TiAlCN) showed higher in roughness and lower wear resistance.

The lower wear resistance coatings showed similar damage. Indentation of particles, fatiguing and cutting actions were the main wear mechanisms caused the coating were removed as chunks from the surface particularly at high impact angles, but also some scratches, pits, grooves and craters on both, high and low, impact angles was seen due to the cutting and fatiging actions.

11

Conclusions

11.1 Introduction

This chapter brings together the conclusions drawn from each of the sections of the study:

- Information on erosion from previous studies and current test methods.
- New test method development and justification.
- Initial wear studies and ball motion analysis (for flat specimens).
- Cylindrical specimen studies.
- Temperature effects.
- Effect of surface treatments and coatings.

11.2 Die Failure Analysis

Failure analysis has been carried out on aluminium die casting dies from industry and by study of previous work in this area. The effect of process parameters on material removal was examined in detail including the effect of metal velocity, angle of impact, die geometry and metal temperature. Visual examination disclosed that all dies sent back for evaluation (100,000 shots) had acquired a black oxide layer and pits on the surface (from erosion damage). Thermal cracks were examined microscopically. Dissolution and soldering mechanisms of H13 die steel were observed on the part of the core pin exposed to the melt.

Erosion can cause severe damage to the die, where the molten jet first hits the die surface resulting in loss of equipment and production downtime since it decreases of production quality.

11.3 Development of a New Laboratory Test

A new laboratory test has been developed based on apparatus for erosive wear tests. This was used to:

- To accelerate the wear effects and to allow for quantifiable erosive wear in a reasonable number of shots.
- To evaluate different materials or surface coatings, flat and cylindrical surfaces.
- Permit variation of the impact velocities, the impact frequency and the number of impacts for erodent particles on a specimen, and central/ eccentric impact.

- Give a realistic laboratory based simulation of erosive wear in aluminium die casting by achieving the important conceptions involve in die casting such as, dynamic load, temperature, pulsed load, oblique, geometry contacts due to varying die.

- Achieve a cost reduction over typical current test methods that involve actual casting machines.

11.4 Initial tests

Initial tests were carried out on flat specimens of different materials with continuous and pulsed flow using different impact angles and velocities. The wear scars were characterised by an elliptical shape at 30° and a circular shape at 90°.

Plastic deformation was characterised by deep indentation craters on the specimen surface. Cutting wear was characterised by pitting on the surface and craters without lips around them, and a ploughing action by craters with material piled up on the sides and in front of the particle impact direction. More damage was seen in the central section of the samples due to more particles impacting there with a higher kinetic energy.

Wear mechanisms were emphasized depending on the particle behaviour and impact angles. A cutting and ploughing combination was observed at 30° whereas a higher plastic deformation was present near or at a normal impact angle (60° and 90°), although the images showed a higher roughness of the surface at normal impact due to the deeper craters than those inflicting at low impact angles. In addition, impact velocity is another factor to consider. Higher particle velocities inflicted higher erosion rates and larger craters resulted on the surfaces.

The results obtained from the erosion testing indicated that H13 steel samples had a ductile behaviour showing a maximum erosion rate at 30°, then, decreasing at higher impact angles. At low impact angles the cutting seen leads to greater material loss than at higher angles where deformation dominates.

From the experimentation, it is possible to conclude that parameters such as: testing time, testing clearance, impingement angles and impact velocity are important. All these parameters can determine the physical damage to the surface and therefore the cumulative mass loss.

11.5 Cylindrical Surface Erosion Testing

A technique has been detailed that has enabled erosion rate to be measured for specimens mounted in two positions: central to and offset from the particle flow. A die casting mold has different shapes so the ability to replicate these is important.

From high speed photographs four regimes of particle behaviour were observed, impact only, impact and sliding, sliding only and pressure only.

The wear mechanisms have been identified as a combination of indentation, cutting and ploughing actions. However, damage at zones with high impact angles presented a more marked indentation and deformation actions, whilst for zones with low impact angles, damage was inflicted by aluminium balls presented a more marked cutting and ploughing actions.

Indentation action was characterized by craters with lips around them, cutting wear was characterised by craters without lips and pits on the surface and a ploughing action by craters with material piled up on the sides and in front of the particle impact direction.

A roughness analysis was conducted showed a difference in measured values of testing dependent on the location of impact on the surface material. Tests displayed a smooth profile at section with low impact angles due to domination of sliding. Deformation mechanisms presented of deeper craters with high roughness at central zones.

Different values for mechanical properties measurement in (micro-indentation) due to the mechanical behaviour of different orientations although the attributed to the effect of microstructure inhomogeneity were gathered from the sectional of bulk material. Comparable measurements indicated that a higher work-hardening was occurring in the central section of impact.

11.6 Temperature

Tests were run using two different temperatures in the system: 200°C which represented the temperature of injection of a semi-solid aluminium into the die, and 400°C which represented the temperature of molten aluminium injected into the die. The effects of increased temperature variation from 50°C to 400°C were also studied.

The results obtained showed a higher erosion rate compared to those results obtained with tests carried out at room temperature. It is assumed that this performance is due to the materials softening.

Wear mechanisms observed in tests were similar to those observed in room temperature tests. In addition, the erosion testing displayed an important factor to be considered when elevated the temperature in the system, oxidation formed on the surface which could cause a transition from ductile-to-brittle in mechanical behaviour.

11.7 Surface Treatment

The trial set of tests were conducted on surface treatments and coatings. It is possible to conclude that the Plasma nitride (PN) with coating material presented a higher erosion resistance at all impact angles, and had a a brittle behaviour. SEM sectioning image and micrograph observation revealed two main processes were contributing to the wear of the surface of the coating materials. The first was a brittle erosion process that caused progression and intersection of microcracks resulting in formation of fragments of coatings. Subsequent particle impacts on the surface resulted in the detachment of these fragments from the substrate and removal of fragments from eroded areas. The second was a cutting type process upon particle impingement which caused the cutting edges from local eroded areas and each impact removes an infinitely small amount of coating material. Cutting was characterised by the presence of the pits in areas where the coating was still remaining, and propagated grooves in areas where the coating was completely worn out. In addition, irregular and random scratches were present, particularly at low impact angles.

Examination of coating materials revealed an important parameter associated with the failure of the coating materials. This was adhesion of the coating material to the substrate surface. A well-adhered coating withstands wear much better compared to the poorest-adhering coating.

The results obtained from the roughness measurement indicated that the coated surface of the samples was gradually roughened by subsequent impact particles. Further, the roughness values associated with adhesion of coating materials with the substrate, the well-adhered coating material presents a lower roughness value compared to the poorest-adhered coatings.

11.8 Future Work

This work was carried out on material H13 steel, using solid spheroid particles, varying impact velocity, temperature and surface treatment. A greater understanding of how the impact of particles can be affected using different coating materials achieved by a variety of coating methods is now needed. This will increase the knowledge of the erosive wear resistance of coating materials as well as improve die life.

Specifically, details of studies are needed to see how with coatings:

- pits and craters grow with time and temperature.
- micro-cracks propagate in coating layers.
- lubricants can help reduce the damage to surfaces.
- different application techniques, such as: Physical Vapor Deposition (PVD), Chemical Vapor Deposition (CVD) and thermal spray affect impact resistance.

12. References

[1] L. Kosec, F. Kosel, M. Sokovic, Temperature field and failure analysis of die-casting die, International Scientific Journal 28 (2007) 182-187.

[2] M. Yu, R. Shivpuri, R. Rapp, Effects of molten aluminum on H13 dies and coatings, Journal of Materials Engineering and Performance 4 (1995) 175-181.

[3] E. J. Vinarcik, High integrity die casting processes, John Wiley Press, New Jersey, 2002.

[4] B. Upton, Pressure diecasting (part l), Metals, machines, furnaces, Oxford Pergamon, 1982.

[5] D. Heim, F. Holler, C. Mitterer, Hard coatings produced by PACVD applied to aluminium die casting, Surface and Coatings Technology 116-119 (1999) 530-536.

[6] R. Shivpuri, Y.L. Chu, K. Venkatesan, J.R. Conrad, K. Sridharan, M. Shamim, R. P. Fetherston, An evaluation of metallic coatings for erosive wear resistance in die casting applications, Wear 192 (1996) 49-55.

[7] I. Finnie, Erosion of surfaces by solid particles, Wear 3 (1960) 87-103.

[8] A. Street, The Die Casting Book, Portcullis Press Ltd., 1977, pp. 3-7, 349-351.

[9] L. J. D. Sully, 9th ed., Metals Handbook vol. 15, ASM International, Metals Park, OH, 1988, p. 286.

[10] H. Doehler, Die Casting, McGraw Hill Book Company, New York, 1951.

[11] NADCA, About Die casting Available at**:** http://www.diecasting.org/faq/. (last visited 25 July, 2010).

[12] D. F. Allsop, D. Kennedy, Pressure Die casting, Part 2: The Technology of the Casting and the Die, Pergamon Press, Oxford, 1983.

[13] J. R. Davis (Ed.), ASM Speciality Handbook, Tool Materials, ASM International, Materials Park, Ohio, 1995, p. 251-252.

[14] C. O. Herb, Die-casting: The Die-casting Process and Its Application in Modern Manufacture, Industrial Press, 1958.

[15] P. R. Beeley, Foundry technology, Butterworth-Heinemann, 2001.

[16] M. Blair, T. L. Stevens, Steel castings handbook, Steel Founders' Society of America, 1995.

[17] Mechanical properties H13 steel Available at: http://www.vegasfastener.com/steel-specials-H13.php. (last visited 19 June, 2011).

[18] B. S. N. Parashar, R.K. Mittal, Elements of Manufacturing Processes, Prentice-Hall of India, 2004.

[19] B. Andresen, Die casting engineering: a hydraulic, thermal, and mechanical process, Marcel Dekker, 2005.

[20] R. J. Keeley, I.C. Schools, Non-ferrous casting, International textbook, 1943.

[21] J. R. Beer, Gravity die-casting of aluminum and its alloys, Public Library of South Australia, 1966.

[22] G. E. Totten, K. Funatani, L. Xie, Handbook of metallurgical process design, Marcel Dekker, 2004.

[23] M. Tiryakioglu, A. International, Advances in the metallurgy of aluminum alloys: proceedings from Materials Solutions Conference 2001, the James T. Staley Honorary Symposium on Aluminum Alloys, 5-8 November 2001, Indianapolis, Indiana, ASM International, 2001.

[24] G. E. Totten, D. S. MacKenzie, Handbook of Aluminum: Alloy production and materials manufacturing, Marcel Dekker, Inc., 2003.

[25] W. J. Poole, M. A. Wells, D. J. Lloyd, Aluminium alloys 2006: research through innovation and technology, Trans Tech Publications, 2006.

[26] C. Tai, J. C. Lin, A runner-optimization design study of a die-casting die, Journal of Materials Processing Technology 84 (1998) 1-12.

[27] H. K. Barton, L. C. Barton, Diecasting die design, Machinery Pub. Co., 1955.

[28] W. Kurz, D. J. Fisher, Fundamentals of solidification, Trans Tech Publications, 1986.

[29] B. Chalmers, Principles of solidification, Wiley, 1964.

[30] D. A. Smith, Die design handbook, Society of Manufacturing Engineers, 1990.

[31] A. S. Sabau, R. B. Dinwiddie, Characterization of spray lubricants for the high pressure die casting processes, Journal of materials processing technology 195 (2008) 267-274.

[32] M. Muhic, J. Tusek, F. Kosel, D. Klobc, M. Pleterski, Thermal fatigue cracking of die casting dies, Materials Science and Engineering, A 472 (2008) 198-207.

[33] A. Persson, Strain-based approach to crack growth and thermal fatigue life of hot work tool steels, Scandinavian Journal of Metallurgy 33 (2004) 53-64.

[34] W. Young, Why die-casting dies fail, Paper no. G-T79-092, Proceedings of the 10th SDCE International Die Casting Exposition and Congress, North American Die Casting Association, St. Louis, MO, 1979, 1-7.

[35] A. J. Norwood, P. M. Dickens, R. C. Soar, and R. A. Harris, A new fatigue test procedure for die-casting tool materials. Proceedings of the Institution of Mechanical Engineers, Part B: Journal of Engineering Manufacture 221 (2007) 955-965.

[36] D. Klobcar, L. Kosec, B. Kosec, J. Tusek, Thermo fatigue cracking of die casting dies, Engineering Failure Analysis 20 (2012) 43-53.

[37]] D. Klobcar, J. Tusek, B. Taljat, Thermal fatigue of materials for die-casting tooling, Materials Science and Engineering: A, 472 (2008) 198-207.

[38] A. Perssona, J. Bergstrom, Ch. Burmana, S. Hogmark, Influence of deposition temperature and time during PVD coating of CrN on corrosive wear in liquid aluminium, Surface and Coatings Technology 146 –147 (2001) 42–47.

[39] C. Mitterer, F. Holle, F. Ustel and D. Heim, Application of hard coatings in aluminium die casting - soldering, erosion and thermal fatigue behaviour, Surface and Coatings Technology 125 (2000) 233-239.

[40] V. Joshi, R. Shivpuri, Investigating Tribochemical Behaviour of Nitrided die casting die surfaces, Surface and Coatings Technology 146-147 (2001) 338–343.

[41] A. Srivastava, V. Joshi, R. Shivipuri, Computer modeling and prediction of thermal fatigue cracking in die-casting tooling, Wear 256 (2004) 38-43.

[42] O. Salas, K. Kearns, S. Carrera, J.J. Moore, tribological behavior of candidate coatings for aluminum die casting dies, Surface and Coatings Technology 172 (2003) 117-127.

[43]   P. Panjan, M. Čekada, R. Kirn, M. Soković, Improvement of die-casting tools with duplex treatment ,Surface and Coatings Technology 180–181 (2004) 561-565.

[44] K. S. Klimek, A. Gebauer-Teichmann, P. Kaestner, K.T. Rie, Duplex-PACVD coating of surfaces for die casting tools, Surface and Coatings Technology 201 (2007) 5628-5632.

[45] C. Pfohl, K. T. Rie, M. K. Hirschfeld, J.W. Schultze, Evaluation of the corrosion behaviour of wear-resistant PACVD coatings, Surface and Coatings Technology 112 (1999) 114-117.

[46] K. T. Rie, C. Pfohl, S. H. Lee, C. S. Kang, Development of zirconium and boron containing coatings for the application on aluminium diecasting tools by means of MO–PACVD, Surface and Coatings Technology 97 (1997) 232-237.

[47] A. Lousa, J. Romero, E. Martínez, J. Esteve, F. Montalà, L. Carreras, Multilayered chromium/chromium nitride coatings for use in pressure die-casting, Surface and Coatings Technology 146–147 (2001) 268-273.

[48] A. Alexandrou, F. Bardinet, W. Loue, Mathematical and computational modeling of die filling in semisolid metal processing, Journal of Materials Processing Technology 96 (1999) 59-72.

[49] I. M. Hutchings, Tribology: Friction and Wear of Engineering Materials, Edward Arnold, London, 1992.

[50] B. Bharat, Principles and Applications of Tribology, Available at: http://books.google.co.uk/books, p 480 (last visited 15 July, 2010).

[51] J. A. Williams, Engineering Tribology, Oxford Science Publication, 1994.

[52] S. R. Paital, N.B. Dahotre, Calcium phosphate coatings for bio-implant applications: Materials, performance factors, and methodologies, Materials Science and Engineering: R: Reports, 66 (2009) 1-70.

[53] Y. Xue, H. M. Wang, Microstructure and dry sliding wear resistance of CoTi intermetallic alloy, Intermetallics, 17 (2009) 89-97.

[54] J. A. Williams, Wear modeling: analytical, computational and mapping: a continuum mechanics approach, Journal of Wear 225-229 (1999) 1-17.

[55] J. T. Burwell, Survey of possible wear mechanisms, Journal of Wear 1:119–141, 1958.

[56] E. Rabinowicz, Friction and Wear of Materials, 2 nd ed., 1995.

[57] N.P. Suh, An overview of the delamination theory of wear , Wear 44 (1977) 1-16.

[58] ASM Handbook Volume. 11 Failure Analysis and Prevention. (ASM International), Published: 2002, p1013-1018.

[59] J. G. A. Bitter, A study of erosion phenomena part I, , Wear 6 (1963) 5-21.

[60] F. J. Heymann, High-speed impact between a liquid drop and a solid surface, Journal of Applied Physics 40 (1969) 5113-5122.

[61] J. H. Brunton, J. E. Field, G. P. Thomas, The deformation of solids by the impact of liquids, and its relation to rain damage in aircraft and missiles, to blade erosion in steam turbines, and to cavitation erosion, Wear 8 (1972) 495-497.

[62] J. E. Field, M. B. Lesser, J. P. Dear, Studies of two-dimensional liquid-wedge impact and their relevance to liquid-drop impact problems, Proceedings of The Royal Society of London, Series A: Mathematical and Physical Sciences 401 (1985) 225-249.

[63] J. E. Field, ELSI conference: invited lecture: Liquid impact: theory, experiment, applications, Wear 233-235 (1999) 1-12.

[64] J. E. Field, The physics of liquid impact, shock wave interactions with cavities, and the implications to shock wave lithotripsy, Physics in Medicine and Biology 36 (1991) 1475-1484.

[65] Q. Zhou, N. Li, X. Chen, T. Xu, S. Hui, D. Zhang, Analysis of water drop erosion on turbine blades based on a nonlinear liquid-solid impact model, International Journal of Impact Engineering 36 (2009) 1156-1171.

[66] ASM Handbook Volume. 18 Friction, lubricant and wear technology. 1992, ASM International, United State.

[67] J. A, Laitone, Aerodynamic effects in the erosion process, Wear, 56 (1979) 239-246.

[68] G. L. Sheldon and I. Finnie, On the ductile behavior of nominally brittle materials during erosive cutting, Trans. ASME, 888 (1966) 387-392.

[69] I, Finnie, Some observations on the erosion of ductile metals, Wear 19 (1972) 81-90.

[70] I. Finnie, Some reflections on the past and future of erosion, Wear 186-187, Part 1 (1995) 1-10.

[71] I. M. Hutchings, R.E. Winter, Particle erosion of ductile metals: A mechanism of material removal, Wear, 27 (1974) 121-128.

[72] I. M. Hutchings, R.E. Winter, Solid particle erosion studies using single angular particles, Wear 29 (1974) 181-194.

[73] I. M. Hutchings, A model for the erosion of metals by spherical-particles at normal incidence. Wear 70 (1981) 269-281.

[74] J. G. A, Bitter, A study of erosion phenomena: Part II, Wear 6 (1963) 169-190.

[75] G. P. Tilly, W. Sage, The interaction of particle and material behaviour in erosion processes, Wear 16 (1970) 447-465.

[76] G. P, Tilly, A two stage mechanism of ductile erosion, Wear, 23 (1973) 87-96.

[77] M. Buijs, Erosion of glass as modeled by indentation theory, Journal of the American Ceramic Society 77 (1994) 1676-1678.

[78] P. H. Shipway, I. M. Hutchings, The role of particle properties in the erosion of brittle materials, Wear 193 (1996) 105-113.

[79] I. Hussainova, J. Kübarsepp, I. Shcheglov, Investigation of impact of solid particles against hardmetal and cermet targets, Tribology International 32 (1999) 337-344.

[80] P. A. Rizkalla, Development of a Hydroerosion Model using a Semi-Empirical Method Coupled with an Euler-Euler Approach, Thesis submitted for PhD Royal Melbourne Institute of Technology (RMIT), 2007.

[81] A. V. Levy, P. Yau, Erosion of steels in liquid slurries, Wear 98 (1984) 163-182.

[82] J. F. Santa, L.A. Espitia, J.A. Blanco, S.A. Romo, A. Toro, Slurry and cavitation erosion resistance of thermal spray coatings, Wear 267 (2009) 160-167.

[83] Yan, M., Fan, Z. Durability of materials in molten aluminum alloys, Journal of Materials Science 36 (2001).

[84] A. V. Levy, G. Hickey, Liquid-solid particle slurry erosion of steels, Wear 117 (1987) 129-146.

[85] V. Riddei, G. Roch, Cavitation erosion-A survey of the literature 1940-1970, Wear 23 (1973) 133-136.

[86] S. Hattori, E. Nakao, Cavitation erosion mechanisms and quantitative evaluation based on erosion particles, Wear 249 (2002) 839–845.

[87] About cavitation Available at: http://www.badgermetal.com/ml-dc/cavitation-effect.htm. (last visited 12 April, 2011).

[88] H. W. Bargmann, The mechanics of erosion by liquid and solid impact, International Journal of Solids and Structures 29 (1992) 1685-1698.

[89] H. W, Bargmann, On the time-dependence of the erosion rate—a probabilistic approach to erosion, Theoretical and Applied Fracture Mechanics 6 (1986) 207-215.

[90] D. R. Andrews, J. E. Field, The erosion of metals by the normal impingement of hard solid spheres, Journal of Physics 5 (1982) 571-578.

[91] R. Ghafouri-Azar, S. Shakeri, S. Chandra, J. Mostaghimi, Interactions between molten metal droplets impinging on a solid surface,International Journal of Heat and Mass Transfer 46 (2003) 1395-1407.

[92] H. Xie, X. Wu, Y. Min, Influence of Chemical Composition on Phase Transformation Temperature and Thermal Expansion Coefficient of Hot Work Die Steel, Journal of Iron and Steel Research, International 15 (2008) 56-61.

[93] A. Bahrami, S.H.M. Anijdan, M.A. Golozar, M. Shamanian, N. Varahram, Effects of conventional heat treatment on wear resistance of AISI H13 tool steel, Wear 258 (2005) 846-851.

[94] G. Li, X. Li, J. Wu, Study of the thermal fatigue crack initial life of H13 and H21 steels, Journal of Materials Processing Technology 74 (1998) 23-26.

[95] A. J. Smith, M. Stratmann, A.W. Hassel, Investigation of the effect of impingement angle on tribocorrosion using single impacts, Electrochimica Acta, 51 (2006) 6521-6526.

[96] M. Papini, J. K. Spelt, The plowing erosion of organic coatings by spherical particles, Wear 222 (1998) 38-48.

[97] K. Yıldızlı, M. B. Karamış, F. Nair, Erosion mechanisms of nodular and gray cast irons at different impact angles, Wear 261 (2006) 622-633.

[98] S. Dhar, T. Krajac, D. Ciampini, M. Papini, Erosion mechanisms due to impact of single angular particles, Wear 258 (2005) 567-579.

[99] I. M. Pinder, Surface topography of retrieved PCA acetabular liners: Proposal of a Novel Wear Mechanism, Journal of Materials Science Letters, 17 (1998) 1085-1088.

[100] K. Anand, S. K. Hovis, H. Conrad, R. O. Scattergood, Flux effects in solid particle erosion, Wear 118 (1987) 243-257.

[101] A. Levy, The platelet mechanism of erosion of ductile metals, Wear 108, 1-21 (1986).

[102] L. Alan, The solid particle erosion behavior of steel as a function of microstructure, Wear 68 (1981) 269-287.

[103] I. M. Hutchings, R. E. Winter and J. E. Field, Solid particle erosion of metals: The removal of surface material by spherical projectiles, Proceedings of the Royal Society of London. Series A, Mathematical and Physical Sciences 348, No. 1654 (Mar. 9, 1976) 379-392

[104] P. V. Rao, S. G. Young, D. H. Buckley, Morphology of an aluminum alloy eroded by a normally incident jet of angular erodent particles, Wear 92 (1983) 31-49.

[105] C. T. Morrison, R. O. Scattergood, J. L. Routbort, Erosion of 304 stainless steel, Wear 111 (1986) 1-13.

[106] D. Lopez, J. P. Congote, J.R. Cano, A. Toro, A. P. Tschiptschin, Effect of particle velocity and impact angle on the corrosion–erosion of AISI 304 and AISI 420 stainless steels, Wear 259 (2005) 118-124.

[107] H. J. A. C, Fundamentals of fluid motion in erosion by solid particle impact, International Journal of Heat and Fluid Flow 11 (1990) 170-195.

[108] M. J. Griffin, N. H. Macmillan, Longitudinal and transverse ripple formation during the solid particle erosion of lead, Materials Science and Engineering 80 (1986) L1-L4.

[109] A. Karimi, R. K. Schmid, Ripple formation in solid-liquid erosion, Wear 156 (1992) 33-47.

[110] G. Carter, M. J. Nobes, K.I. Arshak, The mechanism of ripple generation on sandblasted ductile solids, Wear 65 (1980) 151-174.

[111] R. J. K. Wood, T. F. Jones, Investigations of sand–water induced erosive wear of AISI 304L stainless steel pipes by pilot-scale and laboratory-scale testing, Wear 255 (2003) 206-218.

[112] A. Hamasaiid, G. Dour, T. Loulou, M. S. Dargusch, A predictive model for the evolution of the thermal conductance at the casting–die interfaces in high pressure die casting, International Journal of Thermal Sciences 49 (2010) 365-372.

[113] H. Oktem, T. Erzurumlu, F. Erzincanli, Prediction of minimum surface roughness in end milling mold parts using neural network and genetic algorithm, Materials and Design, 27 (2006) 735-744.

[114] L. C. Chang, I. C. Hsui, L. H. Chen, T. S. Lui, A study on particle erosion behavior of ductile irons, Scripta Materialia 52 (2005) 609-613.

[115] K. Yıldızlı, M.B. Karamış, F. Nair, Erosion mechanisms of nodular and gray cast irons at different impact angles, Wear 261 (2006) 622-633.

[116] P. V. Rao, D. H. Buckley, U.S.N. Aeronautics, S.A. Scientific, T.I. Branch, Time dependence of solid-particle impingement erosion of an aluminum alloy, National Aeronautics and Space Administration, Scientific and Technical Information Branch, 1983.

[117] F. J. Heymann, "Toward Quantitative Prediction of Liquid Impact Erosion", ASTM STP474, 1970.

[118] B. A. Lindsley, A. R. Marder, The effect of velocity on the solid particle erosion rate of alloys, Wear 225–229, Part 1 (1999) 510-516.

[119] A. N. J. Stevenson, I. M. Hutchings, Scaling laws for particle velocity in the gas-blast erosion test, Wear 181–183, Part 1 (1995) 56-62.

[120] B. A. Lindsley, A.R. Marder, The effect of velocity on the solid particle erosion rate of alloys, Wear 225–229, Part 1 (1999) 510-516.

[121] A.N.J. Stevenson, I.M. Hutchings, Scaling laws for particle velocity in the gas-blast erosion test, Wear 181–183, Part 1 (1995) 56-62.

[122] B. A. Lindsley, A. R. Marder, The effect of velocity on the solid particle erosion rate of alloy, Wear 225–229, Part 1 (1999) 510-516.

[123] M. Naim, S. Bahadur, Effect of microstructure and mechanical properties on the erosion of 18 Ni (250) maraging steel, Wear 112 (1986) 217-234.

[124] A. Levy, Y.-F. Man, Elevated temperature erosion-corrosion of 9Cr-1Mo steel ,Wear 111 (1986) 135-159.

[125] A. V. Levy, J. Yan, J. Patterson, Elevated temperature erosion of steels, Wear 108 (1986) 43-60.

[126] C. S. Ramesh, R. Keshavamurthy, B. H. Channabasappa, S. Pramod, Influence of heat treatment on slurry erosive wear resistance of Al6061 alloy, Material and Design 30 (2009) 3713-3722.

[127] T. E. Howes, P. M. Rogers, J. A. Little, I. M. Hutchings, Erosion-corrosion of mild steel in a temperature gradient, Wear 186–187, Part 1 (1995) 316-324.

[128] W. C. Oliver, G. M. Pharr, An improved technique for determining hardness and elastic-modulus using load and displacement sensing indentation experiments, J. Mater. Res. 7 (1992) 1564-1583.

[129] W. C. Oliver, G. M. Pharr, Measurement of hardness and elastic modulus by instrumented indentation: Advances in understanding and refinements to methodology, J. Mater. Res. 19 (2004) 3-15.

[130] J. Y. Kim, S. H. Kim, J. S. Lee, K. W. Lee, D. Kwon, Mechanical characterization of nano-structured materials using nanoindentation, Met. Mater. Int. 219 (2006) 12-26.

[131] D. Ma, C. Ong, T. Zhang, An instrumented indentation method for Young's Modulus measurement with accuracy estimation, Experimental Mechanics, 49 (2009) 719-729.

[132] J. Malzbender, G. de With, Indentation load–displacement curve, plastic deformation, and energy, J. Mater. Res. 17 (2002) 502–511.

[133] M. Duraiselvam, R. Galun, S. Siegmann, V. Wesling, B. L. Mordike, Liquid impact erosion characteristics of martensitic stainless steel laser clad with Ni-based intermetallic composites and matrix composites, Wear 261 (2006) 1140-1149.

[134] W. D. Nix, Elastic and plastic properties of thin films on substrates: nanoindentation techniques, Materials Science and Engineering: A, 234–236 (1997) 37-44.

[135] J. Gong, Z. Peng, H. Miao, Analysis of the nanoindentation load–displacement curves measured on high-purity fine-grained alumina, Journal of the European Ceramic Society 25 (2005) 649-654.

[136] K. S. SreeHarsha, Principles of Physical Vapor Deposition of Thin Films, Elsevier, 2006

[137] B. G. Mellor, Surface coatings for protection against wear, CRC Press New York, 2006.

[138] M. Berg, Plasma Nitriding, Institute for Fysik Astronomi, Åarhus University, Denmark, 1999.